

MICROCOPY RESOLUTION TEST CHART
NATIONAL BUREAU OF STANDARDS-1963-A

DTIC FILE COPY

(12)

AFGL-TR-86-0221

AD-A184 809

ANALYSIS OF GEOPHYSICAL DATA BASES
AND MODELS FOR SPACECRAFT INTERACTIONS

J. N. Bass	K. H. Bhavnani
N. A. Bonito	D. L. Cooke
K. G. Cottrell	D. E. Delorey
R. J. Eckhardt	K. J. Hahn
W. J. McNeil	M. F. Tautz

RADEX, Inc.
192 Log Hill Road
Carlisle, Massachusetts 01741

Final Report
August 1983 - October 1986

DTIC
ELECTE
SEP 16 1987
S D
CD

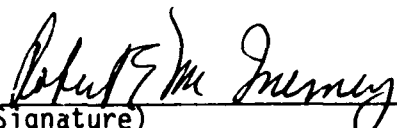
31 October 1986

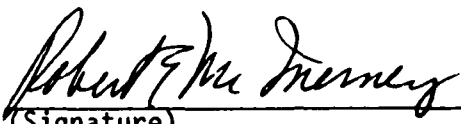
Approved for public release; distribution unlimited

AIR FORCE GEOPHYSICS LABORATORY
AIR FORCE SYSTEMS COMMAND
UNITED STATES AIR FORCE
HANSCOM AFB, MASSACHUSETTS 01731


87 9 14 002

"This technical report has been reviewed and is approved for publication"


(Signature)
ROBERT E. MC INERNEY
Contract Manager


(Signature)
ROBERT E. McINERNEY
Chief
Data Systems Branch

FOR THE COMMANDER


(Signature)
C. NEALON STARK
Director
Aerospace Engineering Division

This report has been reviewed by the ESD Public Affairs Office (PA) and is releasable to the National Technical Information Service (NTIS).

Qualified requestors may obtain additional copies from the Defense Technical Information Center. All others should apply to the National Technical Information Service.

If your address has changed, or if you wish to be removed from the mailing list, or if the addressee is no longer employed by your organization, please notify AFGL/DAA, Hanscom AFB, MA 01731. This will assist us in maintaining a current mailing list.

Do not return copies of this report unless contractual obligations or notices on a specific document require that it be returned.

REPORT DOCUMENTATION PAGE

1a. REPORT SECURITY CLASSIFICATION Unclassified		1b. RESTRICTIVE MARKINGS	
2a. SECURITY CLASSIFICATION AUTHORITY		3. DISTRIBUTION/AVAILABILITY OF REPORT Approved for public release, distribution unlimited	
2b. DECLASSIFICATION/DOWNGRADING SCHEDULE		4. PERFORMING ORGANIZATION REPORT NUMBER(S) RX-861031	
4. PERFORMING ORGANIZATION REPORT NUMBER(S) RX-861031		5. MONITORING ORGANIZATION REPORT NUMBER(S) AFGL-TR-86-0221	
6a. NAME OF PERFORMING ORGANIZATION Radex, Inc.	6b. OFFICE SYMBOL (if applicable)	7a. NAME OF MONITORING ORGANIZATION Air Force Geophysics Laboratory	
6c. ADDRESS (City, State, and ZIP Code) 192 Log Hill Road Carlisle, MA 01741		7b. ADDRESS (City, State, and ZIP Code) Hanscom AFB, MA 01731	
8a. NAME OF FUNDING/SPONSORING ORGANIZATION Aerospace Engineering Division	8b. OFFICE SYMBOL (if applicable) LCY	9. PROCUREMENT INSTRUMENT IDENTIFICATION NUMBER Contract F19628-83-C-0105	
8c. ADDRESS (City, State, and ZIP Code) AFGL/Hanscom AFB, MA 01731		10. SOURCE OF FUNDING NUMBERS	
		PROGRAM ELEMENT NO. 62101F	PROJECT NO. 9993
		TASK NO. XX	WORK UNIT ACCESSION NO. YG
11. TITLE (Include Security Classification) Analysis of Geophysical Data Bases and Models for Spacecraft Interactions			
12. PERSONAL AUTHOR(S) J.N. Bass, K.H. Bhavnani, N.A. Bonito, D.L. Cooke, K.G. Cottrell, R.J. Eckhardt, K.J. Hahn, W.J. McNeil, M.F. Tautz, D.E. Delorey*			
13a. TYPE OF REPORT Final	13b. TIME COVERED FROM 8/83 TO 10/86	14. DATE OF REPORT (Year, Month, Day) 1986 OCT 31	15. PAGE COUNT 276
16. SUPPLEMENTARY NOTATION * Boston College, Chestnut Hill, MA			
17. COSATI CODES		18. SUBJECT TERMS (Continue on reverse if necessary and identify by block number) Spacecraft Charging, Shuttle Contamination, Beam-Plasma Interaction, Magnetospheric Dynamics, Trapped Particles, Magnetometer, CRRES, Atmospheric Structure, SPAN Graphics	
FIELD	GROUP	SUB-GROUP	
19. ABSTRACT (Continue on reverse if necessary and identify by block number) This contract supported on-going as well as planned research into environments and spacecraft interactions in near space. The major projects that were undertaken are summarized in this report. Models and geophysical data bases were investigated for spacecraft charging, shuttle contamination, electrostatic particle pushing codes, beam-plasma interaction in emitting probes, magnetospheric dynamics. adiabatic invariance of trapped particles, fluxgate magnetometer simulation and falling sphere accelerometers. In support of the CRRES project, a data management plan has been provided, and a graphics capability was developed for the SPAN network. Software development was involved in all phases, using CYBER, VAX and RIDGE computers.			
20. DISTRIBUTION/AVAILABILITY OF ABSTRACT <input checked="" type="checkbox"/> UNCLASSIFIED/UNLIMITED <input type="checkbox"/> SAME AS RPT. <input type="checkbox"/> OTC USERS		21. ABSTRACT SECURITY CLASSIFICATION Unclassified	
22a. NAME OF RESPONSIBLE INDIVIDUAL Robert McInerney		22b. TELEPHONE (Include Area Code) (617) 377-3718	22c. OFFICE SYMBOL AFGL/LCY

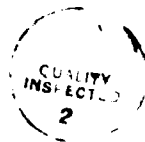
ACKNOWLEDGEMENTS

The work described in this report required the involvement and guidance of a number of individuals at AFGL, and their interest and encouragement is gratefully acknowledged.

Bob McInerney of the Data Systems Branch both initiated and coordinated the activities as Contract Monitor. Ed Robinson, our alternate monitor, and Bob Raistrick of the same branch provided invaluable help in numerous ways.

Various investigators were involved throughout the projects, and provided essential support and the opportunity for some challenging studies in their fields:

Herb Cohen, Mike Heinemann, Shu Lai and Al Rubin	Spacecraft Interactions Branch;
Sue Gussenhoven and Bob Redus	Space Particle Environment Branch;
Delia Donatelli and Jim Ernstmeyer	Active Space Experiments Branch;
Howard Singer	Space Plasmas and Fields Branch;
Russ Philbrick and Dwight Sipler	Ionospheric Interactions Branch.



Accession For	
NTIS CRA&I	<input checked="" type="checkbox"/>
DTIC TAB	<input type="checkbox"/>
Unannounced	<input type="checkbox"/>
Justification	
By	
Date	
Availability Status	
Availability Notes	
<div style="text-align: right; font-weight: bold; font-size: 1.2em;">A-1</div>	

TABLE OF CONTENTS

1.0	Investigation of Spacecraft Charging Models	1
1.1	Spacecraft Charging.	2
1.2	System Implementation and Operation at AFGL.	3
1.3	POLAR Code Validation.	6
1.4	Conclusions.	19
	References.	22
2.0	Investigation of Shuttle Contamination Software	23
2.1	Introduction	23
2.2	Overview of SPACE2	24
2.3	Software Enhancements.	30
2.4	Model Calculations	37
2.5	Conclusions.	47
2.6	Appendix	48
	References.	51
3.0	Development of an Electrostatic Particle Pushing Code	52
3.1	Introduction	52
3.2	General Concepts	53
3.3	Technical Aspects.	60
3.4	Initialization	67
3.5	Tests of the Program	69
3.6	Summary and Recommendations.	80
	References.	85
4.0	Beam-plasma Interaction and Charging in Emitting Probes.	86
4.1	Modeling of Spacecraft Charging with Beam Emission	86
4.2	Investigation of Beam-Plasma Instabilities	102
	References	116
5.0	Numerical Simulation of Magnetospheric Dynamics	117
5.1	Calculation of the Ionospheric Potential	118
5.2	Plasma Convection.	125
5.3	Appendix: Units and Dimensions	134
	References.	136
6.0	Adiabatic Invariant Analysis of Magnetospherically Trapped Particles.	137
6.1	Procedure	138
6.2	Results	143
6.3	Discussion.	162
	References	164

7.0	Simulation and On-orbit Calibration of Tri-axial Magnetometers for CRRES.	166
7.1	Signal Generation	167
7.2	Calibration	171
	7.2.1 Sensor Gain Ratios.	172
	7.2.2 Offset Determination.	173
	7.2.3 Relation to Sensors	173
	7.2.4 Calibration Example	175
7.3	Spin Axis Angle Calculation	175
7.4	Model Field Calibration	180
7.5	Conclusion.	181
8.0	CRRES Data Management Plan	182
8.1	Objectives	183
8.1.1	Experiments, Instruments and Agency Tapes	184
8.1.2	Objective and Scope of Data Reduction Task	185
8.1.3	Objective and Scope of Data Analysis Task	185
8.2	Time History Data Base	187
8.2.1	Design Concepts and Constraints	187
8.2.2	Design Structure and Format	187
	8.2.2.1 Header, Ephemeris, Magnetic Field and Attitude Files	189
	8.2.2.2 Calibration Files	189
	8.2.2.3 Experiment Files	190
8.3	Engineering and Environmental Studies	191
8.3.1	Engineering Studies	192
	8.3.1.1 Microelectronic Package Analysis (MEP)	192
	8.3.1.2 Internal Discharge Monitor (IDM)	194
	8.3.1.3 Gallium Arsenide Solar Panel (GASP) Data Analysis	195
8.3.2	Environmental Studies	195
	8.3.2.1 Statistical Radiation Belt Model	195
	8.3.2.2 Cosmic Ray Model and Flare Analysis	200
	8.3.2.3 Hot Plasma, Field and Wave Maps	202
	8.3.2.4 Radiation Belt Dynamics (High Energy Particles)	205
	8.3.2.5 Radiation Belt Dynamics (Plasma, Waves and Fields)	205
	8.3.2.6 Plasma Wave Analysis	206
8.4	Product Associated Data Base	207
8.4.1	Design Concepts and Constraints	207
8.4.2	Design Structure and Format	207
	8.4.2.1 Directory and Log Files	209
	8.4.2.2 Study Files	209
	8.4.2.3 Models and Geophysical Support Data	209
References	210

9.0	Structure of Atmospheric Density, Temperature and Winds from Rocket Sphere Experiments	211
9.1	Solution Procedures for Analyses of Falling Sphere Data.	213
9.2	Coordinate Systems and Glossary.	221
9.3	Data Demodulation and Reduction.	225
9.4	The Calibration Package.	227
9.5	Resource File.	234
9.6	Main Components of the Processing System	244
	References.	251
10.0	Graphics Capability for the SPAN Network	252
10.1	Introduction	252
10.2	Approach	254
10.3	Generating Metacode on the CYBER	254
10.4	Transmitting and Converting to VAX Metacode	258
10.5	Using SPAN	258
10.6	User's Guide	260
10.7	NCAR Metacode on CYBER and VAX	264
	References.	264

LIST OF FIGURES

1.0	Investigation of Spacecraft Charging Models	
1.1	POLAR Operational System on Cyber 750	4
1.2	Ion Density vs. Radius	7
1.3	c(e) Potential versus Radius	8
1.4	Surface Potential as a Function of h for $f_0 = 60^\circ$	11
1.5A	POLAR Contour Plot	13
1.5B	POLAR Ion Trajectories	13
1.5C	MACH Potential Contours	13
1.6A	POLAR and MACH Potentials in Ram for Mach 5	15
1.6B	POLAR and MACH Ion Number Density in Ram for Mach 5	15
1.7A	POLAR and MACH Potentials in the Transverse Direction for Mach 5	16
1.7B	POLAR and MACH Ion Number Density in the Transverse Direction for Mach 5	16
1.8	POLAR and MACH Ion Number Density in Wake for Mach 5	17
1.9	POLAR 2D Slice Plot Through the Middle of the 3D Grid and Disk	20
1.10	POLAR Model of DMSP Satellite.	21
2.0	Investigation of Shuttle Contamination Software	
2.1	Program ISODNPL Input Requirements31, 32
2.2	Constant density surface (4×10^{-13} g/cc) for water dumps.33
2.3	2-D contours of water densities 10m above payload during water dumps34
2.4	Program LINPLOT Input Requirements35
2.5	Densities along selected lines of sight from payload during water dumps.36
2.6	Total density outgasser and desorber contaminants along selected lines of sight39
2.7	Constant density surface for contamination around payload due to outgassers and desorbers40
2.8	2-D isodensity contours of fuel contaminant 15m above payload.41
2.9	Water vapor isodensity contours due to vent # 6877 10m above payload.45

3.0	Development of an Electrostatic Particle Pushing Code	
3.1	Making Macroparticles.54
3.2	Particle in Cell Density59
3.3	Energy Conservation for Plasma Oscillations.71
3.4	$r_k f_k$ for Excitation in the Second Mode73
3.5	$r_k f_k$ for the First Five Modes74
3.6	$r_k f_k$ for the Second Five Modes75
3.7	Dispersion Relation for Plasma Oscillations.76
3.8	Harmonic Motion Induced by a Velocity Curve.78
3.9	Energy Conservation for Hybrid Oscillations.81
3.10	$r_k f_k$ for Hybrid Oscillations82
3.11	Dispersion Relation in Hybrid Oscillations.83
4.0	Beam-plasma Interaction and Charging in Emitting Probes	
4.1	Predicted Voltage at Several Beam Currents for Four Charging Models at BERT Altitude of 150 km89
4.2	I-V Curves from the PLAS3 Model.92
4.3	Contours of Constant Critical Current and Peak Voltage for a Range of Flux and Neutral Pressure Expected in the Johnson Test Chamber93
4.4	I-V Curve Observed in the Johnson Test Chamber95
4.5	I-V Curve Observed During BERT Flight.96
4.6	Boom Potential and Sun Angle from SCATHA98
4.7	Total Current With and Without Photoionization as a Function of Spacecraft Potential	101
4.8	Schematic Diagram of the Model with Zero Order Distribution Function.	105
4.9	Dispersion Solutions for a 200 km BERT Environment	108
4.10	Dispersion Solutions for BERT Apogee.	109
4.11	Ray Trace of Reflected Wave	112
4.12	Ray Trace of Escaping Wave.	113
4.13	Oscillatory and Stochastic Ion Heating.	115
5.0	Numerical Simulation of Magnetospheric Dynamics	
5.1	Plasma per Unit Flux at 60T after Injection.	131
5.2	Plasma per Unit Flux at 175T after Injection	132
5.3	Plasma per Unit Flux at 435T after Injection	133

6.0	Adiabatic Invariant Analysis	
6.1	Omnidirection Energy Density in Mead Field Deduced by Adiabatic Variation for 300-400 KeV Electrons . .	145
6.2	Average Omnidirectional Energy in Mead Field	146
6.3	Energy Density at 90° Equatorial Pitch Angles in the Mead Field	147
6.4	Average Energy at 90° Equatorial Pitch Angles in Mead Field	148
6.5	Same as Figure 6.3, but for 40° Equatorial Pitch Angle.	149
6.6	Same as Figure 6.4, but for 40° Equatorial Pitch Angle.	150
6.7	Anisotropy Index at 270 KeV in Mead Field.	151
6.8	The Olson-Pfizer Model and Measured Magnetic Fields vs L During the Ascending Portion of the SCATHA Orbit; Electron Distribution Function at 218 KeV . .	153
6.9	Comparison of Measured (Symbols) and Fit (Curves) Distribution Functions on April 20, 1979	155
6.10	Same as Figure 6.9 but for 218 KeV Electrons. . . .	156
6.11	Noon Anisotropies for 218 KeV Electrons (Circles) and 275 KeV Ions (Triangles) from SCATHA Data . . .	158
6.12	Model Magnetic Field Parameters ALPHA, BETA, and DPHI.	159
6.13	Comparison of SCATHA Observations (Symbols) with Predictions Based on Adiabatic Variation (Lines). .	160
6.14	Same as Figure 6.13, except for 218 KeV Electrons .	161
7.0	Simulation and On-Orbit Calibration of Tri-axial Magnetometers for CRRES	
7.1	Definition of the Spacecraft Spin Axis in Earth Centered Inertial (ECI) frame	168
7.2	The Definition of the Orientation of One of the Magnetometers in the Coordinate System used for Spin Axis Angle Calculation	170
7.3	The difference between the magnetic field components input to the simulation system and those despun with the calibration factors calculated with this analysis at 0, 1 and 5 hours into the simulated orbit.	177

8.0	CRRES Data Management Plan	
8.1	Data Reduction (Time History Data Base)	
	Flow Chart.	186
8.2	Data Analysis (Product Associated Data Base)	
	Flow Chart.	186
8.3	Data Reduction (Time History Data Base)	
	Flow Chart.	188
8.4	Data Analysis (Product Associated Data Base)	
	Flow Chart.	207
9.0	Structure of Atmospheric Density, Temperature and Winds from Rocket Sphere Experiments	
9.1	Typical Sensor Signals around 130 km altitude . . .	226
9.2	X4, Y4 Sensor Signals at Uncaging	229
9.3	Z3 Sensor Signal at Uncaging.	230
9.4	Nutation Sensor Signal at Sphere Eject.	231
9.5	Z and Nutation Sensor Signals in Downleg Dynamic Range	232
9.6	Demodulated Z and Nutation Sensor Signals	233
9.7	Rocket Sphere Processing System	245
10.0	Graphics Capability for the SPAN Network	
10.1	Flow chart of Procedure to Transmit BDISPLO Graphics Over SPAN.	253
10.2	Original BDISPLO Tektronix Plot (CYBER)	255
10.3	TEKSIM Procedures which call NCAR Routines.	256
10.4	BDISPLO Tektronix Plot Using NCAR Routines.	257
10.5	Description of Program CONVMET.FOR.	259
10.8	Procedure to Run BDISPLO with NCAR Routines and Translate the NCAR Metacode on the CYBER.	261

LIST OF TABLES

SECTION 2

Table 1.	Ten-Second Payload Contamination.	43
Table 2.	36-Hour Contamination Due to Desorbers.	44
Table 3.	N ₂ Pressures Over Wing	47

SECTION 5

Table 1.	Computer Execution Times.	124
Table A.1	Units and Dimensions.	135

SECTION 7

Table 7.1	Results of Calibration.	176
-----------	---------------------------------	-----

SECTION 9

Table 9.1	Resource File Parameters for AC10.	235
Table 9.2	Resource File Parameters for AC12.	236
Table 9.3	Resource File Parameters for AC13.	237
Table 9.4	Resource File Parameters for AC14.	238
Table 9.5	Resource File Parameters for AC15.	239
Table 9.6	Resource File Parameters for AC16.	240
Table 9.7	Resource File Parameters for AC17.	241
Table 9.8	Resource File Parameters for AC08.	242
Table 9.9	Resource File Parameters for AC18.	243

1.0 Investigation of Spacecraft Charging Models

The charging of spacecraft and/or spacecraft surfaces by energetic electrons has been observed at geosynchronous orbits (GEO) and Medium (≈ 1000 km) altitudes with the AFGL satellites SCATHA and DMSP. It has been predicted that auroral electrons can cause large objects to charge in low Earth orbit (LEO). In addition, high spacecraft potentials can be produced by the effect of unneutralized particle emitters.

AFGL experiments include the SCATHA satellite, intended specifically to study charging at GEO; the DMSP satellites which have observed auroral charging at medium altitude; and the planned IMPS package that will study charged particle emissions.

1.1 Spacecraft Charging

AFGL has placed a strong emphasis on accurate modeling of charging phenomena, and contracted for the production of two sophisticated models, NASCAP,^(1,2,3) and POLAR,^(4,5) both written by S-Cubed. Installation, operation and evaluation of these programs was performed on CDC/CYBER computers and subsequently on a dedicated RIDGE computer.

The NASCAP program, comprehensively represents these processes at GEO. This program represents an attempt to faithfully simulate and depict spacecraft charging by numerically solving the full three dimensional problem. Elaborate plasma and material characteristics may be formulated in NASCAP, along with complex geometries and electrical connectivities of the surfaces. The NASCAP model uses a quasi-static Vlasov equation approximation to obtain surface charging fluxes, given potential distributions and the ambient environment conditions. After calculation of

dielectric charge transport and surface charge distributions, the spatial potential problem (Laplace's equation) is solved using a finite element, nested-mesh technique. The iterative cycle then returns to the Vlasov flux charging equation.

For lower earth and near polar orbits, the higher density plasmas that are encountered requires the consideration and treatment of more complicated processes. The numerical procedures must solve, in a mutually consistent way, a complicated system of non-linear coupled equations:

- a) computation of the grid space potentials ϕ given the net charge density ρ surrounding the object, by means of Poisson's equation

$$\nabla^2\phi = \rho/\epsilon_0;$$

- b) calculation of density ρ , given the electric fields, assuming the Vlasov equation

$$Df/Dt = 0$$

for constant distribution function f along particle orbits and determination of the net currents \bar{I} to the surface;

- c) updating of surface potentials \bar{V} on the vehicle using a circuit model analogy

$$\bar{I} = c d\bar{V}/dt + \sigma \bar{V}$$

where c and σ are the capacitor and conductivity matrices.

The grid potentials are determined by the conjugate gradient algorithm, the particle densities are obtained by outside-in tracking from the sheath edge and the circuit model is solved

by the ICCG method. The progress of new space missions in these orbits, such as the space shuttle and the space based radar, signals that the charging of large space structures is of concern. The POLAR code is designed to simulate and investigate these conditions.

The NASCAP program was first installed at AFGL in 1978. Subsequent to that, and through many revisions, technical help was provided in maintaining and validating this code. NASCAP was also used in the investigation of GEO charging phenomena. NASCAP is still being maintained and used, but the focus is now on POLAR and other supportive models such as MACH⁽⁶⁾ and the Cooke-Dubs model.⁽⁷⁾

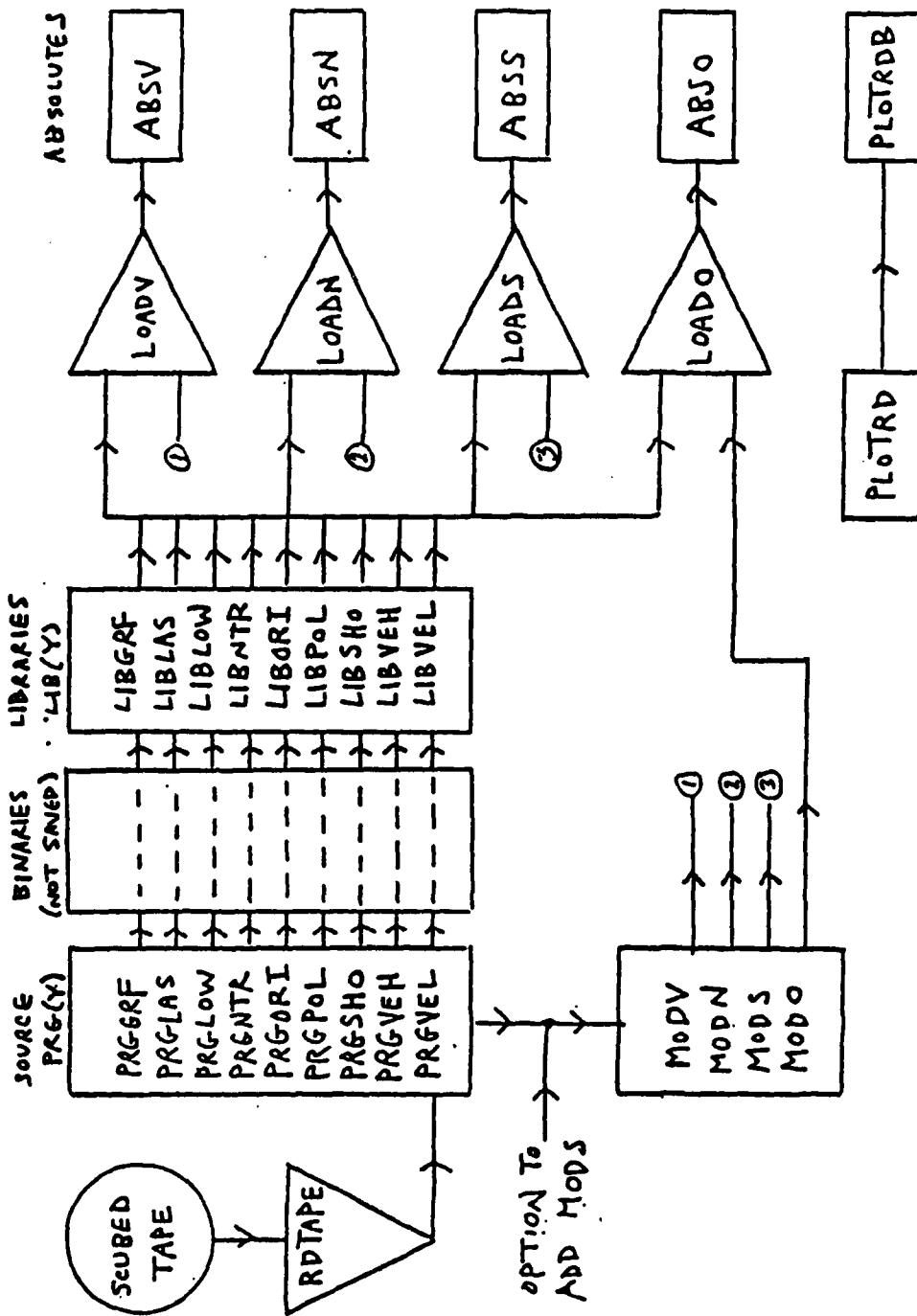
POLAR was installed at AFGL in 1983, and is now the object of an extensive validation effort. Some notable achievements include the development and use of the MACH code to evaluate POLAR error in the treatment of the wake of a charged satellite, and the Cooke-Dubs model of magnetic effects on electron collection which validated the POLAR approximation while discovering a few grid resolution effects.

1.2 System Implementation and Operation at AFGL

The NASCAP code and its auxiliary programs and POLAR⁽⁸⁾ have been installed on the CDC-6600 and CYBER-750 mainframes under two operating systems (NOS/BE and NOS). A comprehensive system was implemented to facilitate program maintenance and operational logistics. Figure 1.1 illustrates schematically the operational system employed for POLAR on the CYBER-750.

In 1984 the RIDGE 32 computer was acquired by PHK for dedicated POLAR running. Since the RIDGE is a self-contained mini-computer, most of the system management tasks fall to the user. System management support for POLAR on the RIDGE includes:

Figure 1.1 POLAR Operational System on CYBER 750



- a) a working knowledge of UNIX operating systems (Bourne and C shells)
- b) administration of system setup and account files; archiving results files on floppy disk
- c) monitoring disk usage and doing periodic compactions of the hard disk
- d) interfacing with Ridge personnel regarding system problems and hardware breakdowns.
- e) overviewing the operation of the QMS laser printer; setting up various font options and providing for Tektronix output.
- f) setting up port connections for terminal and modem use and providing for transport of files to and from the VAX-780 for printing or QMS output.

Operational support for running POLAR on the RIDGE requires:

- a) creating job input files for start and continue runs using POLAR keywords
- b) configuring and modifying spatial objects and their charging properties
- c) interpreting intermediate and final results to determine further runs or changes
- d) execution of POLAR auxiliary codes e.g. GRAPH3 (UNIX line plotter) and TEKPLOT (2D contour plotter) for graphical display

Code modifications are handled in a way similar to the method

used on the CYBER (see Figure 1.1). All modified routines are kept in separate UNIX sub-directories and are merged with the main code at the linkage stage, thus keeping the original source code untouched for easy reference.

1.3 POLAR Code Validation

In preparation for the arrival of POLAR at AFGL a study was made of the sheath structure for a spherical probe in a short Debye length plasma⁽¹¹⁾. The purpose of this study was to gain some insight into the type of solutions to be obtained in the POLAR region. This problem is governed by the Bernstein-Rabinowitz differential equation⁽¹²⁾ assuming a stationary plasma, Boltzmann electrons and a mon-energetic ion distribution at infinity. This equation cannot be solved as a conventional initial value or boundary value problem due to two side conditions occurring on the expression for ion density. A unique approximation scheme was developed which solved the side conditions numerically via bi-section and then generated the remainder of the solution using Runge-Kutta integration. A program called PROBE was written to implement this procedure. This code was used to compute sheath profiles over a wide range of parameter values. Figure 1.2, shows a family of curves obtained by this method for the ion density surrounding the probe. The curves illustrate the sharp sheath edge behavior which is found in short Debye length plasmas. Figure 1.3 shows the corresponding potentials in the sheath region. By analysing these results in detail we were able to show that the sheath width follows a power law behavior with respect to dimensionless potential.

The initial POLAR code runs looked at ion current collection by a quasisphere in a stationary plasma. The parameter range for surface potential and plasma Debye length was chosen to enable comparison to be made with computed results by

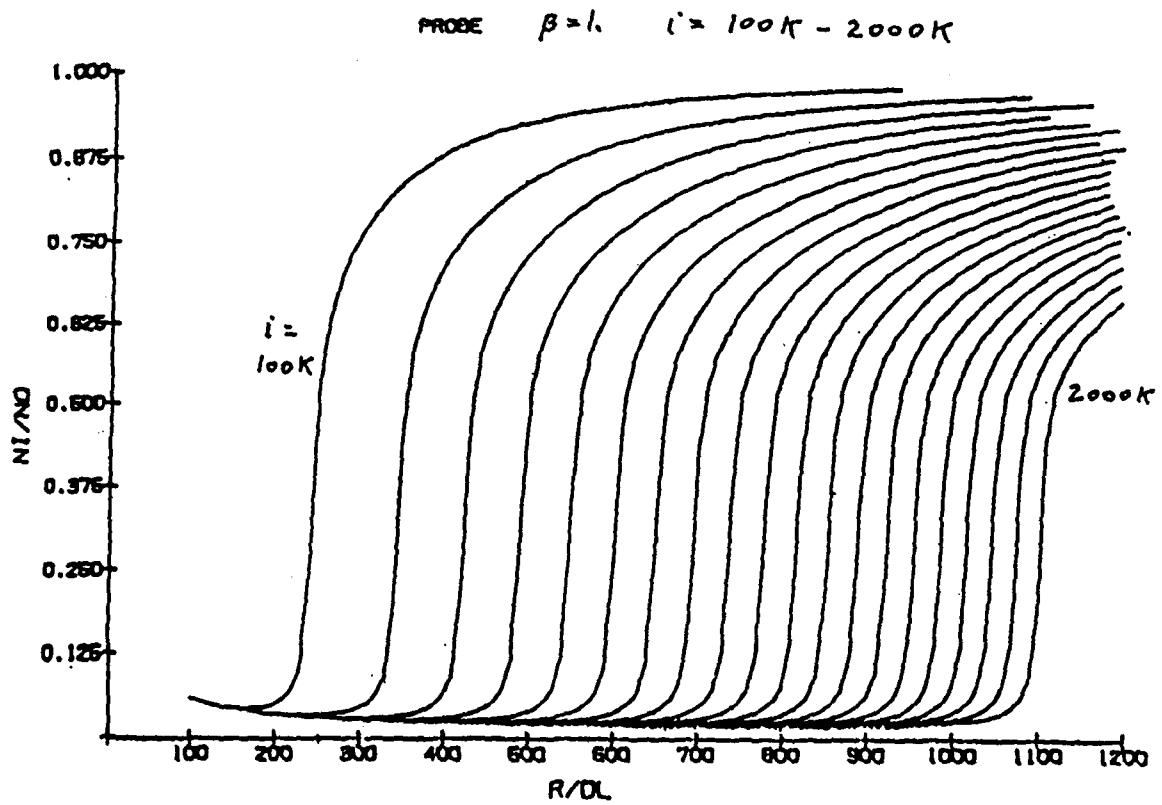


Figure 1.2 $n_i(r)$ Ion Density versus Radius

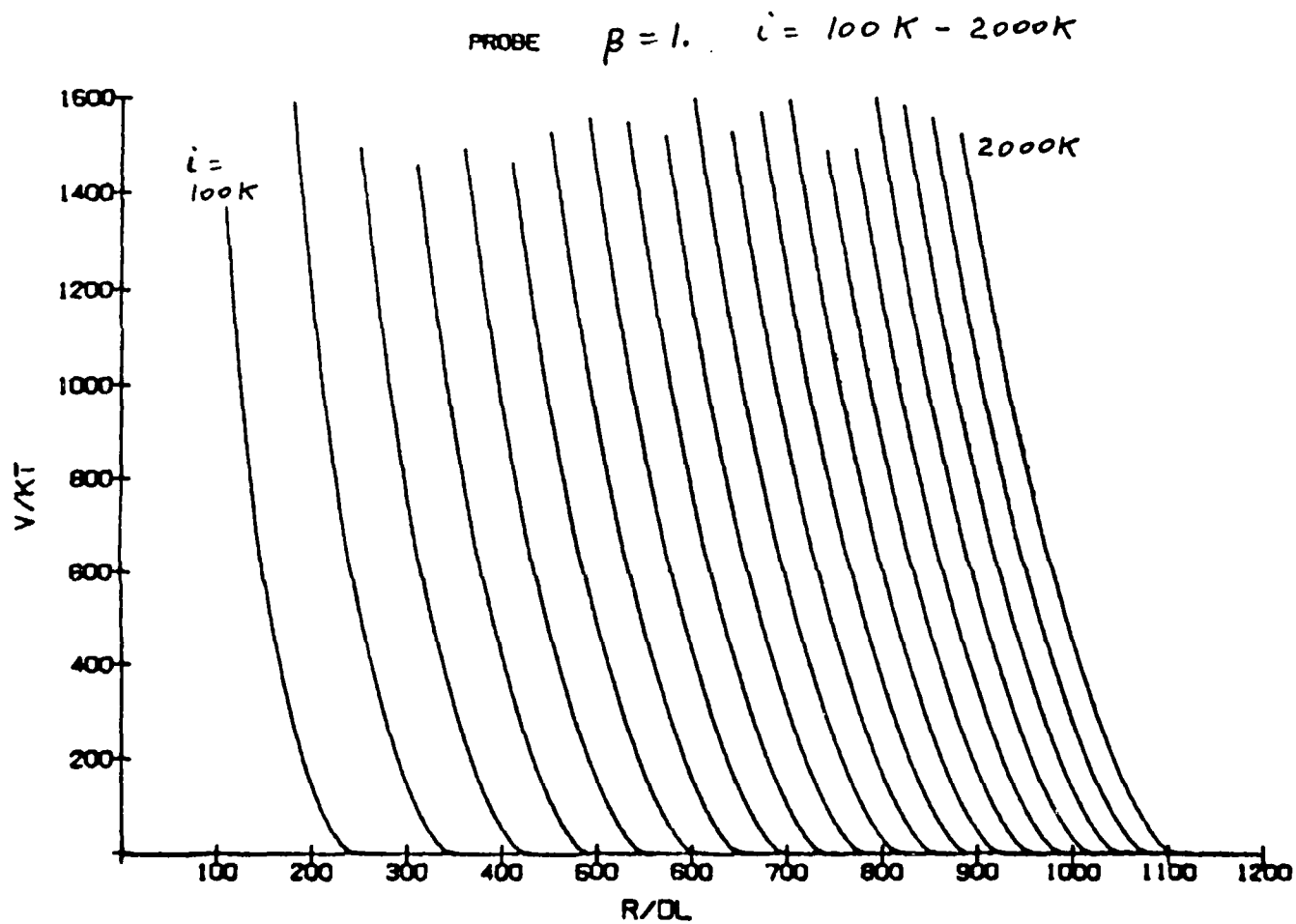


Figure 1.3 $x(\epsilon)$ Potential versus Radius

LaFramboise,⁽¹³⁾ theoretical values by Alpert et.al.⁽¹⁴⁾ and measured probe data by Makita and Kurika⁽¹⁵⁾. This study led to the discovery of some computation bugs in POLAR. After these errors were corrected the ion current was in satisfactory agreement with the known results.

An investigation was made of the behavior of a material surface in a Non-Maxwellian plasma using the current balance condition. A program, CURBAL, was written to estimate the charging on a satellite moving in an ionospheric plasma. The program integrates the ion and electron distribution functions numerically to obtain the magnetospheric currents to the vehicle. Secondary emission and backscatter effects in the surface material are taken into account. Ion drift currents are computed using an equation of Gurevich et al. which depends on the relative ion concentrations and on the complement of the Mach angle ϕ_0 . The charging voltage on the surface is determined from the current balance condition. The model has been applied to the DMSP/F6 satellite charging event of day 10, 1983. The measured electron and ion distribution functions for UT=74722 sec were input to the program and the following results were obtained:

- a) the currents calculated for magnetospheric ions are small compared to the electron currents.
- b) the effects of secondary emission and backscatter are of importance and reduce the electron current by $\approx 30\%$.
- c) the net electron current can be balanced by the flow current, but this condition does not uniquely define the model parameters ϕ_0 and N_{He^+}/N_0 .
- d) the charging potentials in the wake region can be estimated, assuming that the parameters ϕ_0 and N_{He^+}/N_0 are fixed by requiring a current balance at the detector location. This procedure leads to wake potentials of

approximately 1 KV. This result is relatively insensitive to the angle ϕ_0 .

The Figure 1.4 shows the surface potentials, obtained by procedure d) above, as a function of the angle θ which ranges from the ram direction ($\theta=0$) to the satellite wake ($\theta=180$).

Engineering design of spacecraft requires that computer codes, such as POLAR, be developed to simulate the spacecraft/environment interaction. In order to test such codes, there are three general lines of attack available: comparison with (1) experiment, (2) analytical results and (3) other computer codes. These approaches are limited by the fact that comprehensive experimental results are not yet available and that the interaction between a spacecraft and a flowing plasma is sufficiently complex that no comprehensive exact solutions exist for conditions typical of the low Earth orbit environment. As a consequence, the most effective tool for code verification is comparison with other computer codes. As part of the effort involved in the verification of the POLAR code, we have developed an independent computer code, called MACH, designed to validate the physical and numerical methods of POLAR.

The methodology of MACH (Mesothermal Auroral Charging) is somewhat closer to first principles than POLAR. MACH solves the same Vlasov-Poisson equations as POLAR but under different conditions. The most important difference is that no assumption about the sheath edge is made; the sheath and wake are determined as self-consistent solutions to the Vlasov-Poisson equations. However, the geometry of MACH is restricted to two dimensions, precluding detailed application to real spacecraft. The MACH program is an adaptation of TDWAKE.⁽¹⁶⁾

The MACH program was first brought up on the CYBER-750 and then ported to the RIDGE and converted from Fortran 5 to

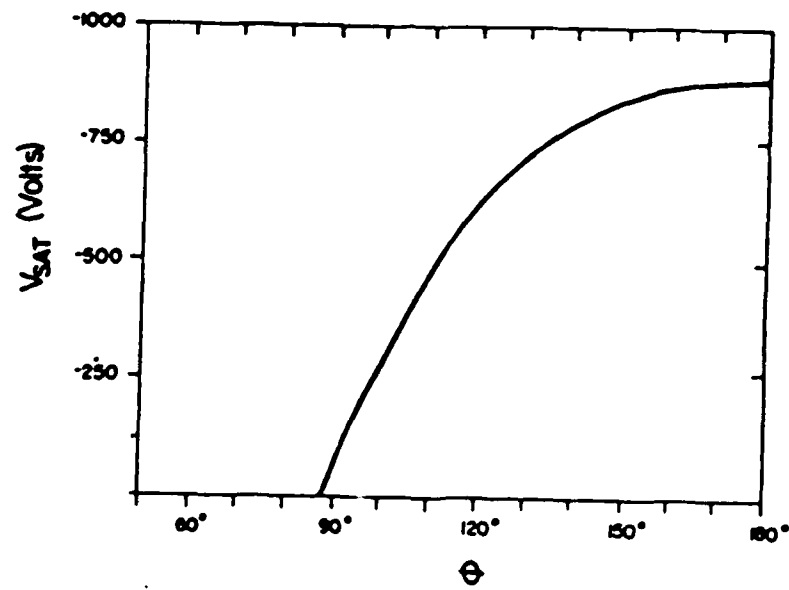


Figure 1.4 Surface potential as a function of θ for $\phi_0 = 60^\circ$.

Fortran 77. A considerable development effort has been put into MACH in order to make it into an effective analysis tool. This work included:

- a) reformatting of input and output. The program is now completely keyword driven with an interactive mode available for setup or diagnostic runs.
- b) addition of new geometrical objects (sphere and infinite cylinder) and physics computations (particle flow velocity)
- c) connections made to UNIX line plotter and to a 2D contour plotter MACHCON
- d) revamping of the particle tracking algorithm. The code now uses a modified leap-frog method.
- e) improvement of the track generator algorithm to allow for changes in flow velocity direction.
- f) implementation of a charge stabilization algorithm to improve the convergence properties of the potential solver.

MACH has passed a variety of Laplacian and Poisson (non-zero plasma density) tests and shows agreement with simple analytic models.

To compute models of the spacecraft interaction, we have specialized the spacecraft in both MACH and POLAR to charged disks in flowing plasmas.

For purposes of comparison, we show in Figure 1.5 a POLAR contour plot of the electrostatic potential. This figure clearly shows the division of the potential structure into near wake and far wake. To a first approximation, the near wake is symmetric in ram and wake, much like the potential about a disk in a nonflowing plasma. The far wake is a

POLAR WAKE MODEL

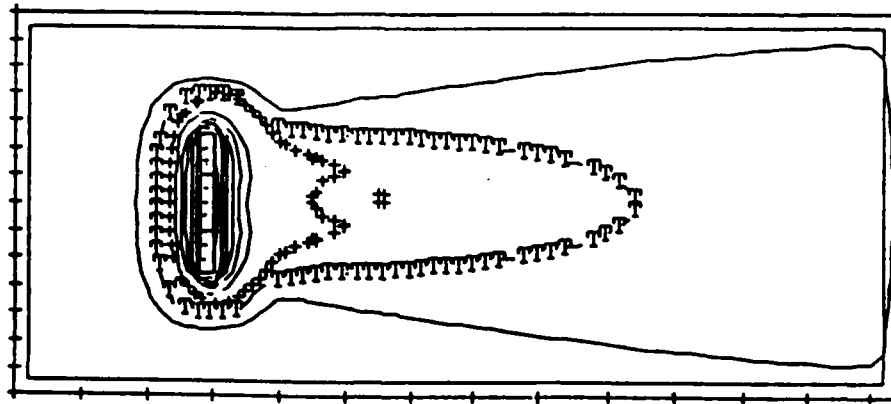


Figure 1.5A POLAR Contour Plot

POLAR WAKE MODEL

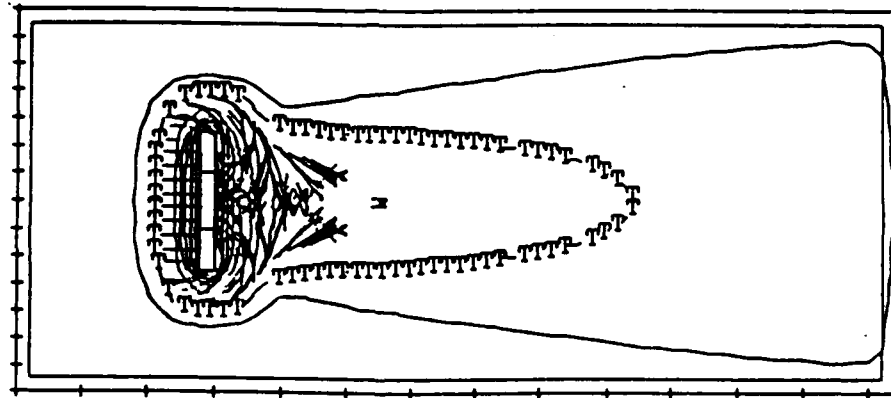


Figure 1.5B POLAR Ion Trajectories

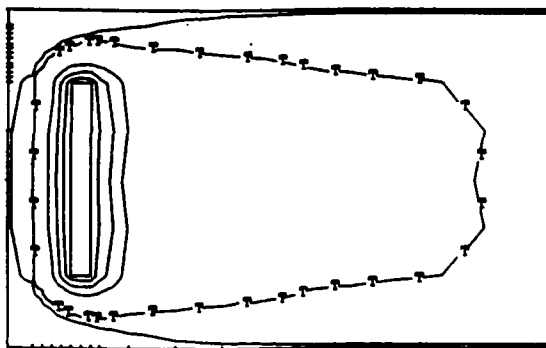


Figure 1.5C MACH Potential Contours

quasineutral wake similar to the geometric shadowing of the downstream flow by the disk. The size of the near wake in comparison with the far wake is an artifact of the POLAR code. The shadowing of the ions in POLAR is due to the spacecraft only and not the spacecraft plus sheath; one would expect that the narrowest part of the far wake to be about as wide as the near wake. Figure 1.5b shows ion trajectories from POLAR; it illustrates the nature of the ion flow on both sides of the disk, as discussed above. Potential contours from MACH are shown in Figure 1.5c. In contrast to the POLAR results, the shadowing in the wake is determined by the sheath radius rather than the disk radius. The line labeled "T" is the potential $X = e\phi/KT = 1$; the remaining contours represent $X = 0.25, 0.5, \dots, 64, 128$.

Figures 1.6a and 1.6b show POLAR and MACH profiles of electrostatic potential and ion number density, respectively, in ram for Mach 5. The POLAR potential is too broad and demonstrates a known tendency of POLAR to increase the sheath thickness by about one grid spacing. Figures 1.7a and 1.7b show the same profiles in the rim direction. The same tendency toward overexpansion of the sheath is apparent. The density profiles show fluctuations on the order of 10 to 20% of ambient which may be taken to be the order of magnitude of the error in the models at low resolution. Figure 1.8 shows ion number density contours in wake. We attribute errors on the order of 10% to 20% to both MACH and POLAR beyond a few disk radii in wake. Both codes show large density peaks in wake, MACH to twice ambient and POLAR to about 0.7 times ambient. Both figures are surprisingly high.

The MACH program does not currently handle magnetic field effects whereas these can be important in the spacecraft charging problem. In this area we have modeled the transport of electrons across a plane sheath in a magnetic field⁽⁷⁾ and compared the results to the POLAR code treatment. In the absence of a magnetic field, POLAR treats electron collection

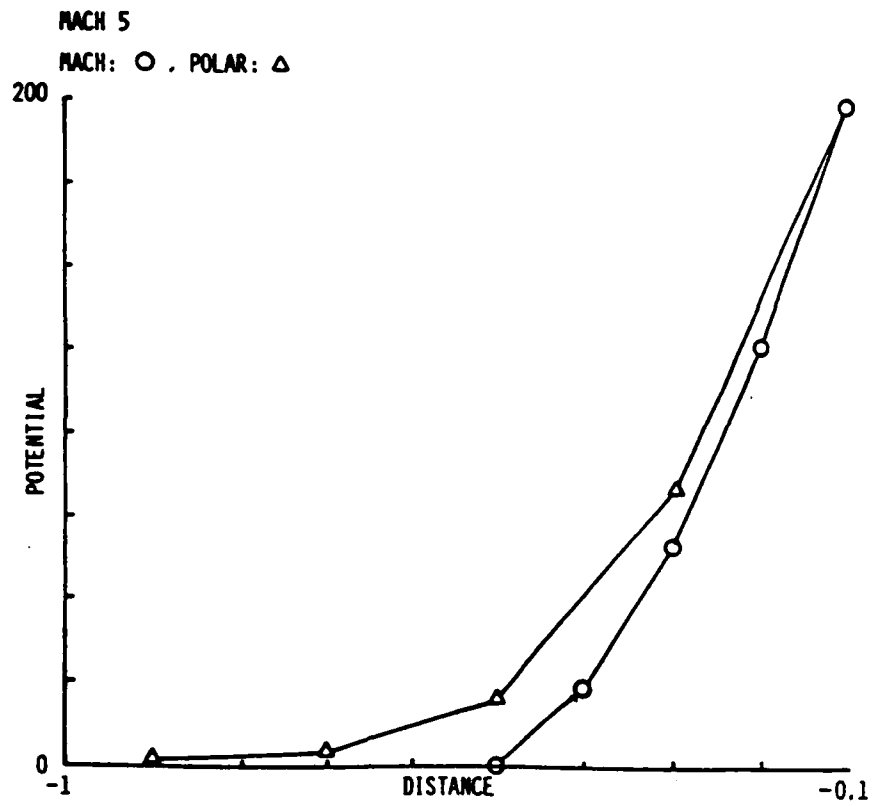


Figure 1.6A POLAR and MACH Potentials in Ram for Mach 5

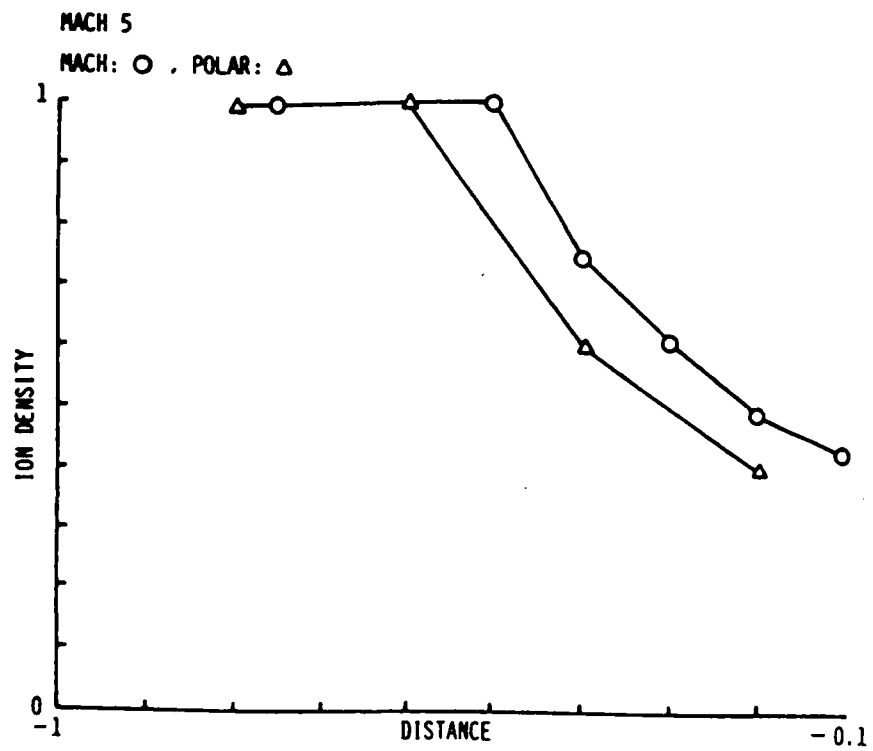


Figure 1.6B POLAR and MACH Ion Number Density on Ram for Mach 5

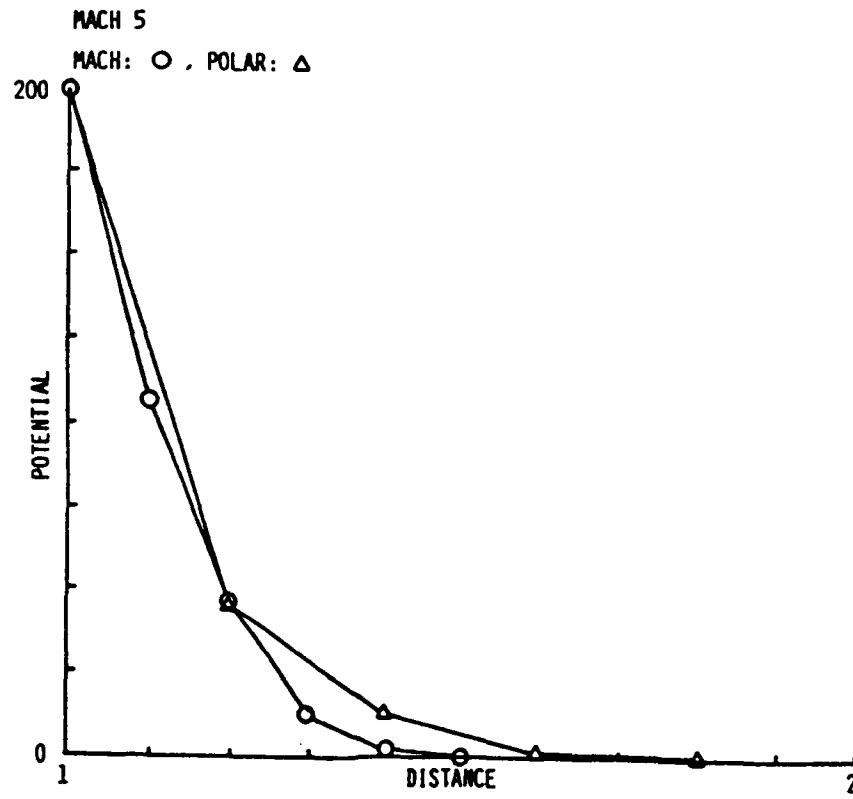


Figure 1.7A POLAR and MACH Potentials in the Transverse Direction for Mach 5

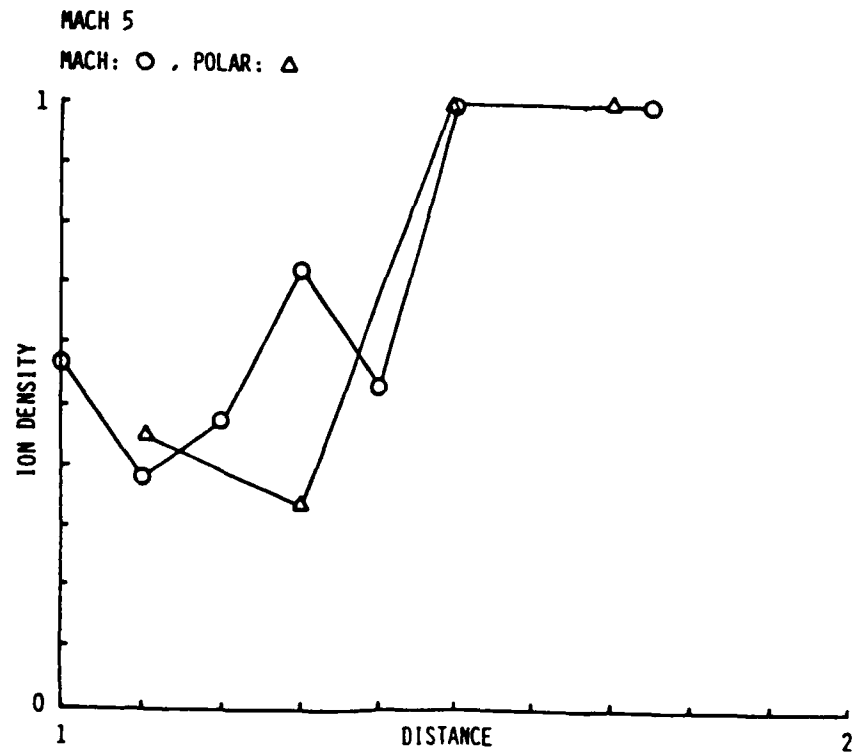


Figure 1.7B POLAR and MACH Ion Number Density in the Transverse Direction for Mach 5

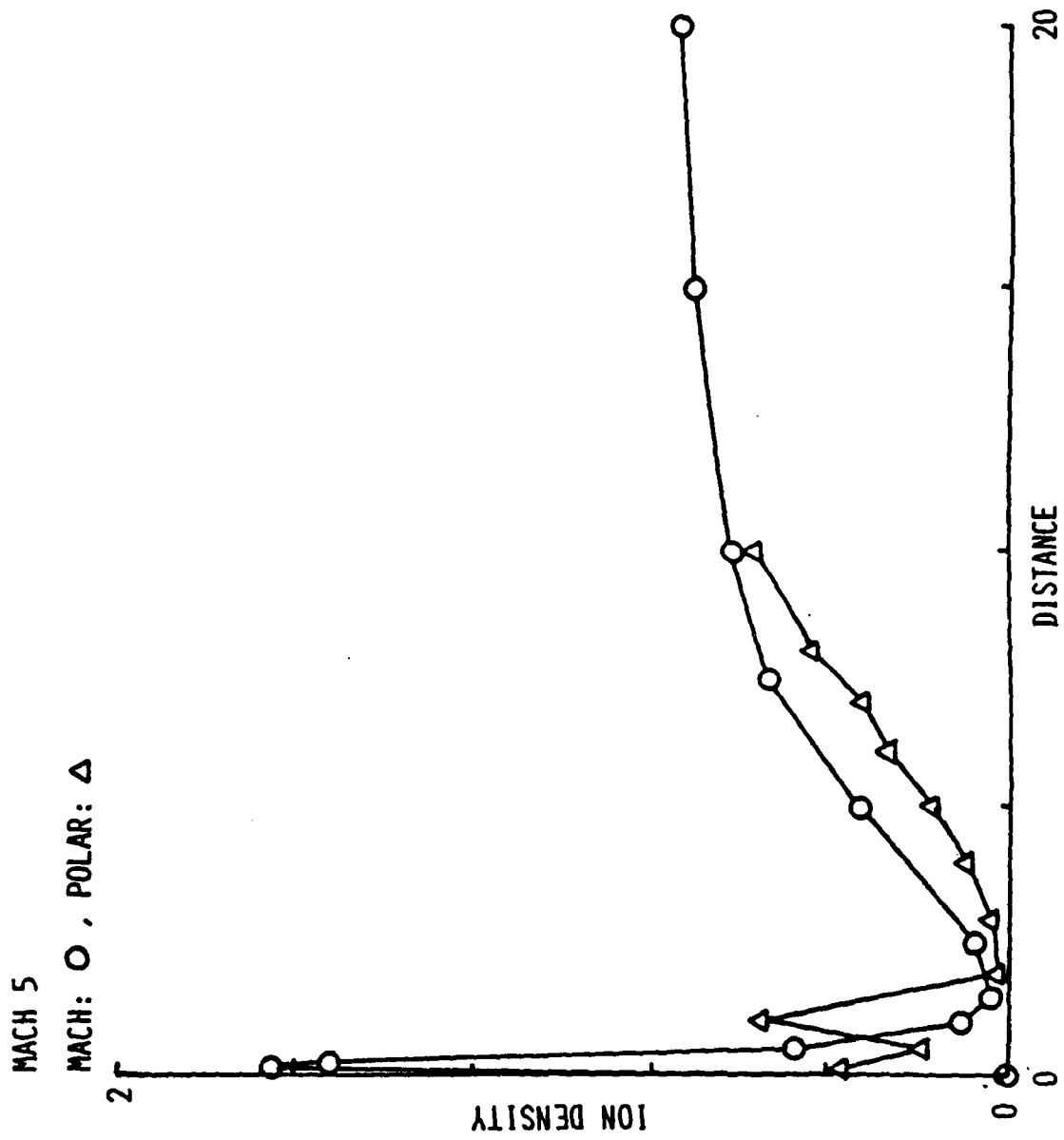


Figure 1.8 POLAR and MACH Ion Number Density in Wake for Mach 5

essentially as it does ion collection, i.e. with a sheath-edge dependent particle tracking method with different formulie for ion or electron presheath effects (ref Polar Manual). However, when there exists a magnetic field, both ion and electron trajectories can be affected, with the electron feeling the effects at much lower levels of B due to their lighter mass.

The model considered here is a flat plate moving through a plasma with a face normal to the ram and parallel to B. When charged to a 100kT/e positive potential, electrons, if they are to be collected, must be transported across a sheath much thicker than an ambient gyro-radius. At low levels of B, electron rejectories are relatively unaffected by the magnetic field, but as B is increased beyond a critical level given by $q_c = M_e * \omega_{pe}^2 / \omega_{ce}^2 = nm / (\epsilon_0 B^2)$, where ω_{pe} and ω_{ce} are the electron plasma and cyclotron frequencies, and M_e is the electron mach number, the electron trajectories curve back towards the sheath and are not collected. POLAR performed according to expectations provided the sheath was adequately resolved. We found that when the sheath is resolved with fewer than 3 or 4 mesh intervals, electron trajectories begin to curve back to the sheath edge at values of B greater than the anticipated critical level. From this study we conclude that

- a) the variable $q \approx n/B^2$ is of importance in this problem where n is the number of density and B is the magnetic field strength
- b) turbulence is not required to form a Child-Langmuir like sheath for $q > \frac{1}{2}$
- c) sheath edge instabilities may be important at $q \approx 1$
- d) end effects seem inescapable for $q < \frac{1}{2}$

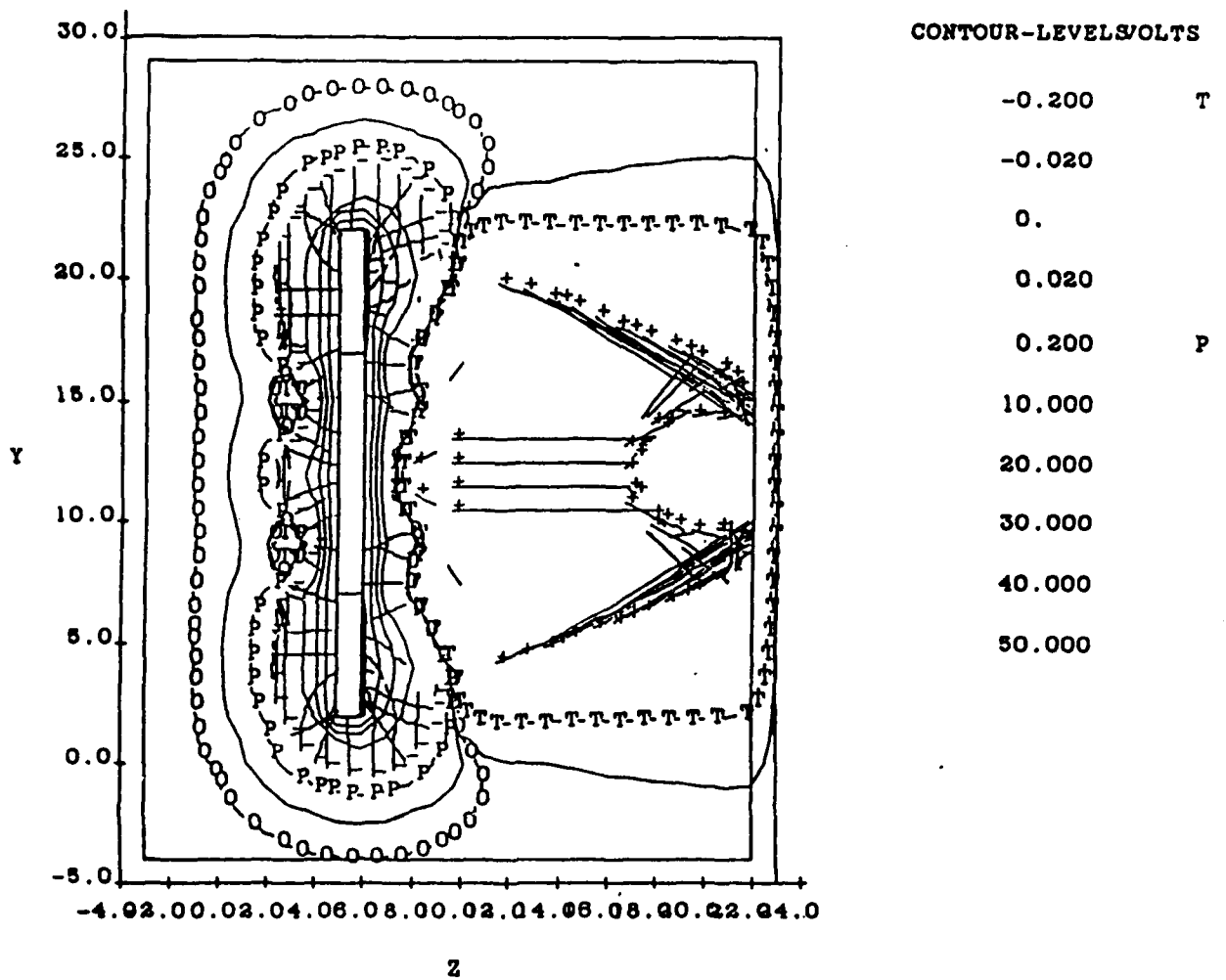
e) POLAR performs satisfactorily

Figure 1.9 shows the POLAR representation of the sheath edge formed around a large (planar) disk with magnetic field out of the page.

1.4 Conclusions

The ultimate aim is to develop POLAR to calculate the space craft interaction in a quite general way. The approach being taken is a bootstrap method; begin with a restricted code (MACH) which does the fundamental physics correctly, check it by available analytical and physical means and then use it as a standard of comparison for the more general code (POLAR). The first pass comparison of the results of the two codes for the case of the charged disk has demonstrated the effectiveness and feasibility of this approach. The MACH vs POLAR comparison needs to be continued for different geometrical objects and over a wider parameter range.

The comparison of one code (POLAR) against another (MACH), as discussed above, can prove the consistency of the solutions but cannot reveal the absence of a significant physics component. This could only be found by detailed comparison of code results with measured charging data. Large scale POLAR simulations have been limited to this point by lack of comprehensive experimental data and restrictive disk space on the RIDGE. With the planned acquisition of the 440 Megabyte hard disk there should be ample memory resources. There are three simulations under consideration. DMSP charging, SEPAC analysis and space shuttle modeling. A start was made on DMSP simulations by configuring a POLAR representation of the satellite as shown in Figure 1.10.



MODEL 2 $q = 220$, $q_d = 1.1$, $B = 0.3 \text{ G } \uparrow$
 $M_i = 8.0$, $M_e = 0.05$, $V_o = 43.0 \text{ v}$, $R = 1.8 \text{ m}$
 $N_o = 20 \times 10^5 \text{ cc}^{-1}$, $kT = 0.2 \text{ eV}$, $\lambda_d = 0.74 \text{ cm}$

Figure 1.9 POLAR 2D Slice Plot Through the Middle of the 3D Grid and Disk. Plasma Flows from the Left. Electron Trajectories are Started at the Sheath Edge Indicated by Symbol P.

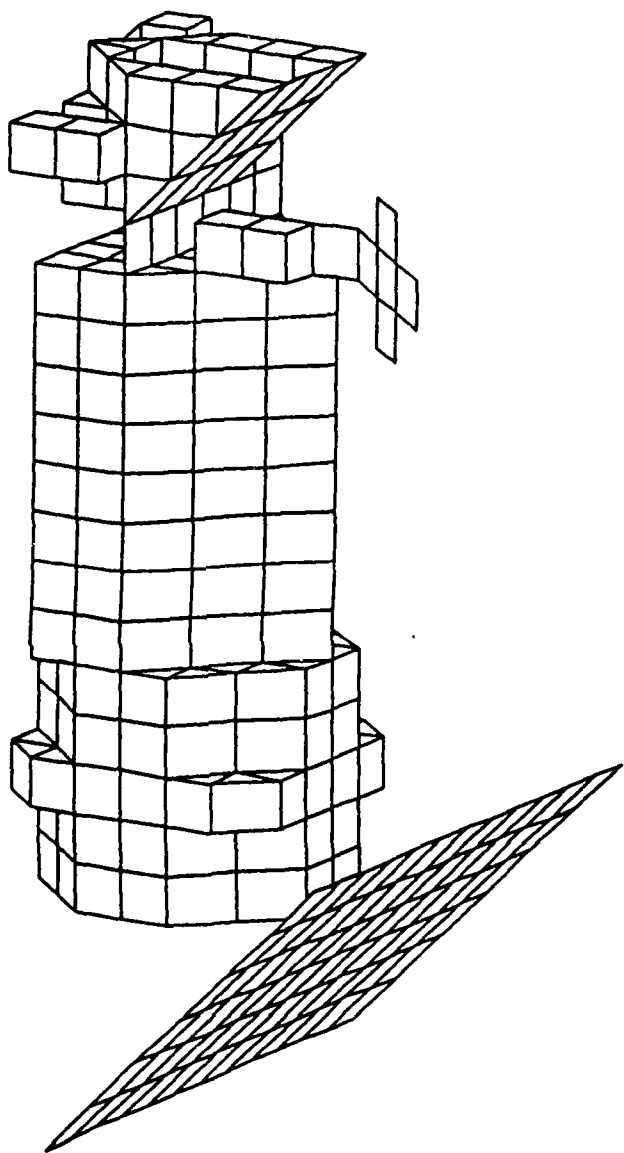


Figure 1.10 POLAR Model of DMPS Satellite

References

1. Katz, I. et al, "Extension, Validation and Application of the Nascap Code", Final Report, SSS-R-79-3904, January 1979, NASA CR-159595.
2. Stannard, P.R. et al, "NASCAP Programmer's Reference Manual", SSS-R-82-5443, March 1982.
3. Katz, I. et al, "Plasma Interactions of Spacecraft in Polar Orbit", SSS-R-83-6050.
4. Cooke, D.L. et al, "Preliminary Documentation for the POLAR Code", SSS-R-83-6027, October 1984.
5. Lilley, J.R. et al, "POLAR Users Guide", SSS-R-86-7563, AFGL-TR-85-0246, ADA173758.
6. Heinemann, M. et al, "Computer Models of the Spacecraft Wake", AGARD conference, The Hague, Netherlands, June 1986.
7. Cooke, D. et al, "Cross-Field Transport of Electrons; Implications for the POLAR Code; Spacecraft Charging", AGU 1986 Spring Meeting.
8. Tautz, M.F. et al, Private Communication
9. Tautz, M.F. et al, "Prediction of Materials Charging in Magnetospheric Plasmas", AFGL-TR-81-0088, ADA102906.
10. Tautz, M.F., and Rubin, A.G., "Threshold Conditions for Materials Charging in Maxwellian Plasmas", AFGL-TR-85-0020 ADA157123.
11. Tautz, M. and Rubin, A.G., Private Communication
12. Bernstein, I.B. and Rabinowitz, I., Phys. of Fluids 2, 112. (1959)
13. Laframboise, J.G., "Theory of Spherical and Cylindrical Langmuir Probes in a Collisionless Plasma at Rest", UTIAS Report #100.
14. Alpert, Y. et al, "Space Physics with Artificial Satellites", Consultants Bureau, N.Y. (1965).
15. Makita, H. and Kurika, K., "Current Collection by a Spherical Langmuir Probe Drifting in a Collisionless Plasma", Phys. Fluids, 21 (8), Aug. 1978.
16. Parker, L.W., "Computation of Collisionless Steady-State Plasma Flow Past a Charged Disk", NASA CR-144159.

2.0 Investigation of Shuttle Contamination Software

2.1 Introduction

Program SPACE2⁽¹⁾ models self-induced neutral molecular contamination for various space shuttle configurations. This system predicts surface mass loss rates, engine and vent plume flow rates, line-of-sight column densities of the resulting contaminants, and contaminant fluxes and deposition on surfaces. Transport mechanisms modeled include direct (straight line) transport from source (emitting surface, engine, or vent) to receiver (contaminated surface), surface reflection, scattering by ambient atmospheric molecules, and scattering of contaminant molecules by each other.

A version of SPACE2 has been acquired for use at AFGL. This version at present handles only the shuttle orbiter configuration, but could be expanded to handle spacelab configurations if certain configuration-specific data files and software modules are obtained. To handle other, arbitrary, configurations it would be necessary to use program TRASYS (available but not yet acquired by AFGL), or a similar program, to generate some of these data files. A further limitation of the present AFGL version is that it lacks the on-line plotting capability, using the DISSPLA package. All that exists is the option to write certain files, TAPE20 and TAPE22, formatted for offline use of DISSPLA. The information on these files is fortunately meaningful data rather than "metacode", so they could in principle be used in-house.

The next section provides an overview of the principal features of SPACE2, as acquired by AFGL. This includes a critique of the scattering model used. Section 2.3 will describe software enhancements made at AFGL, principally in graphics. Section 2.4 describes some calculations done with

the code at AFGL. Section 2.5 summarizes the current status of the system at AFGL. An appendix details additional software modules and data files which are felt to be necessary for fully independent and successful operation of SPACE2 for modeling of contamination of arbitrary space shuttle systems.

2.2 Overview of SPACE2

Figure 2-2 (User's Manual⁽¹⁾) shows nodal surface number assignments for the orbiter configuration. The following parameters for this configuration have been supplied to us either on data files or in data statements in the code:

Alphanumeric names of 20 types of materials, such as "LINER", "TEFLON", etc. (Table B-II, User's Manual)

Alphanumeric names of possible surface locations, e.g. "BAY", "CREW", etc. (Table B-II)

Mass loss rate parameters RTE (constant coefficient) and TAU (time decay constant) by molecular species and material type (Table B-II)

Molecular species names, molecular weights, and diameters (Table B-II).

Engine and vent plume flow model parameters and composition data (Table B-II)

Location, material type, and area of each surface (Table B-III).

Location, type, and on-time (duration of activity) of each engine and vent (Table B-III)

Surface temperatures (TAPE10) - seven profiles from which one is chosen (Table B-Ib)

Mass transport factors: source-to-surface (TAPE12) and source-to-point (TAPE14)

Mission profile data (Table B-IV).

All of the above, except the mass transport factors, can be altered conveniently with card input. The files TAPE12 and TAPE14 are those mentioned earlier as generated by program TRASYS. These incorporate the geometry (i.e. shadowing) specific to the configuration. The three surface loss mechanisms modeled are early desorption, outgassing, and leakage. Early desorption and outgassing have time dependencies distinguished by the decay time constants TAU mentioned above (default: 4100 hrs for outgassed molecules, 18 hrs for early desorbed molecules). Contrary to what is indicated in the User's Manual, the temperature dependence for all molecules is computed by $e^{(T-100)/29}$,

where T is the temperature, for the first 8 materials in the default list, i.e. for these materials there is no switchover to the form $e^{-E/RT}$ for early desorbed species.

This switchover does take place for materials 9,10, and 17 ("MTCS" "PTCS", and "IUSM") with $E = 7500$ cal/mole, $R = 1.98$ cal/mole/K. For these latter three materials, the "outgassing" form is modified to

$$e^{(T-125)/11} \quad \text{for "MTCS"}$$

and

$$e^{(T-125)/20} \quad \text{for "PTCS" and "IUSM".}$$

Materials "SOLAR", "ELECT" and "P80" employ the same temperature formulation as the first 8 materials for all

molecules, while the remaining materials are regarded as leakers, with a time -- and temperature -- independent loss rate for each specie.

The transport geometry is embodied in the mass transport factors, each of which indicates the fraction of the mass emitted from a source which reaches a given surface or point. The source to surface factors (TAPE12) control the amount of contamination directly transported to surfaces, while the source to point factors (TAPE14) determine the column densities of extended clouds above a surface, and with the appropriate scattering models, the amount of contamination scattered into a surface from the surrounding volume. As mentioned before, generation of these files requires a complex procedure, such as program TRASYS, to properly account for the geometry of the given configuration. For point sources (plumes) the direct fluxes at receiving surfaces and points are calculated directly with the Simons analytic flow-field model; mass transport factors are not used. Nevertheless the corresponding directional information, viz. centerline directions, is included in the mass transport files. The addition of a special software module, subroutine LOCATE (not presently in the AFGL version), would permit access to the Lockheed MOC or TIP flow-field models stored on tapes. The contamination for up to 25 surfaces can be evaluated. Each surface is accompanied by a user defined volume, which consists of a specified portion of a cone centered at the surface. The column density (mass or number) is found by integrating the volume density along the line of sight normal to the surface. The return flux is found by integrating the scattering contributions over the user-specified (conical) volume. The scattering model, described in a Lockheed report, Ref.10, Section 8 of the User's Manual, is based on the Bhatnagar/Gross/Krook⁽²⁾ model of the Boltzmann equation. (See discussion below).

Surface reflection is accounted for by adding, to the contamination originating from each reflecting surface, the contamination which reaches that surface from others but does not stick. The deposition rate on the surface for a particular gas is the product of the flux and the sticking coefficient. For outgassing molecules, the "source" temperature T_j used in Eq. A-33 p. A-29 of the User's Manual is the local gas mixture T^* , which is computed as the mean local temperature of all contaminants from all sources, i.e. a source-averaged sticking coefficient is used. For MMH-Nitrate the coefficient is unity. For all other cases the sticking coefficient depends on the surface evaporation rate as indicated in the User's Manual. This is given by Eq. A-31 (p. A-27) with the vapor pressure given by

$$P_{vj} = 2.9 \times 10^{10} e^{-12200/(1.987 T)}$$

where T is the surface temperature.

2.2.1 Discussion of SPACE2 Scattering Model

The scattering, by ambient atmospheric molecules, of contaminant molecules released from the surface of a spacecraft, is an important consideration in the evaluation of the contamination of other surfaces on the same spacecraft, due to these molecules. If the ratio (Knudsen number) of the mean free path of such a molecule to a typical spacecraft dimension is either very large or very small, it is often possible to analytically estimate the effects of the scattering process. For very small Knudsen number, one can sometimes use the Bhatnagar-Gross-Krook (BGK)⁽²⁾ approximation, as is done in program SPACE2 in the calculation of Space Shuttle contamination. This approximation invokes a Maxwellian distribution for the velocities of the scattered particles, which would not be valid unless the particles undergo many collisions. For

very large Knudsen numbers, scattering is negligible. However, for Knudsen numbers near unity, where scattering is still important, analytic approximation is usually impossible. Unfortunately, as shown below, the altitude range of the Space Shuttle encompasses both regions of high Knudsen number and low Knudsen number; we find order of magnitude unity near 200 km altitude. Since SPACE2 uses the BGK approximation at all altitudes, this aspect of the code merits further study.

In calculating the mean free path of a contaminant molecule, relative to a moving spacecraft, one must note that the contaminant speed, relative to the spacecraft, is much smaller than the supersonic speed of the ambient stream. Then the mean free time of a released contaminant molecule, prior to collision with an ambient molecule, is approximately:

$$t = \frac{1}{n_A \sigma_{AC} V_A}$$

where n_A = ambient number density
 σ_{AC} = ambient-contaminant collision cross section
 V_A = ambient velocity, relative to spacecraft

The mean free path is then

$$\lambda = V_c t = \frac{V_c}{n_A \sigma_{AC} V_A}$$

where

V_c = typical (most probable) contaminant speed

$$\sqrt{\frac{2 R T_c}{M_c}}$$

where

T_c = contaminant temperature

R = Universal Gas Constant

M_c = contaminant molecular mass

Using

$$\sigma_{AC} = \frac{\pi}{4} (d_A + d_c)^2$$

where

d_A = ambient molecular diameter = 3×10^{-10} m

d_c = contaminant molecular diameter = 5×10^{-10} m

$T_c = 300$ K; $M_c = 30$; $V_A = 7800$ m/sec;

we obtain the following table:

Altitude Km	n_A m ⁻³ (Ref.3)	λ , m	Knudsen Number (30 m vehicle length)
105	5×10^{18}	.02	6.7×10^{-4}
200	7×10^{15}	14.8	0.5
400	1×10^{14}	1040	34
2500	3×10^{10}	3×10^6	1×10^5

2.3 Software Enhancements

The original SPACE2 graphics function at NASA was performed by the commercially available DISSPLA⁽⁴⁾ graphics package. Since this package is not available at AFGL, a set of stand-alone programs have been developed which use existing AFGL facilities to display data saved on the SPACE2 output file TAPE22. These will be described below.

The computation of partial contaminant pressures, for points surrounding selected surfaces, has been added to SPACE2 to provide model comparison with pressure-gauge data.

2.3.1 Graphics

Three-dimensional graphics makes use of NCAR subroutine ISOSRF⁽⁵⁾ to draw selected constant density surfaces. Program ISODNPL (see Figure 2.1) accesses the SPACE2 output file TAPE22 and stores the data according to user specs, for the isodensity value requested. Subroutine BRACKT has been pirated from SPACE2 to assist in the interpolation of the TAPE22 data specified on a spherical coordinate grid, onto a rectangular grid. Figure 2.2 shows a sample output.

Program ISODNPL also generates on option, a file suitable for use by our interactive 2-dimensional display program SUACON⁽⁶⁾. A sample output is shown in Figure 2.3.

Program LINPLOT (Figures 2.4, 2.5) has been written to generate line-of-sight density plots.

2.3.2 Pressure Computations

The following partial pressure computation has been added to SPACE2 subroutine RTFMCD:

```

PROGRAM ISODNPL (INPUT, OUTPUT, TAPE22, TAPE6, TAPE8, TAPE9, TAPE10)
GENERATES NCAR SUBROUTINE ISOSRF METACODE FOR
SPACE2 ISODENSITY PLOT FROM DATA ON TAPE22
AND CREATES, ON OPTION, INPUT FILES FOR 2D CONTOURS
GENERATED BY PROGRAM SUACON.
COMMON/TOAT/NX, NY, NZ, XE(3), YX(3), T(11, 11, 21)
COMMON/GRID/ETA(9), RL(25), ZETA(8), NET, NS, NZETA, TP22DEN(2000),
1 ISOURCE, ISPEC
COMMON/J3SCALE/XSC, YSC, ZSC
DIMENSION SLA=(23, 23), EYE(3)
DIMENSION IOENT(300), JIOENT(300), ASPEC(10)
COMMON/TWOD/I2DPLN, TWODVL, TWODHD(5), HORZL9(3), VERTL3(3),
1 IHORZV, SCAL20
COMMON/NSPEC/NSPEC
INPUTS - NAMELIST/PLOTIN/ (DEFAULTS IN PARENTHESES)
ISOURCE - SOURCE NUMBER OF DENSITY TO PLOT (1)
          POSITIVE FOR SURFACES
          NEGATIVE FOR POINTS
          IF .GT. -300 TOTAL SURFACE CONTRIBUTION IS PLOTTED
          IF .LT. -50 TOTAL POINT SOURCE CONTRIBUTION IS PLOTTED
          IF 0, TOTAL OVER ALL SOURCES IS PLOTTED
ISPEC - SPECIE NUMBER OF DENSITY TO PLOT (1)
        IF .GT. 10 TOTAL OVER ALL SPECIES WILL BE PLOTTED
NX - NUMBER OF X POINTS IN THREE-DIMENSIONAL MESH
     FOR WHICH T ARRAY IS TO BE GENERATED (11)
NY - NUMBER OF Y POINTS IN THIS MESH (11)
NZ - NUMBER OF Z POINTS IN THIS MESH (11)
X0 - ARRAY OF 3 - X, Y, Z COORDINATES AT LOWER
     LEFT HAND CORNER OF MESH (-100.0, -100.0, 0.0)
DX - ARRAY OF 3 - INCRMENTS IN X, Y, Z USED TO DEFINE POINTS ON MESH
     (20.0, 20.0, 10.0)
EYE - ARRAY OF 3 - COORDINATES OF "EYE" FROM WHICH DISPLAY
     IS TO BE VIEWED (900.0, 600.0, 200.0)
TISO - ISO-DENSITY VALUE USED TO DEFINE THE SURFACE
       TO BE PLOTTED (1.0E10)
IFLAG - FLAG USED BY SUBROUTINE ISOSRF TO DETERMINE
        THE TYPES OF LINES TO BE DRAWN ON THE ISOSURFACE
        AND WHETHER VALUES GREATER THAN, OR LESS THAN,
        TISO ARE TO BE INSIDE THE SURFACE --SEE
        ISOSRF WRITEUP, P. 83 OF NCAR DOCUMENTATION (-7)
I2DPLN - IF NONZERO, CONTOUR PLOT DATA FOR A PLANE SPECIFIED
         BELOW IS SAVED ON TAPE10 (0)
         I2DPLN=1 - X=CONSTANT PLANE
         I2DPLN=2 - Y=CONSTANT PLANE
         I2DPLN=3 - Z=CONSTANT PLANE
TWODVL - X, Y, OR Z VALUE OF PLANE FOR WHICH 2D
         DATA IS TO BE SAVED
         (0.0)
I2DHD - IF NONZERO, HEADER OF 2D PLOT WILL BE MODIFIED
        BY READING READER CARD (SEE BELOW) (J)
IHORZL9 - IF NONZERO, HORIZ. LABEL WILL BE SIMILARLY MODIFIED (J)
IVERTL3 - IF NONZERO, VERT. LABEL WILL BE SIMILARLY MODIFIED (J)
IHORZV - HORIZONTAL AXIS VARIABLE NUMBER FOR 2D PLOTS
         1=X, 2=Y, 3=Z (1)
SCAL20 - SCALE FACTOR TO BE APPLIED TO DATA BEFORE
         SAVING ON TAPE10 FOR 2D PLOTS (10.0E16)
ITERM - TERMINATE JOB IF NON-ZERO (0)

```

Fig.2.1a Program ISODNPL Input Requirements:
NAMELIST/PLOTIN/ Parameters

```

FORMATTED CARDS
CARD 1 - 20 PLOT HEADER (50 CHARACTERS STARTING IN COLUMN 1),
        READ ONLY IF I2OPLN AND I2OHD ARE BOTH NONZERO
        (INITIALLY SET TO "SPACE2 CONTAMINATION DENSITY *1.0E17")
CARD 2 - 20 PLOT HORIZ. LABEL (30 CHARACTERS STARTING IN COLUMN 1),
        READ ONLY IF I2OPLN AND IHORZLB ARE BOTH NONZERO
        (INITIALLY SET TO "X(KM)")
CARD 3 - 20 PLOT VERT. LABEL (30 CHARACTERS STARTING IN COLUMN 1),
        READ ONLY IF I2OPLN AND IVERTLB ARE BOTH NONZERO
        (INITIALLY SET TO "Y(KM)")

TAPE22 INPUT - BINARY HEADER RECORD
NSPEC, (ASPEC(I), I=1, NSPEC),
JKEEP, (IDENT(I), I=1, JKEEP),
KTOTAL, (JIDENT(I), I=1, KTOTAL),
NSPEC - NUMBER OF MOLECULAR SPECIES
ASPEC(I) - 3CD NAME OF ITH SPECIE
JKEEP - NUMBER OF SURFACE SOURCES
IDENT(I) - NODE # OF ITH SURFACE SOURCE

KTOTAL - NUMBER OF POINT SOURCES
JIDENT(I) - NODE # OF ITH POINT SOURCE

TAPE22 INPUT -- BINARY DATA RECORDS
IS, IRECV, LOS, LPT, S, THETA, PHI, JKEEP,
((SNEN(J, M), M=1, NSPEC), J=1, JKEEP), KTOTAL,
((COEN(K, M), M=1, NSPEC), K=1, KTOTAL),
(TSDEN(M), M=1, NSPEC), (TCOEN(M), M=1, NSPEC),
TSDENA, TCOENA, TDOENAL
IS - RECEIVING SURFACE NUMBER
IRECV - SURFACE NODAL NUMBER OF RECEIVING SURFACE
LCS - LINE OF SIGHT NUMBER
LPT - RADIAL POINT NUMBER
S - DISTANCE (METERS) FROM SURFACE TO POINT AT WHICH
      FOLLOWING DENSITIES ARE GIVEN
THETA, PHI - POLAR COORDINATES (DEG) OF THIS POINT
JKEEP - NUMBER OF SURFACE SOURCES
SOEN(J, M) - MASS DENSITY (G/CC) OF SPECIE M FROM
      SURFACE SOURCE J
KTOTAL - NUMBER OF POINT SOURCES
COEN(K, M) - MASS DENSITY, SPECIE M, FROM POINT
      SOURCE K
TSDEN(M) - TOTAL MASS DENSITY, SPECIE M, FROM
      ALL SURFACE SOURCES
TCOEN(M) - TOTAL MASS DENSITY, SPECIE M, FROM
      ALL POINT SOURCES
TSDENA - TOTAL MASS DENSITY, ALL SPECIES,
      FROM ALL SURFACE SOURCES
TCOENA - TOTAL MASS DENSITY, ALL SPECIES,
      FROM ALL POINT SOURCES
TDOENAL - TOTAL MASS DENSITY, ALL SPECIES,
      FROM ALL SOURCES

```

Fig. 2.1b Program ISODNPL Input Requirements:
Formatted Cards and TAPE22 Format

SPACECRAFT ISODENSITY FIELD
 $\rho_{H_2O} = 4.00E-13 \text{ G/CC}$

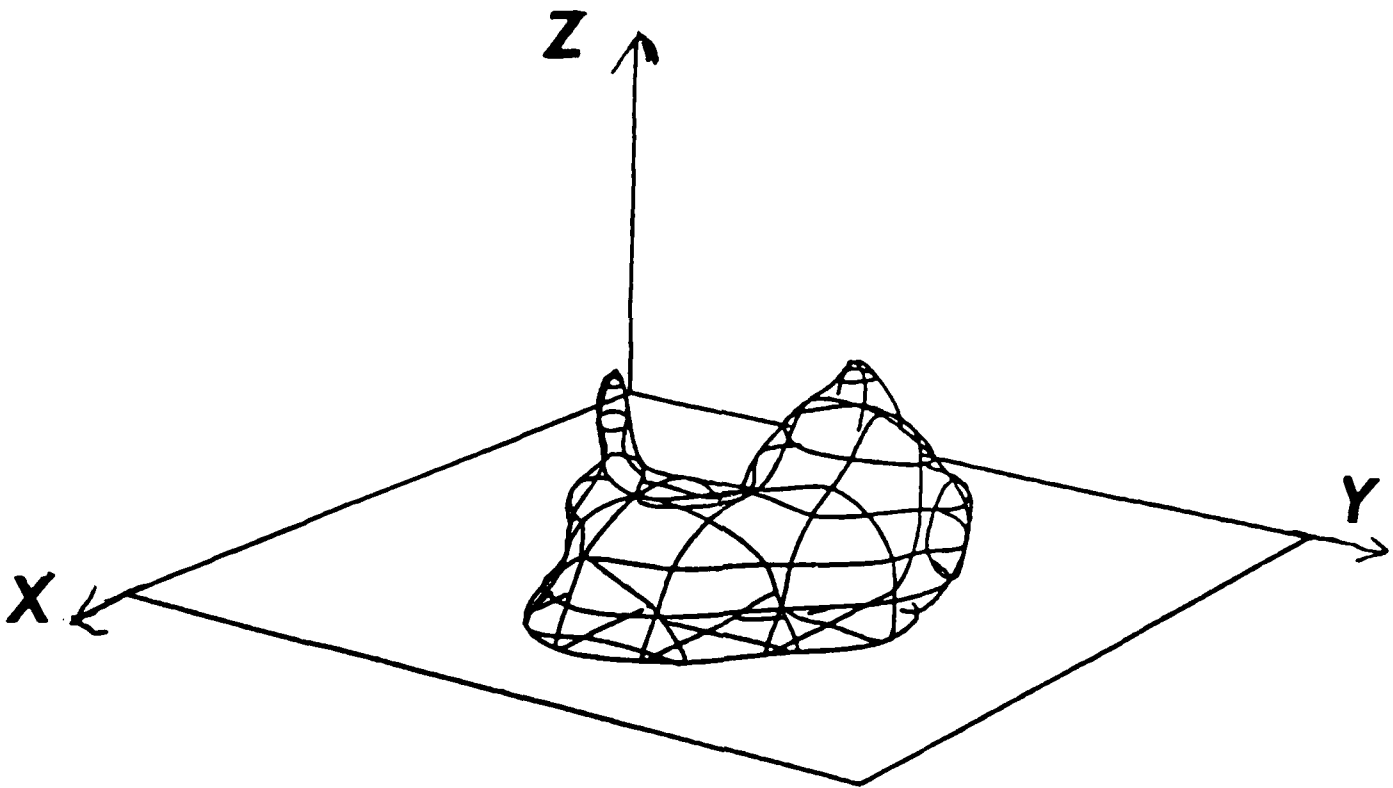


Fig. 2.2 Constant density surface ($4 \times 10^{-13} \text{ g/cc}$) for water dumps. The plane is $Z=0$. The top of the vertical (Z) axis is $Z=100\text{m}$. The corner behind the surface is $X=-100\text{m}$, $Y=-100\text{m}$, the opposite corner $X=+100\text{m}$, $Y=+100\text{m}$. The origin is at the payload.

SPACE2 CONTAMINATION DENSITY = 1.0E13

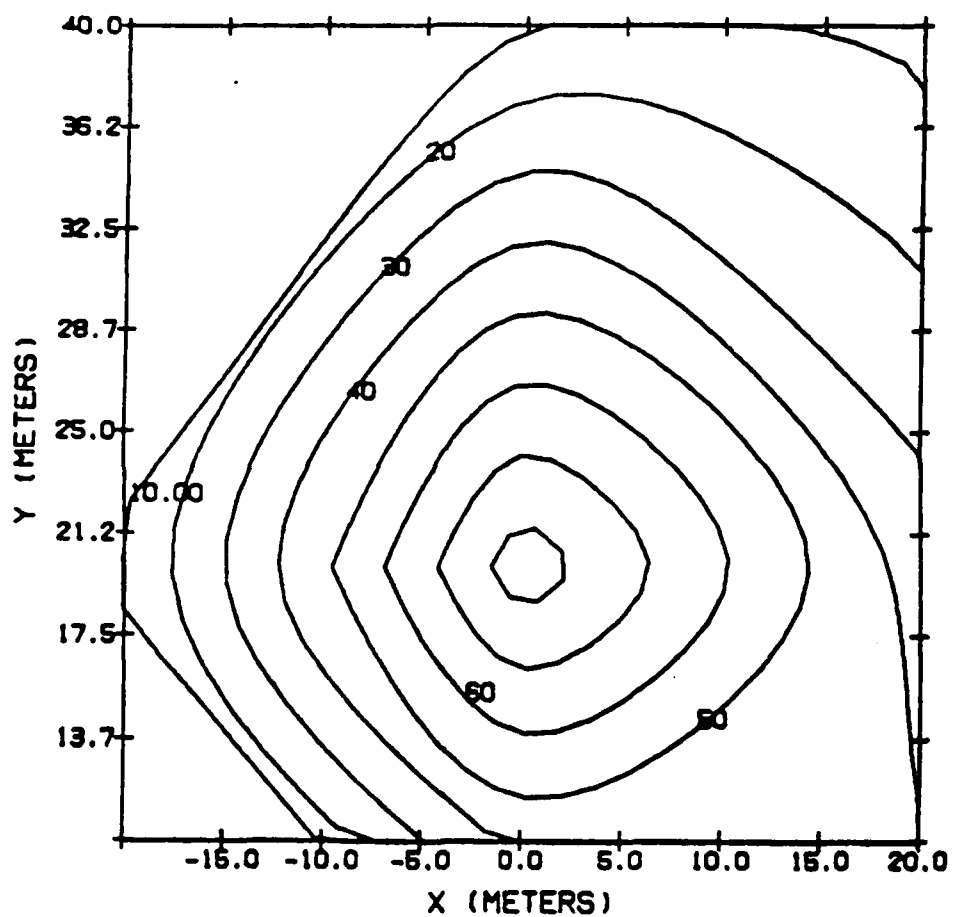


Fig.2.3 2-D contours of water densities 10m above payload during water dumps.

```

PROGRAM LINPLOT(INPUT=65,OUTPUT=55,TAPE22=527,TAPE39)
THIS PROGRAM PRODUCES LINE PLOTS OF CONTAMINATION DENSITY
VS DISTANCE FOR A SELECTED SHUTTLE RECEIVER SURFACE. USER ALSO
SELECTS THE MOLECULAR SPECIES, OR TOTAL OVER ALL SPECIES.
INPUTS - NAMELIST/PLOTIN/ (DEFAULTS IN PARENTHESIS)
  ISOJCE - SOURCE NUMBER (1)
    POSITIVE FOR SURFACES
    NEGATIVE FOR POINTS
  IF .GT. 300, TOTAL SURFACE CONTRIBUTION IS PLOTTED
  IF .LT. -50, TOTAL POINT SOURCE CONTRIBUTION IS PLOTTED
  IF ZERO SUM OVER ALL SOURCES IS PLOTTED
  ISPEC - SPECIE NUMBER (1)
  IF .GT. 10, SUM OVER ALL SPECIES WILL BE PLOTTED
  LOS(1) - LOS(5) - LINE OF SIGHT NUMBERS (1,2,3,4,5)

```

Fig. 2.4 Program LINPLOT Input Requirements.
(TAPE22 as for ISODNPL)

SPACECRAFT LOS DENSITIES

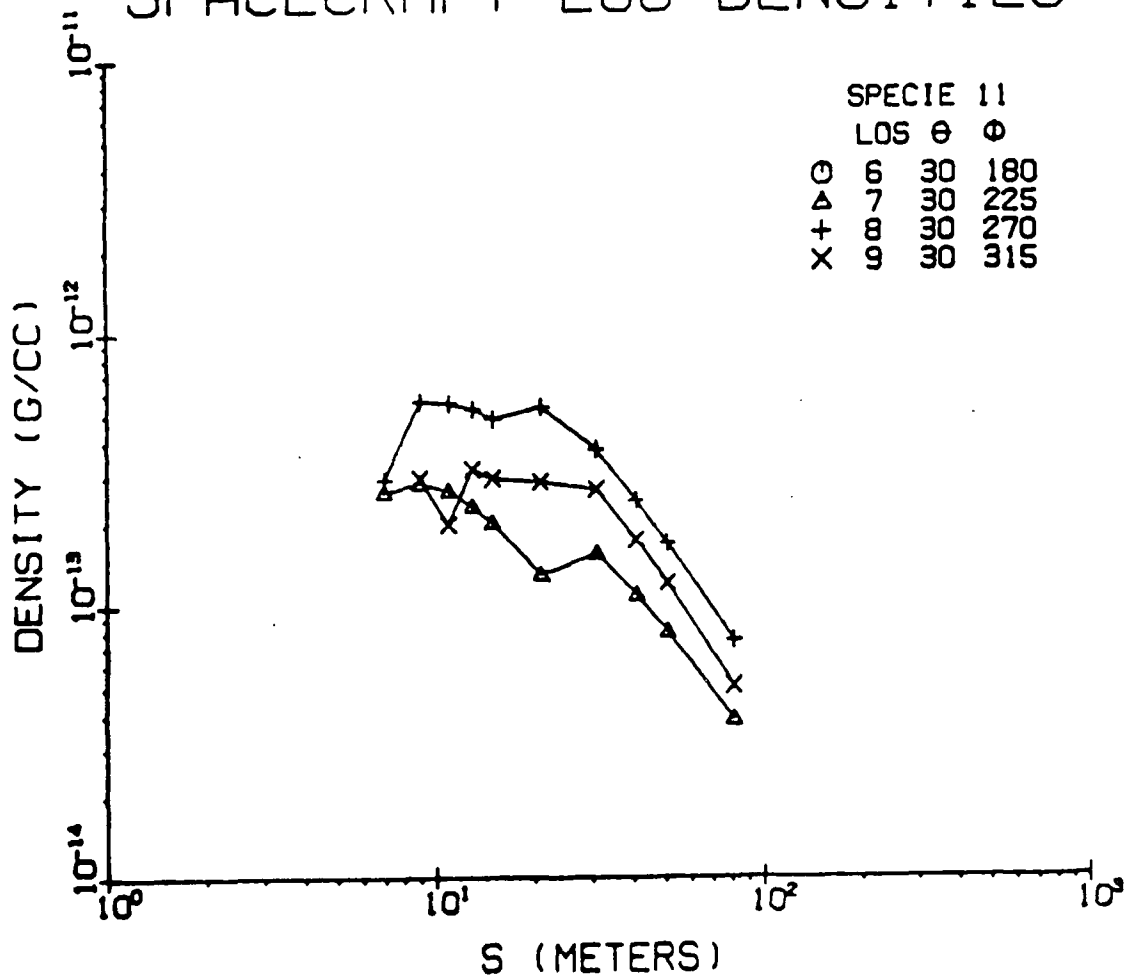


Fig. 2.5 Densities along selected lines of sight from payload during water dumps.

$$P(\text{torr}) = 7.501 \times 10^{-4} NKT^*$$

where

$$N = N_A (\rho_s + \rho_c) / M$$

$$N_A = \text{Avogadro's Number } (6.022 \times 10^{23} \text{ /gm mole})$$

$$\rho_s = \text{density (g/cc) of the gas from surface sources}$$

$$\rho_c = \text{density of the gas from concentrated sources}$$

$$M = \text{molecular weight of the gas}$$

$$K = \text{Boltzmann constant } (1.381 \times 10^{-16} \text{ erg/K})$$

$$T^* = \text{local gas temperature (K)}$$

The output of partial and total pressures has been incorporated into SPACE2's Report #32 printouts.

2.4. Model Calculations

Program SPACE2 was successfully compiled with the FTN5 compiler after several modifications to eliminate fatal compiler errors. A segmented load run deck was next set up following Fig. 2-7 (p. 2-27) of the User's Manual. Next, Sample Case 1 (User's Manual Section 5) was attempted, with the exception that the orbiter configuration was run rather than the LMOP, since as mentioned previously, we currently can handle only the orbiter. After some adjustments in file declarations (program statement) a successful run was completed. Since the output was not comparable with the test case result, Test Case 4, the only orbiter run in the Manual, was next attempted. This run was also successful, but again did not reproduce the print-outs given in the Manual. Further examination has revealed that both the surface temperature file (TAPE10) and the source to points mass transport file (TAPE14) that we received differ from those used in generation of the output of the Manual. The surface temperature file used in the manual corresponds to the Table B-Ia listing (maximum and minimum temperatures only) while we have the data shown in Table B-Ib (seven

profiles).

Our TAPE14 does not include any mass transport factors from surface nodes 1-8, contrary to the partial listing shown on p. 2-52 of the User's Manual. These nodes should dominate the contributions to the densities computed in the example (in the vertical column above the point X=1107, Y=0, Z=507; see Fig. 2-2 which shows these nodes directly below the region of interest). This is in fact true in the Manual's output (p. 5-22), but these nodes are absent from our output, because of their absence from our TAPE14. This file was apparently generated either for a different configuration, or the same configuration with a different numbering system.

2.4.1 Additional Calculations

2.4.1.1 Ten-Second Payload Contamination History

The payload location is assumed to be at the center of the payload bay liner with coordinates X = 1000 in, Y = 0, Z = 334 in (for reference the shuttle nose X,Y,Z coordinates are 238 in, 0 in, 400 in; the tail is located at 1542 in, 0 in, 480 in). RCS engine #7125, firing an 870 lb thrust in the +Z direction, is turned on for one second (4.5 sec - 5.5 sec) in the middle of the 10 second period. The thruster is located near the front of the vehicle at X = 350 in, Y = 0, Z = 395 in. Vehicle altitude is 200 Km.

Table 1 summarizes contaminant fluxes and deposition to the payload for this period. Figures 2.6-2.8 illustrate contaminant cloud densities surrounding the payload.

Desorbers do not deposit since the vapor pressure is greater than the effective pressure due to the incoming flux.

SPACECRAFT LOS DENSITIES

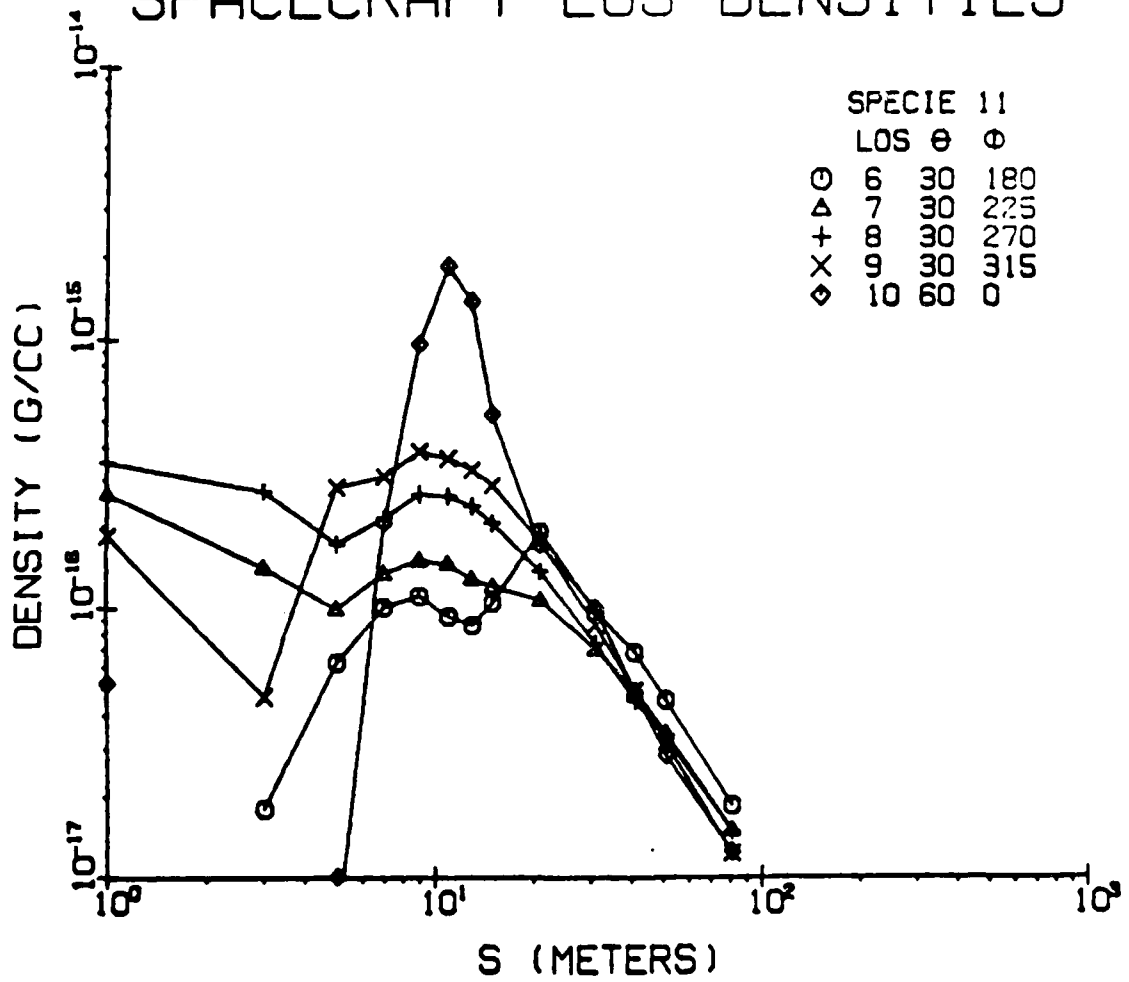


Fig. 2.6 Total density outgasser and desorber contaminants along selected lines of sight measured from payload.

SPACECRAFT ISODENSITY FIELD
 $\rho_{10} = 1.00E-17 \text{ G/CC}$

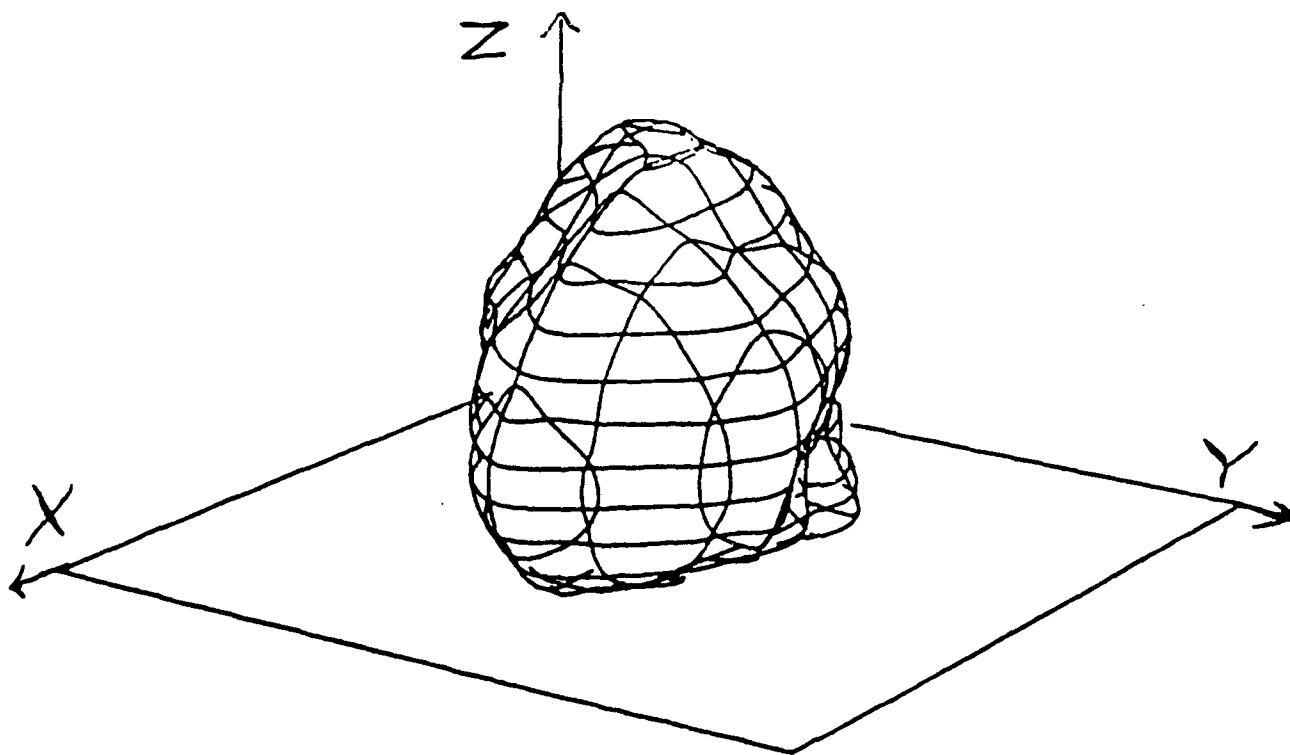


Fig. 2.7 Constant density (10^{-17} g/cc) surface for contamination around payload due to outgassers and desorbers. Same scale as for Fig. 2.

SPACE2 CONTAMINATION DENSITY ■1.0E13

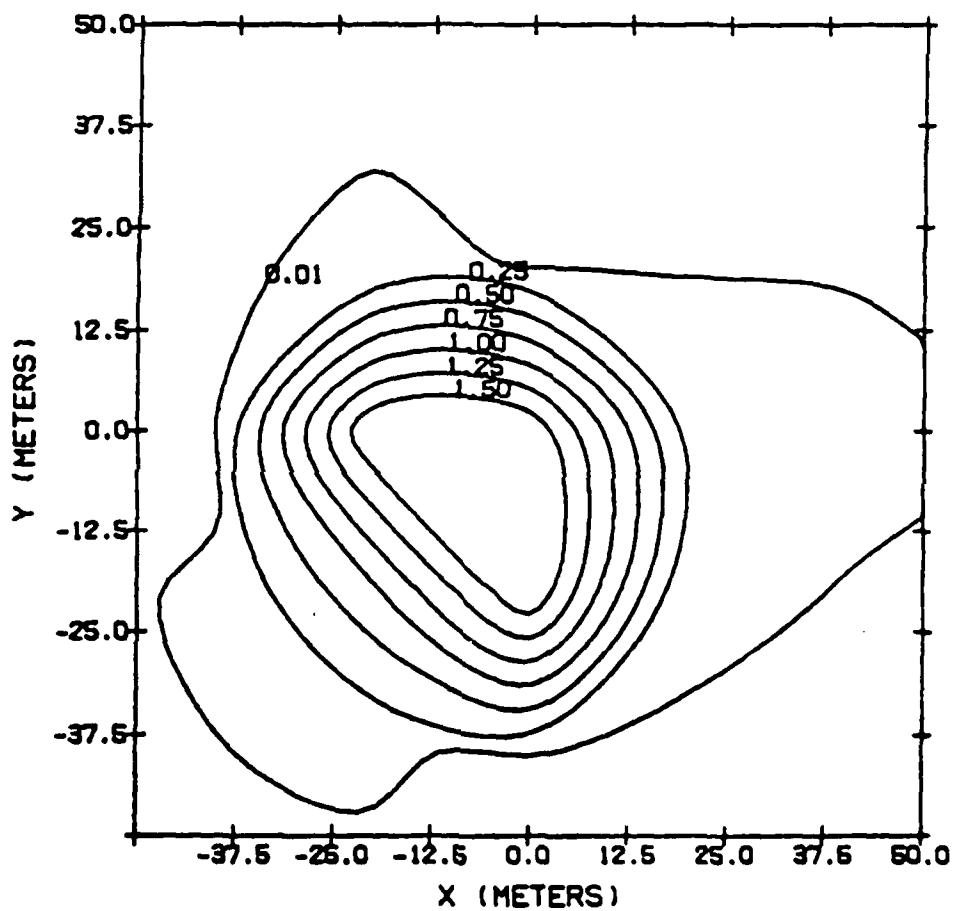


Fig. 2.82-0 isodensity contours of fuel contaminant 15m above payload.

Almost all deposition by outgassers is due to scattering. This is apparently because all sources which can directly impact the target surface (payload liner) are colder, and thus the model predicts zero deposition. For scattered molecules, however the average contamination cloud temperature is used, which can be warmer, since it includes all sources.

The plume effluents tend to inhibit outgas scattering to the target. The scattering model includes an attenuation factor due to the contaminant cloud between the scattering center and the target.

The desorber fluxes include those due to the light constituents in the plume (H_2O , CO_2 , etc).

Table 1. Ten-Second Payload Contamination

		Fluxes to Payload (gm/cm ² /s)		
		Outgas	Desorber	MMHNO ₃
0-4.5 sec	Direct	1.4x10 ⁻¹²	1.1x10 ⁻¹⁰	0
	Scattered	3.4x10 ⁻¹³	9.2x10 ⁻¹³	0
4.5 - 5.5 sec	Direct	1.4x10 ⁻¹³	1.1x10 ⁻¹⁰	0
	Scattered	1.8x10 ⁻¹³	1.2x10 ⁻⁸	2.4x10 ⁻¹¹
5.5 - 10 sec	Same as for 0-4.5 sec.			

Total Deposition (gm/cm²)

	Outgas	Desorber	MMHNO ₃
0-4.5 sec	2.8x10 ⁻¹³	0	0
4.5-5.5 sec	3.1x10 ⁻¹⁴	0	2.4x10 ⁻¹¹
5.5-10 sec	2.8x10 ⁻¹³	0	0
Total	5.9x10 ⁻¹³	0	2.4x10 ⁻¹¹

The apparent failure of contaminant densities along different lines of sight (Fig.2.6) to converge as the radial distance approaches zero is due to the highly directionally dependent shadowing in the vicinity of the payload location. This is evident by an inspection of the mass transport factors to points in this region.

2.4.1.2 One-Second Water Dumps

In this test the following two water vapor vents, in the rear of the vehicle, are turned on for one second at 200 km

altitude.

Vent #	X, in.	Y, in.	Z, in.	Direction
6877	1506	127	305	+Y
6879	1506	-127	305	-Y

The payload is completely shadowed from the two vents, so that it receives no direct flux. However flux due to scattering by ambient atmospheric molecules was found to be 7.8×10^{-10} g/cm²/s. As for the desorbers in the previous test, the contaminant does not deposit permanently onto the payload surface. At 10 m above the payload, where shadowing is considerably reduced, Figure 2.9 shows a considerable concentration of contaminant.

2.4.1.3 36-Hour Payload Contamination by Desorbers

The direct and scattered flux to the payload was calculated for successive 6-hour periods. The results (Table 2) are consistent with the expected 18 hour lifetime (exponential decay) of the desorber emission rates.

Table 2. 36-Hour Contamination Due to Desorbers

Time	Direct Flux (g/cm ² /s)	Scattered Flux (g/cm ² /s)
0 - 6 hr.	7.8×10^{-11}	1.8×10^{-12}
6 - 12 hr.	5.6×10^{-11}	1.3×10^{-12}
12- 18 hr.	4.0×10^{-11}	9.5×10^{-13}
18- 24 hr.	2.9×10^{-11}	6.8×10^{-13}
24- 30 hr.	2.1×10^{-11}	4.9×10^{-13}
30- 36 hr.	1.5×10^{-11}	3.5×10^{-13}

Deposition = 0

SPACE2 CONTAMINATION DENSITY = 1.0E13

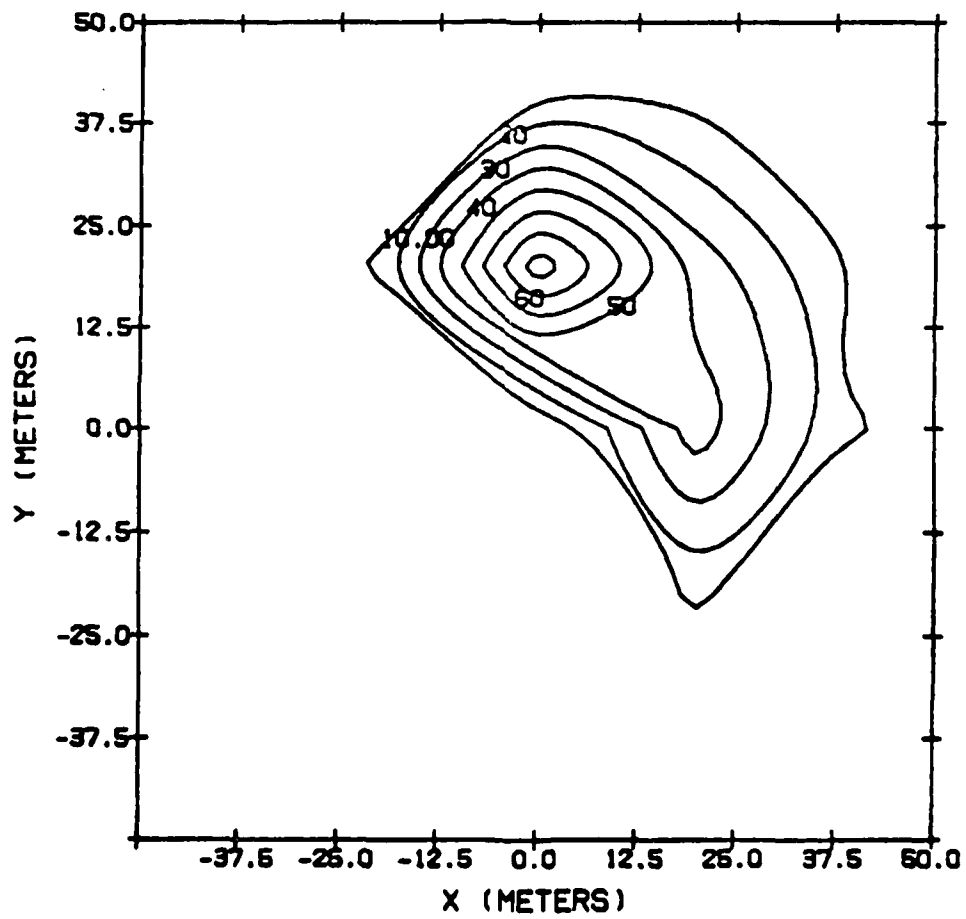


Fig. 2.9 Water vapor isodensity contours due to vent # 6877 10m above payload.

2.4.1.4 N₂ Contaminant Pressures

Table 3 shows model N₂ pressures as may be measured by a pressure gauge mounted on the fuselage over the -Y wing. The coordinates of the mounting are X = 1105 in., Y = -102 in., Z = 370 in. The angle θ is measured from the -Y direction, the angle ϕ counterclockwise from the X direction.

Table 3 N₂ Pressures Over Wing
(10⁻¹⁰ torr)

r, m.	e = 0°		e = 30°		
		φ = 0°	φ = 90°	φ = 180°	φ = 270°
0.2	1.29	1.33	1.24	1.50	1.61
0.4	1.44	1.29	1.12	1.59	1.81
0.6	1.44	1.23	1.10	1.65	1.79
0.8	1.35	1.17	0.90	1.42	1.52
1.0	1.13	1.11	0.77	1.16	1.30
3.0	1.02	1.02	0.60	0.56	0.73
5.0	0.38	1.70	1.03	0.17	0

r, m.	e = 60°			
	φ = 0°	φ = 90°	φ = 180°	φ = 270°
0.2	1.24	1.09	1.55	1.75
0.4	1.13	0.89	1.70	2.23
0.6	1.03	0.73	1.81	2.12
0.8	0.92	0.62	1.73	1.86
1.0	0.83	0.54	1.45	1.60
3.0	0.89	0.47	0.00	0.57
5.0	0.60	0.67	0.03	0

2.5. Conclusions

The shuttle contamination modeling system SPACE2 has been placed into operation at AFGL. Some enhancements have been added to meet particular needs at AFGL. Although plausible results have been obtained for some test cases, validation

awaits availability of experimental data for comparison. Various shortcomings of the system have been mentioned. A detailed list of items desired for more complete modeling capability is given in the Appendix.

2.6. Appendix Items Desired for Improved Capability

1. Program TRASYS II and User's Manual.

This is needed to generate and graphically display arbitrary configurations.

2. Subroutine modules specific to Spacelab configurations:

DSPIUX

FIVPX

LMOPX

P801X

SMPX

3. Temperature file, TAPE10; and MTF files, TAPE12, TAPE14, and TAPE15, required to run the test cases presented in Section 5 of the Feb, 1981 SPACEII User's Manual.

What we currently have appears to be the following:

Temperatures - TAPE10:

OFT-1 Shuttle Orbiter/IECM

Seven temperature file

(Table B-Ib, p. B-7 thru B-9 of the User's Manual);

We do not have the Maximum/Minimum file (Table B-Ia, p.B-3 thru B-6 of the User's Manual), which is used in at least some of the test cases.

Surface to Surface Transport Factors - TAPE12:

We have received only one file, which, from the

surface nodal numbers present (1-1100, plus nodes in the 6000-9000 range presumably used for engines), appears to be for the Long Module/One Pallet Spacelab configuration.

Surface to Point Transport Factors - TAPE14, TAPE15:

We have only one file, which appears to be a TAPE14 (orbiter), from the nodal numbers present (all less than 1000 except for engines in the 6000-9000 range). Furthermore nodes in the bay liner (1-8), radiators (20,22,24,26,30,32,36), and payload bay doors (40,42,44,46,50,52,54,56) are all absent, indicating that this is probably the closed payload bay door configuration. At any rate the configuration for this file appears not to be the same as the configuration for which the surface to surface factors on TAPE12 are given.

If consistent sets of files for the test cases cannot be supplied a consistent set for some configuration would be acceptable, along with output of a test run, so that we may check up here.

4. DISSPLA plot package
5. SPACEII interface to DISSPLA (subroutine calls required to execute the plot options, which have been omitted in the AFGL version).
6. (optional) Subroutine LOCATE and Lockheed MOC plume model tapes.
7. (optional) Surface/Engine/Vent descriptions (TAPE4) for the orbiter and spacelab configurations
8. (optional) Mass transport factors (TAPE12, TAPE15) for the spacelab configurations not included in the test

cases.

9. Literature Requested --

References in Sect. 8 of the User's Manual, particularly Reference 10.

References

1. Martin Marietta Corporation, "Shuttle/Payload Contamination Evaluation Program, Version II: The SPACEII Computer Program User's Manual", February, 1981.
2. Bhatnagar, P.L., Gross, E.P., and Krook, M. (1954), "Model for Collision Processes in Gases", Phys. Rev. 94, P.511
3. Jacchia, L.G., "Thermospheric Temperature, Density, and Composition: New Models", Smithsonian Astrophysical Observatory Special Report 375 (1977). Tables on p.79-80 (Exospheric Temperature = 1000K) were used to estimate N_A
4. Integrated Software Systems Corporation, "DISSPLA User's Manual", 1981.
5. National Center for Atmospheric Research, "NCAR Graphics Software Manual, Version 1.3.", 1980. Software translated for use in the AFGL Computers by Dr. Paul Fougere.
6. Radex, Inc., "Analysis of Spacecraft Charging, Particle Beams, and Geophysical Data Bases", pp. 116-119, 1983 Final Report. AFGL-TR-83-0140 (ADA138632)

3.0 Development of an Electrostatic Particle Pushing Code

3.1 Introduction

This section describes a computer program called SIM1D, designed to simulate a one-dimensional electrostatic plasma in an external magnetic field. We will begin by giving a brief outline of the basic concepts involved in plasma simulation via particle pushing programs. Next we will present our particular implementation of these concepts in sufficient detail so that this note should serve as a guide in future use of the program. Lastly, we will describe two experiments carried out with the program which demonstrate its proper functioning.

In doing particle pushing, one encounters problems of two types. The first is the proper solution of the equations involved, or, writing the program. The second is the possession of sufficient insight and experience to use the program to investigate practical physical problems and to understand the results. With this work, we have overcome the first of these problems, at least within the framework of our relatively simple system. The second problem is, we feel, by far the more difficult of the two and is solved to a large extent only through experience. This explains in part why we chose simple geometries and simple equilibrium problems for this work. We need always to understand the results we generate, or particle pushing becomes merely a programming exercise.

3.2 General Concepts

The objective of a particle-pushing simulation is to follow through time the evaluation of a plasma system. Viewed as an experimental tool, one constructs a mathematical model which behaves like a plasma in instances where plasma

behavior is known. One then introduces into the model a new situation, or initial condition, and observes the behavior, in hopes that the behavior of the model corresponds in some meaningful way to the behavior of a real plasma in the new instance as well. Viewed as a theoretical tool, plasma simulation codes will eventually become powerful tools capable of revealing the detailed dynamical behavior of millions and millions of mutually interacting charged particles.

The microscopic equations describing the motion of plasma particles are simple and well known. We can easily write Newton's equation, describing how each particle must respond to an electric and magnetic field. Likewise, we know how fields evolve in response to particle densities and flux. The stumbling block is that, if we try to follow the time behavior of every particle in a plasma system of sufficient size to be of interest, we find there are hopelessly too many equations to solve, even by computer. Particle pushing attempts to overcome this problem by representing many individual electrons or ions by a single macroparticle, and then representing a plasma system by some manageable number of these particles. It is hoped that the behavior of the macroparticles will mimic the behavior of a plasma, at least insofar as the quantities of interest are concerned.

To see what this amounts to physically, Figure 3.1 is helpful. The first frame shows 30 electrons in a small region of a two-dimensional plasma. We have not considered the ions which are assumed spread out into a neutralizing background.

In frame 2, we have inscribed some shape around each set of five electrons. Here the shape is a circle, although a square might be the more obvious choice, considering the geometry of this system. We are free to choose any shape for the macroparticles. In frame 3, we have taken away the individual electrons and are left with only macroparticles.

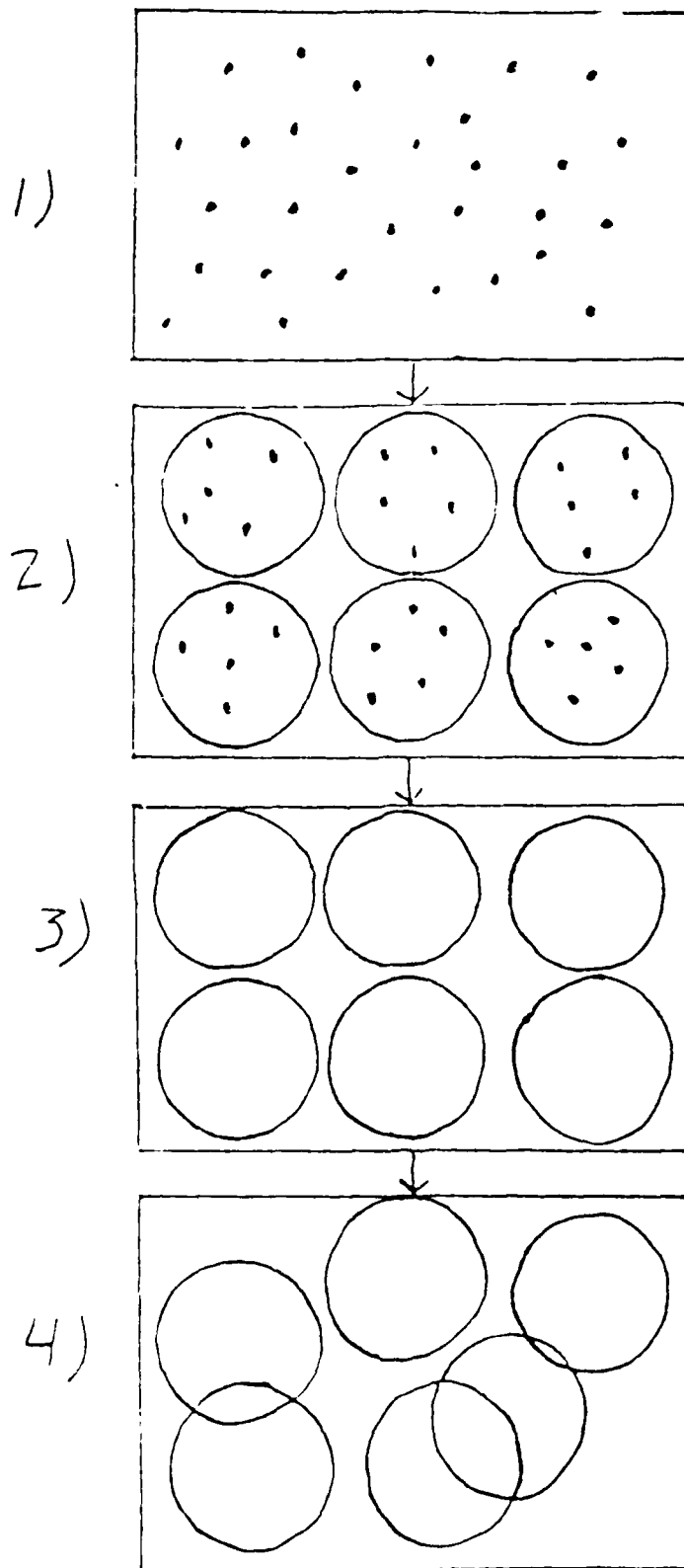


Figure 3.1-- Making Microparticles

Since each macroparticle represents five electrons, its charge is $5q$ and its mass $5m_e$. We further assume that this charge is distributed uniformly throughout the area of the chosen shape. In frame 4, we let the system evolve by moving the macroparticles, allowing them to pass through one another at will. Said another way, we move each electron inside the macroparticle by the same displacement vector. This would be completely appropriate if the particles were small enough so that the electric field were constant over the particle area and, of course, if each electron within the particle had the same initial velocity. This assumption of collective behavior would be valid only if the number of electrons is 10^5 or more. For plasma systems in which there are only a few electrons in a collectively interacting range (Debye sphere) collisional models would be more suitable.

Now if we are given the electric field E and the magnetic field B at each of the particle positions, along with the positions and velocities of each particle for some initial time, we can easily follow the evolution of the system through Newton's equation with the Lorentz force.

$$\frac{dv}{dt} = \frac{q}{m} \left(E + \frac{v \times B}{c} \right)$$

$$\frac{dx}{dt} = v$$

Each of the quantities E and B above are really made up of two components, one due to external fields and another due to induced fields arising from particle interaction.

$$E = E_{ex} + E_{ind}$$

$$B = B_{ex} + B_{ind}$$

We can find E_{ind} by solving Poisson's law

$$\nabla^2 \phi = 4\pi\rho$$

$$E_{ind} = -\nabla\phi$$

E_{ind} represents the force on a particle from all neighboring particles. The nature and simplicity of the model allow us to cut down considerably the work involved in calculating E and B . The problem has been solved in a full 3-dimensional framework. To simplify the problem, we will consider only one-and-one-half dimensions. This means we consider spacial variations in one direction and velocity variations in two. We also assume that the external electric field is zero and that the external magnetic field is static and directed perpendicular to the two velocity directions. Choosing X for the spacial coordinate and X and Y for the velocity directions,

$$B_{ex} = B_z$$

$$E_{ex} = 0$$

We further assume that the only force acting between particles is electrostatic, that is,

$$B_{ind} = 0$$

Since we are dealing with infinite sheets of charge, and since we require charge neutrality in the system, we see that

$$E_{ind y} = E_{ind z} = 0$$

Also if v_z is initially zero, the equations of motion show it will remain so, thus we lose no information by ignoring v_z .

In the special case where $B=0$, this is also true of v_y .
 The final form of Newton's equations is then

$$\frac{dv_x}{dt} = \frac{q}{m} (E_x + \frac{v_y B}{c})$$

$$\frac{dv_y}{dt} = \frac{q}{m} \frac{v_x B}{c}$$

$$\frac{dx}{dt} = v_x$$

$$\frac{dy}{dt} = v_y$$

Since we are assuming sheets of charge, the fourth equation above can be of no interest. In a one-dimensional system, only change in x is considered. Change in y is ignored.

In order to use Poisson's equation to find the induced electric field, we must relate particle positions to charge density. We first define on the system a series of points separated by Dx on which to calculate density. In the simplest approach, we could assign all the charge in a particular macroparticle to the grid point nearest the macroparticle. The charge on a particular grid point, divided by the area attributed to that grid point would give a charge density

$$Dx \rho_i = \sum_j \begin{cases} q & \text{if particle } j \text{ is nearest} \\ & \text{grid point } i \\ 0 & \text{if it is nearest some} \\ & \text{other grid point} \end{cases}$$

This method treats particles as point charges (or infinitely thin sheets in 1-dimension). Intuitively, one might expect this to give rise to a relatively high noise level, since as a particle crosses the midpoint between two grids, the density at each grid changes discontinuously. We could achieve a smoother result by giving each particle a size and shape. This is natural because we have used a macroscopic particle to represent many particles so that the change in distribution must have a finite spread and not be point-like.

The simplest higher order shape to use is that of a sheet of finite thickness. This will be our approach. Further, we choose to let the thickness of each sheet be equal to the grid spacing Dx . This is chosen for simplicity and works well as long as the thickness is smaller than or of the order of the grid size. This allows for additional simplification in the calculation of density, for if we assume that the particle center is located between X_i and X_{i+1} where

$$X_i = (i-1)DX$$

then we allow to X_i the fraction of the particle's charge in the space between $X_{i-1/2}$ and $X_{i+1/2}$ and allow the rest to X_{i+1} . If the particle is at X_p , ($X_{i+1} > X_p > X_i$)

$$\rho_i = \rho_i + q_p (X_{i+1} - X_p)/DX$$

$$\rho_{i+1} = \rho_{i+1} + q_p (X_p - X_i)/DX$$

Another way to see this is to plot the average charge density at X_i due to the particle as it moves continuously from X_{i-1} to X_{i+1} . This is done in Figure 3.2. Once we have accumulated this charge fraction for each particle on each grid point, we divide by the space between grids DX to find the average density. This scheme is known as the "particle in cell" method and has been shown to provide significant noise reduction over the previously mentioned (point particle) scheme.⁽²⁾ The noise is a result of using a few particles to represent many and is therefore unphysical.

We now have all the basics necessary to construct a simple particle pushing simulation loop by carrying out the

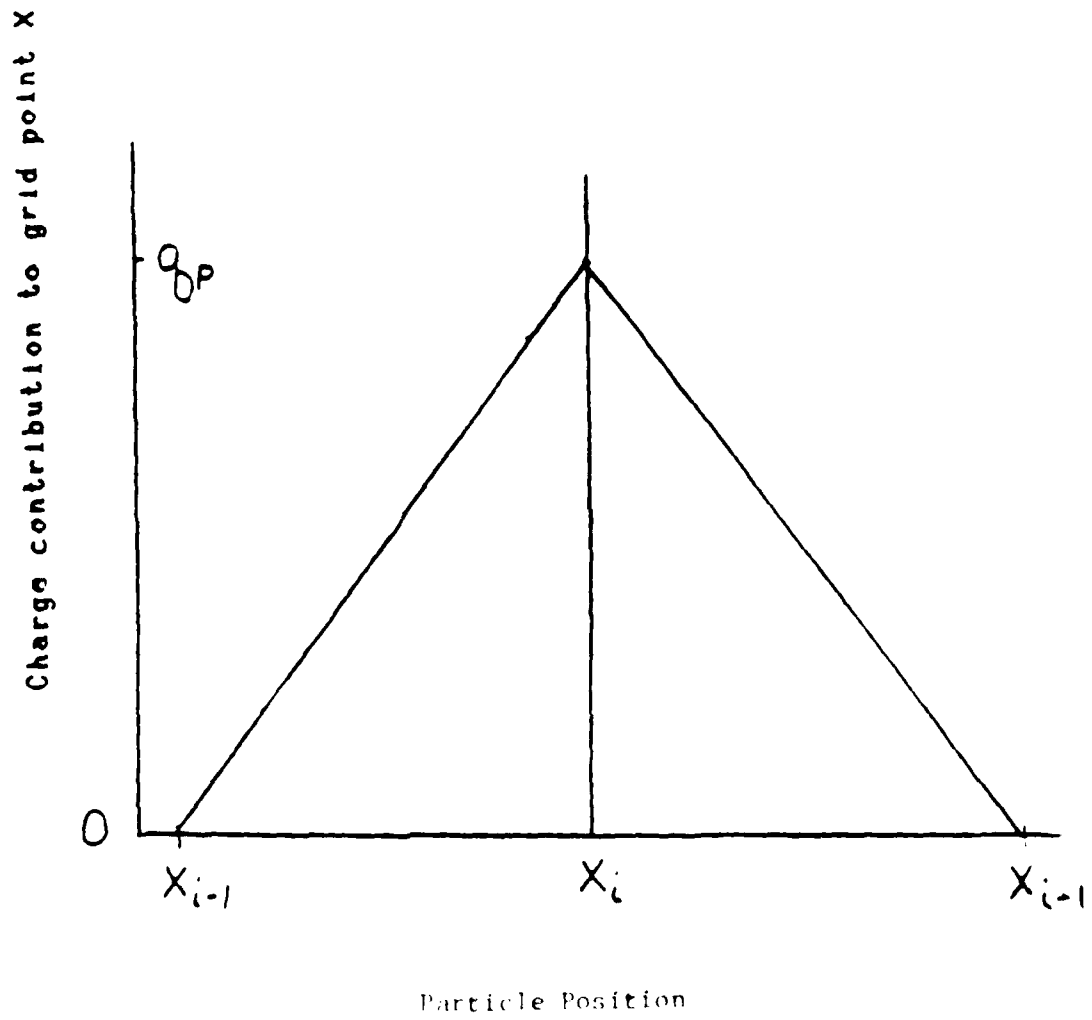


Figure 3.2 - Particle in Cell Density

following steps:

- 1) Initialize particle coordinates, choose initial parameters
- 2) Assign charge to grid points using particle in cell algorithm
- 3) Solve Poisson's law to find electric field
- 4) Use Newton's Equations to find particle accelerations
- 5) Advance particles over a chosen time interval
- 6) Output useful information
- 7) Repeat from step 2

The next section will detail the numerical implementation of these steps.

3.3 Technical Aspects

The first step we defined in the particle simulation scheme was to initialize a set of positions and velocities and to pick various system parameters. We have found, in our limited experience, that the choice of initial parameters is a rather delicate matter and is tied in closely with the particular problem one wants to address. Since the present section deals with specifics of program design and operation and since a discussion of initialization belongs more to the realm of experiment than algorithm, we will save this for last and begin here with a discussion of the second step.

We will assume only that we have been given the following:

- 1) The number of particles - NE
- 2) The charge and mass - Q, M
- 3) The magnitude of the magnetic field - B_z
- 4) The box length and number of grids - BOX, NX
- 5) Initial X, V_x, V_y for each particle at time zero.

Step 2 of the given scheme was to assign a charge to each of the grid points based on the position of the particles. We have already stated our chosen algorithm for this. The steps are as follows:

- 1) for each particle, decide which two grid points the particle lies between.
- 2) find the distance from the particle to each of the two nearest grid points.
- 3) increment the density of each of the two grid points by a fraction equal to the distance to the other grid point divided by the grid spacings DX .

After doing this for each particle, we arrive at a number fraction of particles around each grid point. To convert to a density we divide again by DX and multiply by the charge per particle Q . In our model we have only one type of mobile particle but we wish to preserve charge neutrality of the system as a whole. We thus must subtract from this density the equivalent density of a continuous sheet of oppositely charged particles, or $-Q * BOX * NE / DX$.

We can now move to step 3, solving Poisson's equation. 1

do this, we must choose a finite difference formulation and boundary conditions. We represent the differential equation

$$\frac{\delta^2 \phi}{\delta X^2} = 4\pi\rho$$

by

$$\phi_{i-1} - 2\phi_i + \phi_{i+1} = (DX)^2 4\pi\rho_i$$

$$(i = 0, 1, 2, \dots, NX-1)$$

where the i's refer to the grid points we previously set up with charge densities.

The electric field is then found from

$$E_i = (\phi_{i+1} - \phi_{i-1}) / (2DX)$$

The boundary conditions come from an assumption that the system is periodic in space. This is to say that, if F is any function of distance,

$$F(x+L_x) = F(x)$$

Applying this specifically to the potential equations above, we see that

$$\phi_1 = \phi_{NX-1}$$

We could then replace ϕ_{-1} by ϕ_{NX-1} , and ϕ_{NX} by ϕ_1 to arrive at a system of NX equations in NX unknowns

$$\phi_{NX-1} - 2\phi_1 + \phi_1 = n_1$$

$$\phi_{i-1} - 2\phi_i + \phi_{i+1} = n_i \quad (i=1, 2, \dots, NX-2)$$

$$\phi_{NX-2} - 2\phi_{NX-1} + \phi_1 = n_{NX-1}$$

$$n_i = (DX)^2 4\pi\rho_i$$

In the early stages of this work, we solved this system by relaxation, meaning that we chose an initial set of ϕ_i 's and modified each sequentially in such a way as to bring the residuals of the equations to zero. This was a slow process especially for large NX so we decided to try to find a direct solution instead. The approach was to look for a general formula to invert the matrix describing the above equations.

The matrix is, however, singular. This can be verified by noting that any row is minus the sum of all the other rows. This does not mean that the equations are invalid, but only that we cannot hope to invert the matrix to find solutions. We can see the origin of the singularity by noting that we can add an arbitrary constant to all the ϕ 's without changing either the differential or the difference equation. A non-singular matrix would imply a single set of solutions for the ϕ_i 's, while in fact there is a continuous set. This is because the potential is defined only up to a constant by Poisson's equation. Physically, the motion of the particles depends only on the differences between ϕ 's that is, on the electric field. We see that we must specify one of the ϕ_i 's as a boundary condition in order to arrive at an explicit solution. The choice is arbitrary, but we decided to specify

$$\phi_0 = 0$$

Using this, the above set of equations reduces to

$$\phi_1 + \phi_{NX-1} = \rho_0$$

$$-2\phi_1 + \phi_2 = \rho_1$$

$$\phi_{i-1} - 2\phi_i + \phi_{i+1} = \rho_i \quad \{ i=2,3, \dots, NX-2 \}$$

$$\phi_{NX-2} - \phi_{NX-1} = \rho_{NX-1}$$

We must throw out one of these equations since there is one more equation than unknown. This is due to the periodicity of the system. If one fixes ϕ_0 , one fixes ϕ_{NX} as well. As a result, two values are fixed in a system of NX equations. We left out the final equation in the series. After transforming the matrix of a few cases to upper triangular form, an explicit general solution was apparent.

This was, defining $N = NX-1$,

$$\begin{aligned}\phi_N &= (N+1)^{-1} \sum_{i=0}^N (N-i) n_i \\ \phi_{N-1} &= \sum_{j=0}^{N-1} (N-i-j) n_j - (N-i) \phi_N \\ &\quad \{ N-i = 1, 2, 3, \dots, NX-2 \} \\ \phi_0 &= 0\end{aligned}$$

When programmed, this formula was checked for several cases against the relaxation results and found to agree to within an additive constant.

In interpolating the electric field from the grid points on which it is calculated to the precise particle position, we make use of the same algorithms used to calculate density in a self-consistent fashion. If the particle is between points i and $i+1$ at distance X ,

$$E = E_i \frac{(X_{i+1} - X)}{DX} + E_{i+1} \frac{(X - X_i)}{DX}$$

The chosen algorithm for carrying out the next step, that is, moving the particles given the electric field, was taken from Buneman.⁽³⁾ The algorithm calculates explicitly the position at integral time steps, and the velocity at half-integral steps. The motion is divided into a translation due to the electric field, and a plane rotation due to the perpendicular magnetic field. Rather than reproduce the rather involved equations here, we refer the reader to the clear treatment given in reference 4.

The choice of which of the many possible quantities to output

during a simulation is influenced by the particular system and by one's particular interest.

There are a few quantities however, that should be of interest in many types of simulation, and provisions for these are built in to the SIM1D code. The most basic of these are the kinetic and potential energy. The sum of these should remain relatively constant in any simulation, at least the fluctuation in the sum should be much smaller than the fluctuations in either individually. The methods for calculating energy deserve some note. For kinetic, we wish to sum the squares of the velocities of all particles at time t . Due to the nature of our time integration algorithm, we have stored only velocities at half-integral times, $t-\Delta t/2$ and $t+\Delta t/2$. We find an average velocity at t by multiplying the two, that is,

$$KE = \frac{1}{2} \sum V_i(t-\Delta t/2) V_i(t+\Delta t/2)$$

For potential energy, we integrate the product of charge density and potential over the computational space. Using grid points, this amounts to the sum

$$PE = \sum \rho_i \phi_i DX$$

These quantities are converted to ergs and output to TAPE1 in a format suitable for plotting.

Another important feature is the distribution in velocity space. This could be defined as the number of particles in the system with velocities within a chosen interval. The SIM1D system provides a routine for calculating and plotting the distribution.

Also of interest is the behavior of the Fourier transforms of various properties in the system. For instance, the energy contained in an oscillation is given by the product $\Phi_k \rho_k$.

The frequency of propagation of energy waves of various wavelength can be obtained from the time dependence of this product, since

$$\rho_k \phi_k \approx \exp(i\omega(k)t)$$

Due to the periodic nature of the system, the only spacial waves that can be sustained are those with a wavelength that is some integral fraction of the length of the box. We also cannot hope to resolve oscillations that are smaller in extent than the division between grids. This gives an upper and lower bound on the value of k . The discrete Fourier transform (Q_k) of a set of points (Q_j) is defined as

$$Q_n = DX \sum_{j=0}^{NR-1} Q_j e^{-ix_j k_n}$$

$$x_j = jDX, \quad k_n = 2\pi n/L \quad n=0,1, \dots, NR-1$$

If we consider real and imaginary parts of Q_k , we see there are $2NR$ values, but due to the folding property of finite transforms, $Q_k = Q_{NR-k}$.

We simply ignore the upper half of the spectrum since it contains no new information. SIM1D provides a routine for producing this transform of any distance dependent quantity such as ρ , ϕ , or E . The transforms of the density and potential will be important in the experimental part of this work.

3.4 Initialization

The choice of starting state is of the utmost importance in achieving reasonable results in a particle pushing simulation. We have constructed a program following Birdsall's work, ¹ that provides a start file with enough variability to do some simple experiments. The start file is a list of the parameters the program requires, along with an explanation of their relationship to the problem, where appropriate. The order in that file entered when the start program SPTID is executed:

BOX - the length of the box. This parameter was used throughout this program, but will eventually be replaced by a more general one. The problem to discuss is a system with a convenient system to work in.

NX - the number of particles that are the number of divisions of BOX. This is the number of particles calculated.

MEB - the desired plasma frequency. This is the number of

MEC - the desired frequency of the external magnetic field. The perpendicular magnetic field is

QW - the charge to mass ratio of the particles.

The above quantities are related as follows:

$$\text{Total charge of the system} = \frac{N \cdot QW \cdot \text{BOX}}{2 \cdot \pi \cdot \text{MEB}}$$

$$\text{Magnetic field} = \frac{2 \cdot \pi \cdot \text{MEB} \cdot \text{BOX}}{QW}$$

If there are N particles in the system, the charge to mass ratio is given by

$$QW = \frac{\text{Total charge}}{N}$$

The mass is then

$$m = \frac{QW \cdot \text{BOX}}{2 \cdot \pi \cdot \text{MEB}}$$

NEI - the number of particles of each species. These differences are limited to differences of one particle per species and displacement.

WAVE - the mode of the system to be excited by means of a density wave of the form

$$\rho(x) = A \cos(\pi \cdot WAVE \cdot \frac{x}{\text{BOX}})$$

entering a zero at WAVE in the program will produce an excitation.

X1 - the magnitude of the excitation. The coefficient A above is proportional though not equal to X1.

$$A = \rho_0 * XMODE * X1$$

VDX,VDY - drift velocities in the X and Y dimension. We might introduce a beam by providing a drift velocity for one set of particles and none for another. We could give momentum to a wave by using a drift and density excitation together.

VRX,VRX - sometimes it may be desirable to provide a temperature in the plasma. One way to do this is to give each particle a random velocity. These parameters direct the program to assign a uniform random distribution between -VRX and +VRX in the X direction, and similarly for Y.

NP2 - the number of particles of species two. If this is non-zero, the program asks for excitation, drift and random velocity inputs for species two. If zero, only one species is produced.

In addition to these parameters, there are a few within the program SIM1D that can be adjusted to control the frequency and nature of output. These appear together after line 30

SUADIV - is a scaling factor to control the magnitude of the energy output to the SUATEK file on TAPE1.

IPV - controls the frequency of velocity space distribution plots. IPV = a large number will produce no plots.

VMAX - controls the range of velocities plotted. If VMAX=0, the maximum velocity encountered is taken as VMAX.

IFT - controls Fourier transforms. IFT = 0 leads to no transformation, IFT equals an integer gives transforms on each timestep, output to TAPE2, and a printout every IFT timesteps.

VPERT - allows a second random perturbation in velocity in the X-direction. Zero means no perturbation.

The program itself requires only two input values, the timestep and the number of steps to carry out. With a few hundred particles and a few hundred timesteps, the program can be run interactively. The test cases we carried out, described in the next section, took only a few seconds to execute. It is convenient to run the program interactively, since important criteria such as energy conservation can be immediately checked and the timestep modified accordingly. The program is currently dimensioned for up to 1000

particles and 500 grid points.

3.5 Tests of the Program

In order to demonstrate the proper functioning of the program, we carried out two simulations, one on an electrostatic plasma (without magnetic field), another involving a static magnetic field. The tests were chosen for their simplicity and because detailed descriptions and results were available for systems similar to our own. This was helpful in setting up the experiment or analyzing the results obtained. Also, analytic expressions available for some of the quantities to be measured.

In both cases, we began with a cold plasma, that is, one with no random thermal motion. The plasma was excited by adding energy in the form of a density wave at a chosen wavelength and amplitude. As the system evolved, potential energy was transformed to kinetic and back again. Since the excited mode chosen was in each case one of the normal modes in the system, all the energy remained in the chosen mode, and harmonic motion was observed.

The important quantities we measured were the kinetic, the potential and the total energy, the latter of which should be a constant. We also determined the frequency of the oscillation for several modes. The first simulation involved plasma oscillations. The initial state is given

below, in terms of SET1D variables

Table 1 - Parameters for Plasma Oscillations

BOX	2π
NX	32
OMEGP	1.0
OMEGC	0.0
QDM	1.0
NE1	128
XMODE	1.0
X1	0.001
VDX,VDY	0.,0.
VRX,VRV	0.,0.
NE2	0

The results of running the program through 100 steps at a timestep of 0.2 are shown in Figure 3.3. The kinetic energy begins at zero and rises to the initial value of the potential energy as energy exchange takes place. The total energy, (top line) remains constant except for minor fluctuations. The fluctuations are expected because potential and kinetic energy are not calculated in an entirely self-consistent way. Potential is calculated on the grid points, kinetic energy at the point of the particles. This process is illustrated by Birdsall.⁽²⁾

Since the plasma frequency is the frequency at which electrostatic waves propagate in a plasma, the induced wave should propagate at this frequency. Indeed, the period of oscillation is around 2π plasma periods. Note that a complete oscillation involves two peaks in the potential energy level, not one. Initially there is an accumulation of density in the center of the box, density in the center drops

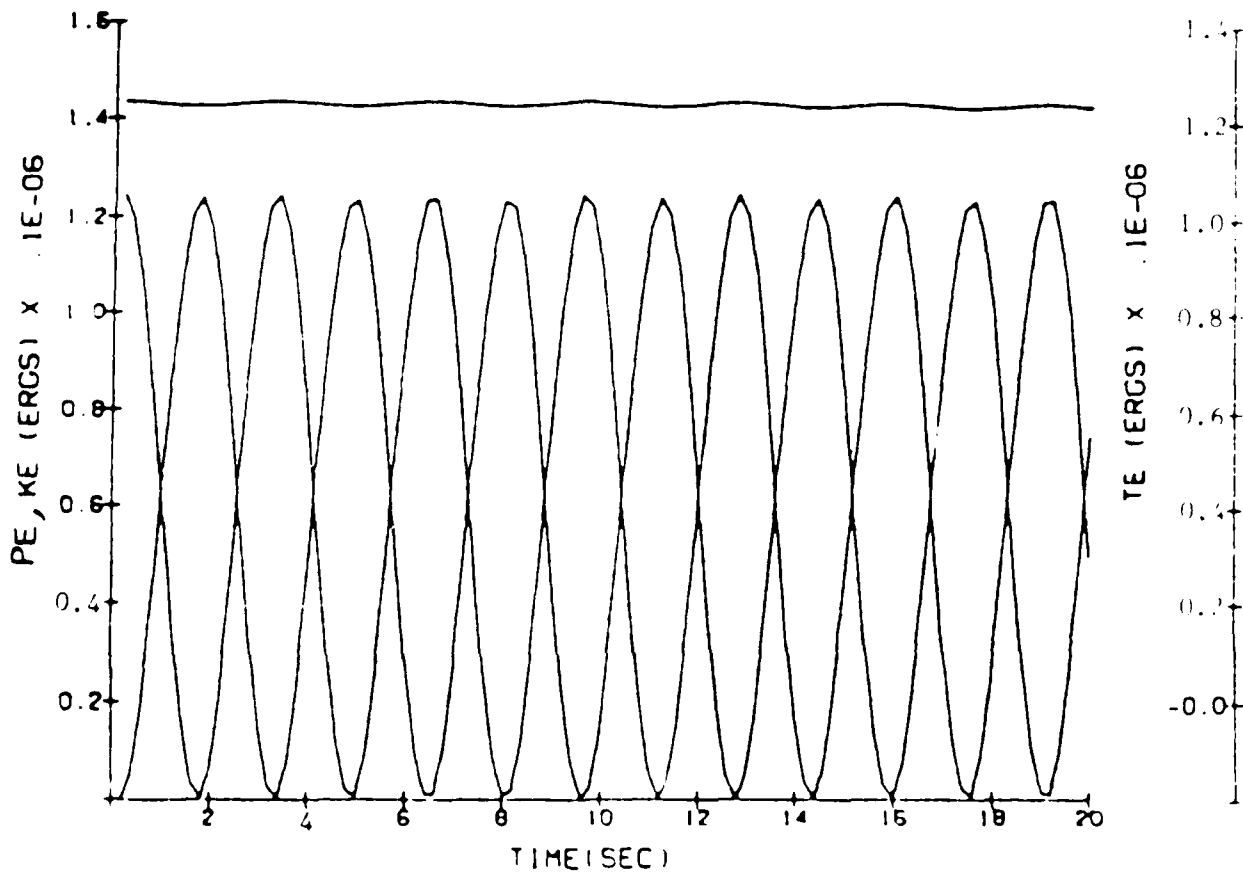


Figure 3.3- Energy Conservation for Plasma Oscillations

and that near the edges rises until another peak is reached, then we return to the initial configurations.

If we were to look at the Fourier modes of some property in the system in this simulation, we would see that the primary mode was oscillating strongly. As long as wave amplitudes are small, we would not expect the other modes, that is $k = 2, 3$, etc., to be active at all. What in fact happens is that the other modes pick up energy from numerical inaccuracies in the trajectory calculations. We can see this in Figure 3.4. Here, we began by activating mode 2. We have normalized all modes to their maximum value in this figure. We can give each mode a little of the potential energy of the initial system by providing a small random velocity execution in the X-direction. We did this by specifying $VRX = .00001$ in SET1D. Figures 3.5 and 3.6 show the results. The $k=2$ mode appears to have some extraneous excitation, but all others are behaving nicely. The quantity being studied is $\rho_k \phi_k$. The time dependence of such a wave ought to be

$$\rho_k \phi_k = \rho_0 \phi_0 \exp(2i\omega(k)t)$$

This is because from linear theory, both density and potential are assumed to be of the form

$$f(x,t) = \sum_k f_0 \exp(i\omega t + kx)$$

Thus the waves are cosines, the real parts at least. We fit the waves in Figures 5 and 6 to the function

$$A \sin \omega t + B \cos \omega t + C$$

to determine $\omega(k)$. The theoretical prediction is⁽⁵⁾

$$\omega(k) = \omega_p \cos k \frac{DX}{2}$$

where DX is the spacing between grids. In Figure 3.7, we plot this function and the measured values. It can be seen that

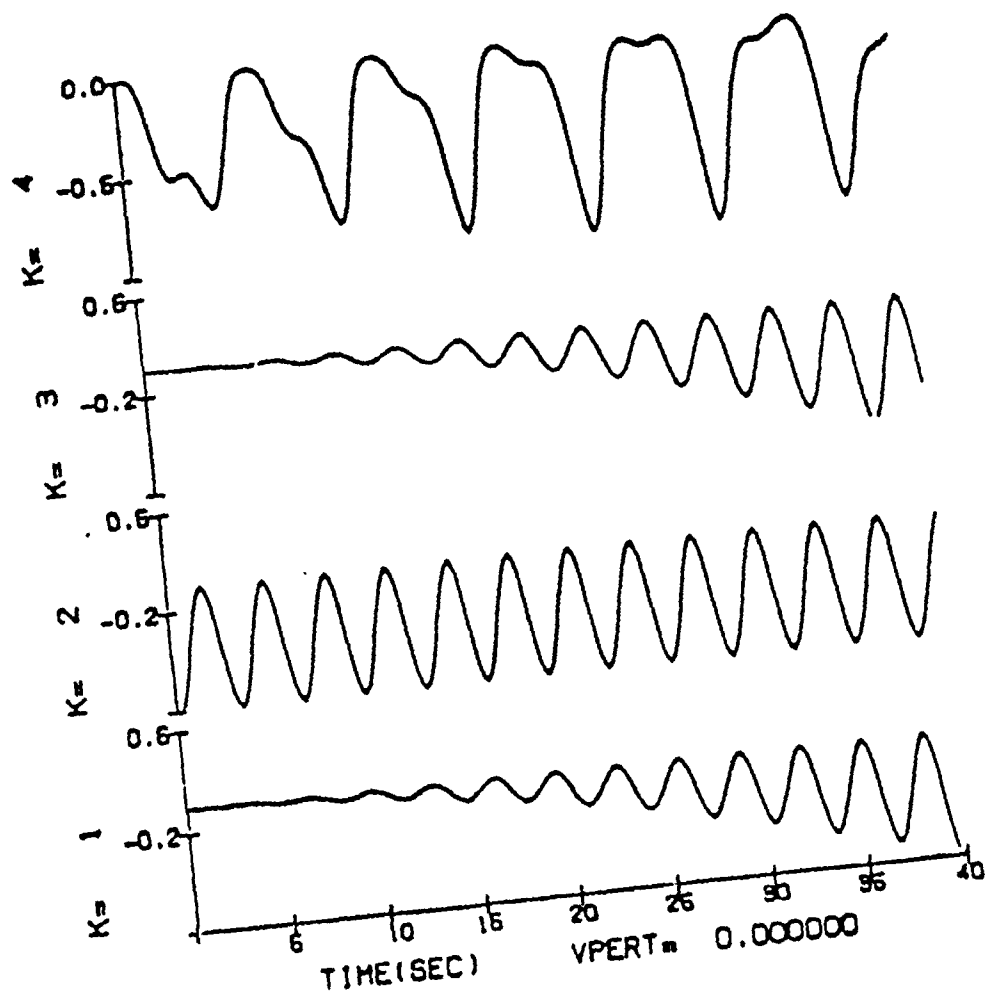


Figure 3.4- $\rho_k \phi_k$ for Excitation in the Second Mode

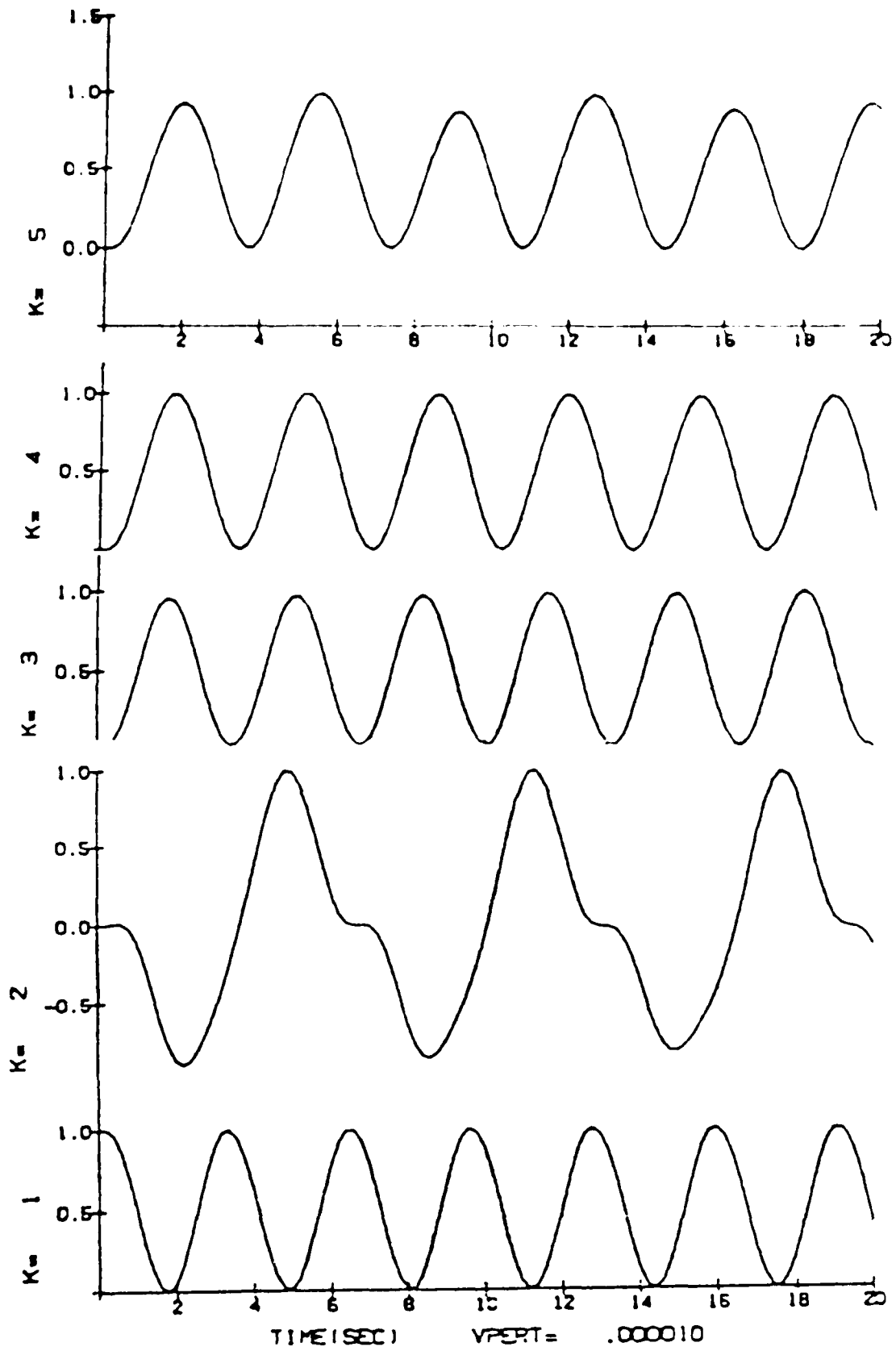


Figure 3.5- $\rho_k \phi_k$ for the First Five Modes

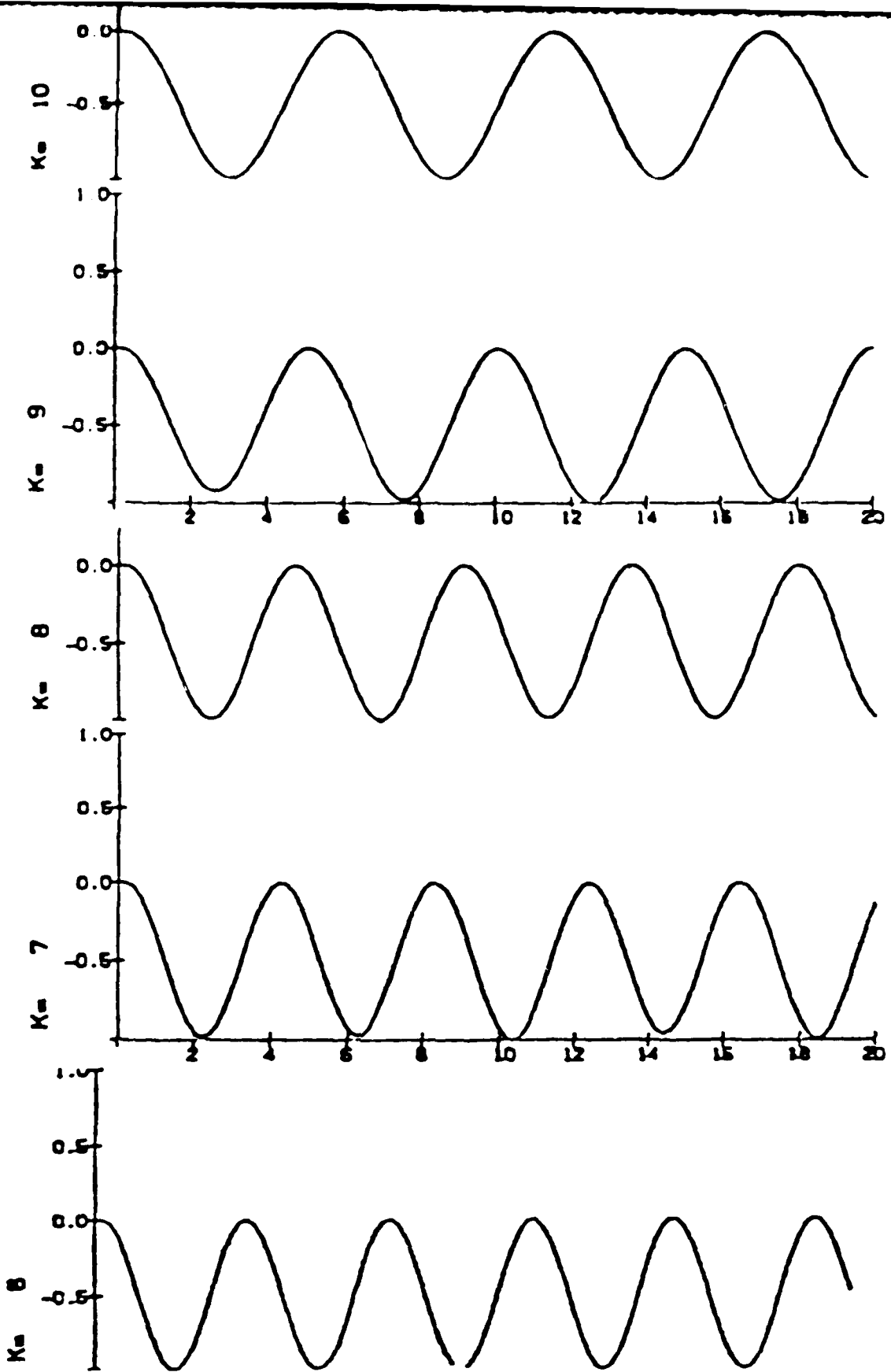


Figure 3.6- $\rho_k \phi_k$ for the Second Five Modes

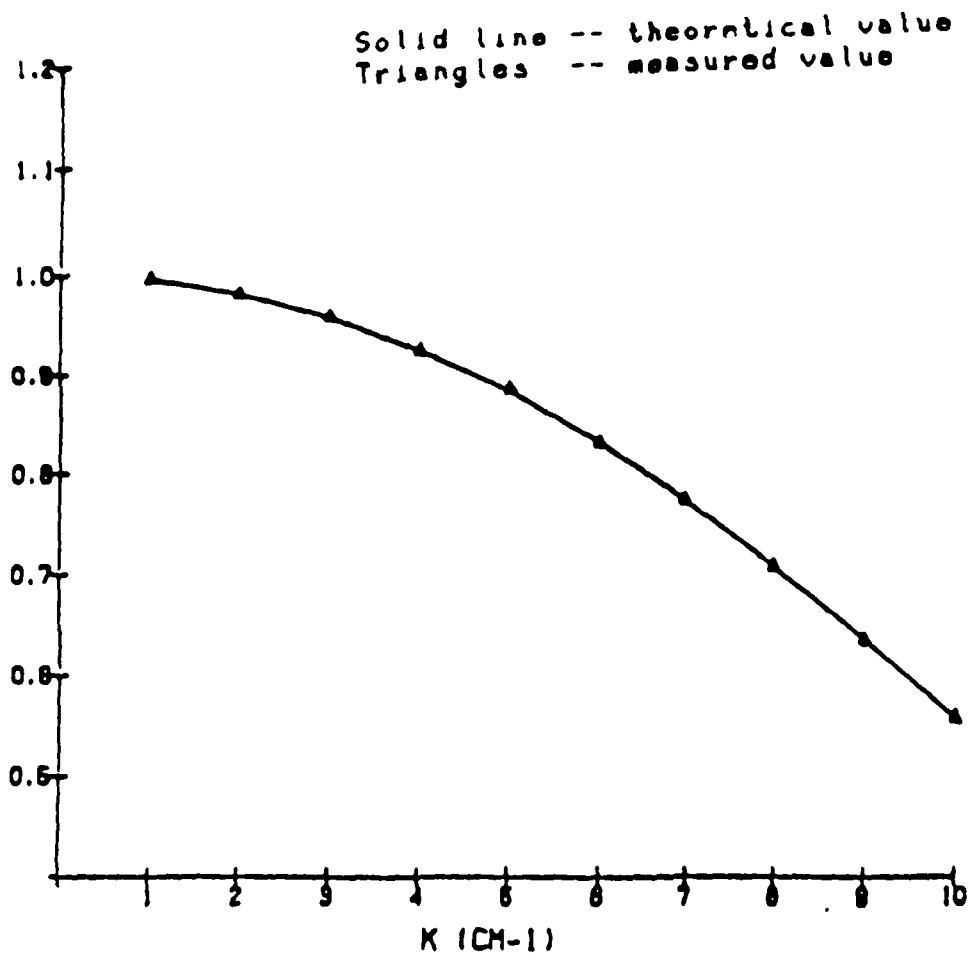


Figure 3.7- Dispersion Relation for Plasma Oscillations

the agreement is nearly perfect. For the $k=2$ mode, which seemed peculiar in Figure 3.5, we fit instead the result of direct excitation at $k=2$, from Figure 3.4.

We also were able to induce harmonic motion in the mode by beginning with a velocity given by

$$v(X) = A \sin X$$

Figure 3.8 shows the energy versus time for this system. Here potential energy begins at zero and kinetic energy is finite. The kinetic energy plotted is really the difference from kinetic energy at time zero. The frequency here appears to be the same as was obtained from an initial density excitation.

The second simulation involved the addition of a static magnetic field. With this, the plasma oscillations are changed to hybrid oscillations. The hybrid frequency is given by

$$\omega_H^2 = \omega_p^2 + \omega_c^2$$

In the following, we will try to find $\omega_H(k)$ in a way analogous to that used previously to find $\omega_p(k)$. We begin by introducing a density perturbation of the form

$$\rho(x) = A \sin kx$$

We must take care, though, to eliminate $E \times B$ drift in the center of mass of the system that could be caused by the magnetic field. In the present case of crossed magnetic and electric fields, the particles will move in circular orbits around a "guiding center". We should choose the initial conditions so that the guiding center remains stationary. We need to do this because we will analyze the dispersion

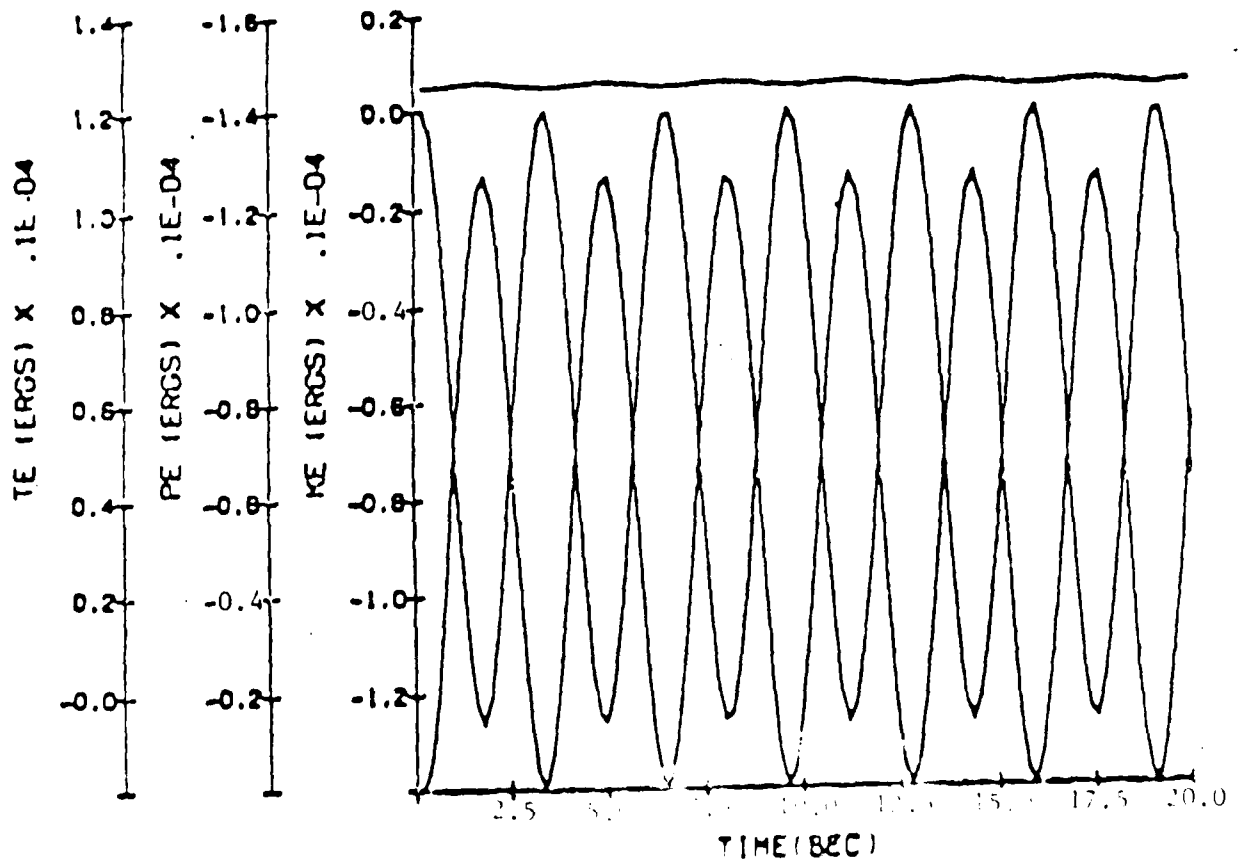


Figure 3.8 - Harmonic Motion Induced by a Velocity Curve

relation $w_H(k)$ by means of the field quantities $\rho_c \Phi_k$. If there is a net movement, the frequencies will be shifted by that motion. If there is a net drift in the Y-direction, the equations of motion tell us that there will be a net acceleration in the X-direction. This is what we wish to avoid. We can keep the Y-drift at zero if we require that

$$v_{y1} = \omega_c X_1$$

where X_1 is the initial perturbation in X displacement and v_{y1} is the perturbation in velocity. We used

$$x_1 = A \sin kx$$

so that

$$v_{y1} = -\omega_c A \sin kx$$

The input parameters for SET1D are given in Table 2.

Table 2 - Parameters for Hybrid Oscillations

BOX	27
NX	32
OMEGP	1.0
OMEGC	0.5
QDM	1.0
NE1	128
XMODE	1, 2, 3, ... *
X1	0.001
VDX, VDY	0., 0.
VRX, URY	0., 0.
NE2	0

* XMODE equal to the chosen mode to be excited

In addition, we added a line to SETID which set the initial V_y of each particle to

$$VY(I) = - OMEGC * XI * SIN(XMODE*(I-1)*BOX/NX)$$

Figure 3.9 shows the energy of the system for a timestep of 0.1 and 200 steps, in agreement with the previous equation. Again energy is conserved quite satisfactorily. Figure 3.10 shows some of the $\rho_k \phi_k$ products. These were obtained by exciting each mode separately in different runs. Again, we fit the time dependence to sine waves. If ω_c does not depend on k , then from the previous, the dispersion relation for ω_H should be

$$\omega_H^2(k) = \omega_p^2 \cos \frac{k^2 DX}{2} + \omega_c$$

Figure 3.11 gives the predicted and measured values for ω_H for the first 10 active modes. The agreement with the prediction is again quite good.

The preceding two simulations give one some confidence that the program is operating correctly, although there could still be problems left undiscovered by the simplicity of the systems considered.

3.6 Summary and Recommendations

We have investigated the numerous algorithms in general use for particle pushing simulation and have chosen from these a set to solve a relatively simple plasma system. We have written a program to simulate this system and have shown the program to reproduce published results⁵ for two simple initial conditions. In trying to go beyond these simple systems, we have encountered some problems. We feel that these are due in part to a lack of experience in choosing the initial state. In dealing with warm plasmas, when there is some random initial velocity, there are inherent problems

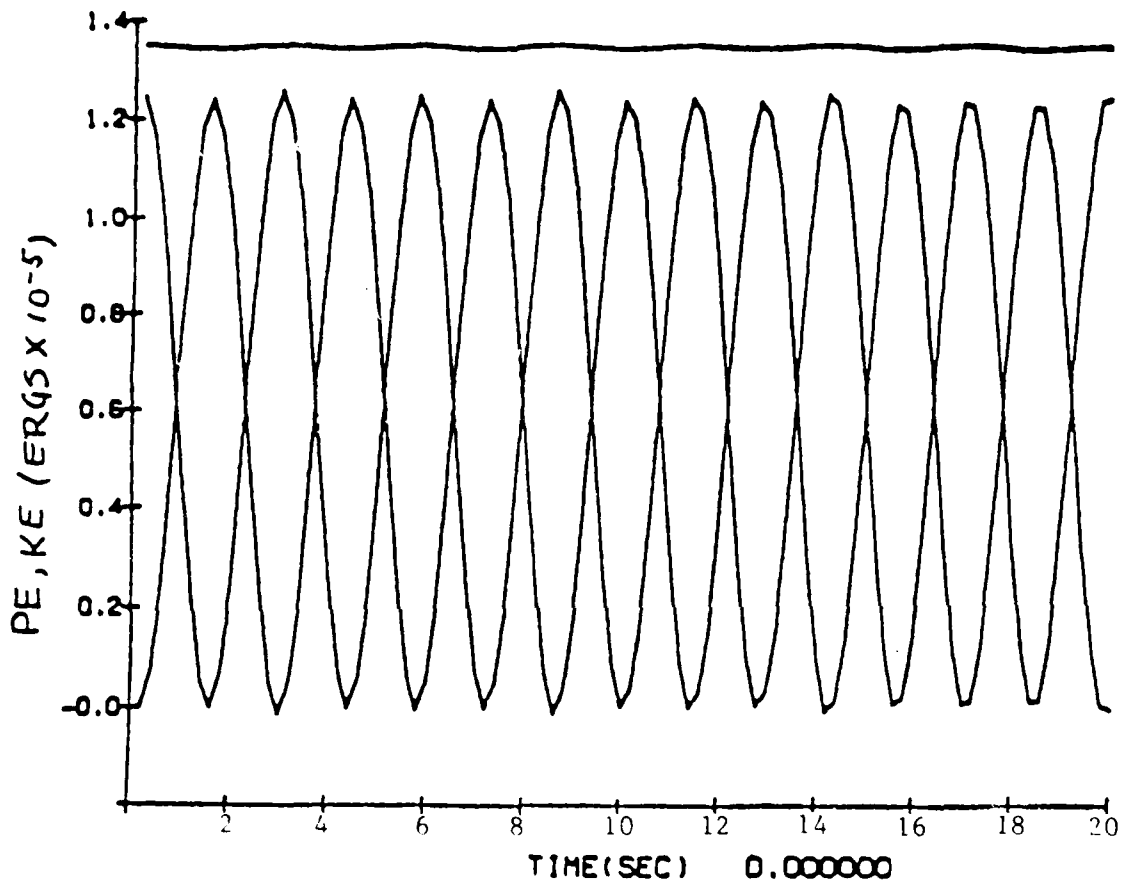


Figure 3.9 - Energy Conservation for Hybrid Oscillations

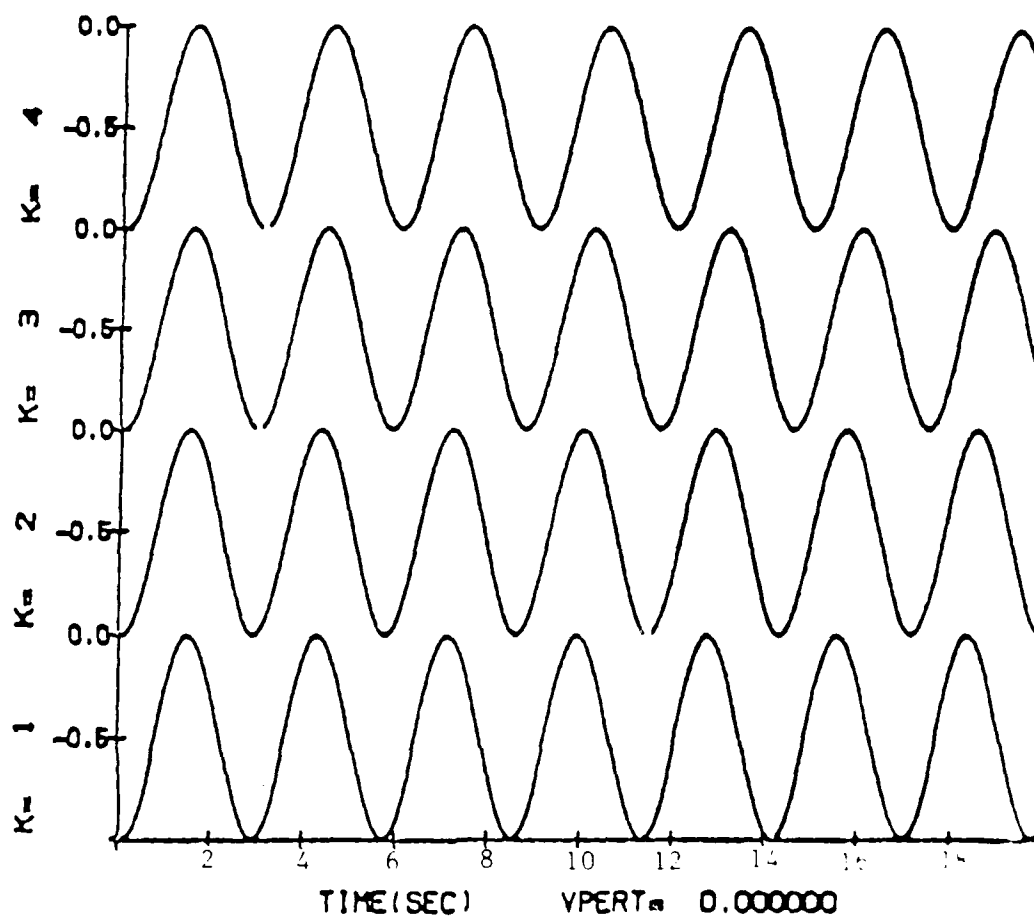
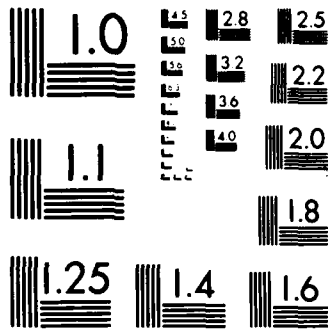


Figure 3.10 - $\rho_k \phi_k$ for Hybrid Oscillator



MICROCOPY RESOLUTION TEST CHART
NATIONAL BUREAU OF STANDARDS 1963-A

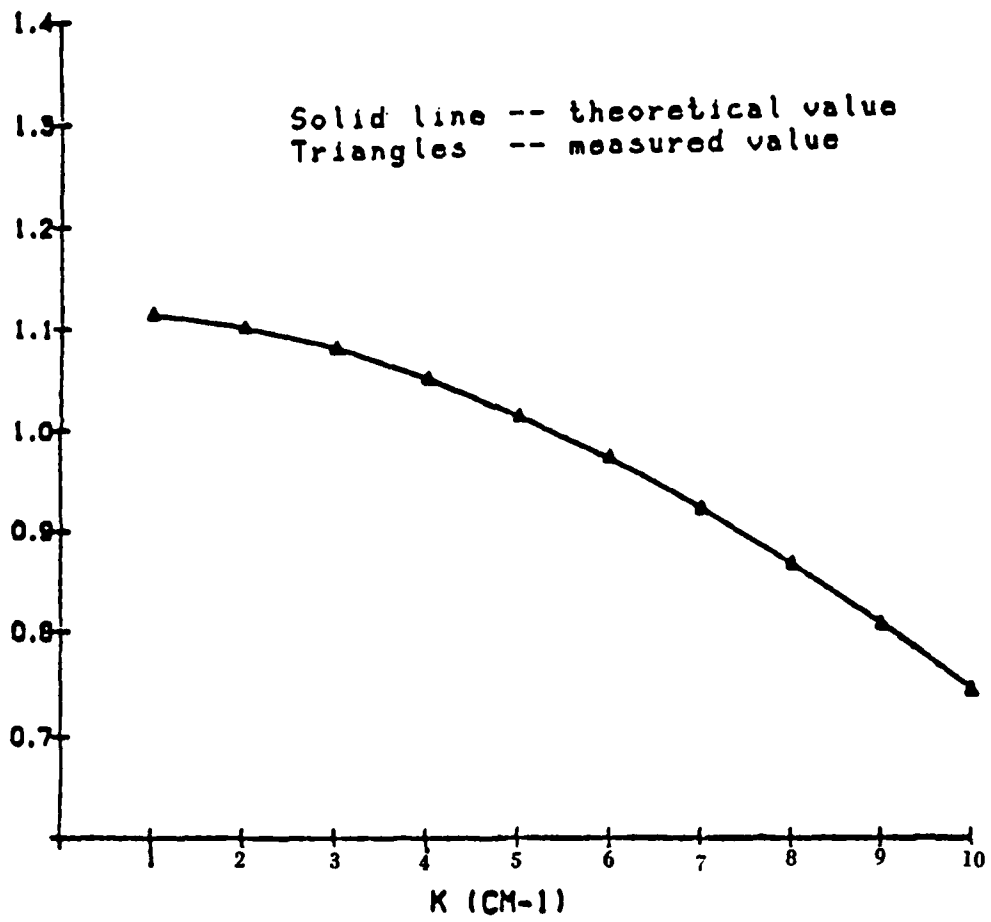


Figure 3.11 - Dispersion Relation in Hybrid Oscillations

in attaining a proper balance between kinetic energy and potential. If one makes the initial velocities large, the particles will simply move in straight lines, unaffected by fluctuations in charge density. In plasma simulation one needs to be very careful in identifying conditions that are physically acceptable or unacceptable artifacts in models.

Understanding the basic physics and writing the program was comparatively easy. That is the technical problem that we have addressed and solved in this work. In doing this, we have gained a substantial advantage over simply borrowing a particle pushing program from someone else. At least the program is not a black box. The question now is, what is needed to derive some useful results from our work? It seems especially true here that asking the right question is at least as difficult as finding the answer. Tackling the area of simulation still remains a substantial undertaking.

References

1. J. M. Dawson, Rev. Mod. Phys., 55, 403 (1983).
2. C. K. Birdsall and P. Fuss, J. Comp. Phys, 3, 494 (1968).
3. O. Buneman, J. Comp. Phys., 12, 124 (1973).
4. A. B. Langdon and B. F. Lasinski, in "Methods in Computational Physics", Volume 9, B. Alder et al, eds., Academic Press, New York, 1970.
5. C. K. Birdsall, "Plasma Physics via Computer Simulation", Private Communication.
6. Krall and Trivelpiece, "Principles of Plasma Physics", McGraw-Hill, New York 1973.

4.0 Beam-plasma Interaction and Charging in Emitting Probes

When a probe ejects a charged particle beam in a plasma environment, the probe itself develops a charge. Charged particles are drawn from the ambient plasma to neutralize this charge and it is believed that a steady state develops with the returning current equal to the beam current and the probe at some potential attractive with respect to the ejected particles.

Two different approaches have been taken to elucidate the details of this system. The first approach takes as a principal assumption that the beam leaves the probe environment completely and addresses the problem of interaction between the charged probe and the surrounding plasma. The second approach ignores the probe charging and attempts to model the interaction between the beam and the ambient plasma.

Our efforts have been primarily in support of the Beam Emitting Rocket Technology program (BERT). In Section 4.1 we describe a mechanism relying on ionization of neutrals by returning current which can be called upon to explain the anomalously low charging levels in electron beam emission. We show how this model has been used for mission planning and compare its predictions to test chamber and flight data. Following in Section 4.2, we describe a second model which has been used to explain the wave data obtained in flight. These waves are assumed to be the result of interaction between the beam and the plasma environment.

4.1 Modeling of Spacecraft Charging with Beam Emission

The Beam Emitting Rocket Technology program (BERT) has been an important element in the investigation of charging of electron beam emitting crafts in the ionosphere. Such

charging has been shown by recent experiments to be much less than the level predicted by most theoretical models⁽¹⁾. A model PLAS3 had previously been developed which invokes the mechanism of ionization of neutrals in the sheath by the return current of electrons to suppress the probe potential. We have recently had the opportunity to test this theory quantitatively against actual experiments made both in a test chamber and during flight. Support was provided both for mission planning, and in the analysis and comparison of the resulting data with theoretical models.

4.1.1 Comparison of 1-dimensional Models of Probe Charging

There are several models which give the current collected by a probe as a function of potential, though unlike PLAS3, they ignore ionization. We wished to compare their predictions for environments appropriate to the BERT mission. We selected five models to examine.

- The Orbital Limited flow model (OLM), based on current collection by a charged probe in a Maxwellian plasma, with the assumption of no sheath formation.
- The Space-Charge limited model (SCL), based on the potential acquired by a probe when surrounded by a sheath of specified radius through which an ambient current of electrons is collected.
- The Keil fit to Laframboise' (LEF) calculations, which is a convenient way to generate I-V curves that closely approximate the calculations of Laframboise.
- The Self-consistent Mott-Smith/Space charge limited equations (MSS), based on Sherman's calculations in which these equations are solved simultaneously for a common current characteristic.

- The Parker-Murphy model (PKM), which allows for the inclusion of a magnetic field.

These were collected and coded together in a single program to produce a variety of comparisons. One such is shown in Figure 4.1. This gives the potential predicted by several models, both in spherical (SP) and cylindrical (CY) symmetry, for a specified altitude in a model BERT environment. The model not shown, MSS, is almost identical to SCL in this parameter range. Of particular interest is that the largest charging is predicted by the model involving a magnetic field, PKM-SP, which leads one to believe that a magnetic field alone cannot be called upon to explain the low levels of charging in electron emission.

A particle tracking study carried out alongside this work may indicate why this is so. In this study, a probe was placed in a magnetic field of about .5 Gauss. Electrons were started some distance away from the probe and given a small velocity. Their path was then followed until they either impacted or missed the probe. We found that the electrons that impacted the probe on the first pass gave rise to a current almost identical to the Parker-Murphy model above. We also found, however, that a large number of electrons missed the probe on the first pass but turned around sometime later and returned to it, eventually making impact. This means that the Parker-Murphy model is really just a lower limit for current collection, or an upper limit for potential. While the current collection restraints imposed by a magnetic field are still an important anomaly in the PLAS3 model, which includes no magnetic field effects, it seems clear that theories that treat collection of only these "first pass" electrons can never explain the remarkable low potentials encountered.

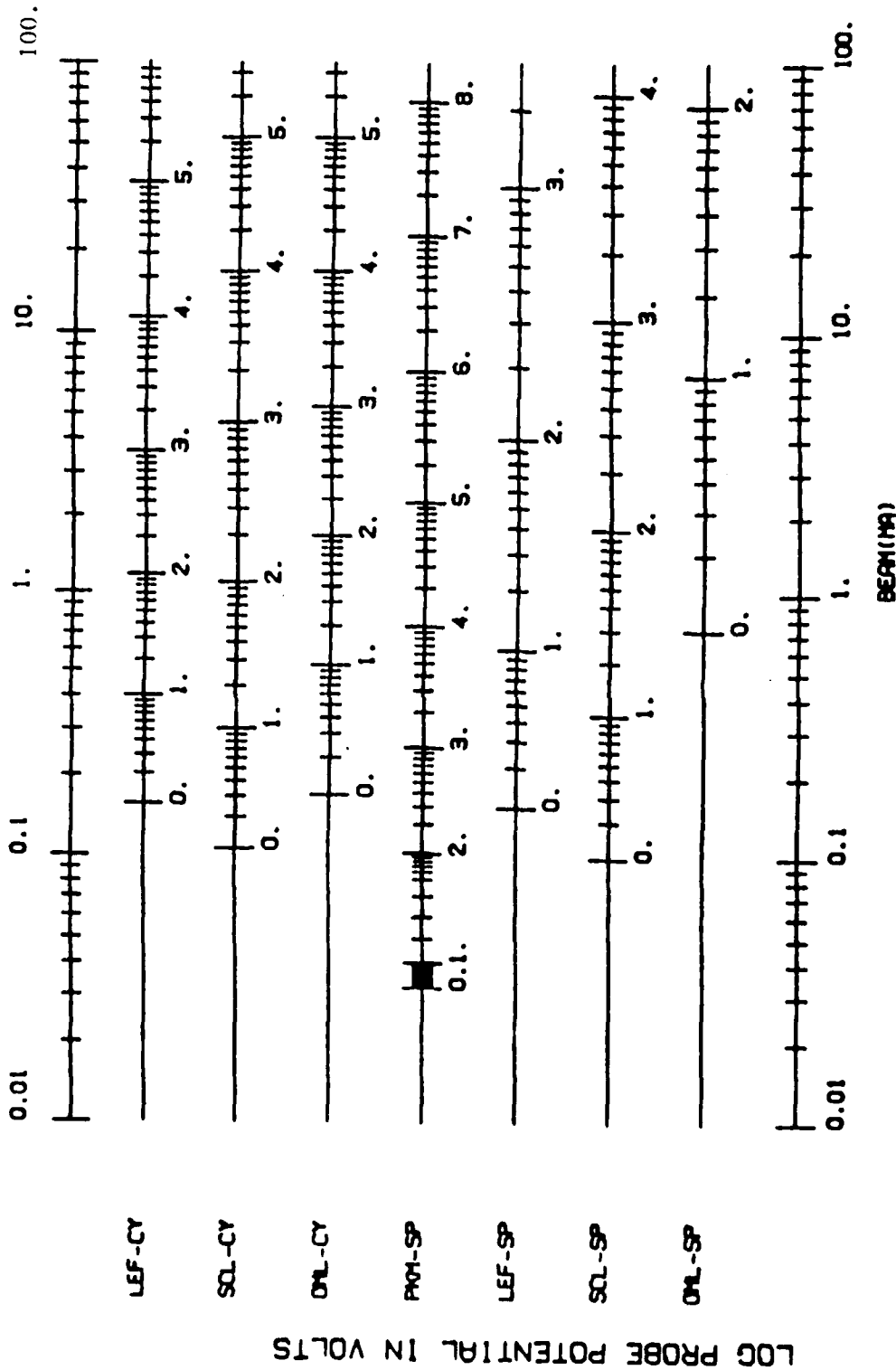


Figure 4.1 Predicted Voltage at Several Beam Currents (top and bottom scale) for Four Charging Models at a BERT Altitude of 150 km.

4.1.2 Mission Planning with PLAS3

The PLAS3 program has been previously described in detail.^(2,3) It is a one-dimensional space charge limited model with no magnetic field. It takes into account the ionization of neutrals surrounding the probe by the return current of ions or electrons. For the ion case, the modification to charging characteristics is minimal. For electrons, however, a substantial suppression of charge is found. This model has been used, in both spherical and cylindrical symmetries to simulate several features in the BERT-1 mission plan.

A study was done to determine the optimum way to arrange the beam pulses during flight. The choice was in the variation of the number of current steps which would constitute one sweep. Each step was of 10 millisecond duration and, using many steps, we could better approximate the continuous sweep desired. However, if a sweep lasted a comparatively long time, environmental conditions might change substantially, complicating the I-V curve. We approached this problem by creating a simulated strip chart of a charging event during BERT-1 flight. We chose a series of altitudes, calculated the rocket velocity and the subsequent altitudes passed during sweeps of 30 and of 256 ten millisecond intervals, using the model environment developed to calculate the potential profile with PLAS3. Our results indicated that the longer sweep preserved the overall shape of the I-V profile, meaning that environmental conditions were reasonably stable over this period. Thus, it was decided that 256 intervals should be used.

Another study was done to help decide the best time to change the capacitance of BERT. The backside of the rocket is normally electrically isolated from the beam end, but can be connected during flight. This effectively changes the surface area of the rocket. Since charging theories predict

a decrease in voltage with increasing surface area, it was desired to make this modification in capacitance sometime during flight. To this end, we calculated curves of potential versus altitude for selected beam currents for a normal sized BERT and one twice as large. PLAS3 was used for electron emission and the space charge limit was used for ions. We found that the reduction in voltage was apparent at all altitudes for all currents, but that it was much smaller in the electron case when ionization was predominant. This suggested that the increase should be made in the electron mode when ionization is weak, or near apogee. For ions, the reduction was nearly the same at all altitudes.

In support of the test chamber experiment, an effort was made to predict voltages of the probe as a function of electron density, electron temperature and neutral pressure. A simplification of this study was made possible when it was realized that the voltages and critical currents are strongly dependent on only two parameters, the neutral pressure and the product of the electron density and the square root of the temperature, a quantity proportional to the thermal flux. This is borne out in Figure 4.2 which shows the I-V curve over two decades of variation in density. It can be seen that the peak voltage and the critical current at which it occurs are nearly constant.

By varying these parameters, making several runs with PLAS3, we produced plots of contours of constant maximum voltage and critical current, such as the one shown in Figure 4.3. These plots can be used to estimate the charging for a known environment, to determine the beam current necessary to observe non-monotonic behavior, or to estimate neutral pressure and density from charging data.

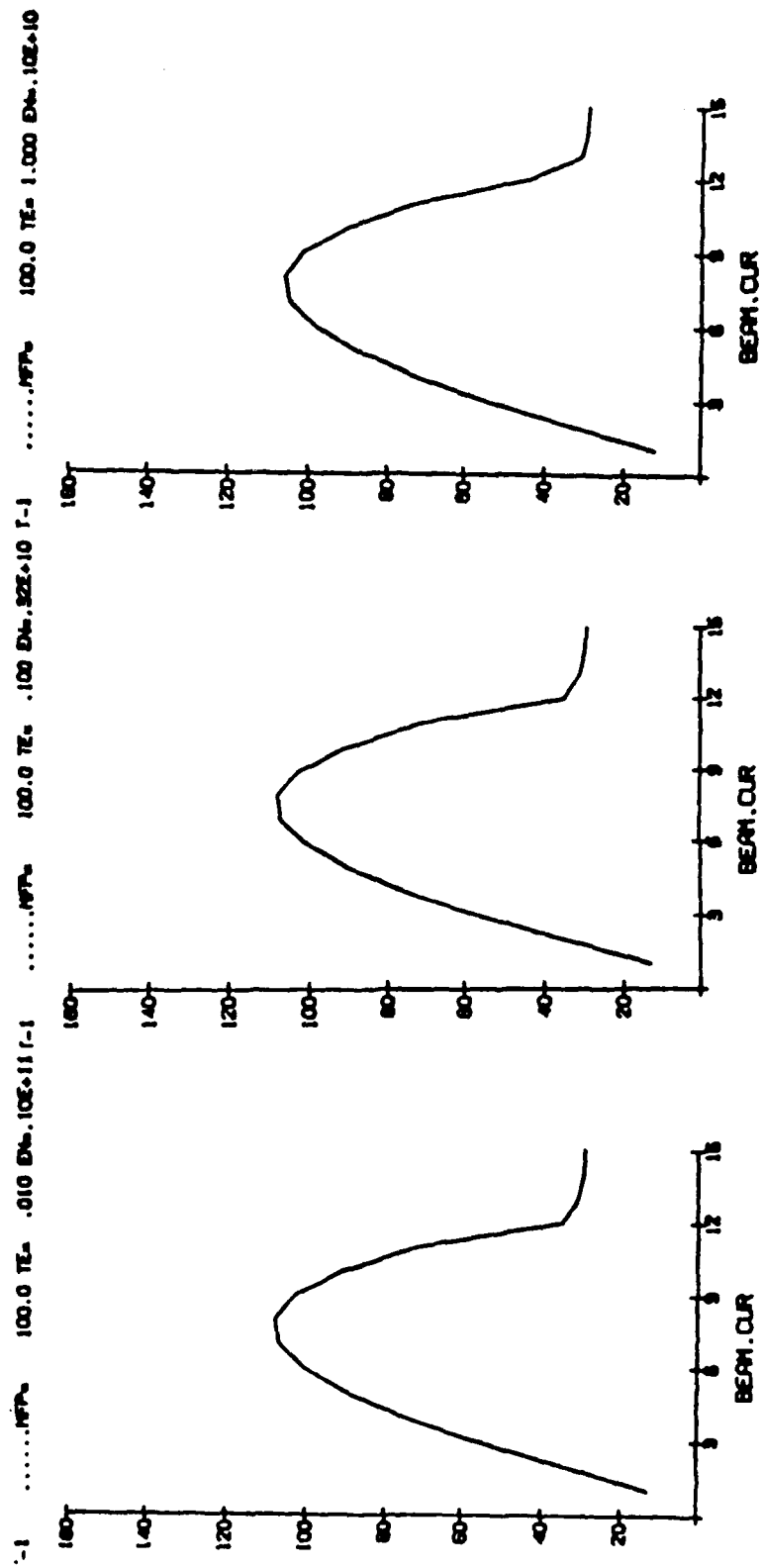
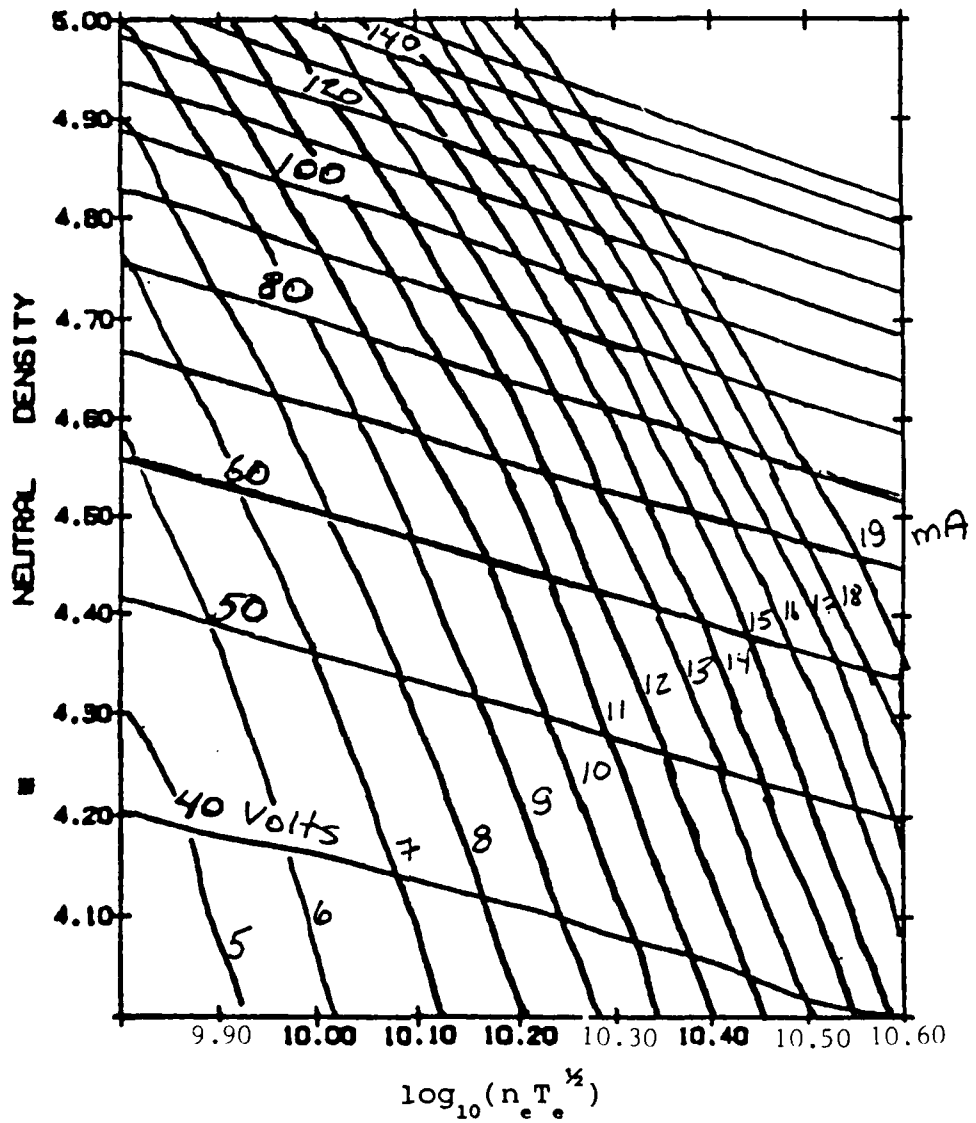


Figure 4.2 IV Curves from the PLAS3 Model at Constant n_{TP} ,
 ($T=0.1, .1, .1$) Showing Constancy of Potential at
 Equal Flux



Neutral Density is 10^{-4} torr
 Electron Density is $10^x/m^3$

Figure 4.3 Contours of Constant Critical Current (vertical) and Peak Voltage for a Range of Flux and Neutral Pressure Expected in the Johnson Test Chamber

4.1.3 Comparisons with Experiment

In March 1985, the BERT-1 payload was put inside the large vacuum chamber at Johnson Space Center. Inside the chamber, an environment was created to simulate the ionosphere. Electrons were ejected over a range of currents, and vehicle charging was measured. One particularly good quality result is shown in Figure 4.4. The non-monotonic behavior is clearly present. Unfortunately, data on neutral pressure and electron density are not available to any degree of precision due to the unstable conditions in the chamber. We can however use the previous Figure 4.3 to estimate from the measured peak charging of 95 volts at a current of about 9 milliamps, that the model would predict a neutral pressure of 1.5×10^{-5} torr and an ambient flux of 9×10^9 electrons/meter³/(eV)^{1/2}.

In June 1985, BERT-1 was launched from White Sands, NM⁽⁴⁾. The rocket attained a maximum altitude of 240 km, but unfortunately, only the first seven seconds of beam emission were processable. From those first few seconds, a reasonable good I-V curve was obtained and is shown in Figure 4.5. The PLAS3 model was used to calculate a theoretical equivalent.

Although electron density and temperature were known to a high degree of precision, outgassing from the spacecraft left the neutral density uncertain. Thus we were forced to vary the neutral pressure within reasonable bounds until the best agreement was obtained. This is shown as the solid line in Figure 4.5. The agreement is quite excellent.

4.1.4 Electron Beam Induced Ionization

A possible alternative to the PLAS3 concept of sheath ionization by returning electrons is the idea that the beam itself may produce substantial ionization. Work with the

JOHNSON TEST/EQUINOX

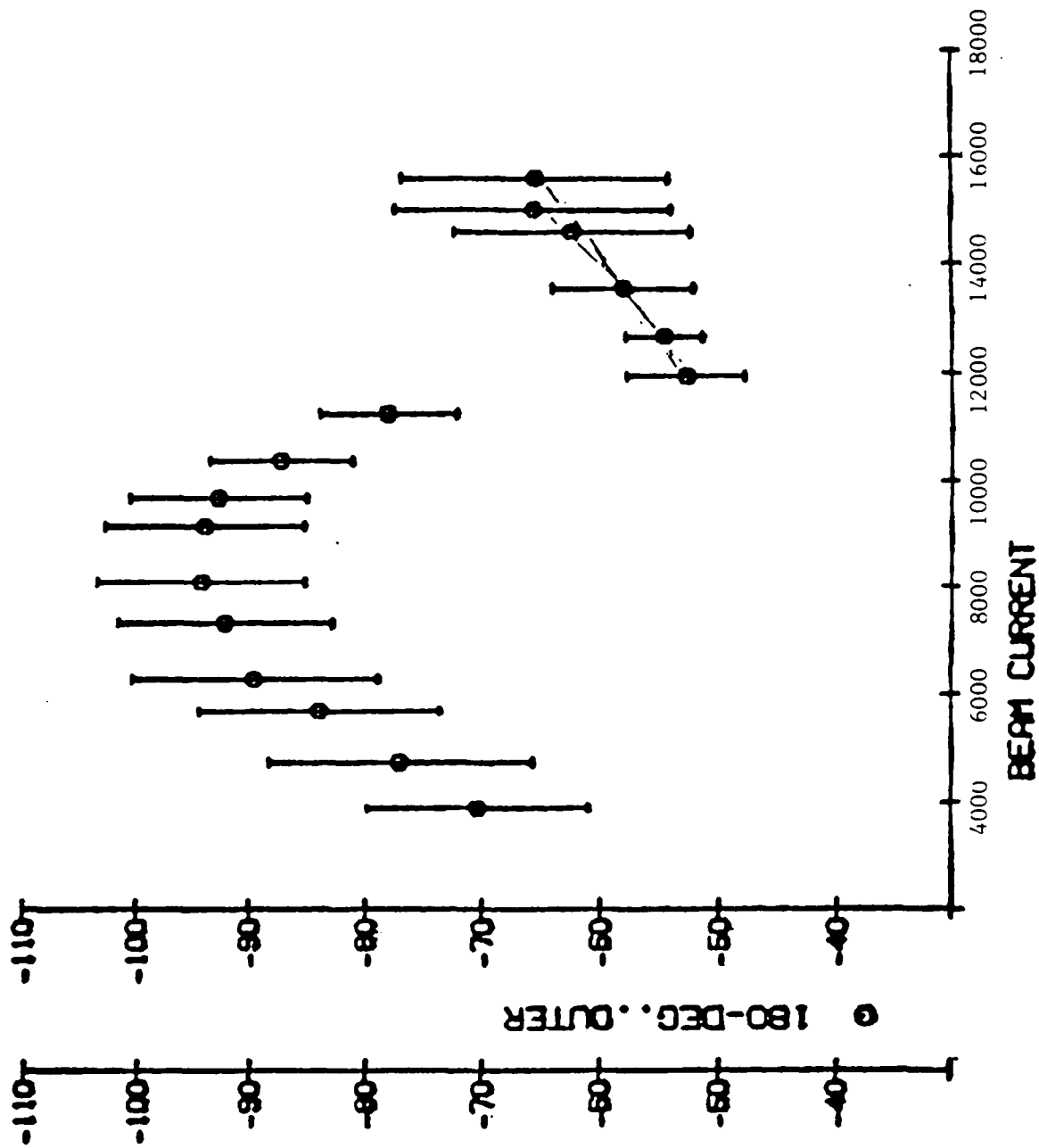


Figure 4.4 IV Curve Observed in the Johnson Test Chamber

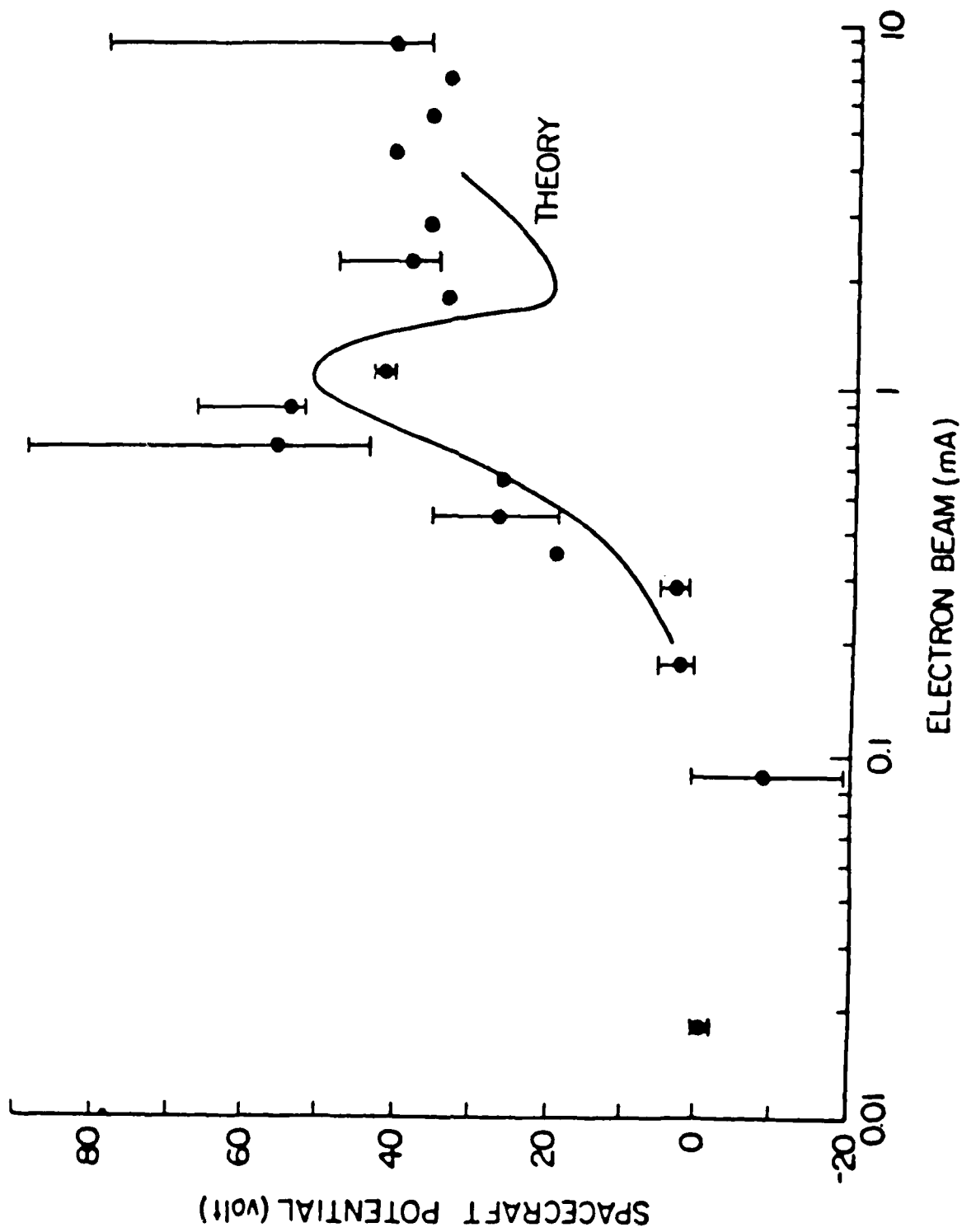


Figure 4.5 IV Curve Observed During BERT Flight

SCEX rocket has shown that there is a critical current beyond which an avalanche effect substantially increases the production of secondary ions by the beam.⁽¹⁾ Below this, beam induced ionization is minimal.

The SCEX rocket was launched into the auroral region in January 1982. It flew to an apogee of 230 km. Electron beams were ejected in a range from 1 to 100 mA and energies from 3 to 9 keV. The luminosity of the ejected beam was measured by an on board photometer pointed directly at the beam. This luminosity was a result of ionization of neutrals by the beam electrons.

The important result insofar as BERT is concerned was that almost no enhancement of luminosity was observed for beam currents less than 10 mA, and below a critical current of about 70 mA, luminosity was minimal. Since BERT operates well below this critical current, we could infer that beam induced ionization is not important. However, this work does suggest a limit beyond which beam ionization must be considered.

4.1.5 Effect of Photocurrent on Satellite Charging

Support was provided for various charging studies of other beam emitters. In this case, the satellite was SCATHA. Since SCATHA operated at geosynchronous altitudes where neutral molecules are scarce, it was not expected that non-monotonic behavior would be observed. Rather, the data of interest involved a potential difference observed when the booms of the satellite rotated in sunlight. The booms were deployed on opposite sides and rotated with the satellite in the equatorial plane. The arrangement was such that these booms pointed nearly directly toward and away from the sun alternately. The correlation between the sun angle to the booms and the potential is shown in Figure 4.6. There is a

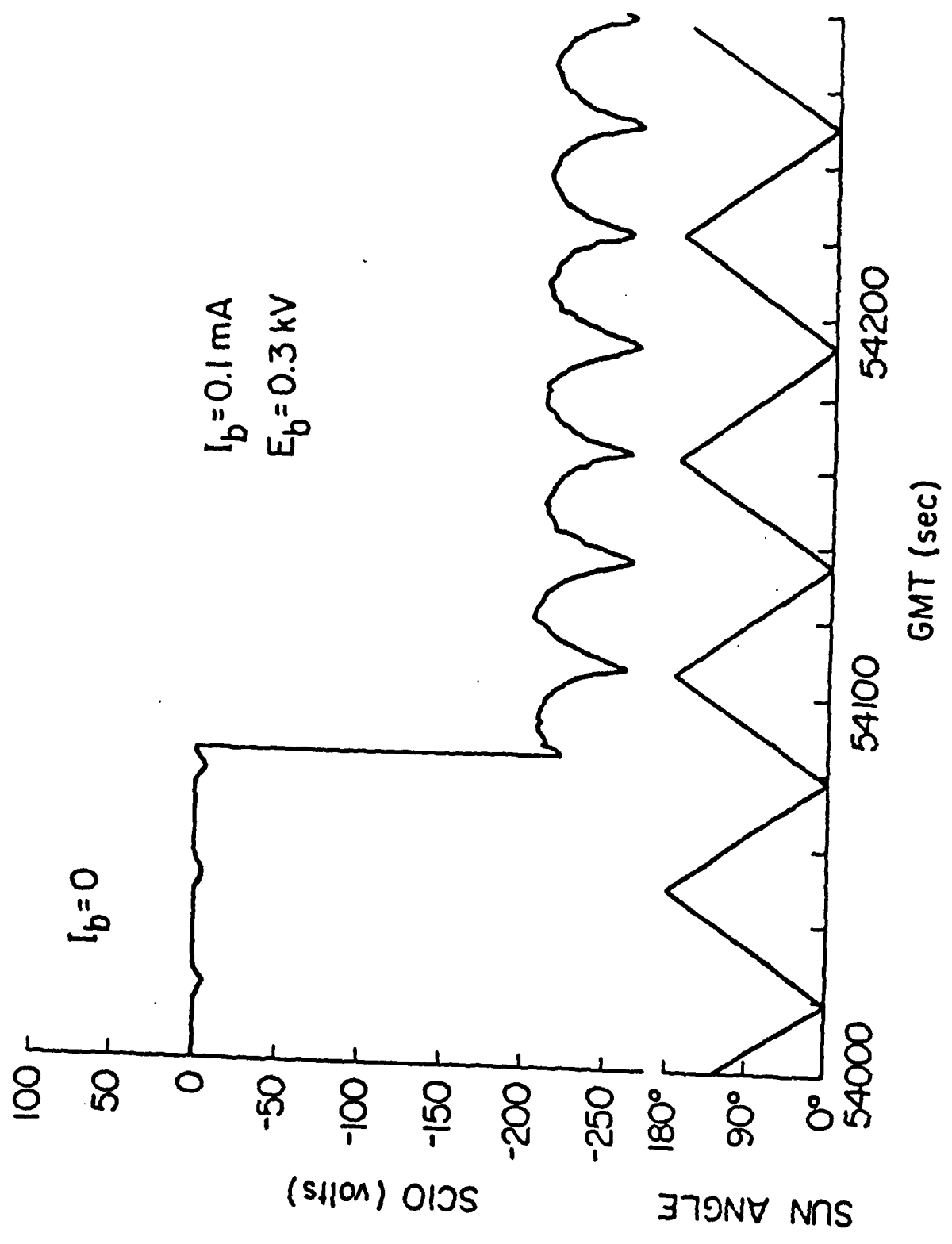


Figure 4.6 Boom Potential and Scin Angle from SCATHA

lowering of potential obtained when the booms are perpendicular to the satellite-sun axis.

The mechanism proposed to explain this data⁽⁶⁾ is photoionization of the boom material, which contributes to the returning electron current and lowers potential. In a steady state, the incoming current must equal the outgoing current due to the beam

$$I_b = I_e + I_{ph} \quad (1)$$

where b refers to beam, e to the ambient current, and ph to the photocurrent. Since the plasma density at geosynchronous altitudes is low, the ambient current is well approximated by the orbit limited probe equation⁽⁷⁾

$$I_e = nv(1 + e\phi/kT) \quad (2)$$

We took the radial dependence of the potential ϕ to be of the Debye form

$$\phi(r) = \phi(0)(R/r+R)\exp(r/\lambda_D) \quad (3)$$

The photoelectrons were assumed to have a Maxwellian distribution with a temperature T_{ph} . The fraction of photoelectrons collected by the probe, originating at a

distance r along a boom is then

$$f(\phi(r)) = \text{Int}(e\phi(r))/\text{Int}(\infty)$$

where

$$\text{Int}(h) = \int_0^h E \exp(-E/kT_{ph}) dE$$

If the photoelectron emissivity is j_{ph} then the current

density generated at any point r along the boom is

$$J_{ph}(r, \phi) = f(\phi(r))j_{ph}$$

To get the total current collected, we must integrate this over the length of the boom L . Also, the sun angle dependence is introduced as being proportional to the surface area of the boom perpendicular to the satellite/sun axis. With sun angle θ

$$I_{ph}(\theta, \phi(0)) = 2D|\sin\theta| \int_0^L J_{ph}(r, \phi) dr$$

A plot was made, shown in Figure 4.7, giving the current expected when θ is 90 degrees and when it is zero, the case for no photoionization. By comparing the values for potential at constant current, one can determine the amplitude of the expected oscillation. For the data shown in Figure 4.6, a difference of about 50 volts is found, which is in good agreement with experiment.

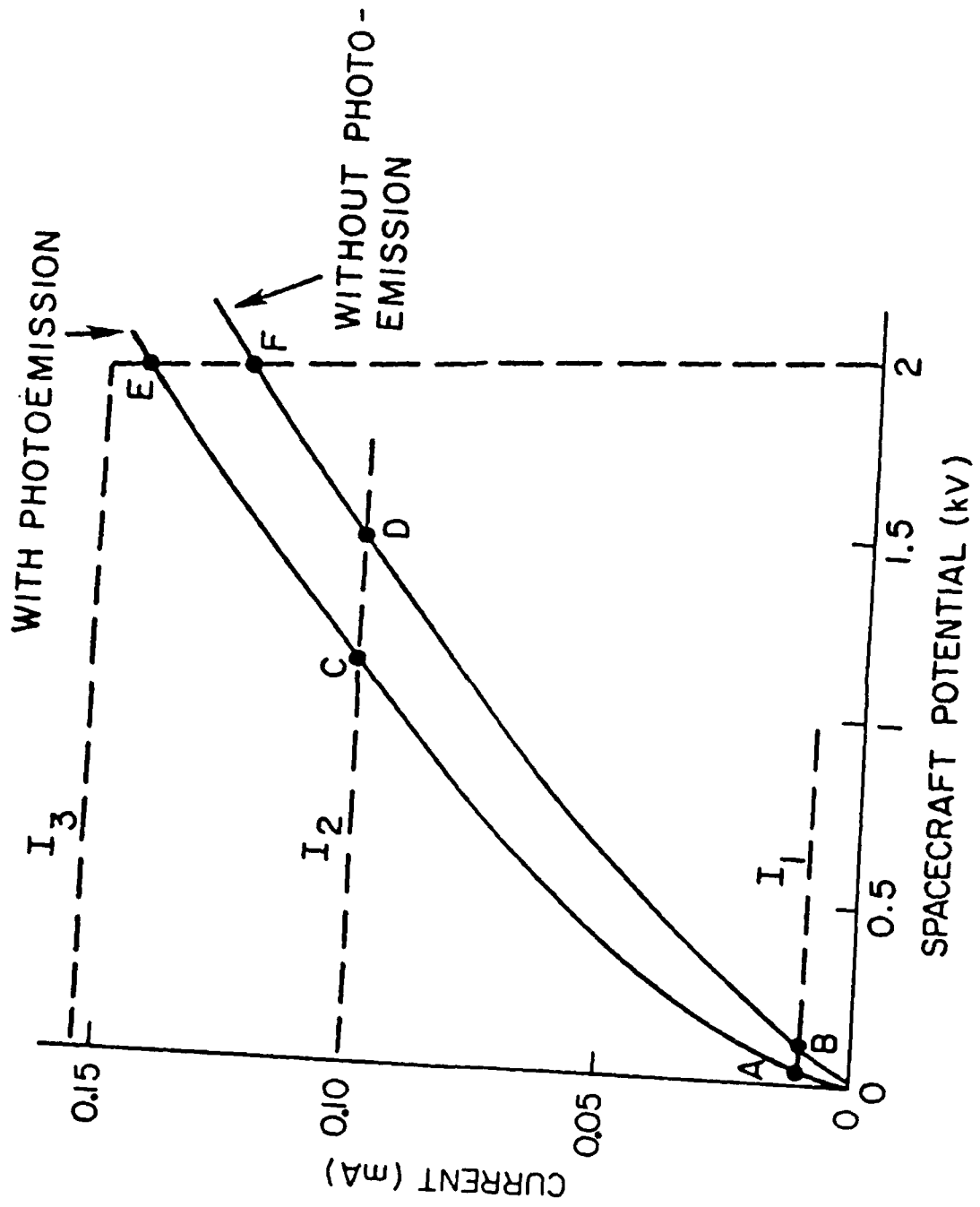


Figure 4.7 Total Current With and Without Photoionization as a Function of Spacecraft Potential

4.2. Investigation of Beam-Plasma Instabilities

Along with the main BERT-1 payload, described in Section 4.1, the rocket carried a daughter, ERNIE, which was separated during flight and functioned to measure the spectrum of ion waves generated during electron emission events. Although much of the charging data from BERT appears to be unusable, the data from ERNIE was not affected and has proved to contain a wealth of interesting observations. A model was implemented and maintained, relying on linear Vlasov theory, and has been used to explain some of this wave data. Additionally, a model has been created describing the stochastic heating of ions, a necessary element in the chain of events invoked to explain these results.

The mechanism consists of several steps, which we outline as follows⁽⁸⁾. The electron beam creates ions by the ionization of ambient neutrals. The resulting plasma consists of warm beam produced ions and cold background ions. Our model predicts that this system is capable of producing unstable electrostatic ion cyclotron (EIC) waves. The constituents of this plasma will be the ionization products of abundant neutrals, O^+ and N_2^+ in the beam, and naturally occurring O^+ , NO^+ and O_2^+ in the background.

The waves produced by these instabilities in the plasma cloud surrounding BERT then propagate into the background surrounding ERNIE. We use ray tracing to show that these waves can escape. Once there, they are capable of stochastically heating ambient hydrogen ions; again we show this through simulation. Now, the daughter is immersed in a warm hydrogen plasma, capable of producing electromagnetic Bernstein waves. This instability was shown to exist from previous work supported by Radex using another model.⁽¹⁰⁾ The two pieces of ERNIE data that we will attempt to explain are the observations of EIC waves at .1 to .24 times the oxygen plasma frequency, and ion Bernstein waves.

4.2.1 EIC Instabilities

The purpose of this section is to show that EIC waves are generated at frequencies close to .1 times the ion plasma frequency. We will first describe a model which we first solved for electron beams. We will generalize this to a multi-component ion plasma, letting the warm ions take the place of the beam and the cold ions take the place of the background.

The model is based on solutions to the linear Vlasov equation,⁽⁹⁾ assuming an electrostatic approximation in which all terms involving the induced magnetic field are ignored.

$$2f_1/2t + v \cdot \nabla_x f_1 + (e/m)(v \times B_0/c) \cdot \nabla_v f_1 + (e/m)(E_1 \cdot \nabla_v f_0) = 0$$

The model includes a static, uniform magnetic field and is inhomogeneous in one direction perpendicular to that field. This complicates the Vlasov equation in that solutions are dependent on spatial gradients. We make what is called a local approximation, which says that the Vlasov equation can be solved at any point in space as if the system is homogeneous with respect to spatial variation. The end product of this solution is a characterization of the type of waves that can propagate in the system, both their frequency ω and their wave numbers k . Specifically, we can find ω as a function of k , and when a frequency is found to contain an imaginary component, this is interpreted as an instability which oscillates at a frequency equal to $\text{Re}(\omega)$ and grows in amplitude at a rate $\text{Im}(\omega)$.

The derivation of the dispersion relation is quite laborious and the algebra has undergone substantial cross checking and correction, but we omit it here. We will concentrate on a description of what is called the zero order distribution function, which defines the problem. The idea is that if we set up such a system, it would evolve in time, at least for

a relatively short time compared to collision times, via the predictions of the theory. Beginning with the background plasma, we assume it is cold with no velocity in B-field perpendicular or parallel directions.

$$f_{o,back} = n_o / (2\pi v_p) \delta(v_p) \delta(v_r) \quad (1)$$

where p and r mean perpendicular and parallel to the magnetic field, and δ is the Dirac delta function. When this distribution is passed through the Vlasov equations with the assumptions noted above, we find that it contributes a term of the form

$$\omega_p^2 k_p^2 / (\omega^2 - \omega_c^2) - \omega_p^2 k_r^2 / \omega^2 \quad (2)$$

to the dispersion relation. k_p and k_r are again the wave vector components in the magnetic field perpendicular and parallel directions. ω_p and ω_c are the plasma and cyclotron frequencies.

For the beam, we assume that electrons have a cold velocity distribution with two components v_{rb} and v_{pb} , defined as before. The v_{rb} is along the magnetic field and the v_{pb} is distributed uniformly through the plane perpendicular to the field. This velocity distribution is called a ring and is adopted not so much for authenticity as to simplify calculations. To model a system with a finite beam, we restrict the gyrocenters of the beam electrons to the negative x half of the xy plane, as shown in Figure 4.8. (the magnetic field is assumed along z).

Since the beam electrons have a constant velocity v_{pb} they will all oscillate around the field lines with the same gyroradius ρ_L . This means that if we confine the gyrocenters to the left half of the x axis, there will be some beam electrons between zero and ρ_L . Likewise, there will be some depletion of beam density from $-\rho_L$ to zero. The schematic of

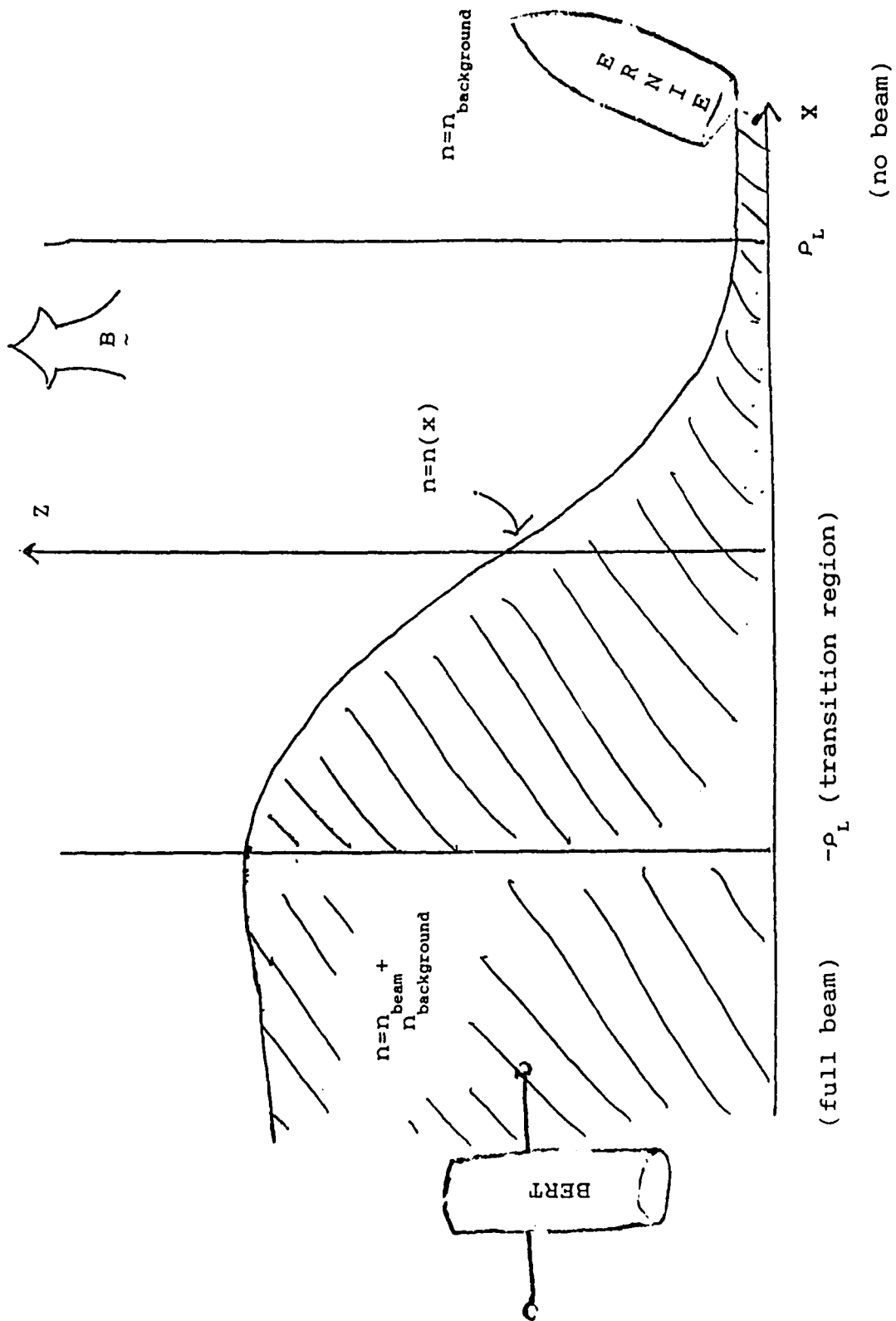


Figure 4.8 Schematic Diagram of the Model With Zero Order Distribution Function

this density profile in Figure 4.8 also points out our assumption that BERT is inside the beam while ERNIE is outside. The actual distribution function looks like

$$f_{o,beam} = n_b / (2\pi v_{pb}) \delta(v_p - v_{pb}) \delta(v_r - b_{rb}) [1 - H(x - \rho_L \sin \psi)] \quad (3)$$

where H is the Heavyside function and ψ is the angle v_{pb} makes with the x axis. Sending this through the Vlasov equations leads again to two terms,

$$\begin{aligned} & - (k_p / \omega_c \rho_L) (n_b / \pi) \omega_p^2 \sum_n (J_n J_m)' a_n^m / (\omega_c n - \omega + k_r v_{rb}) \\ & + (k_r^2) (n_b / \pi) \omega_p^2 \sum_n J_n J_m a_n^m / (\omega_c n - \omega + k_r v_{rb})^2 \end{aligned} \quad (4)$$

where $J_n = J_n(\rho_L k_p)$ is the nth order Bessel function and

$$a_n^m = \cos[(n-m)3\pi/2] \sin[(n-m)\xi] / (n-m)$$

which is just π when $n=m$ and where

$$\xi = \arcsin(x/\rho_L) - \pi/2$$

Now, according to Vlasov theory, those waves which can exist in the system have wavelengths and frequencies determined by the solutions to the following equation.

$$1 + D(\omega, k, x) = 0 \quad (5)$$

where D is the sum of equations 2 and 4.

We have used this model for various parametric studies of electron beam plasma instabilities, but for this particular application, we had to generalize Equation 5 to deal with a multi-component ion plasma. This can be done by replacing

all terms which involve the mass of the electron by the following relations.

$$\omega_{pi}^2 = \omega_{pe}^2 / r$$

$$v_{bi} = v_{be}$$

$$\omega_{ci} = \omega_{ce} / r$$

$$\rho_{Li} = \rho_{Le} / r$$

$$r = m_i / m_e \quad (6)$$

We have coded these equations, substituting 6 into 2 for the background terms of O^+ , NO^+ and O_2^+ and for beam terms in Equation 4 for N_2^+ and O^+ and have used the root solving software DISPER to generate plots of solutions for ω as a function of k . One such plot that corresponds to conditions near 200 km in the BERT mission is shown in Figure 4.9. The dashed lines help relate the imaginary component, or growth rate, plotted on the lower axis with the real component, or frequency of the wave plotted above. This plot is for a wave vector purely perpendicular to the magnetic field and ω is normalized to the plasma frequency of oxygen so that we see that the theory does indeed predict a strong instability around $.1\omega_p$. A corresponding plot for the BERT-1 apogee is shown in Figure 4.10. Again we find a substantial instability reasonably close to $.24\omega_p$ as desired.

4.2.2 Ray Tracing

Now that we have verified that EIC waves of the proper frequency could have been generated in the vicinity of BERT, we move on to see if these waves can leave the plasma cloud and reach the detector, ERNIE, in the no beam region. This amounts to following a specific wave characterized by a k and

DNBM= 5.0 ...P1=16.XVAL= -1.0...H= .050V1V0= 1.
ANGLE= 90.000 VRAT= .000 P2= 28.

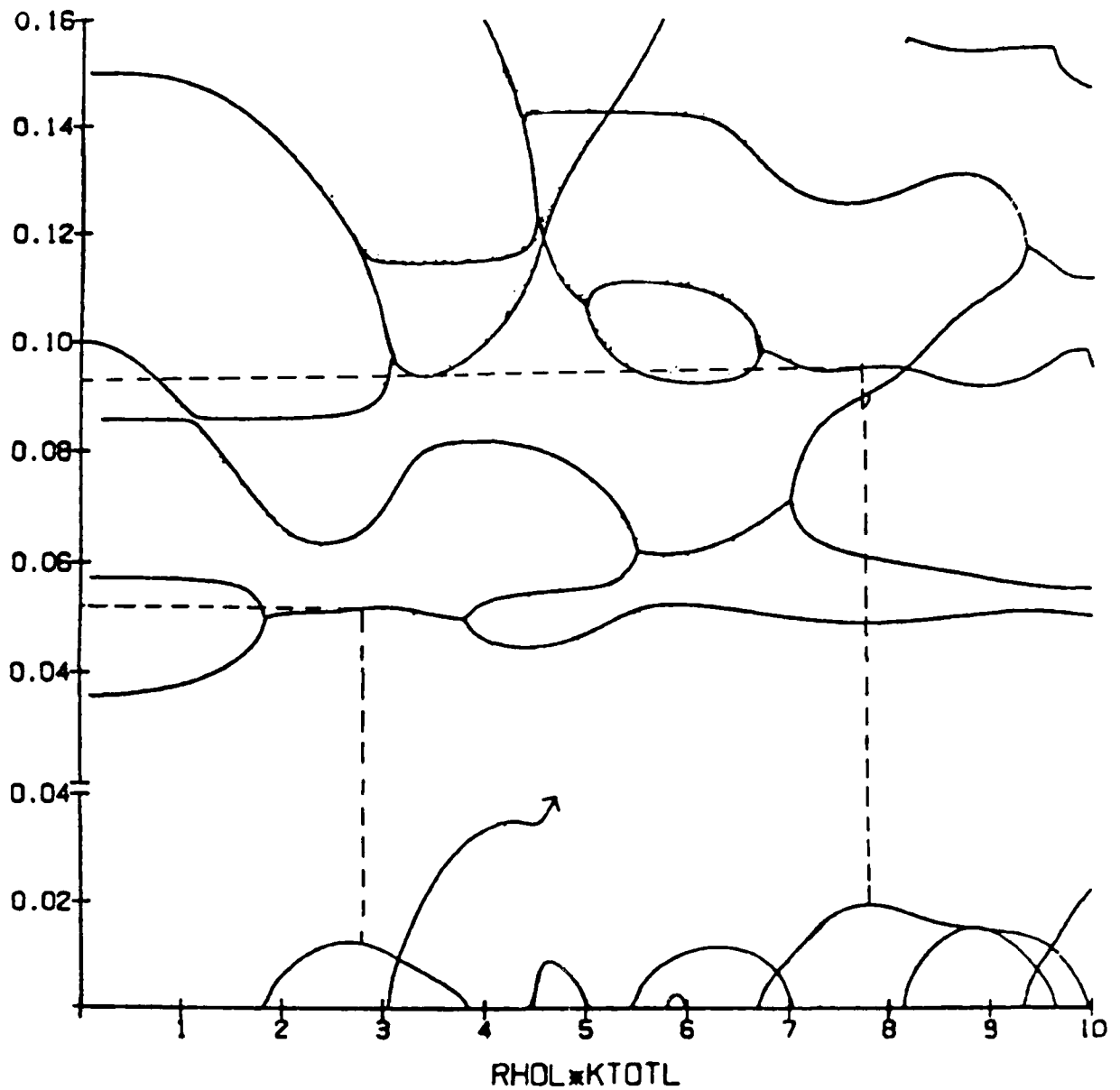


Figure 4.9 Dispersion Solutions for a 200 km BERT Environment

DNEM= 1.0 ...P1=16.XVAL= -1.0...H= .100VIVO= 1.
ANGLE= 90.000 VRAT= .000 P2= 28.

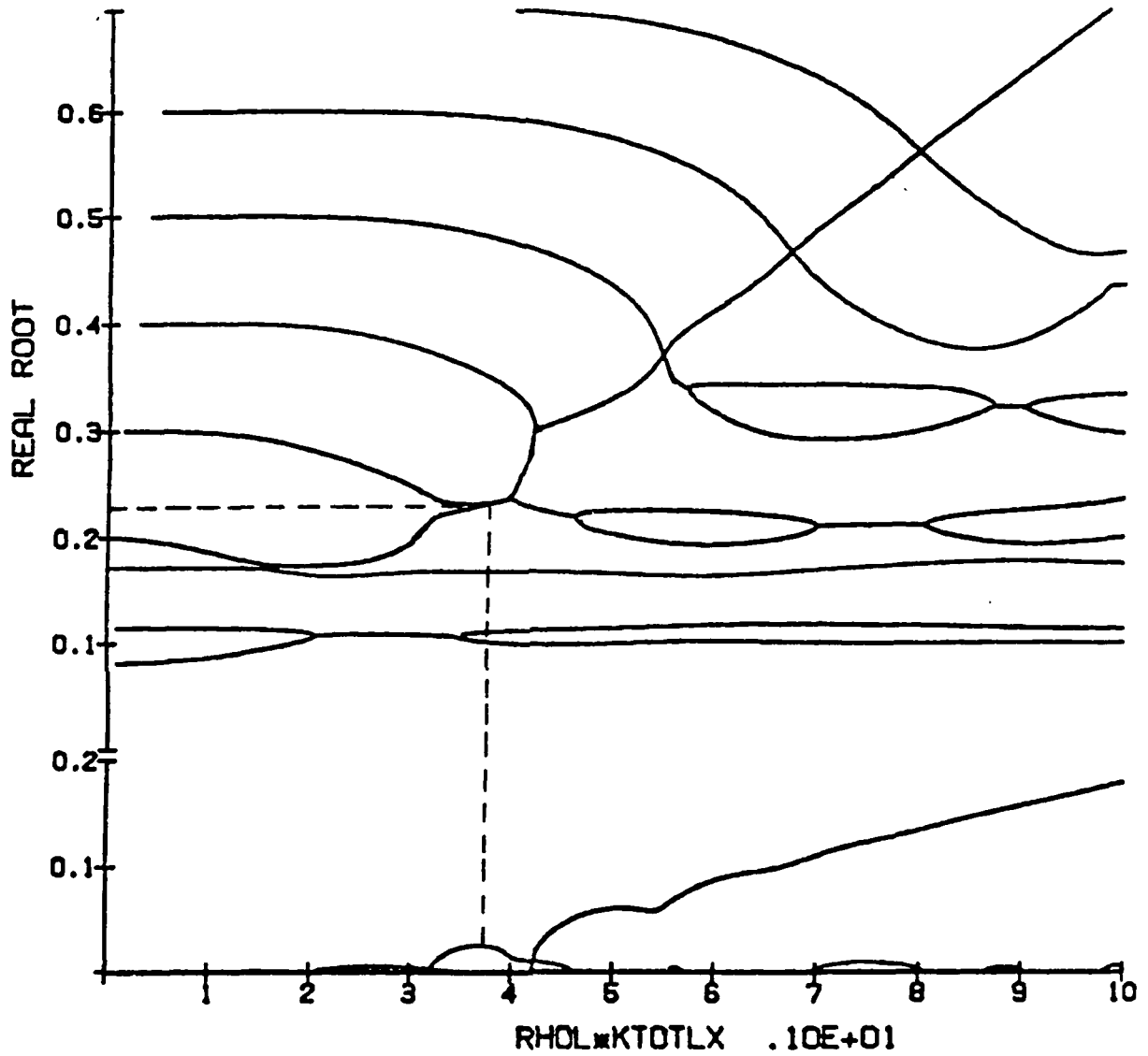


Figure 4.10 Dispersion Solutions for BERT Apogee

an ω from the full beam to the no beam end of the system. Suppose we have determined that a wave can exist at $-\rho_L$. We can follow it via the group velocity⁽¹⁰⁾

$$dx/dt = \delta\omega/\delta k \quad (8)$$

We don't actually know this quantity but we can find it through implicit differentiation

$$\delta\omega/\delta k = (\delta D/\delta k)/(\delta D/\delta\omega) \quad (9)$$

where $D(k, x, \omega)$ is the dispersion relation for the system. We could simply move x by some small increment then solve the dispersion relation at a constant ω for the corresponding k , but there is a better way. We form

$$dD/dt = (\delta D/\delta k)dk/dt + (\delta D/\delta x)dx/dt \quad (10)$$

We wish the new value of k to solve the dispersion relation, meaning that $1+D(k', x', \omega)$ is zero, but since $1+D(k, x, \omega)$ is zero as well, it must be that dD/dt is zero throughout. If we choose

$$dk/dt = -(\delta D/\delta x)/(\delta D/\delta\omega) \quad (11)$$

we can see by substituting Equation 11 and 8 into 10 that dD/dt is zero. Thus 8 and 11 constitute a method to follow the evolution of both the position and the wave vector of the wave in time. Since there are two independent directions in our system, there are actually four equations to solve simultaneously

$$dx/dt = (\delta D/\delta k_p)/(\delta D/\delta \omega)$$

$$dz/dt = (\delta D/\delta k_r)/(\delta D/\delta \omega)$$

$$dk_p/dt = (\delta D/\delta x)/(\delta D/\delta \omega)$$

$$dk_r/dt = (\delta D/\delta z)/(\delta D/\delta \omega) \quad (12)$$

In a ray trace, one of three things can happen. If dx/dt is negative at the outset, the wave will travel into the beam instead of out of it and never reach the detector. If dx/dt becomes negative somewhere along the way before the wave reaches $+\rho_L$, then the wave can be thought of as being reflected and likewise will not reach the detector. If the wave reaches $+\rho_L$ with positive dx/dt , we can be assured that it will continue to propagate since the dispersion relation is a constant with respect to x above ρ_L . Thus it can be detected.

The more interesting case in our studies turned out to be that for electrons. In our work, we chose to keep the magnitude of the k vector constant and vary the direction it made with the magnetic field. For small angles, the wave was turned back into the beam. Figure 4.11 shows one such plot at 30 degrees off parallel. At larger angles, as shown in Figure 4.12, the wave was able to escape.

For the ion beam case, similar runs showed that all angles gave rise to waves able to escape the beam and propagate to the detector, which was the desired result anyway.

4.2.3 Stochastic Heating of Hydrogen Ions

Stochastic heating arises from the interaction of the cyclotron motion of an independent charged particle with an

$\theta = 30.0^\circ$

H= .0500 DB= 2.0 VR= 1.00 KPAR= 1.73

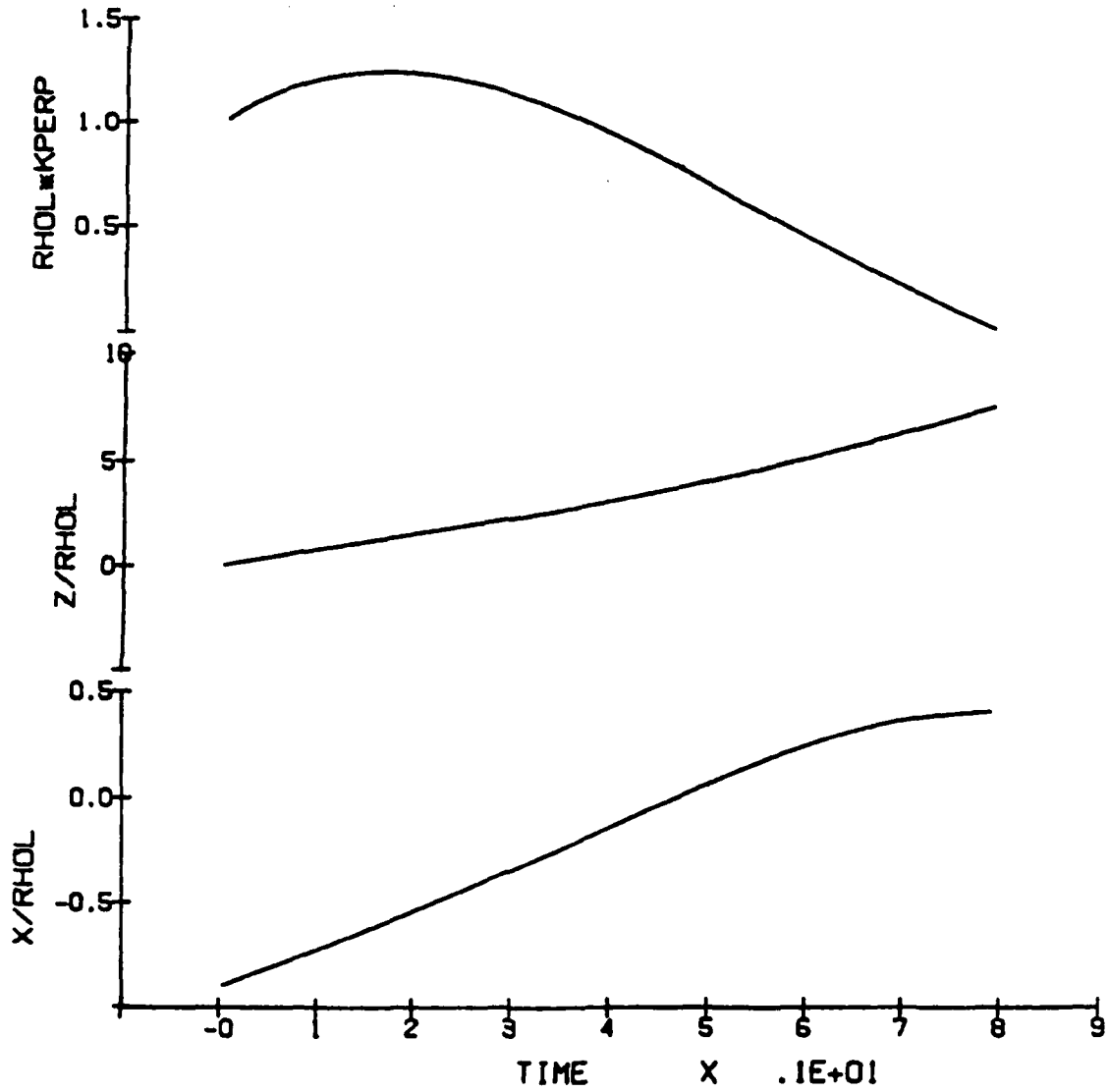


Figure 4.11 Ray Trace of Reflected Wave

$\theta = 38.7^\circ$

H= .0500 DB= 2.0 VR= 1.00 KPAR= 1.56

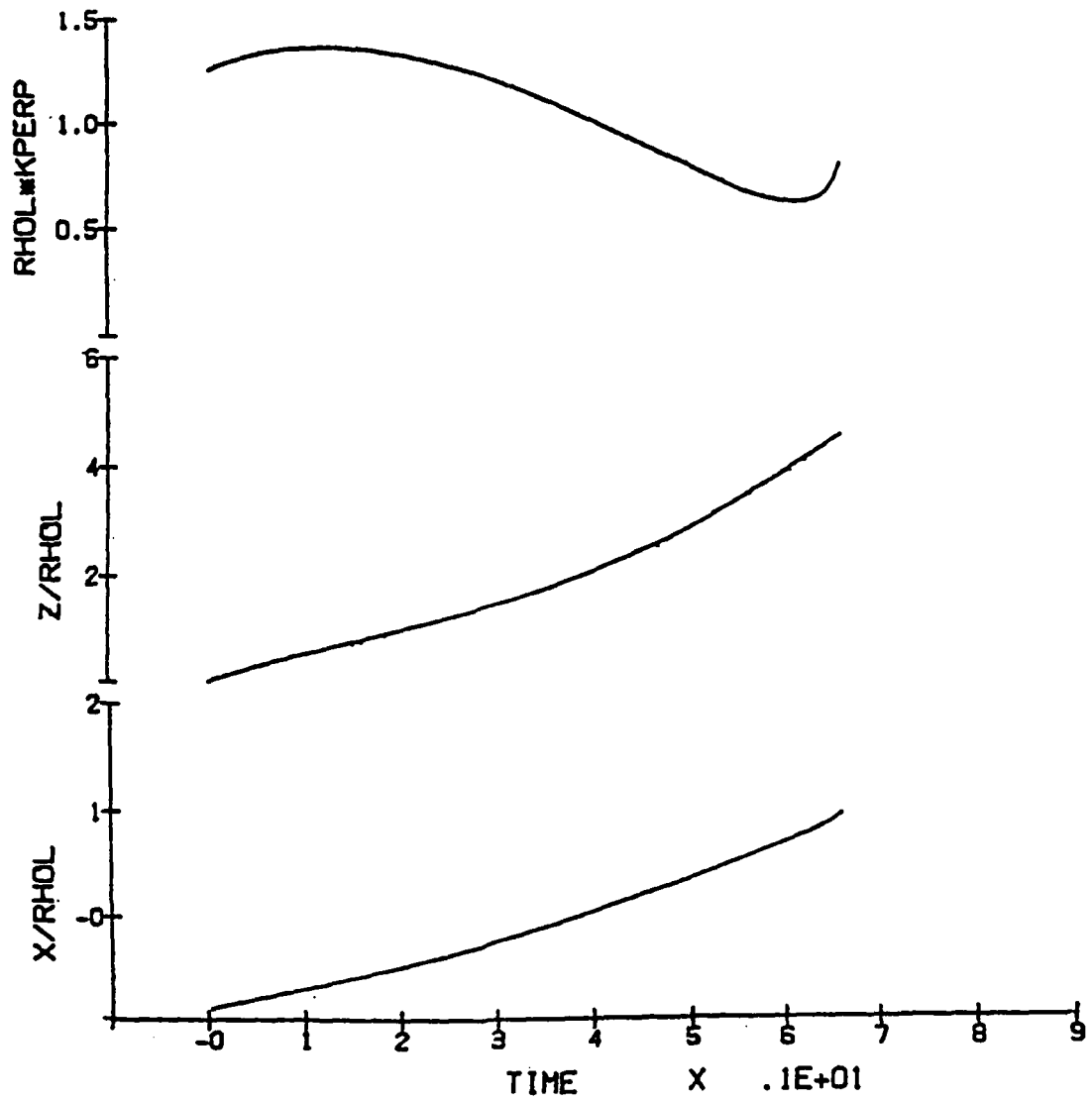


Figure 4.12 Ray Trace of Escaping Wave

electrostatic wave. The process produces two regimes. Below a critical amplitude, a particle will exhibit harmonic motion, but above, the particle's kinetic energy will increase to many times the potential energy of the carrier wave. The phenomenon is rather difficult to visualize but can be simulated by numerical integration of the equations of motion of a single particle. The Hamiltonian of such a system is

$$H = p_x^2/2 + p_y^2/2 + \eta \sin(x - \omega/\omega_c t)$$

where p is the momentum and η is the wave energy defined as

$$\eta = (e/m) \sqrt{((\omega^2 - \omega_c^2)/v_s^2)/\omega_c^2} |\delta E|$$

where δE is the EIC wave power.

A study of this equation was done for conditions similar to the BERT mission. The dramatic difference between oscillatory and stochastic heating is shown in Figure 4.13, which contrasts a case for $\eta=1.3$ and $\eta=1.5$. This figure is a plot of the x momentum vs. the x position. Data from ERNIE indicate that η is around 2.1 which means that EIC waves should have been in the stochastic regime. Thus we conclude that this model predicts stochastic heating of hydrogen ions in the vicinity of ERNIE.

The final step relies on data from a previous study that was supported for Donatelli,⁽¹⁰⁾ in which it was shown that a hot, Maxwellian population of hydrogen ions was conducive to the production of unstable Bernstein waves, which were indeed observed by ERNIE.

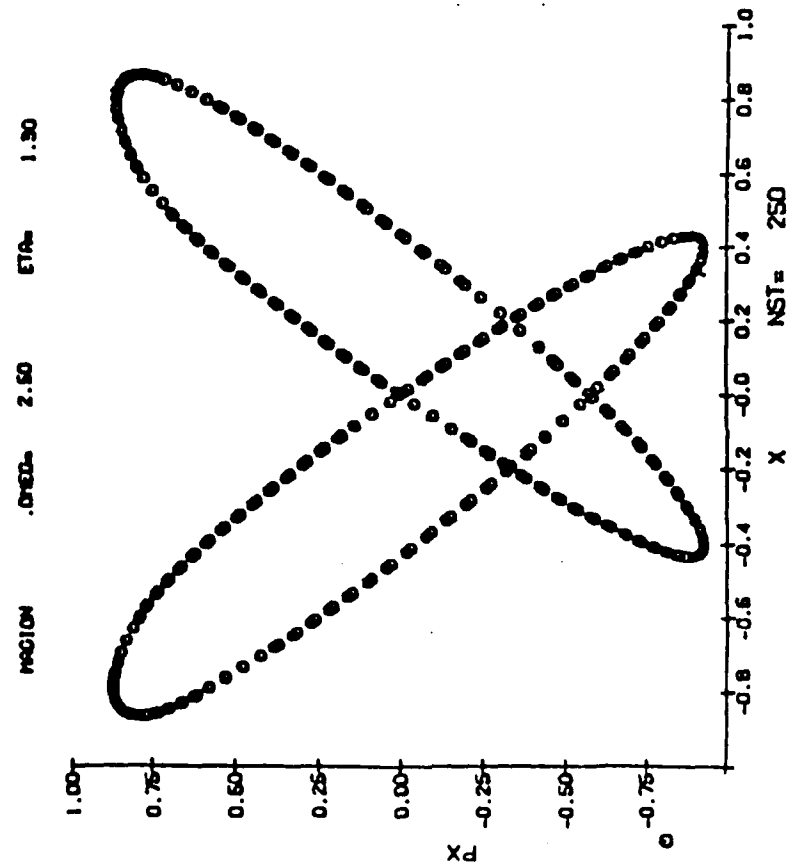
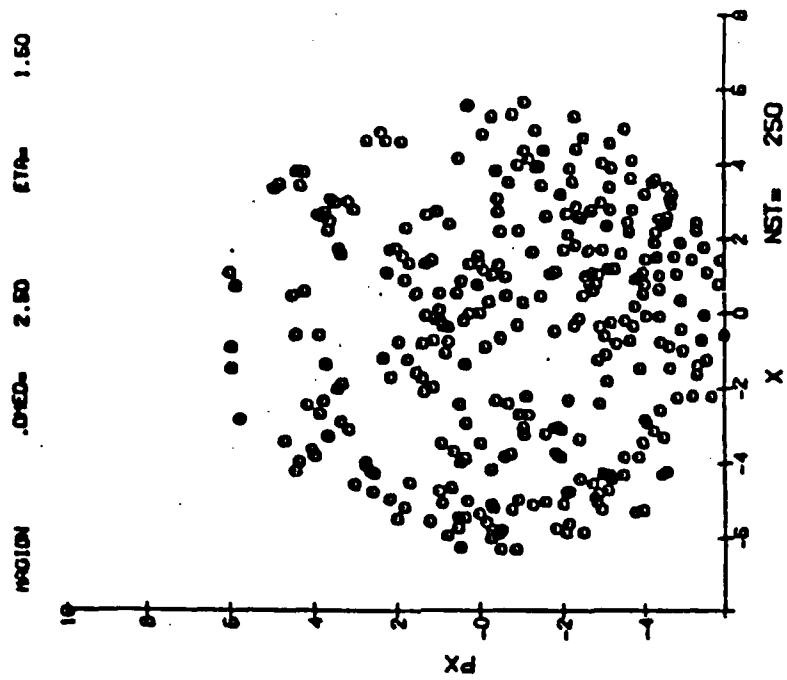


Figure 4.13 Oscillatory (left) and Stochastic Ion Heating

References

1. Cohen, H.A., Mullen, E.G., and Sherman, C., "Spacecraft Charging due to Positive Ion Emissions: an Experimental Study", *Geophys. Res. Lett.*, p. 515, 1979.
2. Cohen, H.A., Lai, S.T., McNeil, W.J., Weenas, E.P., and Leadon, R.E., "Spacecraft Charging with Beam Emission in an Ionizable Environment", *EOS Vol. 64, No. 18*, p. 301, 1983.
3. Lai, S.T., Cohen, H.A., and McNeil, W.J., "Spacecraft Sheath Modification During Beam Ejection", AFGL-TR-85-0215, ADA166604.
4. Cohen, H.A., Lai, S.T., and McNeil, W.J., "Vehical Potential Caused by Ejected Electron Beam Current", paper #SM423-08, AGU Fall Meeting, San Francisco, Dec. 1985.
5. Cohen, H.A., Lai, S.T., and McNeil, W.J., "Electron Beam Luminosity on the SCEX Rocket", *EOS Vol. 66, No. 18*, p. 348(1985).
6. Lai, S.T., Cohen, H.A., Aggson, T.L., and McNeil, W.J., "The Effect of Photoelectrons on Boom-Satellite Potential Differences During Electron Beam Ejection", *JGR*, AFGL-TR-86-0241, ADA174441.
7. Chen, F.F., *Electric Probes*, in "Plasma Diagnostic Techniques", ed. by R.H. Huddlestone and L.L. Lennard, Academic Press, N.Y. 1965.
8. Ernstmeyer, J. "Collisionless Heating of Ionospheric Plasma by an Electron Beam", XXVI COSPAR, Toulouse, France, June 1986.
9. Nicholson, D.R., "Introduction to Plasma Theory", John Wiley & Sons, New York, 1983.
10. Donatelli, D.E. and Chang, T.S., "Electron Beam Induced Electromagnetic Waves in a Magnetospheric Plasma", AFGL-TR-83-0085, 1983, ADA130116.

5.0 Numerical Simulation of Magnetospheric Dynamics

This section describes portions of the development of a magnetospheric modeling code at AFGL. The code is intended to incorporate the coupled dynamics of plasma sheet convection, currents, and ionospheric electric fields. It follows much of the physics and logic of the model published by Harel, et.al.,⁽¹⁾ but it includes a detailed spatial account of the plasma sheet density for a single specie, rather than the locations of the edges for multiple-species. The first section of this report describes the implementation of the Incomplete Cholesky Conjugate Gradient (ICCG) method⁽²⁾ as an alternative to the relaxation method for solving the set of simultaneous linear equations for the ionospheric potential. The second section describes the numerical simulation of the plasma convection. An appendix describes the system of units and dimensions used in the code.

5.1 Calculation of the Ionospheric Potential

The ionospheric potential is computed, as by Harel, et.al.,⁽¹⁾ by solving a set of difference equations resulting from the ionospheric current conservation equations. A 9-point differencing scheme is used. For a 32 by 21 longitude-latitude grid there are 672 simultaneous linear equations, including the equations for fixed boundary values at the highest latitude, and zero leakage current at the lowest latitude. Two alternative methods of solution have been implemented, the relaxation method used by Harel, et.al., and the Incomplete Cholesky Conjugate Gradient Method (ICCG) described by Kershaw⁽²⁾. The latter method has been implemented in an attempt to obtain accelerated convergence to the solution.

5.1.1 The Incomplete Cholesky Conjugate Gradient Method

The ICCG method is especially suited to large systems of equations with sparse matrices. The ionospheric potential system satisfies this requirement. However the left-hand-side matrix A is not symmetric and positive definite, as is also required by ICCG. Two methods of resolving this problem are available:

- a) multiply both sides of the equations by the transpose of A ; the resulting system matrix $A^T A$ then satisfies the ICCG requirements of being symmetric and positive definite.
- b) use Kershaw's generalization of the ICCG method to arbitrary nonsingular sparse matrices, described in his Appendix A.⁽²⁾

The first approach has been implemented here since a FORTRAN package already exists, within the NASCAP code, for the ICCG method for symmetric, positive-definite matrices. A group of front-end routines SOLVMAT has been constructed to set up the matrix $A^T A$, and the right hand side $A^T b$, and call the

NASCAP routine ICCG. A description of these routines follows:

5.1.1.1 SOLVMAT - A System for Solving Large Sparse Matrices

SOLVMAT is a routine to solve the system of equations

$$\begin{array}{c} \rightarrow \quad \rightarrow \\ A x = b \end{array}$$

where A is a large, sparse matrix. The matrix is loaded and solved by a series of subroutines described below. The user must provide work areas as follows in the calling program

```
AMAT(NMAX), LIST(NMAX), MRKR(NEQ)
S1(NEQ), S2(NEQ), S3(NEQ), S4(NEQ)
```

where NEQ is the number of equations, and NMAX is a number at least equal to the number of non-zero elements in the matrix $A^T A$. This number is not generally known, but the routine will calculate it and print a diagnostic error message if the specified NMAX is less than the actual number of elements. In addition, three tape units are required, referred to here as NT1, NT2, NT3. The parameters are initialized by a call to

```
INITMAT (NEQ,NMAX,AMAT,LIST,MRKR,NT1,NT2,NT3)
```

The matrix is loaded by a series of calls to

```
LOADMAT (I,J,VALUE,AMAT,LIST,MRKR)
```

where VALUE is the matrix element I,J. If I or J is outside the bounds of the matrix, the call is ignored. If a call to LOADMAT occurs twice with the same values for I and J, an error message is printed and the first value is retained. This would be valuable in debugging matrices that are

complicated to load. The order of calls to LOADMAT is unimportant since elements are sorted during processing, but a sequence in which the value of I increases is the most efficient.

The solution is accomplished by a call to

```
SOLVMAT (P,RHS,AMAT,LIST,MRKR,IFIX,S1,S2,S3,S4,  
          IPRINT,MAXIT,CONV)
```

where

P is a guess for the solution on call
and is the solution upon return.

RHS is the right hand side of the matrix equation.

IFIX is an NEQ dimensioned vector giving the boundary conditions

IFIX(I) = 0 means that P(I) is a variable

IFIX(I) = 1 means that P(I) is a fixed boundary condition, the value given by P(I)

IPRNT = 0 gives no information from the routine
= 1 gives size of $A^T A$ and traces iterations
= 2 in addition to 1 gives a portion of the matrix, the full RHS, initial P and solution P.

MAXIT is the maximum number of iterations

CONV is a convergence criterion based on change in the magnitude of the vector P.

The guess for P can be set equal to RHS if a better guess is not available. In a time dependent problem, one might want to use the solution P from the previous timestep as an initial guess for the next step. This is easily done by leaving P alone between calls.

If the same matrix is to be called with several values in RHS, a considerable savings of time can be had by making the second and subsequent calls to another routine.

```
SOLVTWO (P,RHS,AMAT,UST,MRKR,IFIX,S1,S2,S3,S4,  
        IPRNT,MAXIT,CONV)
```

The same result could be obtained, however, by sequential calls to SOLVMAT. Reinitialization of the matrix is not required in either case.

If the original matrix is symmetric and positive definite, one can save considerable time by a call to the solver itself. This is done by

```
SYMMAT (P,RHS,AMAT,LIST,MRKR,IFIX,S1,S2,S3,S4,  
        IPRNT,MAXIT,CONV)
```

5.1.1.2 Test Case

A test case was run under the assumption of constant ionospheric conductivities, therefore constant A. Computation times (CDC Cyber 750) for various steps in the ICCG and relaxation methods are given in Table 1. Since the Cholesky decomposition, like the computation of $A^T A$, need only be done initially for constant A, it was found expedient to modify subroutine ICCG to use the previously saved Cholesky result, when so instructed through an additional parameter in the calling sequence. The following additional changes to NASCAP'S ICCG package were also found necessary:

a) When negative diagonal elements are encountered in the incomplete Cholesky decomposition, they were originally set to a small positive number. As remarked by Kershaw, this does not destroy the procedure if there are not too many occurrences. However in this test case the procedure blew up due to the resulting proliferation of large numbers produced by subsequent division by the offending diagonal element. Setting the diagonal to the square root of its absolute value has circumvented the problem.

b) An erroneous reference to MRKR (N+1), where N is the dimension of the array MRKR, was found in subroutine LLTIV. This produces negligible error in most cases and was likely unnoticed in NASCAP operations. This has been corrected.

c) The convergence criterion is now

$$\sqrt{\sum_{i=1}^N r_i^2 / (A^T A)_{ii}} \leq \text{CONV}$$

where r_i is the residual for the i th equation in the system

$$A^T A x = A^T y.$$

The previous convergence criterion was $\text{RDOTR}_k / \text{RDOTR}_0 \leq \text{CONV}$

where

$$RDOTR_k = [r_k, (LL^T)^{-1} r_k]$$

r_k = residual vector for iteration k

L = lower triangular Cholesky matrix, i.e.

$$LL^T = A^T A$$

The new criterion resembles that used originally in the relaxation method. The old criterion has the problem that if the original guess is bad ($RDOTR_0$ very large) it would not take a very accurate solution to produce apparent convergence. Incidentally, the error cited in (b) led to a negative $RDOTR$, so that subroutine ICCG thought it had "converged". On the other hand, if one starts with a near-perfect guess, $RDOTR_0$ could be low and we may never converge.

In the test case a 20 KV cross-polar cap potential was assumed, with a tail plasma injection density initially set to zero but rising smoothly to 1 charge units/ γ Re^2 (see Appendix for discussion on units). The Birkeland currents generated by this plasma were coupled into the ionosphere; however the ionospheric potential was not coupled back to the magnetosphere -- rather a 10 km/sec sunward convection was assumed. Plasma loss was not included.

The relaxation method required 732 iterations on the first call, with an initial guess that the potential depends only on longitude (local time). On subsequent calls, the initial guess was the final answer on the previous call. The number of iterations required thus fell abruptly to less than 10 for the next several calls, but rose ultimately to over 400, as the plasma moved across the field of interest. The ICCG

method required 49 iterations on the first call, subsequently fell to zero, but ultimately rose to 10. In both cases the convergence criterion parameter was set to 10^{-6} . Thus ultimately the ICCG method requirement per time step is about half that of the relaxation method, but it has a very large initial requirement, which cancels out the later savings. Furthermore, this initial requirement, the computation of $A^T A$, would be needed for each time step if A varies with time, thus making the ICCG method several times more expensive. Thus the present attempt to apply the ICCG method to the computation of the ionospheric potential has failed to produce any benefits. In the future Kershaw's method of dealing with arbitrary nonsingular matrices may be attempted.

Table 1. Computer Execution Times
CP Time (CDC Cyber 750)

Method		
<u>ICCG</u>	$A^T A$ computation	63 sec.
	Cholesky Decomposition	7 sec.
	Conjugate Gradient Solution	0.6 sec. / iteration
<u>Relaxation</u>		0.027 sec./iteration

5.2 Plasma Convection

It is shown by Harel, et. al.,⁽¹⁾ that for no precipitation loss the number of particles per unit magnetic flux along a drift path is invariant. Thus to find the plasma per unit flux η at a given point and time step, one merely traces the drift path backwards from the current point to that occupied at the previous time step, i.e.

$$\eta(r,t) = \eta(r-v\Delta t, t-\Delta t) e^{-\Delta t/\tau}$$

where

- η = plasma/unit
- r = current position vector
- t = current time
- v = drift velocity
- Δt = time step interval
- $e^{-\Delta t/\tau}$ = precipitation loss factor

The above equation assumes that the plasma displacement in the interval Δt is sufficiently small that the drift velocity is constant over the displacement. In practice this is enforced by requiring both the x and y components of the equatorial displacement to be less than one spatial step size in magnitude.

Thus the problem of finding η at some grid point r at time t reduces to the problem of interpolation of η specified at time $t-\Delta t$. If r is at some point in the interior of the region being studied, this interpolation is fairly straightforward; a 9-point interpolation scheme is used. However, for points adjacent to the boundary, problems arise: the traced-back point may be outside the boundary, or it may not be surrounded by 9 grid points inside the

boundary. The following procedure has been developed:

Boundary Point η Determination

Definitions

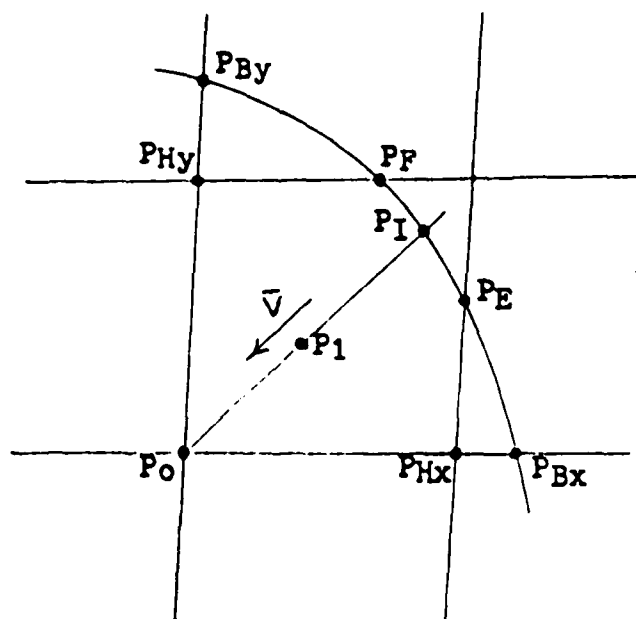
$P_0 = (X_0, Y_0)$ = Point at which we want η

$P_1 = (X_1, Y_1) = (X_0, Y_0) - (V_x, V_y)\Delta t$

= point, at time $t - \Delta t$, occupied by plasma which is located at P_0 at the current time t .

$P_I = (X_I, Y_I)$ = intersection of P_0P_1 , with boundary

P_E, P_F = intersections (if they exist) of boundary with grid square occupied by P_1 .



1. Determine the 4 grid points at the corners of the grid square in which P_1 lies.

2. Are all these 4 points (i.e. the entire square) within the boundary?

Yes: Do 4 point linear interpolation, using these 4 points, to get η at P_1 , $t-\Delta t$

No: Are all 4 points outside boundary?

Yes - quit

No - go on

||

||

\

3. Boundary intersects the square.

Find the 2 intersecting points P_E, P_F .

4. Find the intersection of the line determined by P_0P_1 with the line determined by the boundary intersections with the square. This point is called P_I .

5. Is P_I inside the square?

Yes - find η from boundary condition at P_I , $t-P_0P_I/V$

No - Interpolate linearly, using the three points

(see figure)

P_0

P_{Bx} or P_{Hx} , whichever is closer to P_0

P_{By} or P_{Hy} , whichever is closer to P_0

If steps 1 and 2 determine that the backwards traced point P_1 is surrounded by 4 grid points within the boundary, then the plasma is definitely traveling toward the boundary, i.e. will reach it at a future point in time, rather than a time in the past. Thus the boundary condition must not be used. In this case it is safe to interpolate using the surrounding internal grid points. If all 4 grid points nearest to P_1 are outside the boundary, we have a condition which should not occur if the maximum spatial displacement of one step size, mentioned previously, is enforced. In the more general case we may have P_1 lying in a grid square partially inside, and partially outside, the boundary. In this case the intersection P_I of the drift path with the boundary is located. For this computation it is assumed that the boundary is a straight line determined by that portion of it, $P_E P_F$, within the square, and that the drift path is the straight line determined by $P_0 P_1$. If P_I lies within the square then it is safe to use the boundary value at this point, and the appropriate time, to determine η at P_0 . If outside the square, the accuracy of P_I is in question due to the neglect of the curvatures of the boundary and the drift path. This situation could occur for drift paths nearly parallel to the boundary. In such cases linear interpolation is applied to obtain η at P_1 , using the points P_0 , P_x , and P_y , where P_x is the nearest grid point, or boundary point, to P_0 in the negative V_x direction (see Figure) and similarly for P_y .

5.2.1 Test Case

This plasma convection algorithm was tested for an assumed drift velocity model

$$\vec{V} = \frac{B_{dz}}{B_z} \vec{\Omega} \times \vec{r} + \frac{\vec{E}_o \times \vec{B}}{B^2}$$

where

\vec{B} = Earth's magnetic field (Olson-Pfitzer model⁽³⁾)

B_z = Z - component of Earth's magnetic field

B_{dz} = Z - component of the dipole approximation of Earth's magnetic field

$\vec{\Omega}$ = Earth's angular rotation velocity

\vec{r} = position vector

\vec{E}_o = -0.75 kV/Re in y direction

The plasma loss decay time τ is that given by Harel, et.al.⁽¹⁾

$$\tau = 2(m/2\lambda)^{1/2} B_{ir} (FTV)^{4/3}$$

where λ = electron energy invariant

m = electron mass

B_{ir} = ionospheric magnetic induction

FTV = magnetic flux tube volume

For this test case, $\lambda = 1.0 \text{ keV Re}^{2/3} \gamma^{-2/3}$ was assumed.

The boundary condition was given by

$$\eta_B = 1.0 - \exp [-(X_L/X_M)^2]$$

where

$$X_L = \min \{ 0, X-X_o+Vt \}$$

$$X_o = 25.927 \text{ Re}$$

$$V = 10 \text{ km/sec}$$

$$X_M = 5 \text{ Re}$$

This condition corresponds to a traveling wave whose front reaches the tailward boundary $X = 25.927 \text{ Re}$ at $t = 0$, and which travels at 10 km/sec sunward velocity. The amplitude of the wave rises asymptotically to unity with a rise length of 5 Re.

Figures 5.1-5.3 show some typical plasma sheet configurations as the injection proceeds. The precipitation loss appears to cut the plasma sheet off at 8-12 Re from the earth's surface. Numerical difficulty was encountered near the dusk portion of the boundary, where there is a grid point very close to the boundary and the drift velocity is nearly parallel to the boundary. This resulted from sunward propagation of a numerical error in the 9-point quadratic interpolation scheme; i.e. at points tailward of the point in question, numerical error in interpolation along the wave front produced some negative η values, which propagated to this point. This condition was "fixed" by setting negative values of η to zero, since these negative values are expected to occur only near the wave front where η is close to zero anyway.

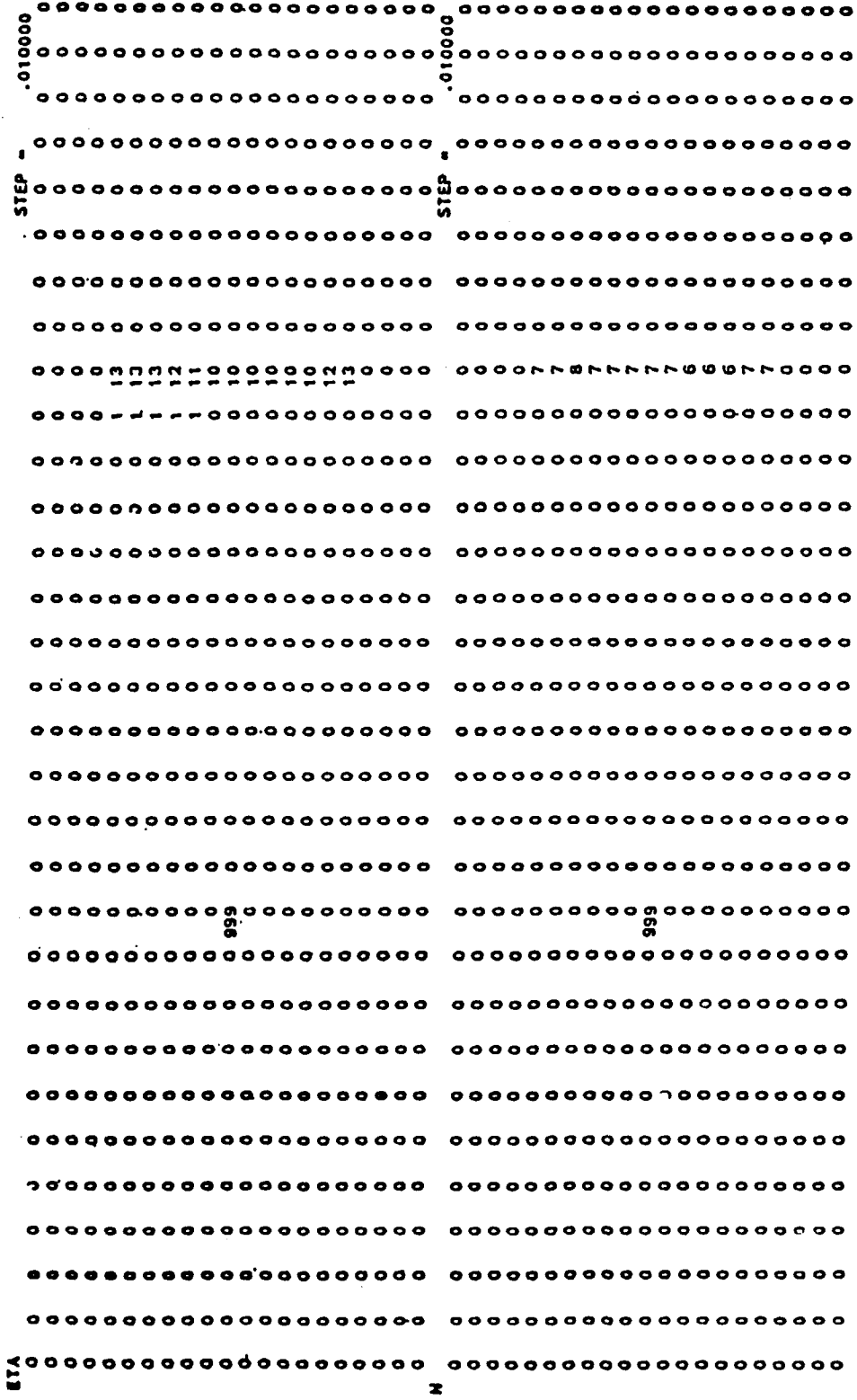


Figure 5.1 Plasma Per Unit Flux (ETA), in Units of $0.01 Q/BL^2$ (see Table 1) and Plasma Per Unit Volume (N), in Units of $0.01 Q/L^3$, at Time 60T After Plasma Injection Front Reaches Tailward Boundary. The Point Marked 999 Designates the Earth. The Sun is to the Left, the Tail to the Right, Dawn at the Top, and Dusk at the Bottom.

5.3 Appendix: Units and Dimensions

The fundamental units have been selected to assure convenient scales for standard quantities in the physics of the problem. Thus the chosen fundamental units are length (earth radii), electric potential (kilovolts), magnetic induction (γ), and current (kiloamps). Although the selection of electric potential and magnetic induction as fundamental units is a departure from the usual convention of selecting mass and time, the pertinence of the field quantities to the problem outweighs the usual significance of mass and time. The use of kilovolts and kiloamps rather than volts and amps is simply a reflection of the scales anticipated for these quantities.

With these units it is possible to express the relevant equations in MKS format, i.e. the speed of light may be replaced by unity where it occurs in equations expressed in the cgs system. Furthermore if plasma amount is expressed in the charge units of this system, rather than number of ions or electrons, the magnitude of the relevant charge is unity rather than the electronic charge. An interesting (and fortuitous) consequence of this system is that the energy of one charge unit of 1 keV singly-charged ions (or electrons) is exactly unity in this system. Not so exciting, but perhaps relevant, are that the number of ions per charge unit is 2.539×10^{23} , and the mass of one charge unit of protons is .2566 mass units. The complete set of units and dimensions follows in Table A.1.

Table A.1. Units and Dimensions

Quantity	Symbol	MKS conversion
Length	L	6.378×10^6 m
Electric Potential	ϕ	103 volts
Magnetic Induction	B	10^{-9} Wb/m ²
Electric Current	I	103 amps
Time	$T = L^2 B/\phi$	40.68 sec
Velocity	$V = \phi/LB$	1.568×10^5 m/sec
Charge	$Q = IL^2 B/\phi$	4.068×10^4 coul
Electric Field	$E = \phi/L$	1.568×10^{-4} volts/m
Force	$F = ILB$	6.378 newtons
Mass	$M = IL^4 B^3/\phi^2$	1.655×10^{-3} kg
Energy	$K = IL^2 B$	4.068×10^7 joules

References

1. Harel, M., Wolf, R.A., Reiff, P.H., Spiro, R.W., Burke, W.J., and Rich, F.J., Quantitative Simulation of a Magnetospheric Substorm 1. Model Logic and Overview, J. Geophys. Res., Vol 86, No. A4, pp. 2217-2241, 1981.
2. Kershaw, D.S., The Incomplete Cholesky - Conjugate Gradient Method for the Iterative Solution of Systems of Linear Equations, J. Comput. Phys., Vol 26, pp. 43-65, 1978.
3. Olson, W.P., and Pfitzer, K.A., A Quantitative Model of the Magnetospheric Magnetic Field, J. Geophys. Res., Vol. 79, No. 25, pp. 3739-3748, 1974.

6.0 Adiabatic Invariant Analysis

In the analysis of magnetospherically trapped particle distributions it is necessary to distinguish between variations caused by sources and sinks from those caused by responses of the trajectories of pre-existing particles to variations in the magnetic field. If the field is sufficiently slowly varying, the particle trajectories are determined by the conservation of the three adiabatic invariants. The adiabatic invariants, and the equations representing their conservation, depend on specification of a time-varying magnetic field. From this it also follows that the adiabatic behavior of a class of trapped particles could be used as a monitor to classify magnetic field variations.

This section summarizes preliminary research⁽¹⁾ in an effort to develop analysis techniques for use with the forthcoming CRRES data. This analysis will require accurate, but practically applicable techniques for ordering the data by magnetic field variations. A efficient approach that was developed and implemented is described for calculating adiabatic invariants and deriving changes in the particle distribution functions, under the condition that the adiabatic invariants are conserved in the presence of a simple time-varying model magnetic field. This will allow one to easily separate adiabatic variations in particle distribution functions from variations due to sources and sinks, and to select adiabatically behaving particles with distribution parameters, such as pitch angle anisotropy, which might be used as monitors of global magnetic field variations, and therefore as parameters by which to sort all particle data.

A two day period of SCATHA magnetometer and particle observations⁽²⁾ has been chosen for this study. The first day is exceptionally quiet, thus serving as a baseline for quiet magnetic field and particle distribution models. On

the second day, a moderately disturbed day, a time-varying magnetic field is determined from the magnetometer data, and used to calculate the particle distribution functions, assuming conservation of the adiabatic invariants, and using the magnetic field and particle distribution functions derived from the previous day. Comparisons with the observed particle distribution functions for the second day indicates that much of the variations can be attributed to adiabatic response to the magnetic decompression which occurred. The pronounced butterfly distributions observed in the midnight sector concurrent with this decompression are in agreement with the adiabatic calculations. This result suggests that particles might be used as remote sensors of long-term global magnetic field variations. If we can identify classes of particles, by species and energy range, which are found to behave predominantly adiabatically, we can turn the above process around and use their variations to infer global changes in the magnetic field. This would be an important aid in CRRES analysis if standard global indices, such as solar wind parameters, are not available.

6.1 PROCEDURE

For particles observed at specified energies, pitch angles, and positions in a specified Mead-type field, we compute their energies, noon equatorial crossings, and noon equatorial pitch angles in a different Mead-type field, assuming their adiabatic invariants are the same in both fields. The field in which the particles are observed will be referred to in this discussion as the "current" field, while the field in which the noon local time parameters are to be computed will be called the "reference" field. The Pennington-Stern⁽³⁻⁵⁾ equations are used first to estimate the mirror-point L-shell values of the observed particles in the current field (these depend on equatorial pitch angle), and then to set up equations for the constancy of the

adiabatic invariants. These equations are then solved for the energy, pitch angles, and equatorial radial distances in the reference field at noon local time. Given the noon distribution function in the reference field, the distribution function in the current field is easily obtained via the Liouville Theorem.

6.1.1 Pennington-Stern Equations

The Pennington-Stern equation for the equatorial crossing of a drift shell in a Mead field is

$$r_e = L(1 - \bar{\alpha}_1^0 \bar{g}_1^0 L^3 / g_1^0 - \bar{\alpha}_2^1 \bar{g}_2^1 L^4 \cos[\phi + \Delta] / g_1^0),$$

where:

L = L-shell value;

ϕ = local time (midnight = 0 degrees);

Δ = westward rotation of symmetry plane.

The Mead field in the equatorial plane is given by:

$$B = -g_1^0 / r_e^3 - \bar{g}_1^0 - \sqrt{3} \bar{g}_2^1 r_e \cos(\phi + \Delta).$$

The $\bar{\alpha}_i^j$ are the same as the α_i^j defined by Pennington⁽³⁾ except that $(-n)$ is replaced in all equations by $(n+1)$ (see Ref. 5). This reflects the fact that Pennington's original development was for the internal multipoles of the field, which contain terms in r^{-n} , while the present development involves external multipoles, containing r^{n+1} . These coefficients depend explicitly on the effective dipole mirror point colatitude e_m , which is related to the

equatorial pitch angle α_e by

$$\sin\alpha_e = (\sin^3\theta_m)/(1+3\cos^2\theta_m)^{1/4}.$$

The mirror-point L-shell values are obtained by solving the drift shell equation for L to first order in the Mead perturbation parameters \bar{g}_1^0 and \bar{g}_2^1 (Ref. 4):

$$L = r_e(1 + \bar{\alpha}_1^0 \bar{g}_1^0 r_e^3 / g_1^0 + \bar{\alpha}_2^1 \bar{g}_2^1 r_e^4 \cos[\phi + \Delta] / g_1^0).$$

The first and second invariants are:

$$\mu = p^2/2B;$$

$$J = 2pI,$$

where p is the particle momentum, B is the magnetic field value at the particle's mirror points, and I is the familiar longitudinal invariant integral between the mirror points, for which we use an analytic approximation given by Schulz and Lanzerotti.⁽⁶⁾

The third invariant, to first order in the Mead perturbation parameters, is computed as:

$$F = (2\pi g_1^0/L)[1 + (\bar{\alpha}_1^0 - \frac{1}{2})\bar{g}_1^0 L^3/g_1^0].$$

6.1.2 Determination of Reference Drift Orbits

The three adiabatic invariant conditions are solved to determine the L-shell values, mirror-point magnetic inductions, and momenta in the reference magnetic field, given these values for the current field. The L-shell values are

determined first by linearizing the third invariant in L:

$$\Delta L = -\Delta F / (\delta F / \delta L),$$

where ΔL is the change in L (reference-current), ΔF is the corresponding change in F, for fixed L, and the partial of F with respect to L (in the parentheses) is taken in a fixed dipole field (neglecting the Mead perturbations):

$$\delta F / \delta L = -2\pi g_1^0 / L^2$$

This forms an initial guess for a Newton-Raphson procedure to obtain the exact solution accounting for the nonlinearity of the third adiabatic invariant in L.

The conditions for the first two adiabatic invariants are then solved for the momenta p and mirror-point magnetic inductions B in the reference field, after substitution of the L values just obtained for the reference field.

These equations reduce to:

$$\sqrt{BI(L, B)} = \text{constant}$$

This is solved for B by the Newton-Raphson method, using as the initial guess:

$$B = B_c L_c^3 / L^3$$

where the subscript c designates the current field. The particle momentum (and thus energy) is then easily obtained by substitution of the resulting solution for B into the equation for the first adiabatic invariant.

6.1.3 Noon Parameters

The noon equatorial crossing is computed directly from the

Pennington-Stern drift shell equation, substituting $\phi = \pi$, and using the reference value of L. The reference Mead induction B_e at this equator crossing is then computed and used to define the equatorial pitch angle in the reference field:

$$\alpha_e = \sin^{-1}[\sqrt{B_e/B}]$$

If the argument of the inverse sin exceeds one, as may result due to the approximations made, it is set to one to avoid an undefined condition. This difficulty only occurs for particles mirroring near the equator, but not, however, for particles mirroring exactly on the equator, since these these maintain their precisely 90° pitch angles.

6.1.4 Quiet Modeling

The magnetometer data for a quiet day (one full SCATHA orbit) are fit to a Mead-type (three parameter) model as specified above. We emphasize that this resulting model therefore is not identical to the original Mead model,⁽⁷⁾ which incorporates only magnetopause surface currents to augment the central dipole; rather, as suggested by Luhmann and Schulz,⁽⁸⁾ the fit attempts to empirically simulate the real effects of ring and surface currents as well. In contrast to those authors, all the data for a quiet day were used, rather than just the local noon and midnight magnetometer readings, and the local time symmetry axis was allowed to differ from the traditionally assumed noon-midnight meridian.

Also following Luhmann and Schulz the observed particle distributions for the quiet period are traced to local noon, using the Pennington-Stern drift shell equations, in the hope of finding nearly L-independent pitch angle distribution functions. However we have found that, for the larger L-range covered by SCATHA, it is prudent to use L-dependent

pitch angle distributions at local noon. This has been done, expressing the pitch angle distribution as a linear combination of the first two orthonormal basis function of Schulz and Boucher,⁽⁹⁾ Eqn. 14, with L-dependent coefficients chosen to normalize the distributions to unity at 90° and reproduce the observed ratio F(45)/F(90). Thus we in general define our distribution functions as

$$F(\alpha, L) = f(\alpha, L)g(L)$$

where f is the L-dependent normalized pitch angle distribution just described, and g , as for Luhmann and Schulz, is the distribution function in L for particles with 90° pitch angles.

6.1.5 Disturbed Magnetic Field Modeling

The magnetometer data for the disturbed period is fit in piecewise segments to simulate the observed time dependence. The resulting model is then used with the quiet field and particle models just described to predict the disturbed particle distribution functions from the adiabatic theory described previously.

6.2 RESULTS

Illustrative

Before proceeding to the SCATHA analysis we first present some results illustrating effects predicted by our theory. We discuss what happens to a group of electrons initially distributed uniformly in a circular ring of inner radius $6.5 R_E$ and outer radius $7 R_E$, while under the influence of a dipole field. The distribution function F for these

particles in the dipole field is given by:

$$F/c^3 = 1\text{km}^{-3}\text{kev}^{-3}\sin \alpha,$$

for particles within this ring, and in the energy interval 300-400 kev, while outside F vanishes. Figures 6.1-6.7 illustrate properties of the modified distribution resulting from adiabatic response of these particles to a perturbation given by:

$$\bar{g}_1^0 = 10 \text{ nT};$$

$$\bar{g}_2^1 = 2 \text{ nT};$$

$$\Delta = 0.$$

Figure 6.1 shows the omnidirectional energy density. This is computed by integrating the energy times the distribution function over energy and pitch angle. The energy integration is done analytically, and the pitch angle integration is done by summing over 10 degree bins. Note the large radial spread at local noon, a consequence of the varying distortions of the drift orbits. Figure 6.2 shows the omnidirectional average energies, and illustrates the predominant deceleration of the electrons (recall that the average energy in the dipole field was 350 kev). Figures 6.3 and 6.4 show the energy density and average energy, respectively, for the equatorially mirroring particles, and we see that these are spread out the most spatially and suffer the most deceleration. Figures 6.5 and 6.6 show these quantities for the electrons with 40 degree pitch angles in the perturbed field. The local time asymmetry in the energy density illustrates the local time dependence of the pitch angle shift caused by the perturbation. The particles seen at local noon at 40 degree pitch angle in the perturbed field had lower pitch angles in the dipole field than those particles seen at local midnight at 40 degree pitch angle in the

ELECTRON ENERGY DENSITY (KEV/KM**3)
(OMNIDIRECTIONAL)

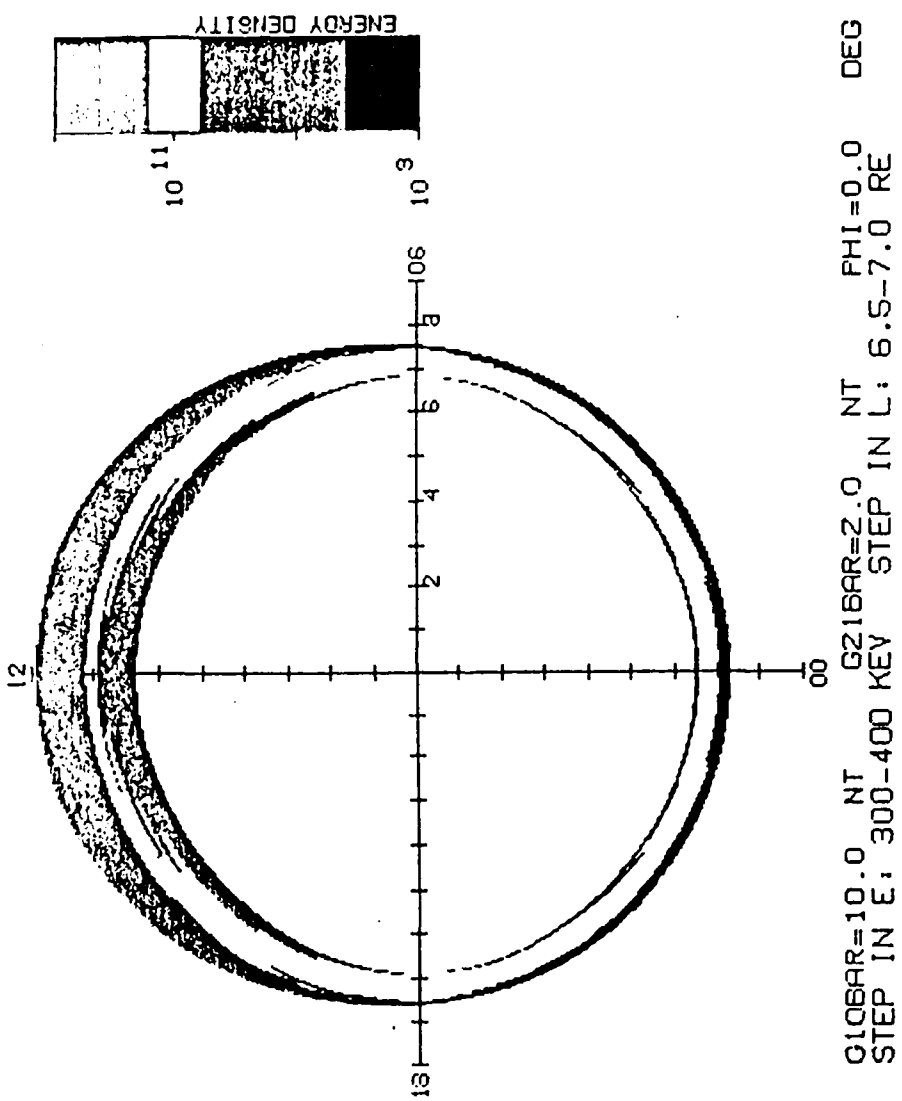
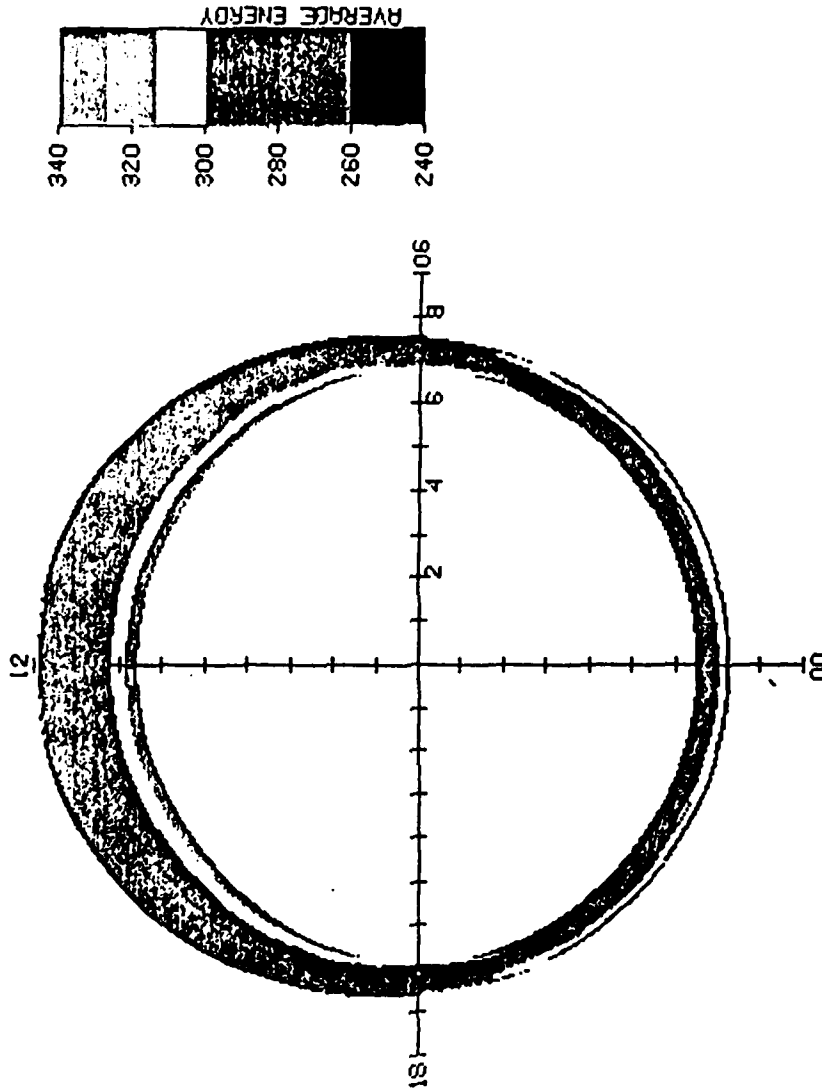


Figure 6.1 Omnidirection Energy Density in Mead Field Deduced by Adiabatic Variation for 300-400 KeV Electrons between 6.5 and 7 RE in Dipole Fields. A $\sin \alpha_e$ Equatorial Pitch Angle Distribution is Assumed in the Dipole Field.

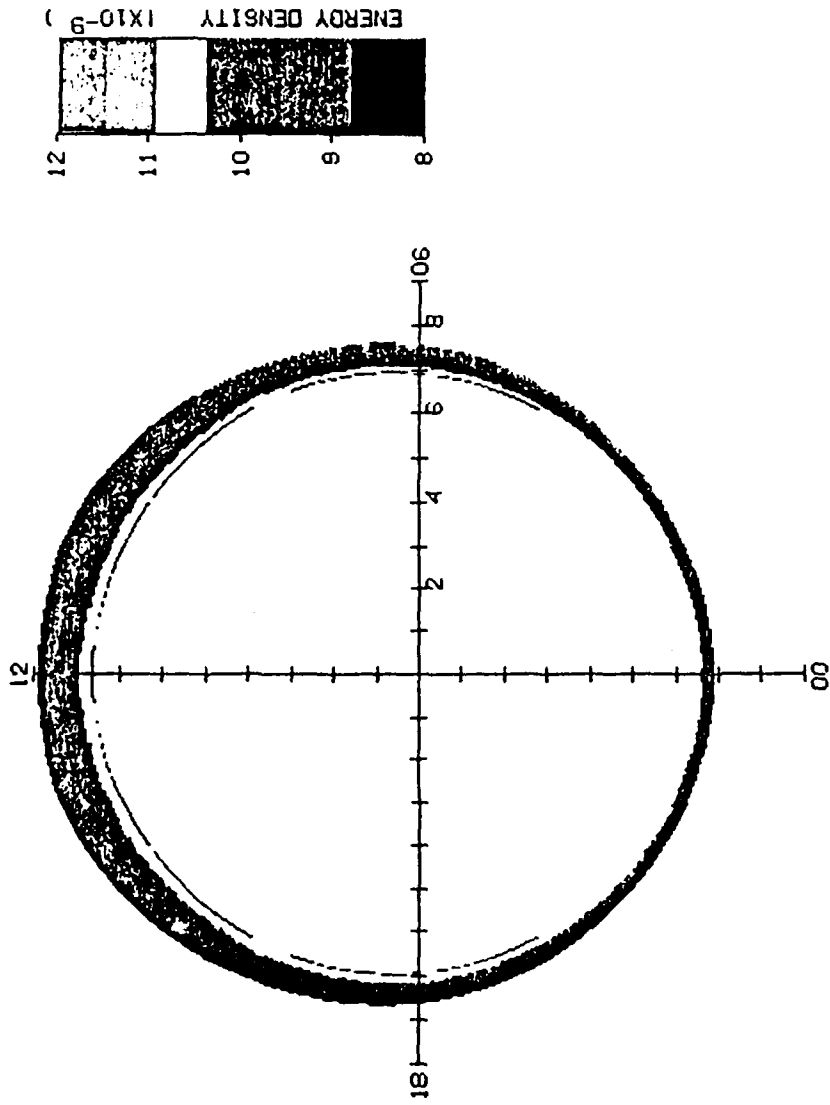
AVERAGE ELECTRON ENERGY (KEV)
(OMNIDIRECTIONAL)



GLOBAR=10.0 NT G216AR=2.0 NT PHI=0.0 DEG
STEP IN E: 300-400 KEV STEP IN L: 6.5-7.0 RE

Figure 6.2 Average Omnidirectional Energy in Mead Field for the Electrons Discussed in Figure 6.1.

ELECTRON ENERGY DENSITY (KEV/KM**3/SR)
 AT 90 DEGREES PITCH ANGLE



G10BAR=10.0 NT G21BAR=2.0 NT PHI=0.0 DEG
 STEP IN E: 300-400 KEV STEP IN L: 6.5-7.0 RE

Figure 6.3 Energy Density at 90° Equatorial Pitch Angles in the Mead Field, for the Electrons of Figure 6.1.

AVERAGE ELECTRON ENERGY (KEV)
 AT 90 DEGREES PITCH ANGLE

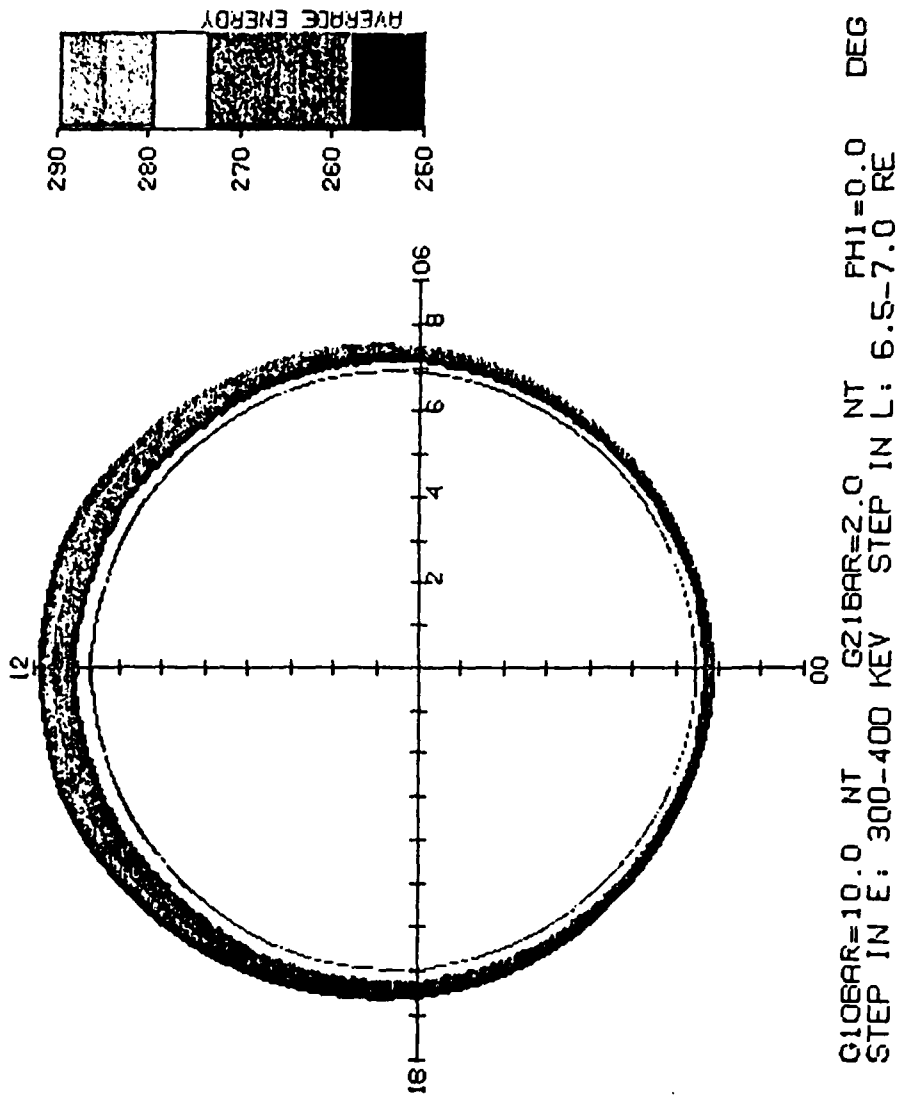
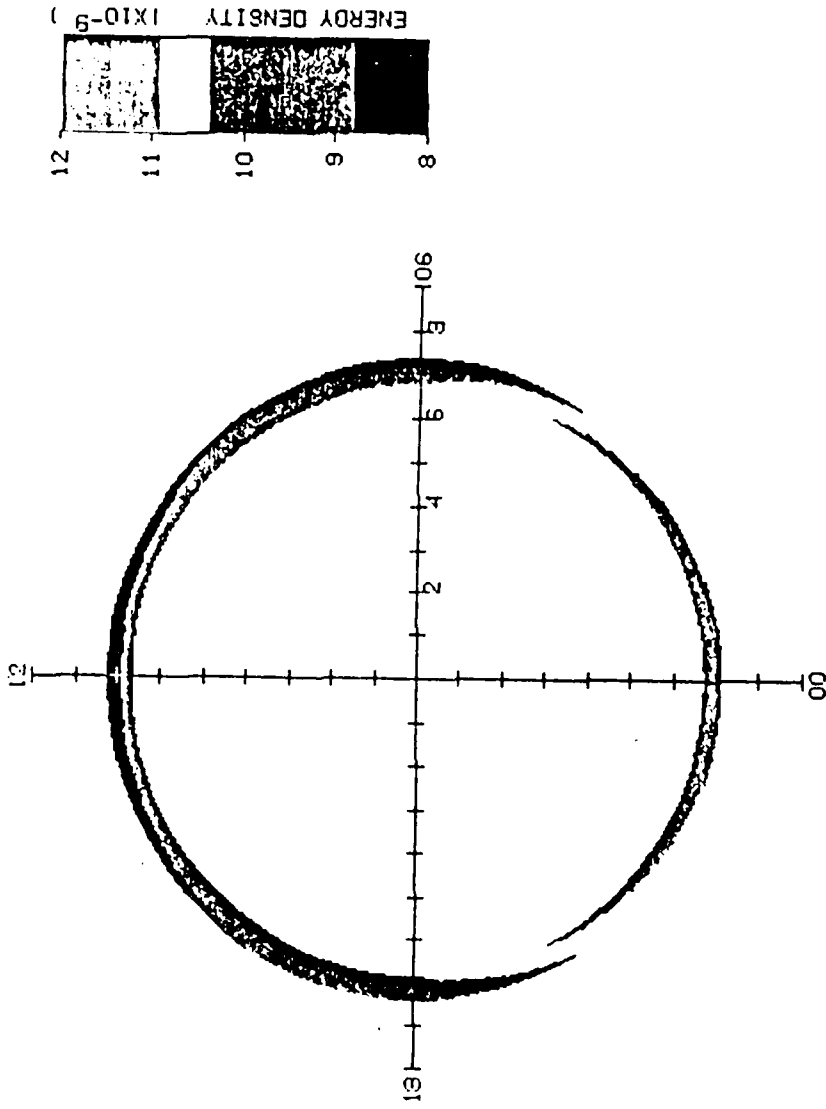


Figure 6.4 Average Energy at 90° Equatorial Pitch Angles in Mead Field, for the Electrons of Figure 6.1.

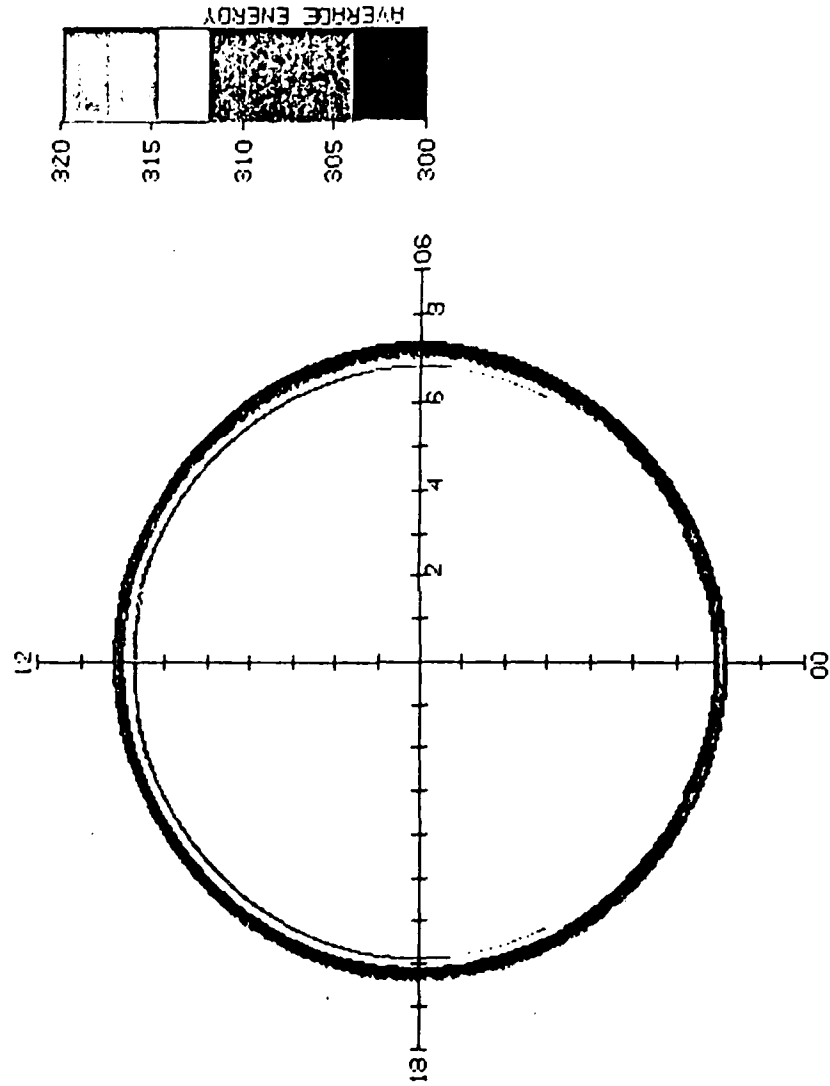
ELECTRON ENERGY DENSITY (KEV/KM**3/SR)
 AT 40 DEGREES PITCH ANGLE



G10BAR=10.0 NT G21BAR=2.0 NT PHI=0.0 DEG
 STEP IN E: 300-400 KEV STEP IN L: 6.5-7.0 RE

Figure 6.5 Same as Figure 6.3, but for 40° Equatorial Pitch Angle.

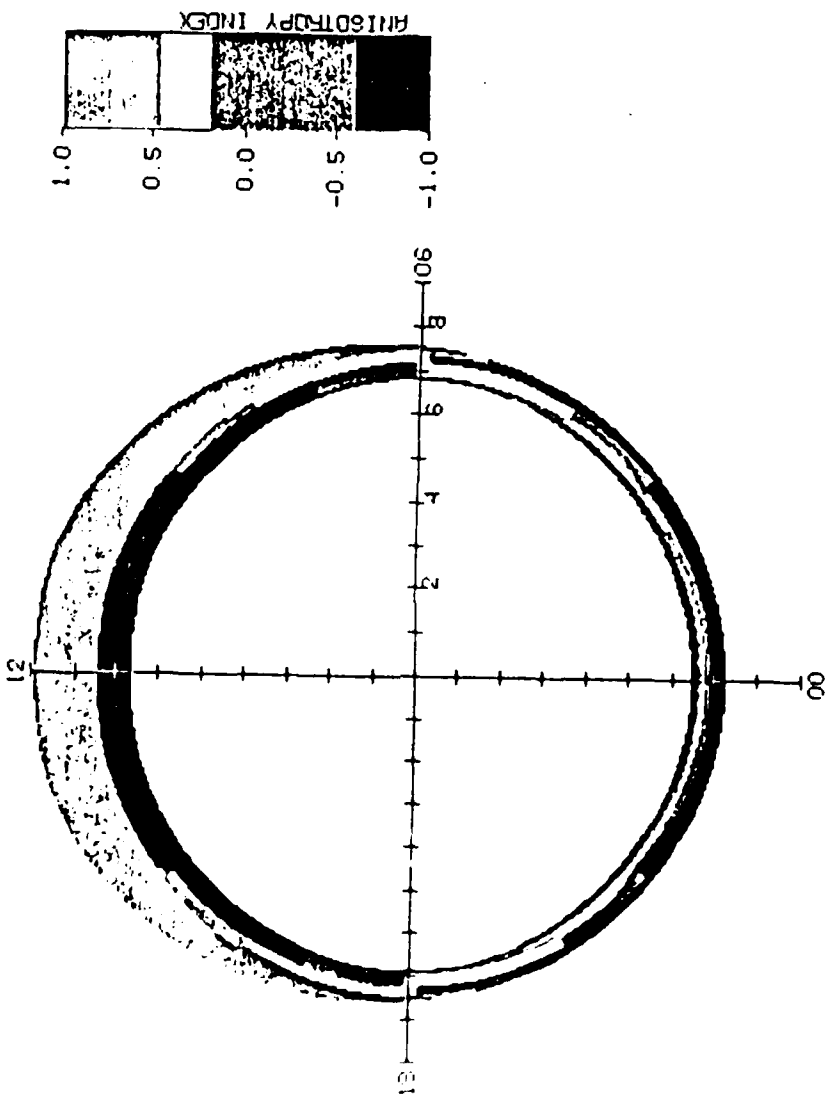
AVERAGE ELECTRON ENERGY (KEV)
AT 40 DEGREES PITCH ANGLE



GLOBAR=10.0 NT G21BAR=2.0 NT PHI=0.0 DEG
STEP IN E: 300-400 KEV STEP IN L: 6.5-7.0 RE

Figure 6.6 Same as Figure 6.4, but for 40° Equatorial Pitch Angle.

ELECTRON ANISOTROPY INDEX
AT 270 KEV



Q10BAR=10.0 NT G21BAR=2.0 NT PHI=0.0 DEG
STEP IN E: 300-400 KEV STEP IN L: 6.5-7.0 RE

Figure 6.1 Anisotropy Index at 270 keV in Mead Field, for the Electrons of Figure 6.1.

perturbed field. Spatially, in contrast to the 90 degree electrons, the 40 degree electrons are almost unaffected by the perturbation. Figure 6.7, which shows the pitch angle anisotropy (-1 for extreme butterfly distribution, +1 for extreme normal distribution) illustrates the almost complete separation of 90 and 40 degree particles at noon and midnight. At noon the higher pitch angle electrons are confined to the outer radii, and the lower pitch angle electrons are confined to the inner radii, while the reverse is true at midnight.

6.2.1 SCATHA Data Analysis

Figure 6.8 shows the 218 kev electron distribution functions vs L-shell observed during the ascending portion of the satellite's orbit on April 21, 1979 (day 111) for 40 and 90 degree pitch angles, along with the observed and model⁽¹⁰⁾ quiet magnetic field. Coincident with the dropoff in the observed magnetic field relative to the model, as the satellite crossed $6.2 R_E$, signifying the start of a magnetic disturbance, there is a significant dropout of 90 degree pitch angle electrons. This is followed by significant dropouts at all pitch angles for L above $7 R_E$. For the corresponding period on the previous day, a particularly quiet period, no such dropouts are observed and the pitch angle distributions remained nearly isotropic over the period, in contrast to the marked butterfly distributions found during the disturbance on April 21. Similar effects are observed for ions at the beginning of the April 21 disturbance but the later dropouts seen for the electrons are not found.

In model this period we first analyzed the magnetic field

21 APRIL 1979 (DAY III) ASCENDING

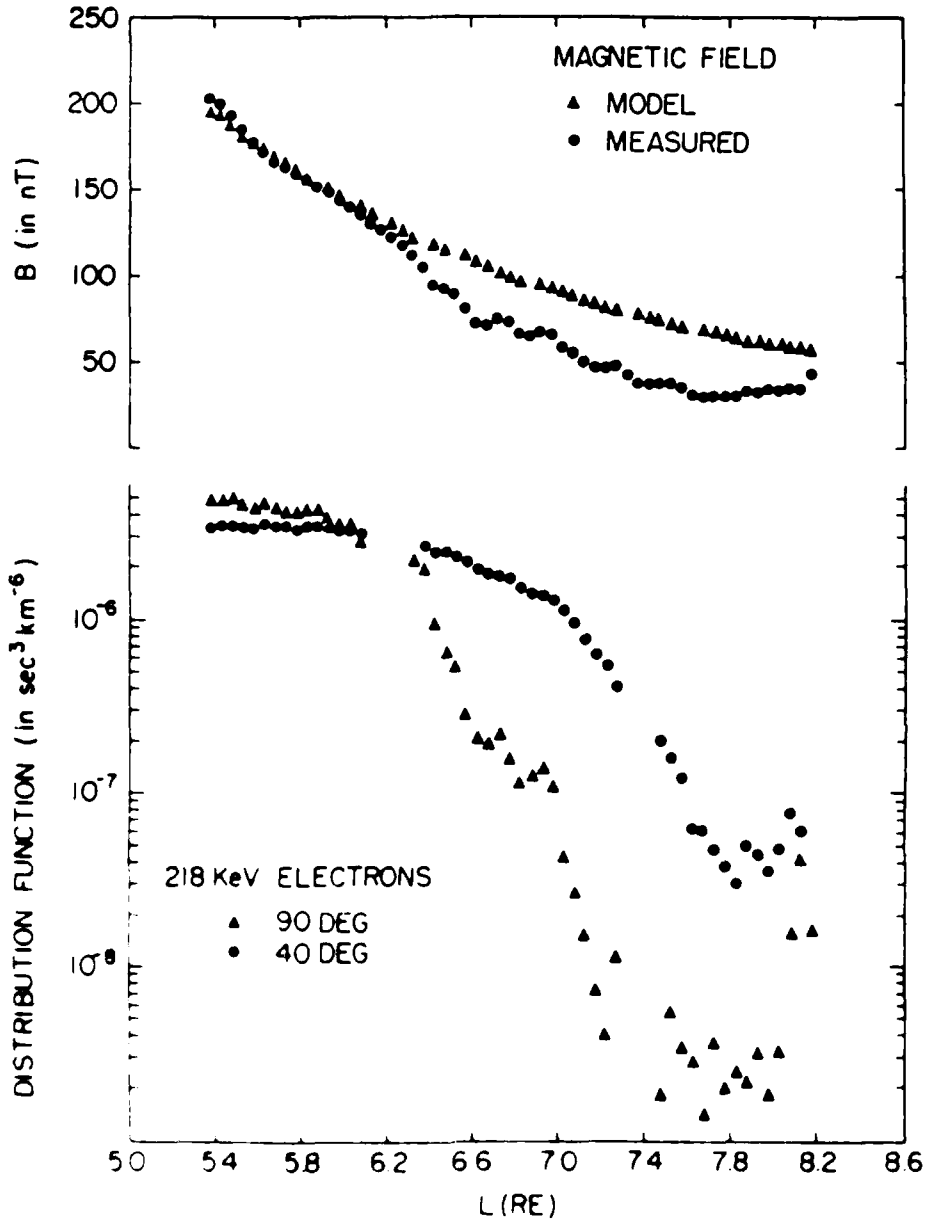


Figure 2.4 Top Panel: The Model (Olson-Pfizer) and Measured Magnetic Fields vs. L during the Ascending Portion of the SCATHA Orbit, 21 April 1979; Bottom Panel: Electron Distribution Function at 218 KeV, 40 and 90 Degree Pitch Angles for the Same Period

observations for the preceding quiet day. We found:

$$\bar{g}_1^0 = 10 \text{ nT}$$

$$\bar{g}_2^1 = 1.455 \text{ nT}$$

$$\Delta = 3 \text{ hr}$$

Note that it was necessary to assume a 3 hour westward rotation of the azimuthal symmetry plane in order to get a good fit to the data. Cummings, et. al.⁽¹¹⁾, and Pfitzer, et. al.⁽¹²⁾, analyzing ATS-1 data, found rotations in the same direction, but only 1-2 hours. The discrepancy is attributed to neglect of higher order multipoles in the magnetic field model in the present study, coupled with the larger radial range of the SCATHA satellite. Thus the radial variation of the neglected terms may be aliased into apparent local time variation. The symmetric perturbation is in good agreement with that found by Mead and Fairfield⁽¹³⁾ for geomagnetically quiet periods. The difference between this result and the value for the original Mead model, for 10 R_E magnetopause distance (-25 nT) is probably due to ring and tail currents not included in the original Mead model.

Figure 6.9 shows data and fits for the 275 keV ions for this period. The 90 degree ion distributions were fit to single decaying exponentials, as functions of the model L-shell value, reflecting typical trapped ion characteristics in the outer radiation belt. High correlation coefficients were found between L-shell and particle distributions for energies above 100 keV, with low correlation coefficients below, in accordance with the conventional wisdom that the magnetic field dominates control of the higher energy particles, i.e., trapping them, while the lower energy particles are influenced also by electric fields. The ions characteristically displayed a steep decay, as shown here, in contrast to the electrons (Figure 6.10) which are influenced

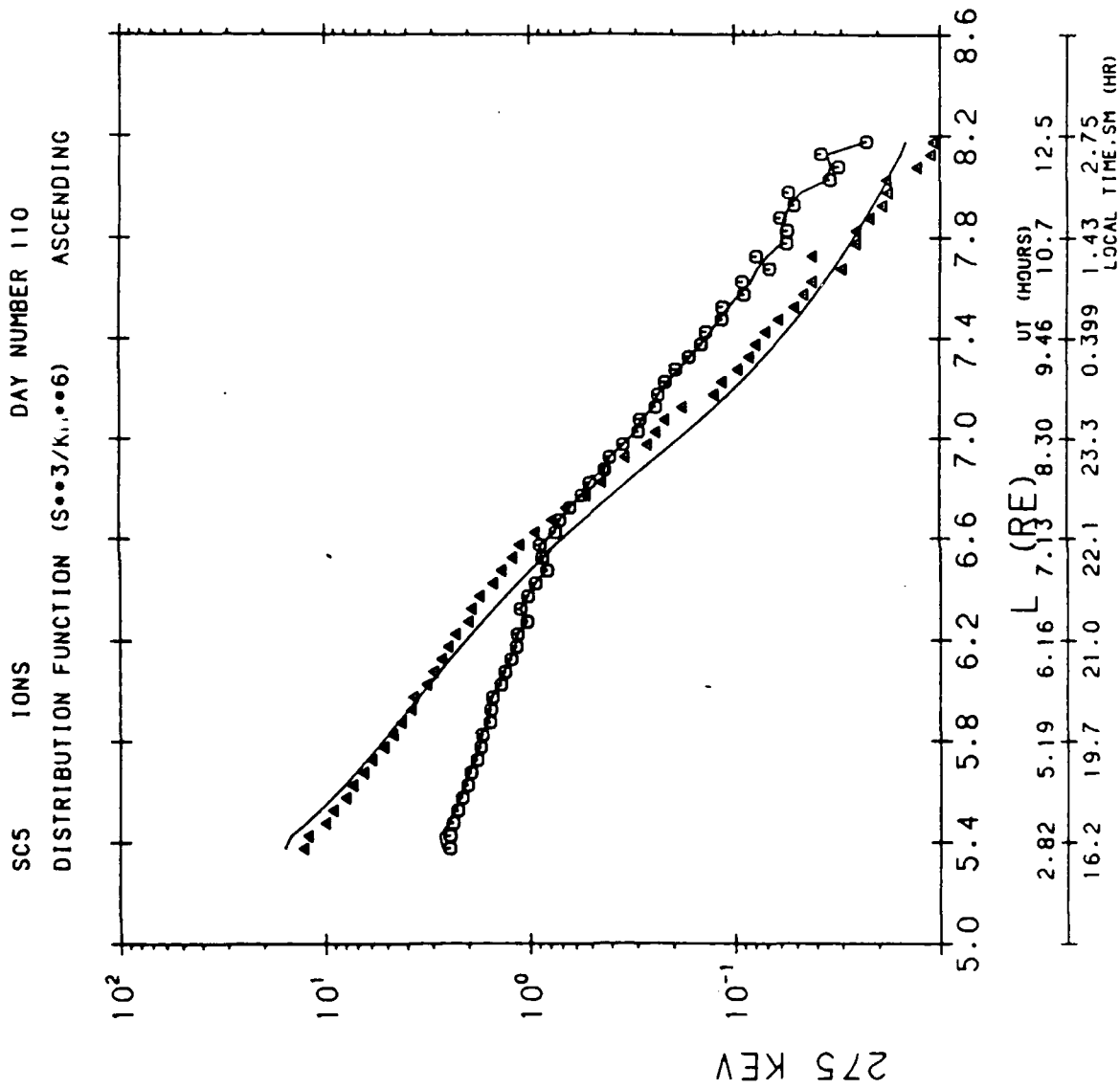
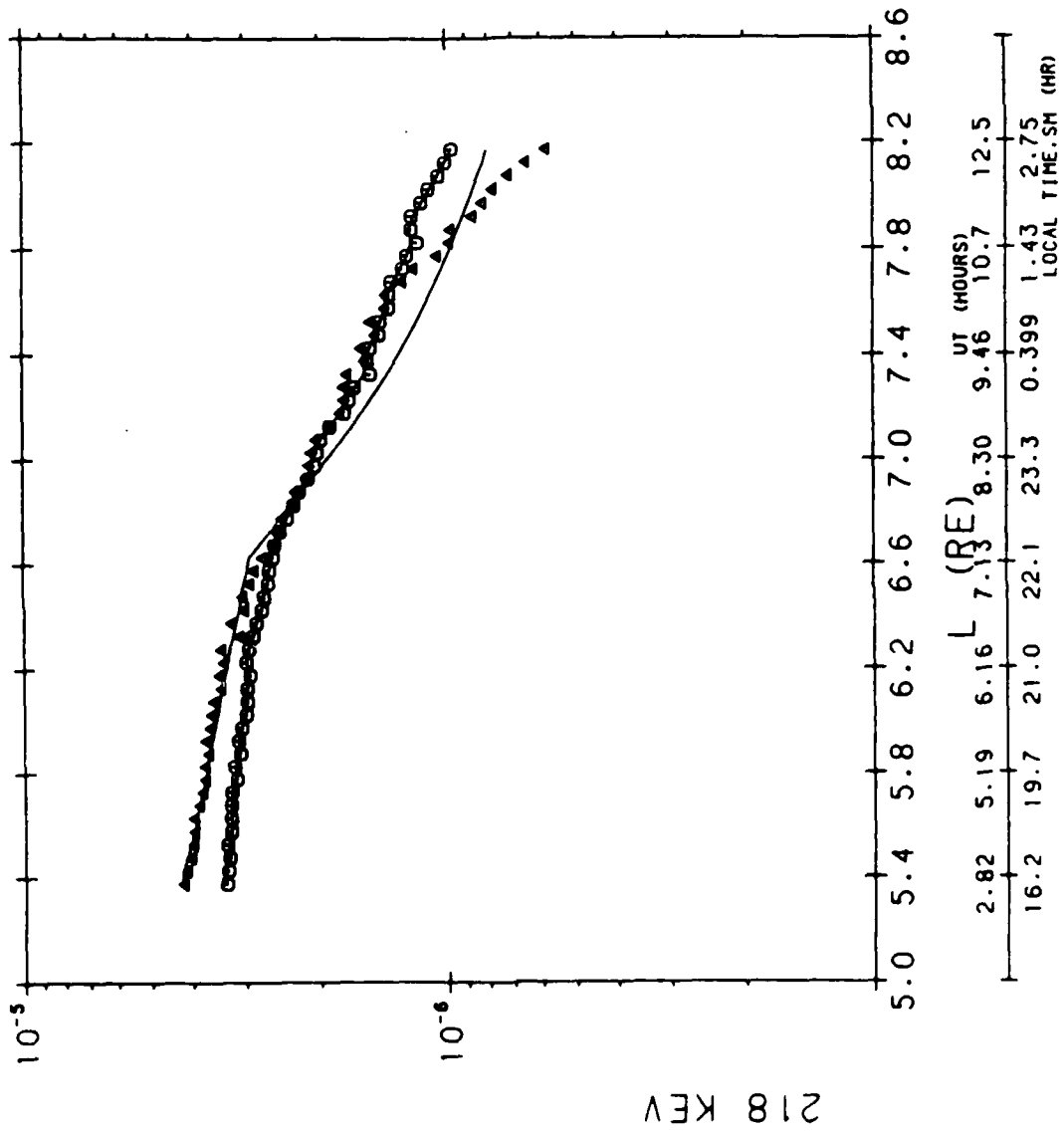


Figure 6.9 Comparison of Measured (Symbols) and Fit (Curves) Distribution Functions on April 20, 1979 for 275 KeV Ions at 40° and 90° Equatorial Pitch Angles.

SCS ELECTRONS DAY NUMBER 110
 DISTRIBUTION FUNCTION (S³/KM³) ASCENDING



PITCH ANGL
 TRI-90 DEG
 CIR-40 DEG

Figure 6.10 Same as Figure 6.9 but for 218 KeV Electrons.

by the approach to the slot region between the inner and outer radiation belts, and therefore could not be fit as well to a single exponentially decaying function. Figure 6.11 shows the L-dependent noon local time anisotropy indices, $1-F_{45}/F_{90}$, found for the 275 keV ions and 218 keV electrons for the quiet period, where F_{45} is the 45 degree distribution function value, and F_{90} is the 90 degree distribution function value. The electron results are in good agreement with the results of statistical analyses of three hour averages of observations⁽²⁾ around noon local time for $KP=0-1$, but the ions agree only approximately in magnitude, and do not exhibit the same L-dependence for this period as found statistically for this activity level.

Figure 6.12 shows the parameters for the model magnetic field used before and during the disturbance on April 21 (day 111). This includes a substantial decompression beginning at 0600 UT, to simulate the observed falloff.

As shown in Figure 6.13, the predicted (curves) 275 keV ion distribution function values agree quite well with the observed values for 90 and 40 degree pitch angles (triangles and circles, respectively) both before and during the initial phase of the disturbance. The 40 degree pitch angle prediction agreement continues through high L, but a 90 degree source at high L is apparent. The agreement for the 218 keV electrons (Figure 6.14) is not nearly so good, although the butterfly distribution characterizing the disturbance is reproduced as for the ions. The relatively poor agreement for the electrons is probably due to their greater interaction with waves. It is expected that the results would be similar for other energies above 100 keV, but these have not been included due to lack of resolution and reliable observation over a sufficiently large energy range.

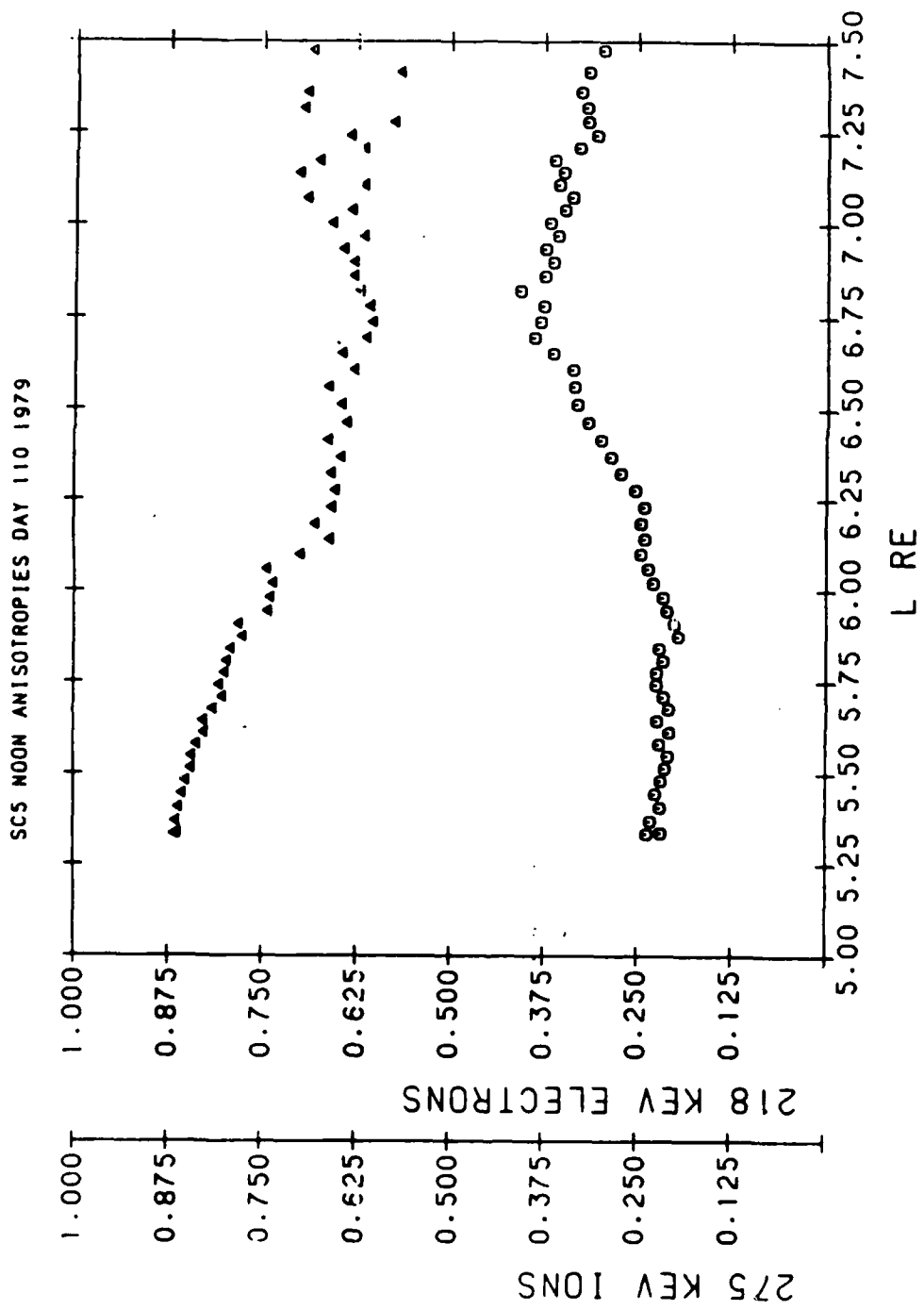


Figure 6.11 Noon Anisotropies for 218 KeV Electrons (Triangles) and 275 KeV Ions (Circles) from SCATHA Data, April 20, 1979.

DAY 111 MEAD PARAMETERS
BETA = 6.4 NT DPHI = 2 HR

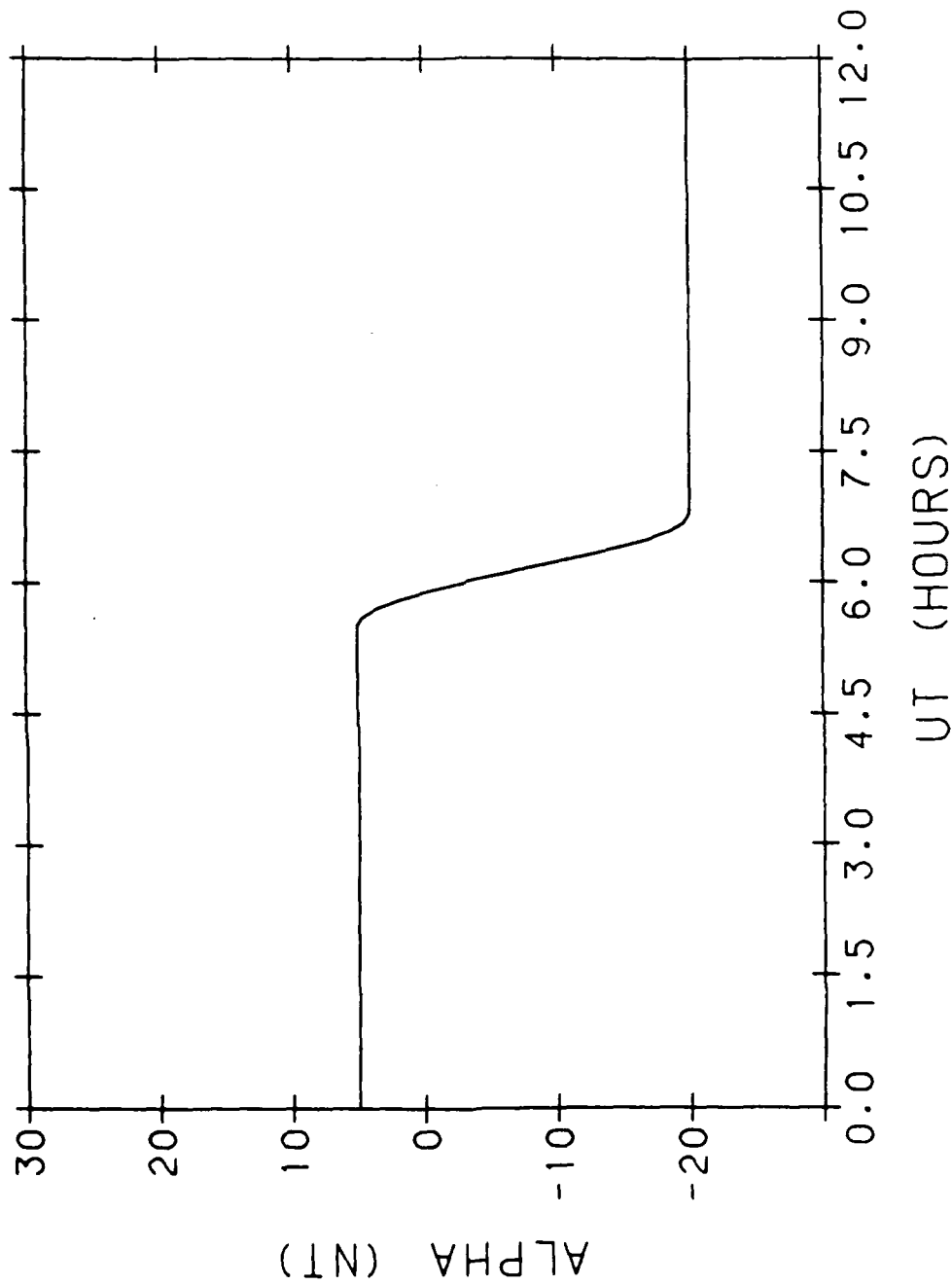


Figure 6.12 Model Magnetic Field Parameters ALPHA= $-\bar{g}_1^0$, BETA= $\sqrt{3} \bar{g}_2^1$, and DPHI= Δ , Used for April 21, 1979.

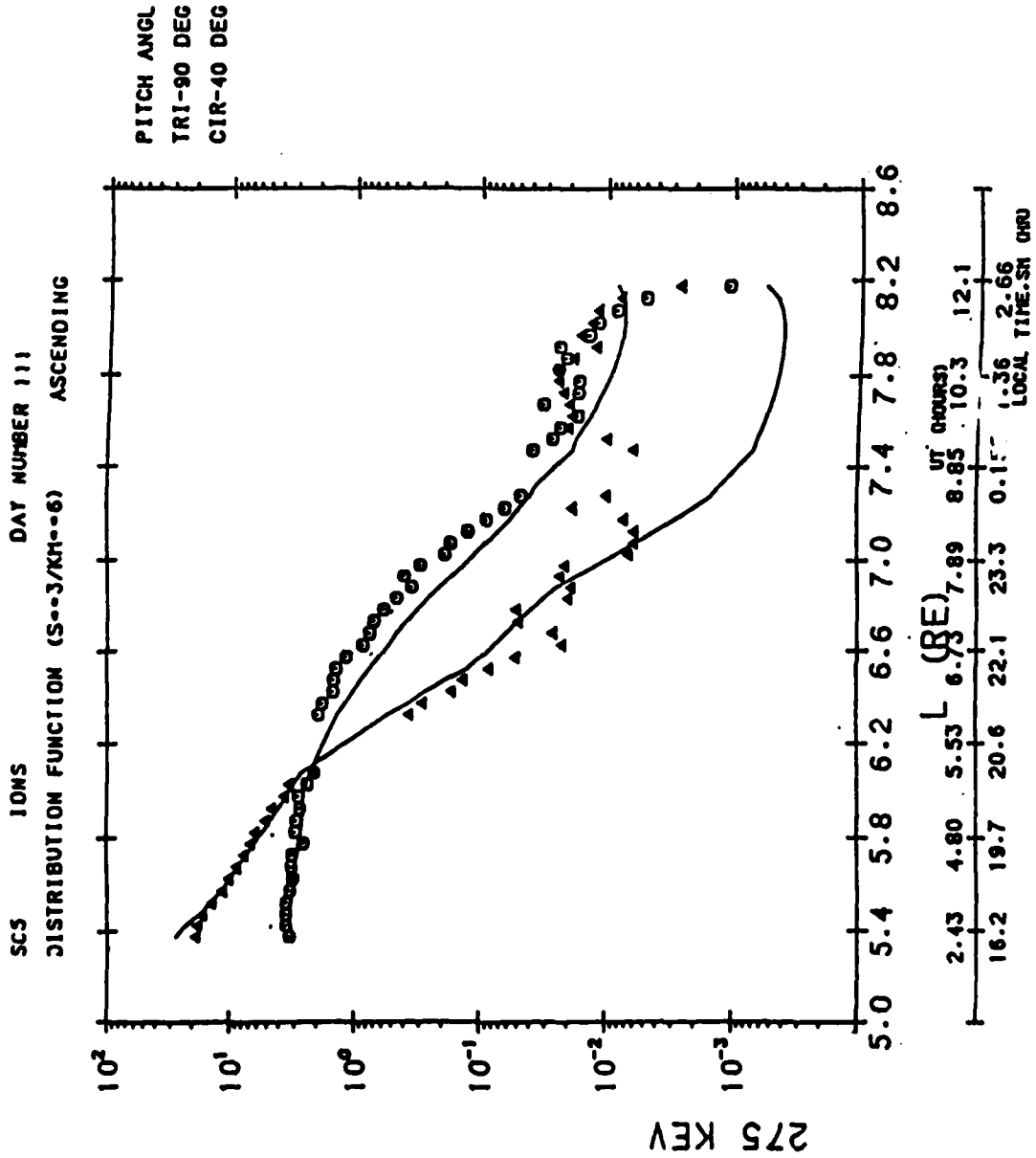


Figure 6.13 Comparison of SCATHA Observations (symbols) of 275 KeV Ions on 21 April 1979, with Predictions Based on Adiabatic Variation (lines) from Previous Day.

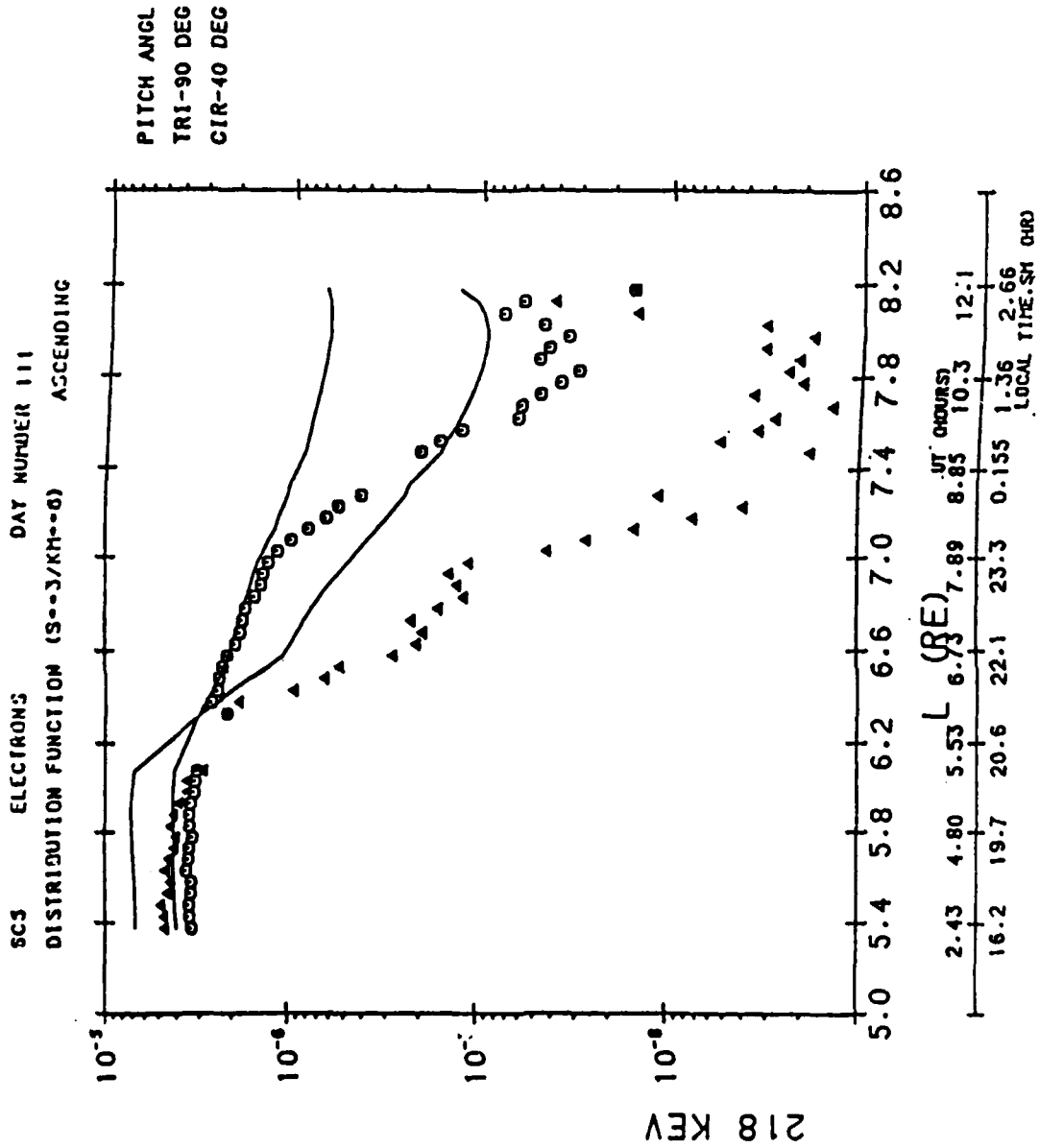


Figure 6.14 Same as Figure 6.13, except for 218 KeV Electrons

6.3 DISCUSSION

Coincident with a factor of two decompression in the magnetic field we have observed a factor of 100 depletion of 90 degree equatorial pitch angle high energy trapped electrons in the outer radiation belt and a factor of 10 depletion of 90 degree equatorial pitch angle high energy trapped ions. Substantially smaller depletions were found for lower pitch angles, thus resulting in the appearance of marked butterfly pitch angle distributions. The predicted adiabatic variations are factor of 10 depletions of both 90 degree electrons and ions and relatively little changes in the 40 degree particles. These variations are in very good agreement with those observed for the ions, except for the observed increases at high L; in particular, the butterfly pitch angle distribution is reproduced. Substantially greater losses are observed for the electrons than predicted for the entire radial range covered during the magnetic decompression, but, as for the ions, the butterfly pitch angle distribution is reproduced. Thus we conclude that adiabatic responses of trapped particle distributions can be large (order of magnitude), and that such responses can be mechanisms for production of butterfly pitch angle distributions. It therefore appears that pitch angle distributions of selected classes of geomagnetically trapped particles could serve as indicators of magnetic disturbances, and could therefore serve as valuable aids in analysis of trapped particle data, such as that expected from the forthcoming CRRES mission; the PAD of a selected particle could be used to estimate a magnetic parameter using the reverse of the procedure followed here.

Limitations of our procedure include the use of a very simple magnetic model. The Mead mathematical form was chosen as a tradeoff between speed and accuracy. In analyzing the large amount of data expected from a mission such as CRRES, a computationally simple technique is essential. The Mead

model did result in a possibly unrealistically large rotation of the azimuthal symmetry plane, but this could be overcome with the use of additional multipole terms without, hopefully, increasing substantially the complexity of the algorithm. The weakness of the model is most significant at large radial distances, where both the adiabatic approximation and the first-order drift shell perturbation method would be expected to break down, anyhow (both spatial and temporal variations are large relative to a zeroth order dipole field). For the example studied here, we note that at large L , the ions and electrons behave differently with respect to the adiabatic predictions (the ion population increases, while the electron population decreases - thus indicating real sources and sinks as the origin of disagreement, rather than simplicity in the magnetic field model). An additional limitation in the present study is at the energy range and resolution of the available data. While the adiabatic theory predicts changes in particle energy response to changes in the magnetic field, specification of the quiet distribution functions over extended energy and radial positions is required to estimate the adiabatic changes in the distributions observed in a particular energy channel. The particular energy channels depicted in this study were chosen because the data coverage in their immediate energy neighborhoods was the best in the SCATHA data set. These results are not expected to be different from those obtained for any reasonable energy distribution, except that the changes with increasing energies will be smaller since the magnetic field would produce a deceleration of adiabatic particles and fewer particles so that those observed in a particular energy channel during the decompression were from a higher energy channel before.

References

1. Bass, J. N., Gussenhoven, M. S., and Redus, R. H., "The Importance of Adiabatic Variations in Trapped Particle Distributions Observed by the SCATHA Satellite", to be submitted to J. Geophys. Res.
2. Mullen, E. G., and Gussenhoven, M. S., SCATHA Environmental Atlas, Tech. Report, AFGL-TR-83-00C2, ADA131456, Air Force Geophysics Laboratory, Hanscom Air Force Base, MA, 1983.
3. Pennington, Ralph H. "Equation of a Charged Particle Shell in a Perturbed Dipole Field", J. Geophys. Res., Vol. 66, No. 3, Pp. 709-712, 1961.
4. Stern, David "Classification of Magnetic Shells", J. Geophys. Res., Vol. 70, No. 15, Pp. 3629-3634 (1965).
5. Stern, David "Euler Potentials and Geomagnetic Drift Shells", J. Geophys. Res., Vol. 73, No. 13, Pp. 4373-4378 (1968).
6. Stern, David "Particle Diffusion in the Magnetosphere", Springer Verlag, Berlin, 1974, Pp. 17-20.
7. Stern, David "Disturbance of the Geomagnetic Field by the Magnetosphere", J. Geophys. Res., Vol. 69, Pp. 1181-1195 (1964).
8. Stern, David "Magnetic Shell Tracing: A Quantitative Modeling of the Magnetosphere", W. H. Rishbeth, Ed., American Geophysical Union, 1974.
9. Stern, David "Orthogonal Basis Functions for the Magnetosphere Theory", Pp. 159-168 in Geophysical Research Letters, Vol. 11, J. Belcher, H. Jasperse, Ed., Springer, MA, 1984.
10. Stern, David "A Quantitative Model of the Magnetosphere", J. Geophys. Res., Vol. 70, Pp. 48-54 (1965).
11. Stern, David, and Stone, G. L., "The Magnetosphere", J. Geophys. Res., Vol. 70, Pp. 48-54 (1965).
12. Stern, David, and Winkler, J. R., "Shell Splitting in the Magnetosphere", J. Geophys. Res., Vol. 74, Pp. 48-54 (1969).

13. Mead, G. D., and Fairfield, D. H., "A Quantitative Magnetospheric Model Derived from Spacecraft Magnetometer Data", J. Geophys. Res., Vol. 80, No. 4, Pp. 523-534, 1975.

2. Simulation and Initial Calibration of Fluxgate Magnetometers for CRRES

The development of software for the performance of specific data reduction tasks is often not vaguely addressed before the data is available. Lack of planning can lead to delays and even the inadvertent omission of crucial parameters in the data base that may be required for successful data analysis. Simulation of the data collection and analysis process as early as possible in the planning of a specific mission is one way to avoid these difficulties.

The work presented here simulates the treatment of fluxgate magnetometer data for the Combined Release and Radiation Effects Satellite (CRRES) mission. A plan for handling the data has evolved through an iterative process to the point where the plan can be put into operation on real data with fewer problems than would otherwise have occurred.

Additionally, the analysis of the simulated signals has conferred a familiarity with the "data" even before the experiment has been carried out. With such familiarity, one can better address additional problems that may arise in practice.

The purpose of this work was thus three-fold. First, we wished to validate the proposed data processing plan by demonstrating that it can be carried out with reasonable effort on simulated data. Second, we determined the algorithms needed for data processing through the combined processes of analysis of the magnetometer system and simulation of the signals and processing itself. Finally, the results of this study should prove valuable as a starting point in dealing with further problems that may arise in the real data once it is obtained.

7.1 Signal Generation

The factors to consider in the generation of simulated magnetometer signals are the spacecraft position, the magnetic field at that point, the spacecraft's attitude and spin phase, the orientation of the magnetometers with respect to the spacecraft and the planned telemetry format.

We wished to simulate the CRRES environment as closely as possible and so a model orbit was generated with an existing satellite orbit generation program LOKANGL. We used the CRRES internal model field with the Olsen-Pfitzer 77 external model to arrive at the magnetic field vector at each point in the orbit. This gave the field in Earth Centered Inertial (ECI) coordinates. From here, it was necessary to transform the field by a series of rotations into the coordinate frame of the magnetometer. This was done in three steps:

- 1) The rotations to transform the original field in ECI to a frame fixed to the spacecraft at a chosen time zero.
- 2) A rotation about the spin axis, chosen to be the spacecraft z-axis, to incorporate spin, and
- 3) Another series of rotations to represent the difference in orientation between the spacecraft axes and the sensor axes.

If we define α and δ as shown in Figure 7.1, the first of these rotations can be accomplished by

$$R_y(\delta-90^\circ)R_z(\alpha) \quad (7.1)$$

where $R_a(\theta)$ means rotation around the a-axis by the angle θ . This will be called the spacecraft (SC) coordinate system and is the basis for all further analysis of the sensor signals.

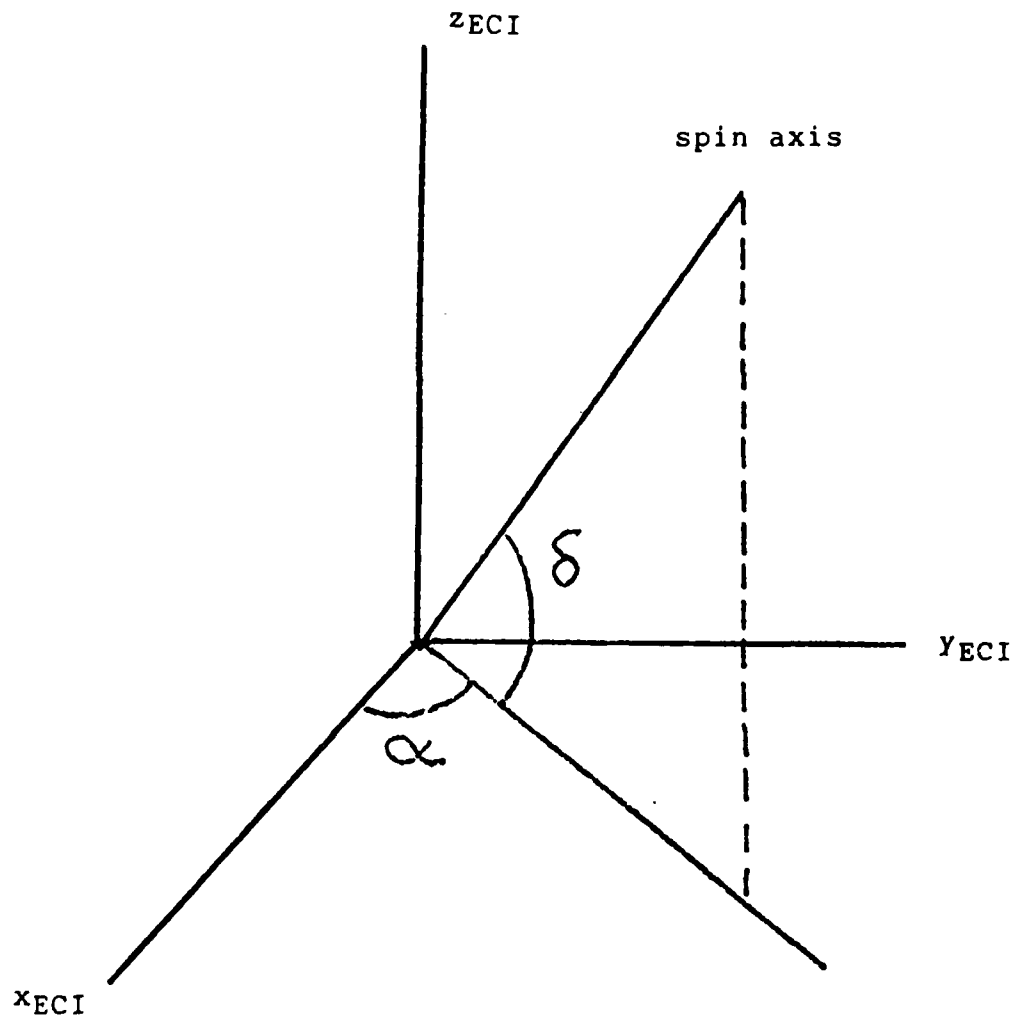


Figure 7.1 Definition of the spacecraft spin axis in the Earth Centered Inertial (ECI) frame.

Let each magnetometer be defined by the angle it makes with the true spacecraft spin axis z_{sc} and with another arbitrary axis x_{sc} perpendicular to the spin axis, as shown in Figure 7.2. The external magnetic field is assumed constant for this analysis, although in practice, we allow it to vary linearly over the course of a few spins. The field is given by its component along the spin axis b_z and by its component in the spin plane b_{xy} . Also let ϕ_b be the angle that b_{xy} makes with x_{sc} at $t=0$. Since the spacecraft spins at a rate ω , the signal from each magnetometer can be written as

$$s_m = g_m \sin \theta_m b_{xy} \cos(\phi_m + \omega t - \phi_b) + g_m b_z \cos \theta_m + d_m \quad (7.2)$$

In the above, d_m ($m=x,y,z$) is the total dc offset for the sensor and g_m is the factor that relates the nominal gain used to generate the simulated signal to the actual field strength. This means that the sensor signal is proportional to but not equal to the magnetic field along the sensor. With this definition, the calibrated field strength is obtained by subtracting d from each sensor component and then dividing by g . The object of calibration will be to determine the g 's and d 's of Equation 2. We assume that different values can exist for each sensor and for each gain state. Additionally, the y-sensor can be switched so that its signal is multiplied by six before digitization. In this x6 mode, the y-sensor is assumed to have different gains and offsets. There are thus 16 calibration factors to be calculated.

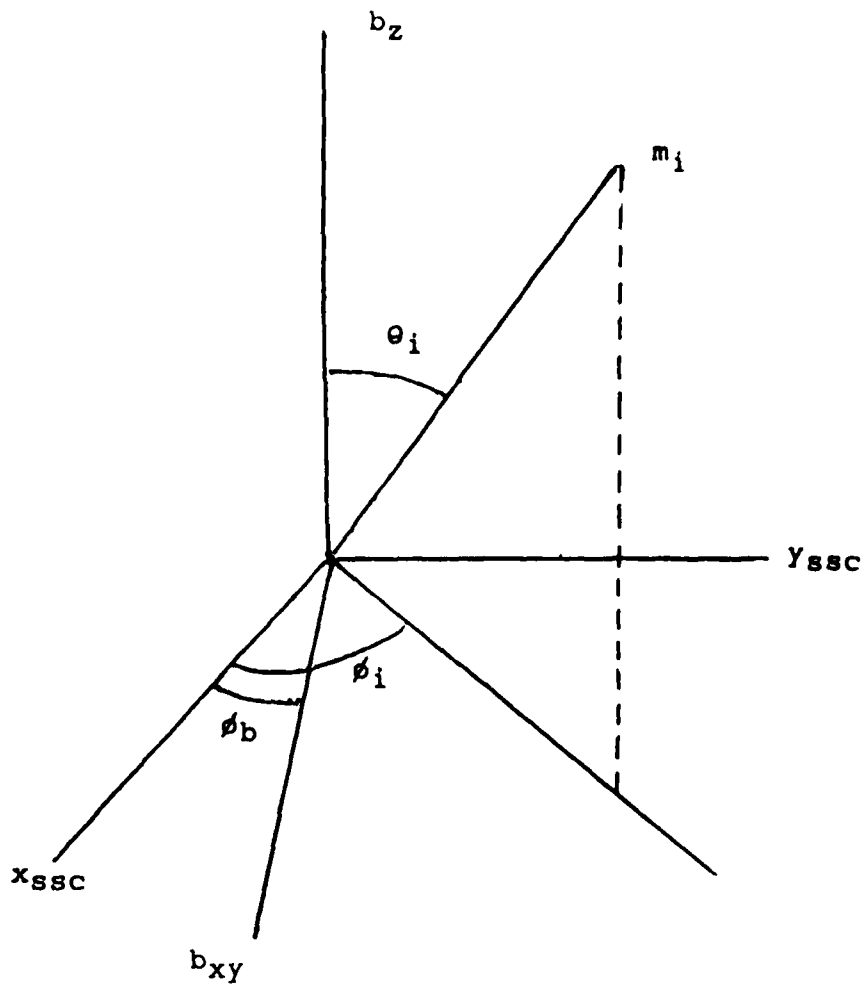


Figure 7.2 The definition of the orientation of one of the magnetometers in the coordinate system used for spin axis angle calculation.

For purposes of simulation, the telemetry format is important because digitization limits the accuracy of a signal. For this experiment, the signals are digitized in one of two levels, high gain for signals in the range ± 900 nT and low gain for signals outside this range but within $\pm 45,000$ nT. Twelve bits are used to represent this information, so the range of the digitized signals is ± 2048 . Thus in this simulation, each signal is converted to an integer according to the above scheme then "unpacked" to imitate the precision that will be encountered in the experiment.

7.2 Calibration

The purpose of calibration is to use the sensor signal itself to determine gains and offsets of each of the magnetometer axes. The basis for this determination is a fit that is performed on each component of the signal. From examination of Equation 2, it can be seen that each sensor signal can be thought of as composed of two different signals, one that is constant in time and one which oscillates at the spin frequency. Since the background field is not really constant in time, we can easily allow it to vary linearly (or to any other order) by performing fits of each sensor signal to a function of the form

$$s_x = \alpha_{x0} \cos \omega t + \alpha_{x1} t \cos \omega t + \beta_{x0} \sin \omega t + \beta_{x1} t \sin \omega t + \delta_{x0} + \delta_{x1} t \quad (7.3)$$

We then use the coefficients of this fit to derive relations between the gains and offsets needed for calibration.

7.2.1 Sensor Gain Ratios

We first use the spin fits to calculate ratios between gains for each sensor in each operational mode. If we square each α and β of Equation 2 and compare to Equation 3, we find

$$\begin{aligned}\alpha_x^2 + \beta_x^2 &= g_x^2 b_{xy}^2 \sin^2 \theta_x \\ \alpha_y^2 + \beta_y^2 &= g_y^2 b_{xy}^2 \sin^2 \theta_y \\ \alpha_z^2 + \beta_z^2 &= g_z^2 b_{xy}^2 \sin^2 \theta_z\end{aligned}\quad (7.4)$$

A result proportional to the ratios of any two gain factors can then be obtained by dividing one line by another

if $k_x = \sqrt{(\alpha_x^2 + \beta_x^2)}$ etc., then

$$\begin{aligned}r_{xy} &= g_x/g_y = k_x/k_y * \sin \theta_y / \sin \theta_x \\ r_{yz} &= g_y/g_z = k_y/k_z * \sin \theta_z / \sin \theta_y \\ r_{xz} &= g_x/g_z = k_x/k_z * \sin \theta_x / \sin \theta_z\end{aligned}\quad (7.5)$$

We will calculate these ratios for fixed low gain and variable gain channels each time a spin fit is carried out. There is another set of gain corrector ratios that will be calculated in specific areas of an orbit when the variable gain channels are in high gain but where the field is still reasonably large to make fixed low gain readings accurate. These are the ratios between high and low gain operation in each magnetometer axis. These are obtained by subtracting the offsets from the fixed low and variable gain channels and forming the ratios

$$\begin{aligned}r_{x1h} &= g_{x1}/g_{xh} = (s_{x1} - d_{x1}) / (s_{xh} - d_{xh}) \\ r_{y1h} &= g_{y1}/g_{yh} = (s_{y1} - d_{y1}) / (s_{yh} - d_{yh}) \\ r_{z1h} &= g_{z1}/g_{zh} = (s_{z1} - d_{z1}) / (s_{zh} - d_{zh})\end{aligned}\quad (7.6)$$

This calculation requires prior knowledge of the dc offsets d_i which must be estimated from ground testing, taken from calibrations performed on earlier orbits or approximated as zero.

7.2.2 Offset Determination

In the derivation of sensor dc offsets, it is convenient to think in terms of a fictitious set of sensors, sensor 1 and sensor 2 in the spin plane and sensor 3 along the spin axis. Spin fits can be used to determine absolute values of the two of these perpendicular to the spin axis, Δ_1 and Δ_2 . Δ_3 cannot be determined from spin fitting since the field along the spin axis does not oscillate with spin and the offset cannot be distinguished from the static external field along the spin axis.

From Equation 2, we see that

$$\begin{aligned}\delta_x &= g_x b_z \cos\theta_x + d_x \\ \delta_y &= g_y b_z \cos\theta_y + d_y \\ \delta_z &= g_z b_z \cos\theta_z + d_z\end{aligned}$$

Elimination of the unknown b_z between first and second and between second and third of these defined Δ_1 and Δ_2 as

$$\begin{aligned}\Delta_1 &= \cos\theta_y \delta_x - r_{xy} \cos\theta_y \delta_y \\ \Delta_2 &= \cos\theta_z \delta_y - r_{yz} \cos\theta_y \delta_z\end{aligned}\tag{7.7}$$

Again, the ratios r_{xy} and r_{yz} are necessary. They can be estimated or taken as calculated for each spin fit from Equation 4.

7.2.3 Relation to Sensors

In order to apply the quantities calculated above to the task of creating a calibrated magnetometer signal, it is necessary to generate the g and d of Equation 2. There are several possible ways to do this and it is probable that any scheme presented at this time might be modified, at least slightly, when processing of the actual data begins to reveal the

ideosyncracies of the instrument. For definiteness, however, we give the specifications for a scheme which worked well in simulated data tests.

First, it is assumed that g_{xh} and g_{x1} are known. In high gain, we use g_{xh} and r_{xyh} or r_{xzh} to find g_{yh} or g_{zh} . In low gain, we use g_{x1} and r_{xz1} to find g_{z1} . We use g_{yh} and r_{y1h} to find g_{y1} however, because this worked better in our tests.

$$\begin{aligned}
 g_{yh} &= g_{xh}/r_{xyh} \\
 g_{zh} &= g_{xh}/r_{xzh} \\
 g_{y1} &= g_{yh} * r_{y1h} \\
 g_{z1} &= g_{x1}/r_{xz1}
 \end{aligned}
 \tag{7.8}$$

Next, we assume that Δ_3 , the offset along the spin axis, is given,

$$\Delta_3 = d_x \cos \theta_x + d_y \cos \theta_y + d_z \cos \theta_z$$

The values for d_x , d_y and d_z are then obtained from the solution of the matrix equation

$$\begin{array}{|c|} \hline \Delta_1 \\ \hline \Delta_2 \\ \hline \Delta_3 \\ \hline \end{array} = \begin{array}{|ccc|} \hline \cos \theta_y & -r_{xy} \cos \theta_x & 0 \\ \hline 0 & \cos \theta_z & -r_{yz} \cos \theta_y \\ \hline \cos \theta_x & \cos \theta_y & \cos \theta_z \\ \hline \end{array} \begin{array}{|c|} \hline d_x \\ \hline d_y \\ \hline d_z \\ \hline \end{array}$$

by inversion.

7.2.4 Calibration Example

An example of the calibration procedure on a simulated orbit of data can now be presented. Gains and offsets for this example were assigned to each sensor in each gain state and the procedure was performed over portions of the simulated orbit where the quantities described before were relatively free of disturbances. These are areas of moderately strong but slowly varying external field.

Table 7.1 presents a summary of input (assumed) and output (calculated) gains and offsets. The table also shows the UT time interval chosen to carry out each average. The lower part of the table shows the quantities necessary for despinning the sensor signals. These were calculated from the data in the upper portion of the table using the relations given earlier. The numbers in () are the actual input values. Figure 7.3 shows the difference between the input magnetic field components and the magnetic field calculated using the calibration factors that resulted from this analysis. The differences are much smaller than the noise that arises from digitization and the calibration process can thus be deemed successful.

7.3 Spin Axis Angle Calculation

Up to this point, we have assumed that the angles between each magnetometer axis and the spin axis were known. In practice, this is likely not to be the case because the spin axis may be slightly different from the planned spin axis and because the boom on which the magnetometer is mounted may flex somewhat during operation. Therefore, it would be valuable to have a method by which the spin axis angles can be calculated from the sensor signals, just as gains and offsets were.

Table 7.1
Results of Calibration

Quantity	Fit over	Value	s.d.	Actual
(high gain measured quantities)				
Δ_1	1.5 -> 10.0	4.3001	.0044	4.3000
Δ_2	1.5 -> 4.5 7.0 -> 10.0	4.6914	.016	4.6900
gx/gy	1.0 -> 4.0 6.5 -> 10.0	1.2219	.0036	1.2222
gx/gz	1.5 -> 10.0	1.0479	.0004	1.0476
gy/gz	1.0 -> 4.0 6.0 -> 10.0	.8572	.0028	.8571
(low gain measured quantities)				
Δ_1	0.5 -> 2.0 8.5 -> 10.5	5.617	0.72	5.600
Δ_2	0.5 -> 2.0 8.5 -> 10.5	8.569	2.4	8.4436
gx/gz	0.0 -> 1.2 9.3 -> 10.5	1.263	.002	1.2632
gyl/gyh	0.7 -> 1.1	1.22207	.009	1.22222

	high gain	low gain
assumed spin parallel dc	-7.1705	-10.2889
derived d_x	4.3001 (4.3000)	5.617 (5.600)
derived d_y	7.4001 (7.4000)	10.605 (10.600)
derived d_z	5.1012 (5.1000)	7.023 (6.900)
assumed g_x	1.1	1.2
derived g_y	0.9002 (0.9000)	1.1001 (1.100)
derived g_z	1.0499 (1.0500)	0.95012 (0.950)

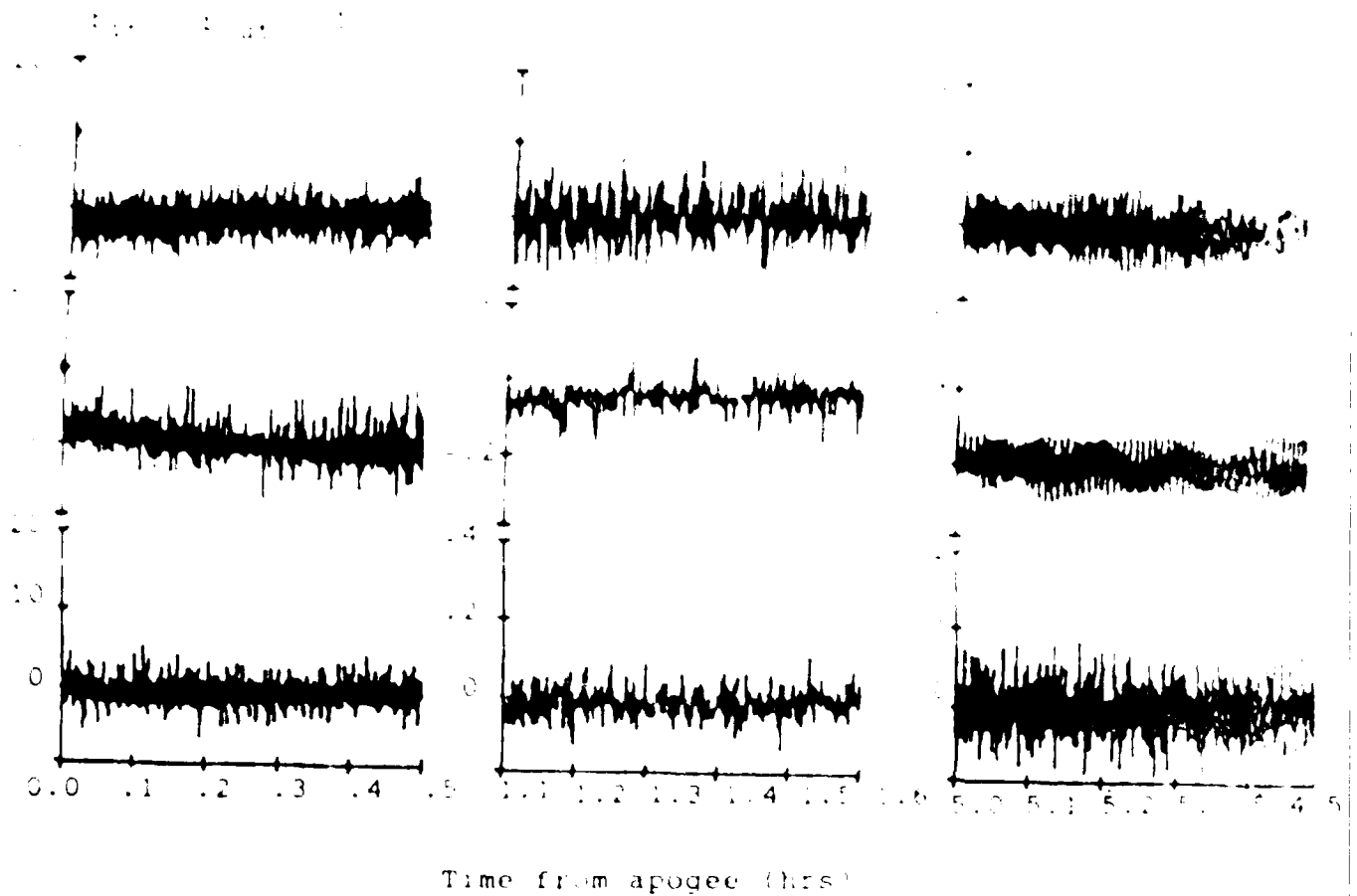


Figure 7.3 The difference between the magnetic field components input to the simulation system and those despun with the calibration factors calculated with this analysis at 0, 1 and 5 hours into the simulated orbit.

In this analysis we define the external magnetic field in a spacecraft (SSC) system, as follows.

z_{ssc} is along the true spin axis, right handed,
 x_{ssc} is in the plane of the x magnetometer (x_m) and
 perpendicular to the z_{ssc} axis and is opposite in sense, and
 y_{ssc} completes a right handed system.

The magnetometer sensors axes are assumed to be orthogonal and are defined relative to the ssc frame by two angles, γ and μ . γ represents a rotation around x_{ssc} and μ is a rotation around y_{ssc} . These two angles completely specify the spin axis angles of the three magnetometers. The transformation matrix between the ssc frame and the magnetometers is

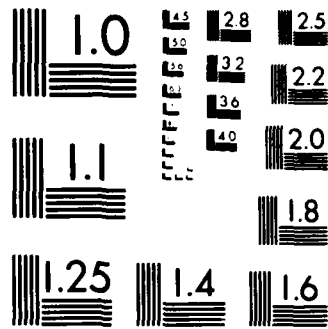
$$\begin{bmatrix} \cos\mu & 0 & \sin\mu \\ -\sin\mu \cos\gamma & -\sin\gamma & -\cos\mu \cos\gamma \\ \sin\mu \sin\gamma & -\cos\gamma & \cos\mu \sin\gamma \end{bmatrix} \quad (7.10)$$

By analogy to Equation 2, the constant components of the sensor signals can be seen to be

$$\begin{aligned} \cos\theta_x &= \sin\mu \\ \cos\theta_y &= -\cos\mu \cos\gamma \\ \cos\theta_z &= \cos\mu \sin\gamma \end{aligned}$$

The analysis relies on the determination of the value of $\cos\theta$ from the slopes of the dc part of the spin rate signals. Each sensor dc follows the relation

$$\delta_i = g_i b_i \cos\theta_i + \dots$$



MICROCOPY RESOLUTION TEST CHART
NATIONAL BUREAU OF STANDARDS 1963-A

Thus, if we determine the rate of change of one dc component with respect to another and use Equation 11, we find

$$\begin{aligned}d\delta_z/d\delta_x &= r_{xz} \tan\mu / \sin\gamma \\d\delta_z/d\delta_y &= -r_{yz} \tan\gamma\end{aligned}$$

These equations are sufficient to determine γ and μ if the ratios r_{xz} and r_{yz} are known. These are available from the oscillating components of the spin fit if the spin axis angles of each sensor are known. We can thus make an iterative calculation as follows.

- 1) Guess values for γ and μ near those expected,
- 2) Perform linear regression on the spin fits of δ values to obtain slopes of one against the other,
- 3) Use the input μ and γ with the spin fit amplitudes to calculate r_{yz} and r_{xz} ,
- 4) Use these ratios to find new values for γ and μ ,
- 5) Go back to 3 until the process converges.

We have found that this process converges quite well if γ and μ are chosen within a few degrees of the actual values. This should be possible to obtain in practice.

7.4 Model Field Calibration

In the previous calculation of gains and offsets, it was necessary to assume a gain value for the x-sensor in one gain mode and a spin axis parallel offset. We can perform a calibration of the gain in the x-sensor by comparison of the signals to a model field. The process will be most reliable when the satellite is at low altitudes, where the accuracy of field models is high.

The idea behind this approach is to use the magnitude, not the direction, of the magnetic field calculated from the sensors compared to a model field to arrive at the gain corrector for one of the sensors. An important element in this method is that it relies on only the magnitude of the model field and not the direction. The magnitude is generally known to higher precision than the direction and, furthermore, such a calculation is independent of spacecraft attitude information.

In this process, the offsets determined are subtracted from each of the three sensor signals. Then the y sensor signal is multiplied by r_{xy} and the z signal is multiplied by r_{xz} . When the magnitude of the resulting vector is taken, this can be compared directly to the magnitude of a model field.

$$|s| = g_x |b_{\text{model}}|$$

This assumes that the signals are orthogonal but does not require their orientation to be known at all. This analysis gave a value of 1.1001 for the gain in the x-sensor when it was performed on the simulated orbit. This extremely accurate result is probably not to be expected in actual data analysis because the model field will differ from the measured field since the model is only an average while the measured field varies in time. In practice, however, this analysis could be carried out over several orbits and

presumably, the values would get better as more data is added. Also, in practice, the gain correctors will probably be much closer to unity than the ones we have used in this simulation.

7.5 Conclusion

In carrying out the simulation of CRRES magnetometer signals and the subsequent development of a data analysis plan, many problems have been confronted that one would face in dealing with the actual data. After deriving the equations for the sensor signals, an averaging procedure was devised for reduction of the data base for calibration purposes. The averaging procedure introduced errors in signal amplitudes; however, it was shown that the error could easily be corrected during despining. The analysis and software allowed for unknown sensor gains and offsets and methods were developed for determining these values and for determining the orientation of the sensors with respect to the spacecraft spin axis. Expressions were also derived to illustrate the ways in which errors in gain and offset propagate into the despun fields. This effort has been more completely described in another report.⁽¹⁾ (1)

The work was characterized throughout by optimization, the discarding of unworkable schemes and the weighing of one possible path against another. Further modifications of the scheme will undoubtedly take place once the processing begins; however, this work has provided a solid foundation for the generation of a reliable and accurate CRRES magnetic field data set.

¹ McNeil, W.J. and H.J. Singer, "Fluxgate Magnetometer Analysis and Simulation Software for the Combined Release and Radiation Effects Satellite (CRRES)", AFGL-TR-86-0222, October 1986. ADA176353

8.0 CRRES DATA MANAGEMENT PLAN

CRRES satellite experiments will perform chemical releases in the near-Earth environment and measure radiation and its effects on state-of-the-art microelectronics devices and other spacecraft components. This section summarizes the data management plan that was compiled to define data bases required for investigations by researchers within AFGL, as well as other Air Force and NASA agencies. CRRES will support the Air Force Geophysics Laboratory (AFGL) Space Radiation Effects Program (SPACERAD), as well as other projects. Space and ground tests will be designed to:

- a) Measure radiation-induced effects on microelectronic devices in known space environments;
- b) Update the static models of the radiation belts and develop the first dynamic models of the high energy particle populations in the near-Earth environment.

During the SPACERAD portion of the mission, the CRRES satellite will have a low inclination (less than 20 degrees), highly elliptical (400 km to 36,600 km) orbit which will traverse the most radiation intense regions of the Earth's inner (proton dominated) and outer (electron dominated) radiation belts. This portion of the mission is known as the Geosynchronous Transfer Orbit (GTO) phase. The satellite will have a 3 year mission goal to accumulate a statistically significant data set for the empirical analyses.

8.1 OBJECTIVES

The data reduction and analysis tasks needed are described as part of this data management plan. The Data Reduction task results in the production of the CRRES Time History Data Base; pertinent CRRES telemetry data from the CRRES agency tapes are converted into engineering and geophysical units (or in a form from which these geophysical units can readily be derived by means of calibration data), and placed in on-line storage. The Data Analysis task results in the production of the CRRES Product Associated Data Base; experimental data from the Time History Data Base and other sources are restructured and merged into unique data sets that are needed to support analysis required to generate individual products and to support other engineering and environmental studies; this data base is placed in on-line storage.

Considerable reference is made in this section to the AFGL reports on experiment descriptions⁽¹⁾ and the data processing task management plan⁽²⁾. Material from these documents was used liberally in developing this data management plan.

8.1.1 Experiments, Instruments and Agency Tapes

The instruments and the parameters being measured are briefly identified here. Detail descriptions of these instruments may be found in Reference 1.

<u>Experiment</u>	<u>Package</u>	<u>Description</u>
1	AFGL 701-1A	Microelectronics Package
2	AFGL 701-1B	Internal Discharge Monitor (IDM)
3	AFGL 701-2	Space Radiation Dosimeter
4	AFGL 701-3	Metal Oxide Semiconductor (MOS) Dosimeter
5	AFGL 701-4	High Energy Electron Fluxmeter (HEEF)
6	AFGL 701-5A	Medium Energy Electron and Proton Spectrometer (MEES)
7	AFGL 701-5B	Electron-Proton-Angle Spectrometer (EPAS)
8	AFGL 701-6	Low Energy Plasma Analyzer (LEPA)
9	AFGL 701-7A	Relativistic Proton Detector
10	AFGL 701-7B	Proton Switches
11	AFGL 701-8,-9	Proton Telescope (PROTEL)
12	AFGL 701-11A	Magnetospheric Ion Composition Sensor (MICS)
13	AFGL 701-11B	Low Energy Magnetospheric Ion Composition Sensor (LOMICS) and Heavy Ion Telescope (HIT)
	701-11C	
14	AFGL 701-13-1	Fluxgate Magnetometer
15	AFGL 701-13-2	Search Coil Magnetometer and
	701-15	Passive Plasma Sounder
16	AFGL 701-14	Langmuir Probe
17	ONR-307-3-1,-2,-3	Spectrometer for Electrons and Protons (SEP)
18	ONR-307-8-1,-2	Low Energy Ion Mass Spectrometer (IMS-LO-1,-2)
19	ONR-307-8-3	Medium Energy Ion Mass Spectrometer (IMS-HI)
20	ONR-604	Isotopes and Solar Flares
21	AFAPL-801	Gallium Arsenide Solar Cell Panel

Measurements from the above instruments provide data at various rates, typically one or more times per minor frame. These constitute the bulk of the telemetry data, and are received in packed format on agency tapes.

8.1.2 Objective and Scope of Data Reduction Task

The objective of the Data Reduction task is the reduction of raw CRRES telemetry data into a form from which engineering and geophysical units are easily derivable. The resultant processed data are placed in the Time History Data Base (THDB) which is used as an intermediate data base from which the Product Associated Data Base (PADB) may draw, and provide support to CRRES experimenters within AFGL and other investigating agencies.

Figure 8.1 illustrates the general data reduction flow needed for the development of the Time History Data Base. In essence, the CRRES Time History Data Base is produced from the raw data contained on the AFGL CRRES agency tapes. Section 8.2 describes the flow to develop the THDB. An effort has been made to keep this data base to a minimum size while retaining all the essential data that are needed to satisfy approved engineering and environmental studies.

8.1.3 Objective and Scope of Data Analysis Task

The objective of the Product Associated Data Base is to provide CRRES experimenters and researchers with the user friendly data bases that are needed to support approved research efforts.

Figure 8.2 illustrates the general data analysis flow needed for the development of the Product Associated Data Base. The CRRES Product Associated Data Base is extracted from the CRRES Time History Data Base with model and geophysical support data added as necessary. Section 8.4 describes the flow to develop the Product Associated Data Base. An effort has been made to place into the data base only the parameters that will be pertinent to project approved analyses.

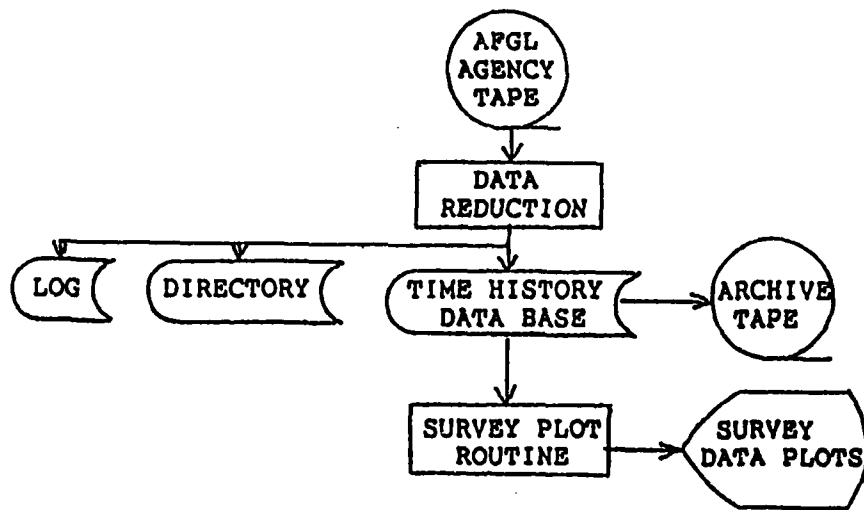


Figure 8.1

DATA REDUCTION (TIME HISTORY DATA BASE) FLOW CHART

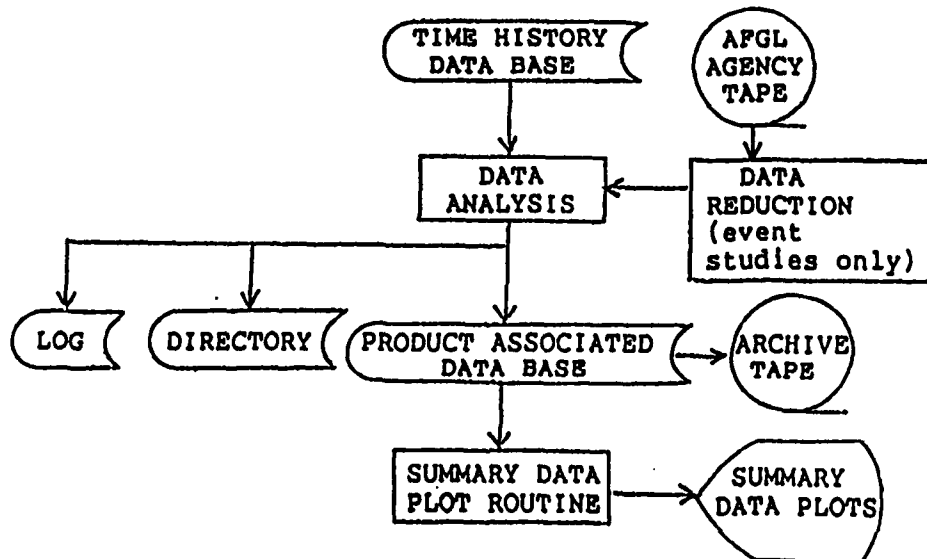


Figure 8.2

DATA ANALYSIS (PRODUCT ASSOCIATED DATA BASE) FLOW CHART

8.2 TIME HISTORY DATA BASE (THDB)

8.2.1 Design Concepts and Constraints

The THDB has been designed to provide high rate data for detailed studies of individual orbits as well as providing the full set of parameters necessary for all studies to be performed through use of the PADB. Since the THDB feeds into the creation of the PADB, it is essential that all PADB parameters be computable from the THDB structure. Details of this file design will be found in Reference 3. Figure 8.3 shows the data reduction developmental flow for the THDB.

One of the prime considerations in formulating the THDB structure was that of not having to recreate files or orbits within the structure due to predictable factors which frequently occur on spacecraft missions. The prime science words would be stored as 32 bit decompressed counts in a logical ordering sequence, such as increasing frequency (or energy). When no decompression algorithms are required, the data are stored as four 8 bit bytes per 32 bit integer.

Converting of the counts to science parameters such as flux will be accomplished through the use of the calibration files. One such file will exist for each experiment. It will consist of a header record identifying the experiment, the date that the file became effective, and the version number. The calibration factors will, in general, be biased multiplicative factors necessary to convert the counts to science parameters.

8.2.2 Design Structure and Format

The Time History Data Base will consist of on-line experiment files containing structured data; ancillary files such as header, ephemeris, magnetic field and attitude coefficients; and log and directory files.

CRRES
DATA REDUCTION (TIME HISTORY DATA BASE) FLOW CHART

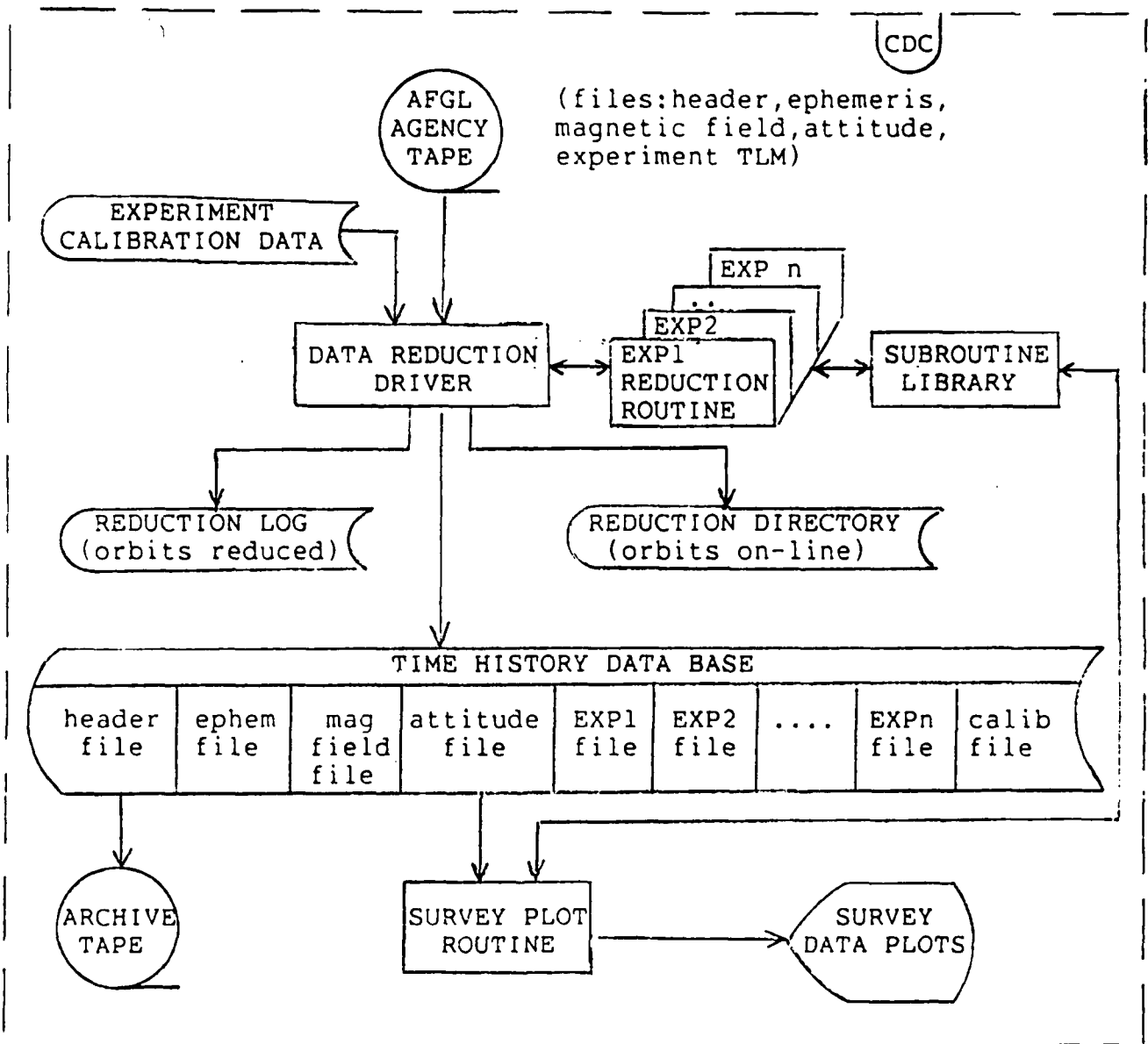


Figure 8.3: Data Reduction (Time History Data Base) Flow Chart

8.2.2.1 Header, Ephemeris, Magnetic Field and Attitude Files

The Header File will contain all the necessary information to identify the orbit of data. (All words 32 bit positive biased integers)

The Ephemeris File will contain orbital, astronomical, and model magnetic field parameter information. These records will be provided at uniform intervals. Longer intervals between records will be acceptable at greater geocentric distances.

The Magnetic Field File will contain parameters calculated from outputs of the science magnetometer.

The Attitude File will contain the output of the attitude determination run, and will consist of sets of time tagged parameters which are coefficients of fits of attitude over various time spans.

8.2.2.2 Calibration Files

The calibration files, one for each experiment, contain the coefficients necessary for computing the science parameters. These files are structured with a header record followed by one or more data records. All words are in 32 bit integer form. The succeeding record, or records, contain information necessary to convert instrument counts to scientific units such as differential flux as well as instrument parameters, e.g. channel energies (for particle detectors).

8.2.2.3 Experiment Files

THDB files will be created for all required experiments on an orbit by orbit basis. All files are of 32 bit positive integer construction. Each file consists of a header record followed by a series of data records. The header record identifies the experiment and contains information unique to the orbit.

The THDB data records consist of a time word (in UT milliseconds) followed by a series of 32 bit words containing the science data. Delta time corrections must be made to compute the actual time associated with each data record.

Telemetry parameters stored in each frame are broken into two categories; prime science data and housekeeping or non-prime data. The prime science words are, in general, stored in decompressed form in the 32 bit integer construction. Word order is consistent with each experiment in the sense that counts values from particle detectors are stored in order of increasing energy, mass spectrometer data is stored in order of increasing mass; and frequency measurements are stored in order of increasing frequency. Points missing due to telemetry dropout will be 1's filled.

8.3 ENGINEERING AND ENVIRONMENTAL STUDIES

Three engineering experiments are being flown on CRRES to measure the adverse effects created by the high energy particle environment on microelectronic devices and sensitive materials . The experiments are the Microelectronics Package (MEP), the Internal Discharge Monitor (IDM), and the Gallium Arsenide Solar Cell Panel (GASP). Components within these experiments will measure the occurrence frequency of single event upsets (SEUs) and total dose degradation in state-of-the-art microelectronic devices and sensitive materials. The occurrence frequency of arc discharges in circuit elements will also be measured. The results of these measurements will be related to the in-situ measurements of the high energy particle environment.

Eighteen instrument packages will measure the CRRES/SPACERAD environment. The data from these instruments will be used in three basic modes:

- 1) Analysis of the engineering experiments flight data.
- 2) Construction of static and quasi-static maps of environmental parameters, such as relativistic particle fluxes.
- 3) Event studies that identify and model dynamical processes in the radiation belts.

Details of these studies are incorporated in Reference 3, and are summarized here. Generally, the data that will be used to complete these studies will be processed from the Time History Data Base or from CRRES agency tape data (in the case of most event studies) to form the Product Associated Data Base (see Section 8.4).

8.3.1 Engineering Studies

8.3.1.1 Microelectronic Package Analysis (MEP)

8.3.1.1.1 Objectives

The MEP will monitor the operations of state-of-the-art silicon devices, VHSIC (Very High Speed Integrated Circuit) devices, and advanced material devices such as gallium arsenide (GaAs) random access memories (RAMs).

Data placed in the Product Associated Data Base for the Microelectronics Package will support engineering studies on the impact of the high energy particle environment on advanced technology, microelectronic devices.

8.3.1.1.2 Products

- Verification of model predictions.
- Evaluations of 3-dimensional computer codes that predict doses inside spacecraft.
- Validation of existing device and SEU models.
- Summaries of the CRRES radiation environment.
- Comparison of device parameters obtained in modeling and ground test programs.
- Correlation of proton upset rates with pitch angle.
- Summaries of upset rates in B,L coordinates in geographical coordinates.
- Summary of proton upset predictions for CRRES using the Monte Carlo approach.

8.3.1.1.3 Data Requirements

- MEP in-flight data:

MEP in-flight data will be processed within AFGL for distribution to selected MEP working group participants.

- Environmental data:

In addition to the specific environmental data available from the instruments listed below, the MEP working group will have available for use the entire data base for the Statistical Radiation Belt Model and all event mode data bases.

<u>Parameter</u>	<u>Experiment</u>
IONS	ISF (25-570 MeV/Nuc)
	HIT (0.1-15 MeV/Nuc)
	MICS (30-300 keV/Q)
PROTONS	REL PRO (>320, >440 MeV) (Cherenkov counter)
	PRO SW (20-40 and 40-80 MeV)
	PROTEL (1-100 MeV)
ELECTRONS	REL PRO (>35, >80 MeV) (Electron Detector)
	HEEF (1-10 MeV)
	MEES (40 keV-2 MeV)
DOSE	SPACE DOSIMETER
	MOS DOSIMETER
FIELDS	LANGMUIR PROBE

Data from the Static Radiation Belt Model Data Base and from the Event Mode Data Base will also be provided as required.

8.3.1.2 Internal Discharge Monitor (IDM) Data Analysis

8.3.1.2.1 Objectives

The Internal Discharge Monitor (IDM) experiment is designed to determine the existence and characteristics of internal discharge phenomena under the CRRES orbital conditions.

Data placed in the product associated data base for the Internal Discharge Monitor will support engineering studies on the impact of arc discharges due to deep dielectric charging on semiconductor materials typically used in or on operational spacecraft.

8.3.1.2.2 Products

- Reports relating the occurrence of IDM discharges to the high energy electron environment
- Characterization of ground test electron beams that simulate space environments
- Validation of electron-caused electromagnetic pulse (ECEMP) predictive models

8.3.1.2.3 Data Requirements

Specific:

<u>Parameter</u>	<u>Experiment</u>
ELECTRONS	MEES (46 keV-2.2 MeV) HEEF (1-10 MeV)
PROTONS	EPAS (.04-2 MeV) PROTEL (1-100 MeV)
DOSE	AFGL-701-3 AFGL-701-2

8.3.1.3 Gallium Arsenide Solar Panel (GASP) Data Analysis

The objectives of this experiment are:

- Evaluations of current radiation damage models.
- Correlations of cell damage with CRRES radiation measurements.
- Improved radiation damage models.

8.3.2 Environmental Studies

8.3.2.1 Statistical Radiation Belt Model

8.3.2.1.1 Objectives

Radiation belt models are used to predict the extent to which the high energy particle populations in space present hazards to electronic devices on spacecraft. Existing static radiation belt models are used to predict the total dose impinging on electronic devices that are placed in space.

Updated models should address not only the principal components of the belts, i.e., electrons and protons, but also of minor constituents of the belts and of cosmic ray LET (linear energy transfer or stopping power) spectra as a function of orbital position and inclination.

The product data base for the Statistical Radiation Belt Model will support the accurate specification of average properties of the radiation environment. The use of the improved instrumentation on CRRES with increased instrument sensitivity, improved time, mass, and energy resolution, and cross-calibration of particle detectors, will:

- Extend energy ranges for electrons (20 keV-~80 MeV) and ions (40 keV-600 MeV),
- Include major ion species (O+, He+, He++),
- Model pitch angle distributions, and
- Extend temporal applicability.

8.3.2.1.2 Products

- SPACERAD Static Radiation Belt Models for electrons, protons, ions (major species), and measured dose.
- Evaluation of magnetic field models (Delta B Model).
- Quasi-static Data Bases, Analysis.
- Static Radiation Belt Data Base for Update of NASA Models.

8.3.2.1.3 Data Requirements

Particle distribution (spectra) data (includes electrons and ions [with emphasis on the four mass groups: H+, He+, He++, and O+]) will be organized by orbit, L-shell bin, and pitch angle bin. L-shell bins will be created at 1/20th intervals (approximately 240 bins (total) for ascending and descending portions of orbit). Pitch angle bins (13 bins) will be created at 15 degree intervals in the range 7.5 to 172.5 degrees, and 7.5 degree intervals between 0 and 7.5 degrees and 172.5 and 180 degrees.

Dose data will be organized by orbit, and L-shell bin. Geophysical support data will include data on solar flares and other Interplanetary Magnetic Field data. For individual events (storms), data from the Time History Data Base will be accessed.

Specific:

<u>Parameter</u>	<u>Experiment</u>
ELECTRONS	REL PRO (>35, >80 MeV) HEES (1-10 MeV) MEES (40 keV-2MeV) EPAS (20-250 MeV) ONR-307-3 is Backup Instrument (20 keV-5 MeV)
PROTONS	REL PRO (>320, >440 MeV) PROTEL (1-100 MeV) PRO SW (20-80 MeV) EPAS (40 keV-2MeV) ONR-307-3 is Backup Instrument (20 keV-5 MeV)
IONS	HIT (0.1-15 MeV/Nuc) MICS (30-400 keV/Q) ONR-307-8 is Backup Instrument (20-8000 keV-Amu/Q ²)
DOSE	SPACE DOSIMETER (701-2)
FIELDS	FLUXGATE MAGNETOMETER

Averaged data points will be tagged with universal time, L values, magnetic latitude, longitude, magnetic local time, standard deviation in the average, number of points in the average.

8.3.2.1.4 Approach

For each type of particle (electrons, ions, dose) in-flight calibration of the instruments listed above will be used to determine a single set of energy channels to specify the particle spectra over the required total energy range. Methods for incorporating the integral channels at the extreme high energies will be devised and evaluated. From the data base containing data at instrument resolution rate, an average data base will be constructed. It will contain count averages (corrected, if necessary, for instrument degradation in flight) of the selected instrument channels. The averages will be taken over fixed altitude and pitch angle intervals (1/20 RE and 15 degrees). The averages will be tagged with universal time, L values from various magnetic field models, magnetic latitude and longitude, magnetic local time, standard deviation of the average, number of points in average. A similar average data base will be constructed for the measured components of the magnetic field. In addition, values of model fields will be part of the magnetic field average data base. The two averaged data bases will be merged to form the Static Model Data Base.

Each averaged data point in the Static Model Data Base will be a single data point for the Static Radiation Belt Model, and will be further averaged as such. Nevertheless, sufficient information will be carried with each point so that averages over all points at instrument resolution can be calculated. New quantities will be defined and calculated for each point, such as the magnetic moment, the second adiabatic invariant, etc.

A three-dimensional gridding system will be used as the model base. The three dimensions will be altitude, magnetic latitude, and either magnetic longitude or magnetic local time (in corrected geomagnetic coordinates) for science studies; and altitude, geographic latitude and longitude for engineering studies. The data will also be sorted by appropriate parameters that indicate the general condition of the magnetospheric magnetic field (ie., small, moderate, large deviations from a chosen model field). Additional parameters that order the radiation belt flux levels will also be sought.

Data will be accumulated for the lifetime of the satellite and/or instruments. Half orbit plots (or spectrograms) will be constructed of points in the Static Model Data Bases as a function of altitude. The pitch angle distributions will be modeled and the coefficients of the model entered into the data base.

To support the engineering experiments, three-dimensional averaged maps of the omnidirectional flux will be constructed monthly in geographic coordinates. Methods of reducing the number of needed dimensions will be checked against the full three dimensional model.

To support science studies and to construct quasi-static radiation belt models, various methods of sorting the data will be devised that are more appropriate to the higher L-shell values where the magnetic field changes are large and asymmetric. For this modeling effort the directional fluxes will be used, by way of average pitch angle values.

8.3.2.2 Cosmic Ray Model and Flare Analysis

8.3.2.2.1 Objectives

An accurate model of the heavy ion radiation environment is required for analysis of the single-event upset data from the CRRES Microelectronics Package. This model will describe the qualitative features of the interplanetary heavy ion development. To produce accurate values of the heavy ion flux for a given time period (a quantitative description of the environment) measurements from the particle sensors aboard the CRRES satellite and data from other sources will be used to define values for time dependent parameters of the model.

8.3.2.2.2 Products

- Cosmic ray model (Quarterly normalization to Adams' model)
- Heavy ion flux data base.
- Reports/papers on flares.

8.3.2.2.3 Data Requirements

AFGL will provide data from the high energy sensor of PROTEL only. Other data will be obtained by researchers of this study through their own sources.

Specific:

<u>Parameter</u>	<u>Experiment</u>
IONS	HIT (AFGL-701-11B)
	ISF (ONR-604)
PROTONS	PROTEL-HI (AFGL-701-9)
	PS (AFGL-701-5B)
	RP (AFGL-701-5A)

8.3.2.2.4 Approach

The proposed model is an analytic description of the flux of each ion specie as a function of energy and time. It will include the two major sources of heavy ion flux in the interplanetary medium: galactic cosmic rays and ions from solar flares. The model will cover the energy range above 10 MeV/nucleon and will also include estimates for elements so low in abundance that they are not well measured.

The intensities of the heavy ion species at energies of interest to the single-event upset problem are so low that a typical sensor must integrate over a long time period (many days) to determine accurate values of the flux intensity for the ions heavier than helium. As a result, the most accurate and effective way to merge the CRRES particle sensor data sets with the environment model will be to use the data to define key parameters of the model. For the galactic cosmic ray components these key parameters will describe the level of solar modulation and the presence of any "anomalous" components. For the solar flare component these key parameters will define the occurrence of the flare, its peak flux, total fluence, composition characteristics, and the form of its energy spectrum.

The sensor data analysis will be focused on the following five element groups: H, He, C-N-O, Ne-Si, and near Fe. The data reduction efforts will produce fluxes for each of these groups in broad energy intervals for each of the sensors.

Time scales for significant changes in the intensities of the galactic cosmic ray flux are long, typically several months or more. Thus a model of the galactic cosmic ray component can be kept accurate and up to date with infrequent changes to its parameters. Similarly, even at maximum solar flare activity, only a few flares per year will be large enough to produce significant increases in heavy ion intensity over the galactic cosmic ray flux levels at high energies.

8.3.2.3 Hot Plasma, Field and Wave Maps

8.3.2.3.1 Objectives

Although the low energy particle environment (here referred to as "hot plasma"), the cold plasma environment, and the magnetospheric electric and magnetic fields (both steady and oscillatory) are not, of their own accord, a hazard to the reliable operation of spacecraft, they play a major role in the acceleration, transport and re-distribution with subsequent loss of radiation belt particles. The dynamics of these interactions must be understood before accurate, short-term predictions of radiation belt changes can be realized.

For the most part the low energy particle populations and the electromagnetic fields contain large quantities of energy that is broadly distributed spatially. Both coherent and stochastic processes between high energy particles and the distributed energy densities of the hot plasma, field and waves are means of energy transfer. No model of large-scale magnetospheric magnetic field variations exist that is sufficiently accurate to allow identification of an exterior source from a local adiabatic increase. Further, while the exchange of energy and momentum from wave to high energy particle populations is known to diffuse particles in pitch angle space (leading to loss) and in physical space (leading to translation) both morphology and source populations for generating the appropriate wave modes are only beginning to be specified, and are found to be very complex.

The principal mechanism for studying radiation belt dynamical processes has, in the past, been the case or event study. It is anticipated that such studies will provide the major input

to a SPACERAD dynamic model of the radiation belts. From previous and from new event studies, those processes of wave-particle energy exchange which play key roles in radiation belt dynamics will be identified and modeled. The passive plasma sounder, search coil magnetometer, and the Langmuir probe experiments will provide more and better quality data on the electron number density and temperature, and the plasma wave environment in the radiation belts than has been available before.

8.3.2.3.2 Products

The high energy particle statistical models are based on a separation of data by altitude (which can be converted into L-shell) and magnetic field magnitude. These parameters best order the high energy data because they are directly related to the magnetic field configuration which is the primary term in equations describing high energy particle motion.

The basic unit for averaging or defining derived quantities for the hot plasma, field and wave data will be the satellite spin period (~.5min). Quantities calculated for each spin for the statistical studies will include moments of the distribution functions for the low energy electrons and ions (including values of the three components of the magnetic and electric fields; average values of the wave power over specified frequency bands; average values of the plasma density.

8.3.2.3.3 Data Requirements

General:

CRRES Time History Data Base and summary data.

Bounding data requirements:

- L-shell data in range 1.1 to 7.0 collected over 1/2 orbit period.
- Magnetic latitude in range -25 to +25 degrees collected over 1 year period at all L.
- Geographic latitude in range -15 to +15 degrees collected over 1 year period at all L.
- Geographic longitude collected over a TBD period.
- Local time (LT) collected over 1 year period for all L.

Binning requirements:

Binning data in a fixed set of bins (equal statistical weight per L-shell bin since satellite spends roughly equal amounts of time in each L-shell bin)

L Boundary	No. L-shell Bins	No. LT bins/LT hour	No. Mag Lat bins /LT hour	Total bins/ LT hour	Total bins/ 24 hours
6-7	5	10	6	300	7200
5-6	5	5	6	150	3600
4-5	5	5	6	150	3600
3-4	4	2	6	48	1152
2-3	2	1.5	3	18	432
1-2	2	1.0	3	6	144
	--	----	--	---	-----
	23	24.5	30	672	16128

8.3.2.4 Radiation Belt Dynamics (High Energy Particles)

8.3.2.4.1 Objectives

Once an event, or class of events, has been identified by review of the statistical data study in paragraph 6.3.4 above, the event mode of data collection will be initiated in order to capture high-resolution data needed for in depth studies. Events could include magnetic storms, storm sudden commencements, sudden impulses, magnetopause crossings, boundary layer crossings, substorms, ionospheric and plasma sheet injections (e.g., "zipper" events, plasma clouds), intense ULF, VLF wave activity, and long periods of magnetic quiet.

8.3.2.4.2 Products

Storm level radiation belt model

8.3.2.5 Radiation Belt Dynamics (Plasma, Waves and Fields)

8.3.2.5.1 Objectives

Once an event, or class of events, has been identified by review of the statistical data study in paragraph 6.3.4 above, the event mode of data collection will be initiated in order to capture high-resolution data needed for in depth studies. Events could include magnetic storms, storm sudden commencements, sudden impulses, magnetopause crossings, boundary layer crossings, substorms, ionospheric and plasma sheet injections (e.g., "zipper" events, plasma clouds), intense ULF, VLF wave activity, and long periods of magnetic quiet.

8.3.2.5.2 Products

Studies addressing improved phenomenological insights into ring currents, injected plasma clouds, zipper events, stably trapped plasmas, plasmopause, plasmatrough, plasmasphere, plasmashet boundary layer, pancake distributions at equator, Alfvén layers, etc.

8.3.2.6 Plasma Wave Analysis

8.3.2.6.1 Objectives

The primary purpose of this investigation is to measure the plasma wave environment in the earth's radiation belts, and wave-particle interaction processes which exchange energy and/or momentum between the waves and the particles. Evaluation of the plasma wave data will allow the characterization of the plasma waves identifying the wave modes and the measurement of the electron number density. The electron number density is used for evaluating wave dispersion relations and determining the resonant energies in the various wave-particle interactions. A comparison of the plasma wave measurements with the plasma and energetic particle measurements will be used to study the various wave-particle interaction processes.

8.4 PRODUCT ASSOCIATED DATA BASE (PADB)

A Product Associated Data Base (PADB) represents the total collection of data needed to uniquely support the engineering and environmental studies described in Section 8.3. Each study produces one or more products that satisfy specific needs as intermediate or final results of the effort.

The Product Associated Data Base (PADB) for a particular study may be a subset of, compacted form of, or binned form of of the Time History Data Base, or high resolution data derived from AFGL CRRES agency tapes, or specially processed data that blends data from several sources.

8.4.1 Design Concepts and Constraints

Only portions of the CRRES telemetry data and/or CRRES Time History Data Base are required for various project-approved engineering and environmental studies. A tremendous amount of CRRES data is available for inclusion in the Product Associated Data Base. On-line mass storage could easily be saturated without judicious planning for the data bases for the individual products.

Figure 8.4 illustrates the developmental flow for the Product Associated Data Base (PADB). Although the primary input to the PADB is the Time History Data Base (THDB), other sources may also be used including Geophysical Support Data (GSD), data derived from model calculations, and AFGL CRRES agency tapes. The generated PADB is resident in on-line storage, and archived on magnetic tape.

8.4.2 Design Structure and Format

The PADB will be a cost-effective, unique, user-friendly data base that may be used with little or no pre-data processing.

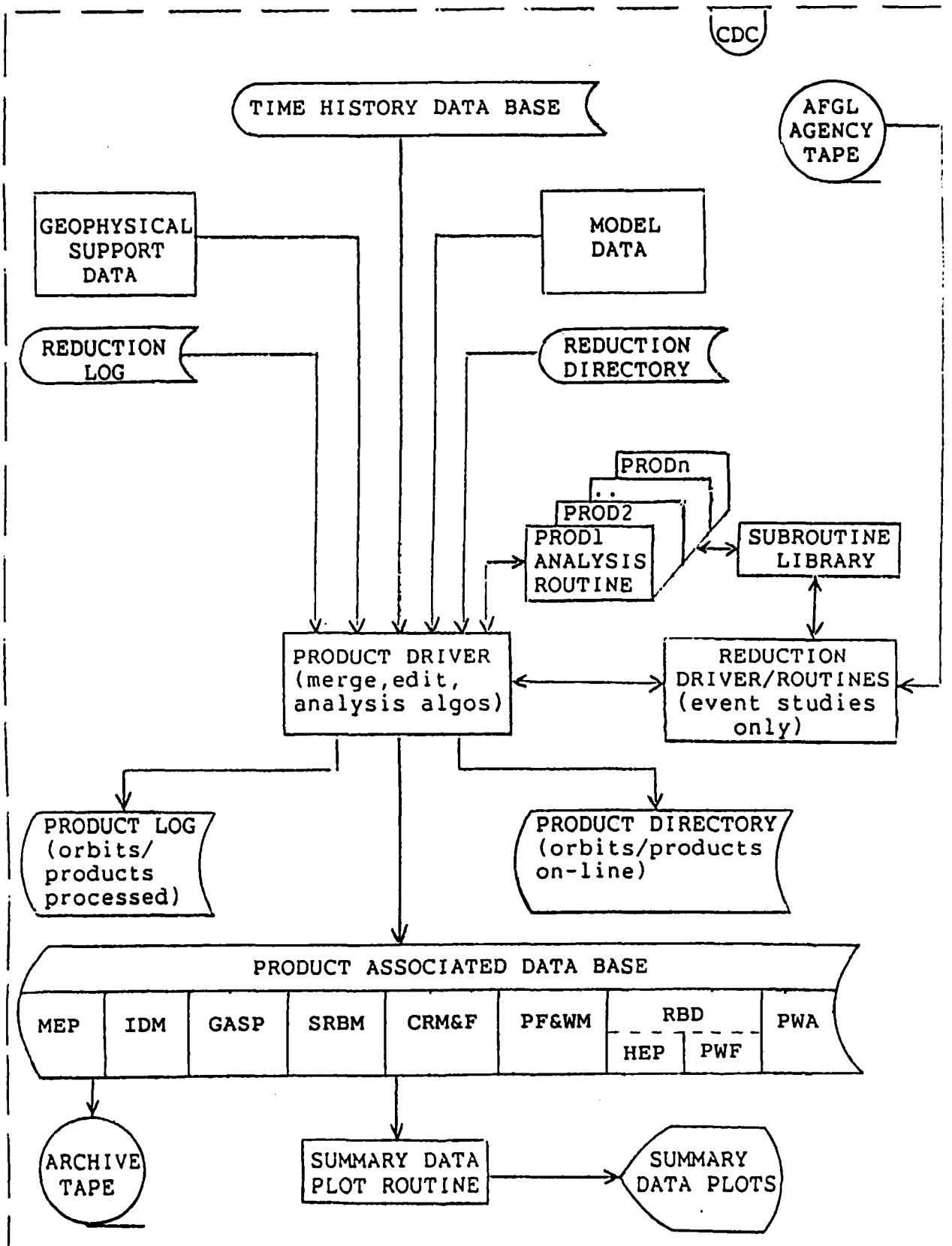


Figure 8.4: Data Analysis (Product Associated Data Base) Flow Chart

8.4.2.1 Directory and Log Files

There will be two index files associated with the Product Associated Data Base:

The Product Log will contain an index as to which CRRES orbital data have been processed into the Product Associated Data Base.

The Product Directory will contain an index as to which CRRES orbital data have been processed into the Product Associated Data Base, and that are currently resident on on-line mass storage.

8.4.2.2 Study Files

Study files with the PADB will support the unique data requirements and data structures of the CRRES engineering and environmental studies.

8.4.2.3 Models and Geophysical Support Data

8.4.2.3.1 Models

Magnetic Field Models

Olson-Pfitzer Dynamic Model

Tsyganenko-Usmanov Model

Mead/Mead-Williams Models

Other Models

8.4.2.3.2 Geophysical Support Data (GSD)

Interplanetary Magnetic Field

Solar Wind parameters

Geomagnetic activity index

DST index

Other parameters

References

- 1) "CRRES/SPACERAD Experiment Descriptions", AFGL-TR-85-0017, January 1985. Editors: M.S. Gussenhoven, E.G. Mullen, R.C. Sagalyn. (ADA160504)
- 2) "CRRES Data Management Plan - Data Processing Task", Private communication; R. McInerney, R. Raistrick, E. Robinson, A. Griffin; June 1986.
- 3) "CRRES Data Management Plan - Data Analysis Task", Private communication; June 1986.

9.0 Structure of Atmospheric Density, Temperature and Winds from Rocket Sphere Experiments

A high resolution processing system was developed and utilized to analyze rocket sphere accelerometer signals for determining atmospheric density and wind profiles. This operational system provided file display, editing and smoothing procedures, as well as techniques for control and updating as the experiment analyses progressed. Functions performed during the analyses included:

- 1) Digitized telemetry data acquisition and splicing
- 2) Calibration of sensors using resonance frequency signals at uncaging
- 3) Evaluation and incorporation of the range trajectory
- 4) Correlation of sensor signals for mutual consistency
- 5) Progressive collection of intermediate results in one resource file per experiment
- 6) Evaluation against results of concurrent Robin sphere and chemical release experiments

The processing analysis takes place in a despun triaxial system defined by the plane of the trajectory. Wherever possible, results were compared with lower altitude density and wind values obtained from Robin sphere measurements, or with upper altitude winds derived from chemical release measurements⁽¹⁻⁴⁾.

The basic sensed acceleration equations in the coordinate system of the sphere are

$$XYZ_{acc} = [(\vec{V}_t + \vec{V}_w)] B(\beta) A(\alpha) [V_r \rho C_d \frac{Area}{2m}]$$

where

subscripts t and w refer to the trajectory and wind respectively, $A(\alpha)$, $B(\beta)$ are velocity transformations corresponding to sphere axis tilt in-, across- the trajectory plane.

Analysis was typically conducted at 1/4 km intervals, but higher resolution corresponding to about half a sphere spin cycle (1/12 sec) is feasible, particularly in the higher portion of the trajectory where the vertical velocity is small. Even near the lowest trajectory altitudes evaluated (60 km), the maximum vertical velocities were ≈ 1.5 km/sec, so that a 1/8 km resolution should always be possible.

Problems that were crucial for accurate analysis of the sphere data were the sphere orientation and spin phase history. Iterative methods were used to solve for sphere tilt that gave self-consistent XY- and Z-sensor signals. The spin phase adjustment procedure in particular consisted in solving for spin rate correction, spin damping, and low altitude spin-down, so that upleg-downleg cross-wind solutions matched. The wind solving procedure took advantage of the fact that the trajectory velocity, and therefore the drag factor R , is essentially constant at the same upleg-downleg altitude. Whenever upleg-downleg data were present this resulted in reliable wind profiles, independent of the density solution. High quality density profiles were then achievable at the accuracy of the calibrations.

The rocket sphere processing system incorporates a number of interactive and graphical techniques, allowing for progressive smoothing and merging of intermediate results.⁽⁵⁾ An error analysis program which parallels the profile calculation algorithms is also implemented to allow for estimating the effects of uncertainties in parameters such as axis tilt or calibrations.

Complete data processing analyses were performed for a number of sphere flights, specifically AC10, AC12, AC13, AC14, AC15, AC16, AC17, AC08, and AC18. Initial parameters as well as parameters determined during the intermediate analysis are presented in Section 9.5 for all the above flights.

9.1 Solution Procedures for Analyses of Falling Sphere Data

In terms of the atmosphere and winds at the time of the experiment, sensed X, Y and Z accelerations are given by

$$XYZ_{acc} = \left[\begin{matrix} \vec{V}_t \\ \vec{V}_w \end{matrix} \right] B(\beta) A(\alpha) \left[V_r \rho C_d \frac{Area}{2m} \right]$$

where subscripts t and w refer to the trajectory and wind respectively; $A(\alpha)$, $B(\beta)$ are velocity transformations corresponding to sphere axis tilt in-, across- the trajectory plane.

1) Sphere spin rate and despun phase are determined initially so as to give matching upleg and downleg cross-winds. This procedure is insensitive to sensor calibrations because any overall gain factor simply scales all cross-winds equally. The spin axis tilt α in the plane of the trajectory affects estimates of the local in-track wind and thus the density, and is therefore determined only indirectly during spin rate and phase optimization.

2) Determination of the axis tilt α is possible using the Z-axis and XY-axis accelerometer data in conjunction. Basic equations for obtaining α are given below, but in practice this has been a difficult undertaking because of calibration uncertainties and large time constants in Z-sensor readings. Other methods for resolving the sphere tilt (and spin-down at low altitudes) involved selecting these parameters so as to match results from concurrent Robin sphere experiments.

3) $R = V_r \rho C_d Area/2m$ and the in-track wind V_{xw} are solved for in various ways, depending on the combination of upleg, downleg, and Z-axis sensor data that are available. Advantage is taken of the fact that upleg and downleg trajectory and wind velocities, and thus the relative velocity V_R with winds included, is equal at like upleg and downleg altitudes. Once the horizontal wind field and V_R are fixed, R gives ρC_D .

4) Integration of an assumed density (ρ) profile under hydrostatic equilibrium gives the kinetic temperature (T_k) profile which in turn gives C_D , and hence a corrected ρ profile. One or two such iterations produce the ρ and T_k profiles. This procedure is also described below.

9.1.1 Solution of Sphere Orientation, Spin Rate and Phase

Mutually corrected values for sphere upleg phase Q_U and downleg phase Q_D as a function of time and/or altitude are obtained by requiring that the upleg and downleg cross-wind solutions match at like altitudes. We start with the zero-adjusted upleg-downleg accelerations and trajectory file XYAPUD which contains values which have been resolved at equally spaced 1/4 km altitude increments.

The sensors in the equatorial plane of the spinning sphere give the modulated acceleration signal with amplitude EACU on upleg, and amplitude EACD on downleg. This file implicitly provides the relative despun phase for the nominal fixed spin rate Ω , and initial reference phase θ . For any arbitrary spin rate ω , reference phase ϕ , and out-of-plane tilt β , the transverse (Y) wind can be solved:

$$\begin{aligned} \text{Let } \theta' &= \theta - \epsilon T + \phi \\ \text{where } \epsilon &= (\omega - \Omega) \end{aligned}$$

Then,

$$V_{Yw} = \frac{1}{R(h)} \cdot \text{EACC} \cdot \frac{\sin \theta'}{\cos \beta} + V_z \cdot \tan \beta$$

$$\text{where } R(h) = V_r \rho C_d \frac{\text{Area}}{2m}$$

Any change in the cross-wind solution is then given by

$$\Delta V_{Yw}(h) = \frac{1}{R(h) \cdot \cos \beta} [\text{EACU} \cdot \sin(\theta_U - \epsilon T_U + \phi) - \text{EACD} \cdot \sin(\theta_D - \epsilon T_D + \phi) + (V_{ZU} - V_{ZD}) \tan \beta]$$

where U and D refer to upleg and downleg respectively.

Define $\theta_U' = \theta_U - \epsilon T_U + \phi$
 and $\theta_D' = \theta_D - \epsilon T_D + \phi$
 Then,

$$\frac{\delta \Delta V_{YW}}{\delta \epsilon} = \frac{1}{R(h) \cdot \cos \beta} [-T_U \cdot EACU \cdot \cos \theta_U' + T_D \cdot EACD \cdot \cos \theta_D']$$

$$\frac{\delta \Delta V_{YW}}{\delta \phi} = \frac{1}{R(h) \cdot \cos \beta} [EACU \cdot \cos \theta_U' - EACD \cdot \cos \theta_D']$$

$$\frac{\delta \Delta V_{YW}}{\delta \beta} = \frac{1}{R(h) \cdot \cos \beta} [EACU \cdot \sin \theta_U' - EACD \cdot \sin \theta_D' + \frac{(V_{ZU} - V_{ZD})}{\cos \beta}]$$

In order to match upleg-downleg cross-winds, ϵ , ϕ and β are iteratively adjusted to minimize the squared sum of the residuals ΔV_{YW} . In practice it is extremely difficult to deduce any sphere axis tilt β across the trajectory plane, because its effect is similar to that of a small continuous drift in the spin rate. β is therefore assumed to be zero.

The range of altitudes used for the data spans a few kilometers below apogee at the upper end, to a few kilometers above sphere release on upleg at the lower end. This range is usually 150 to 85 km. Below 85 km on downleg there is a significant spin-down of the sphere, and a model expression $B \cdot (A-h)^2$ is added for phase correction, where A and B are coefficients of this model.

In addition to the vernier offset correction ϵ in the nominal spin rate Ω , a small but continuous deceleration in the spin rate can occur due to internal damping. This gives rise to a parabolic despun phase effect, such as is clearly evident for AC13, and a constant spin rate drift term was therefore included.

Note that the cross-wind solution V_{YW} obtained here is not final because the axis tilt α and consequently the density solutions are not complete at this stage. An update to V_{YW} is made as part of the subsequent analysis.

9.1.2 Solution of ρC_D and Wind based on Acceleration and Trajectory Data

The amplitude of the equatorially sensed accelerations, EACU on upleg and EACD on downleg, are combined with the corrected upleg phase Q_U and downleg phase Q_D to give the in-track acceleration components in the despun sphere x', y', z' reference frame

$$XACU = EACU \cos Q_U, \quad XACD = EACD \cos Q_D$$

The Z-axis and nutation sensor signals similarly provide the downleg sphere axis acceleration component ZACD. Depending upon the data that are available, the appropriate equations apply at the same altitude upleg and downleg.

9.1.2.1 Solution of α , ρC_D and Winds using all sensor data

If XACU, XACD, and ZACD are available, sphere axis tilt α , ρC_D , V_{XW} , and V_{YW} can all be solved simultaneously. At each altitude upleg and downleg, V_{XT} , V_{XW} and $|V_{ZT}|$ are taken to be equal.

$$\text{Defining } V_H = V_{XT} + V_{XW}, \quad V_Z = |V_{ZT}|$$

$$\text{the relative velocity } \vec{V}_R = |(\vec{V}_t + \vec{V}_w)|$$

is also equal at each altitude upleg and downleg.

The basic equations can be written as

$$XACU = \frac{AV_R}{2m} \rho C_D (V_H \cos \alpha - V_Z \sin \alpha) \quad (1)$$

$$XACD = \frac{AV_R}{2m} \rho C_D (V_H \cos \alpha + V_Z \sin \alpha) \quad (2)$$

$$ZACD = \frac{AV_R}{2m} \rho C_D (-V_H \sin \alpha + V_Z \cos \alpha) \quad (3)$$

Solving:

$$XACD \cos 2\alpha - XACU = ZACD \sin 2\alpha \quad (4)$$

$$\text{i.e. } \cos 2\alpha = \frac{XACD \cdot XACU + ZACD \sqrt{ZACD^2 + XACD^2 - XACU^2}}{(ZACD^2 + XACD^2)} \quad (5)$$

$$2 R V_z \sin \alpha = XACD - XACU \quad (6)$$

$$2 R V_H \cos \alpha = XACD + XACU \quad (7)$$

We thus get in order: α

$$\rho C_D = R \cdot \frac{2m}{AV_R}$$

$$\text{and } V_{xw} = V_H - V_{xt}$$

9.1.2.2 Solution of ρC_D and Winds when XACU is unavailable

From equations (2) and (3):

$$XACD \cos \alpha - ZACD \sin \alpha = R V_H \quad (8)$$

$$XACD \sin \alpha + ZACD \cos \alpha = R V_z \quad (9)$$

$$\text{Define } \tan \gamma = \frac{XACD}{ZACD} \quad \text{and} \quad \tan \beta = \frac{V_H}{V_z}$$

Divide (8) by (9), leading to the relationship

$$\alpha = \gamma - \beta$$

Two options are available, with γ always known:

a) If we take the in-track wind $V_{xw} = 0$,

$$\alpha = \gamma - \tan^{-1} \left(\frac{V_{xt}}{V_z} \right)$$

b) If we fix α at some value

$$V_{xw} = \tan(\gamma - \alpha) \cdot V_z - V_{xt}$$

In either case, next get R and thus ρC_D from (8) and (9).

9.1.2.3 Solution of ρC_D and Winds when ZACD is unavailable

$$\text{Define } R = \rho C_D V_R \frac{A}{2m}$$

where V_R = sphere velocity relative to atmosphere including winds.

$$\text{Let } V_H = V_{XT} + V_{XW}$$

$$\text{Then } V_R = \sqrt{V_H^2 + V_{YW}^2 + V_{ZT}^2}$$

In the x', y', z' coordinate system,

$$V_{SX} = V_H \cos\alpha - V_{ZT} \sin\alpha$$

$$V_{SY} = V_{YW}$$

$$V_{SZ} = V_H \sin\alpha + V_{ZT} \cos\alpha$$

and x', y', z' components of acceleration become

$$R V_{SX}, \quad R V_{SY}, \quad R V_{SZ}$$

$$\text{Taking } V_{SE} = \sqrt{V_{SX}^2 + V_{SY}^2}$$

$$\text{note that } EACC = R \cdot V_{SE}$$

When XY acceleration and phase are known from measurements

$$R V_{SY} = R V_{YW} = EACC \sin\phi$$

$$\text{Therefore, } V_{YW} = EACC \sin\phi / R$$

i.e. if ρC_D and V_R can be solved for, transverse wind is available.

Similarly,

$$V_{SX} = EACC \cos\phi / R$$

$$\text{so that } V_H = V_{SX} / \cos\alpha + V_{ZT} \tan\alpha$$

$$\text{and } V_{XW} = V_{SX} / \cos\alpha + V_{ZT} \tan\alpha - V_{XT}$$

i.e. if ρC_D and V_R (i.e. R) can be solved, and if α is also established, in-track wind is available.

Now, since upleg and downleg V_H , V_{YW} , V_{ZT} are nearly equal in magnitude, V_R and in fact $R = \rho C_D V_R A/2m$ are equal at any altitude, upleg or downleg.

Then, requiring that $V_{XWU} = V_{XWD}$,

defining $XACC = EACC \cos\phi$,

and in-track accel. ratio $AXR = XACU/XACD$

$$\begin{aligned} V_{XW} &= XACU/R\cos\alpha + V_{ZTU} \tan\alpha - V_{XTU} \\ &= XACD/R\cos\alpha + V_{ZTD} \tan\alpha - V_{XTD} \end{aligned}$$

gives

$$R = (XACD - XACU) / [(V_{ZTU} - V_{ZTD})\sin\alpha - (V_{XTU} - V_{XTD})\cos\alpha]$$

$$V_{XW} = \frac{(V_{ZTU} - AXR \cdot V_{ZTD})\tan\alpha - (V_{XTU} - AXR \cdot V_{XTD})}{(1 - AXR)}$$

$$V_{YW} = EACC \sin\phi / R$$

NOTE: The above expressions can be simplified if we take

$$\text{and } \begin{aligned} V_{ZT} &= |V_{ZTU}| = |V_{ZTD}| \\ V_{XT} &= V_{XTU} = V_{XTD} \end{aligned}$$

Then, $R = (XACD - XACU) / (2 V_{ZT} \sin\alpha)$

$$\text{and } V_{XW} = \frac{(1 + AXR) V_{ZT} \tan\alpha - V_{XT}}{1 - AXR}$$

Observe that in any case V_{XW} is determined from upleg and downleg measurements, independent of R or density.

At low altitudes where upleg data are unavailable, a reasonable initial estimate can be found for R by assuming that $V_{XWD} = 0$. V_{YWD} is then solved as before.

Thus, R is available; V_{XW} and V_{YW} gives V_R ; and finally

$$\rho C_D = R / (V_R \cdot A / 2m).$$

9.1.3 Temperature Profile from the Density Profile

Separation of ρ and C_D requires an iterative procedure since the drag coefficient is a function of temperature, and the temperature must be obtained from integration of the density profile⁽⁶⁾. Integration of an assumed density (ρ) profile under hydrostatic equilibrium gives the kinetic temperature (T_k) profile which in turn gives C_D , and hence a corrected ρ profile. One or two such iterations are sufficient.

$$T_M = T_{Mr} \frac{\rho_r}{\rho} - \frac{M_0}{\rho R} \int_{z_r}^z \rho g dz$$

$$T_M = \left(\frac{M_0}{M} \right) T_k$$

where

T_k -- kinetic temperature

T_M -- molecular-scale temperature

M -- mean molecular weight

M_0 -- value of M at sea-level = 28.694 Kg/kmol

R -- universal gas constant = 8314.3 N.m/(kmol. $^{\circ}$ K)

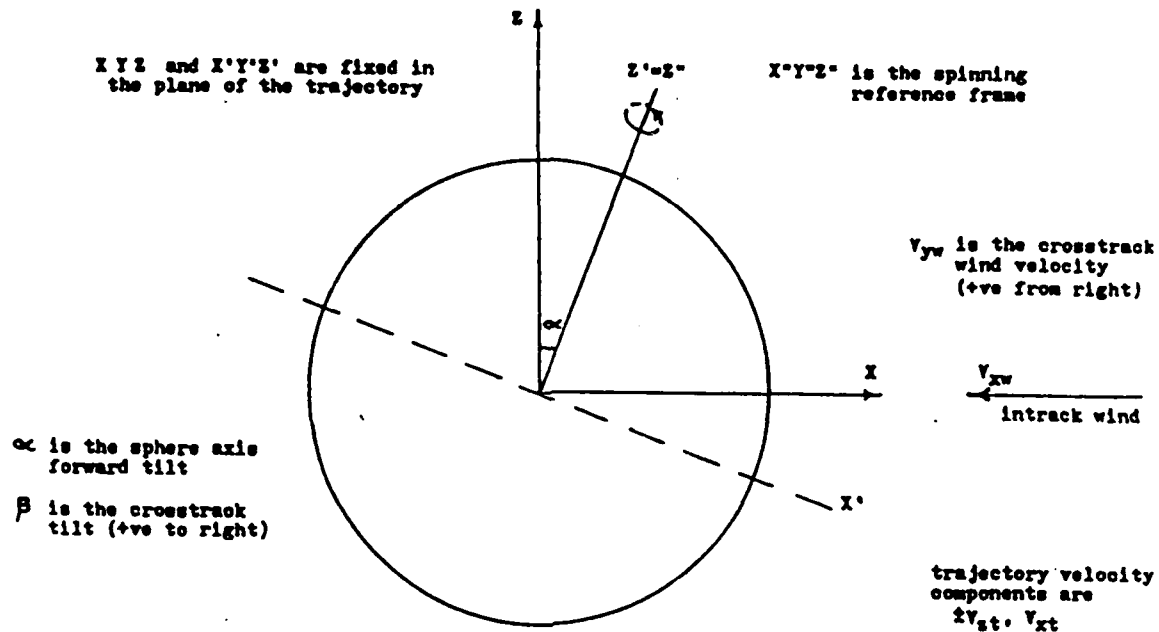
ρ -- atmospheric density Kg/m³

g -- acceleration due to gravity m/sec²

r -- subscript for reference altitude values

T_{Mr} at the reference altitude must be assumed, in order to initiate integration. Any error in this assumption rapidly diminishes by one scale height lower altitude.

9.2 Coordinate Systems and Glossary



Coordinate Systems for the Rocket Sphere

x'', y'', z'' sphere spinning reference frame; sensor X-, Y-, and Z- axis accelerations are measured in this coordinate system, with X- and Y- signals modulated at the spin frequency, and Z- and Nutation signals modulated at the precession frequency with any spin modulation removed by a notch filter:
 z - spin axis direction
 x, y - equatorial plane of the sphere

The above accelerations are converted to:

x', y', z' sphere spin axis reference frame; this is a non-spinning frame, referred to the launcher:
 z - spin axis direction; makes angle with launcher vertical given by axis tilt α
 x - intersection of sphere equatorial plane with trajectory plane
 y - axis completing the triad

The above accelerations are converted to:

x, y, z trajectory plane referred to launcher:
 x - horizontal, line of flight
 y - horizontal, transverse to line of flight
 z - vertical

Glossary

ω	rev/sec	nominal sphere spin rate, taken to be constant to obtain the initial demodulated data file Note: spin rate is typically 6 RPS and is counter-clockwise viewed from above
α	deg.	sphere spin axis tilt forward in trajectory plane, referenced to launch site
β	deg.	sphere spin axis tilt transverse to trajectory plane, (included in development of equations, but usually assumed to be zero since its effect is similar to a slightly different spin rate)
ρ	Kg/m ω	atmospheric density at a specified altitude
C_D		drag coefficient (ranges from 1 to 5 with altitude and velocity in these experiments)
m	Kg	sphere mass (typically 10 Kg)
A	m 2	drag cross-section presented by sphere($\approx .05$ m 2)
T_k	$^{\circ}$ K	atmospheric temperature at specified altitude (determined by integrating the density profile assuming hydrostatic equilibrium)
V_R	m/sec	velocity relative to atmosphere including winds as experienced by the sphere. Since upleg and downleg trajectory and wind velocities are nearly identical at like altitudes, V_R effectively has the same value upleg and downleg
R		= $\rho C_D V_R A/2m$ is a common factor at like upleg and downleg altitudes, since each term turns out to be unchanged upleg or downleg. This nearly exact equality is employed to simplify solution of the equations used.

Glossary (cont'd)

EACU	m/sec ²	equatorially sensed component of acceleration. Obtained as amplitude of spin modulated X or Y sensor signals (U = upleg)
Φ_u	deg.	raw solved phase (peak of sensed acceleration) of the modulated signal, obtained for the assumed constant nominal sphere spin rate ω . This phase is adjusted later so that reference zero is in the trajectory plane, after corrections for vernier changes in spin rate and spin deceleration
Q_u	deg.	final spin-corrected phase; direction relative to the trajectory that the sphere senses the net acceleration due to its motion and winds
EACD	m/sec ²	same as EACU, but downleg
Φ_d	deg.	same as Φ_u , but downleg
Q_d	deg.	same as Q_u , but downleg
XACU	m/sec ²	component of equatorial sensed acceleration in the trajectory plane (= EACU $\cos Q_u$)
XACD	m/sec ²	same as XACU, but downleg
ZACD	m/sec ²	component of acceleration sensed in the direction of the spin axis
AXR		acceleration ratio XACU/XACD for in-track component of equatorial acceleration; direct measure of in-track component of wind for a given trajectory velocity and spin-axis tilt α
V_{xt}	m/sec	horizontal trajectory velocity referred to launcher x,y,z coordinates (+ve forward). This velocity does not change appreciably during flight until re-entry around 50 km
V_{zt}	m/sec	vertical trajectory velocity referred to launcher (+ve upward). Because of the relatively low drag above 50 km, V_{zt} has nearly the same magnitude at any altitude upleg or downleg

Glossary (cont'd)

The analysis assumes a uniform horizontal wind field:

- V_{xw} m/sec component of wind in the direction of the trajectory (+ve head-on)
- V_H m/sec net relative head-on velocity of the atmosphere experienced by the sphere ($= V_{xt} + V_{xw}$)
- V_{yw} m/sec component of wind transverse to the direction of the trajectory (+ve from the right)
If sphere tilt β out of the trajectory plane is zero, then any transverse acceleration sensed by the sphere is due to cross-winds

$$V_{zw} = 0 \quad \text{so that} \quad V_R = (V_H^2 + V_{yw}^2 + V_{zt}^2)^{1/2}$$

In tilted non-spinning sphere axis (x', y', z') coordinates:

- V_{sx} m/sec head-on component of relative velocity of atmosphere, sensed at the sphere equator
- V_{sy} m/sec transverse component of relative velocity of atmosphere, sensed at the sphere equator
- V_{sz} m/sec component of relative velocity of atmosphere sensed along the spin axis
- V_{se} m/sec total component of relative velocity of atmosphere, sensed at the sphere equator
 $= (V_{sx}^2 + V_{sy}^2)^{1/2}$

Equations for relative velocities in above coordinate system:

$$\begin{aligned} V_{sx} &= V_H \cos\alpha - V_{zt} \sin\alpha \\ V_{sy} &= V_{yw} \\ V_{sz} &= V_H \sin\alpha + V_{zt} \cos\alpha \end{aligned}$$

Then, accelerations in the above coordinate system are:

$$RV_{sx}, RV_{sy}, RV_{sz} \quad \text{with } R \text{ previously defined} \quad = \rho C_D V_R A/2m$$

while RV_{se} gives the total equatorial acceleration EACU or EACD, where V_{se} applies either to upleg or to downleg.

9.3 Data Demodulation and Reduction

The X-axis and Y-axis sensors detect accelerations in the equatorial plane of the spinning sphere. These measurements are naturally modulated at the spin frequency, with the amplitude of the sinusoidal signals directly proportional to the drag forces being experienced. Since the sensors are mounted for tri-axial measurements, the X- and Y-axis signals are roughly 90° out of phase, with additional dissimilar phase shifts introduced by the amplifiers at each channel sensitivity level. The X-axis sensitivities are higher than for the Y-sensor, and this allowed for overlap when either sensor was at the extreme of its dynamic range. Figure 9.1 shows the plot for typical signals at 130 km altitude.

The sphere is dynamically balanced during its construction, with the center of the tri-axial sensor configuration located as close as possible to the center of the sphere. However, the X-axis proof mass is mounted around the central Y-axis unit, and tends to experience greater imbalance acceleration forces. The greater harmonic distortion in the X-signal made it unsuitable for demodulation and interpretation at higher altitudes. Therefore, although both channels were demodulated, the Y-sensor data were normally used in the analyses.

The Z- and Nutation sensors detect changes in acceleration forces in the spin axis direction. The sensed signal is always precession modulated, and the modulation must be removed. The change in the resulting d.c. signal gives the acceleration. Figures 9.5 and 9.6 show how Z2, Z3, Z4 and NUT channels are staged in their dynamic ranges on downleg.

AC16 SENSOR COUNTS

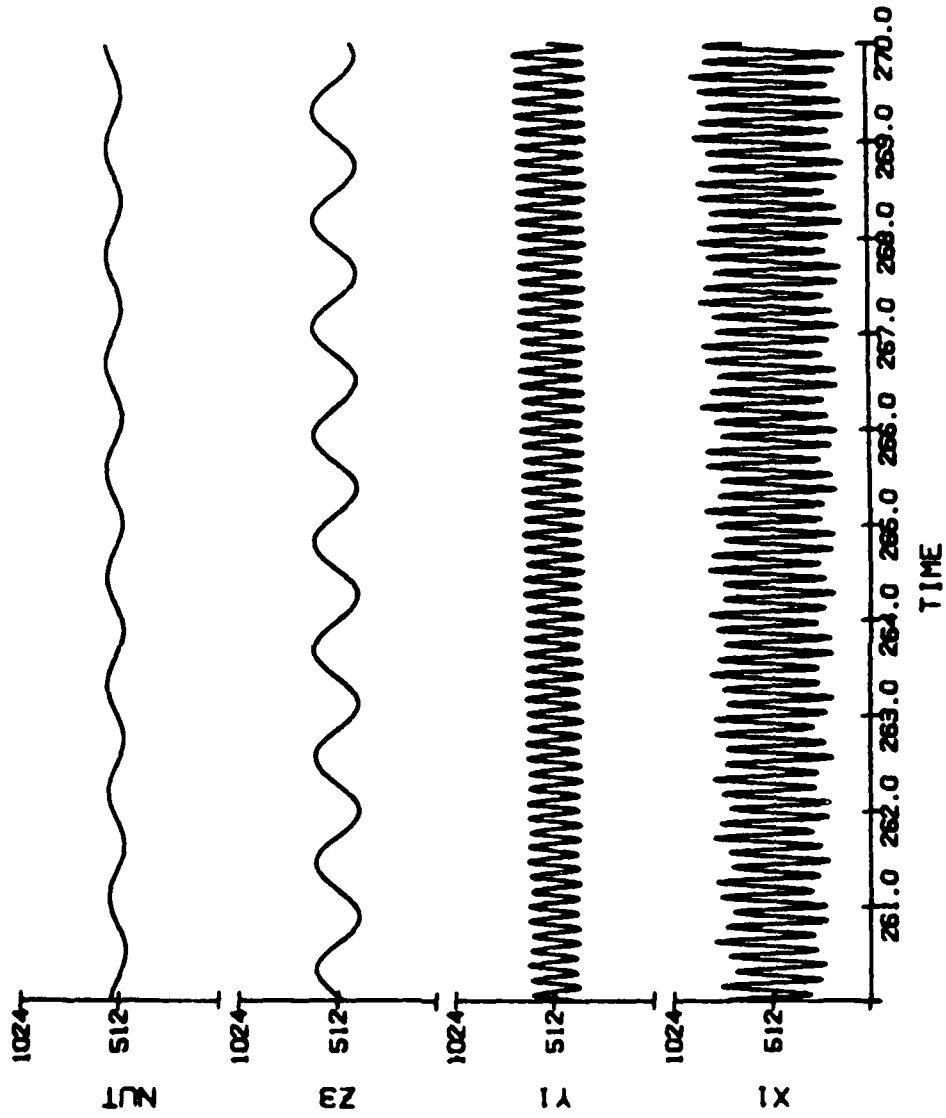


Figure 9.1 Typical Sensor Signals around 130 km altitude

9.4 The Calibration Package

Extensive pre-launch tests of the accelerometers and the instrumentation were carried out to establish the sensitivity of the measurements for each sensor and channel. In the case of the Z-axis and Nutation sensors, attenuation effects due to the sensor filter time constants were also considered. The flight data itself provided an invaluable opportunity for calibrating the piezo-electric crystal sensitivities in the force field experienced in the rotating sphere, taking advantage of the fact that all the sensors are sharply disturbed when they are uncaged after sphere separation. A distinct damped resonant signal is evident on each sensor channel, and since this occurs in the actual force field which is in effect, accurate determination of the resonant frequencies early in the telemetry data analysis allowed for more accurate calibrations. Similarly, Z-axis and Nutation sensor time constant determinations around reentry were made using actual telemetry data.

Computer optimized fitting techniques were used extensively in an interactive mode, once the nominal spin and precession rates had been determined. The Z-axis and Nutation sensors exhibit their resonances superimposed on the precession frequency signal, and these composite signals were optimally matched using the above fitting algorithms. The following pages show typical Pre-Calibration results produced for AC16; the required calibration sensitivities were derived from the parameters of these in-situ measurements.

9.4.1 AC16 Plots and Results for Calibration Use

The plots presented here show the signals and the analyses that were performed for a typical experiment (AC16). Nominal sphere spin rate, resonant frequencies for the X-, Y-, Z- and Nutation sensors, and the Z- and Nutation time constants were determined from these signals by solving for the transient function representations.

<u>Figure</u>	<u>Description</u>	<u>Results</u>
9.1	Typical X-Y signals at 265 sec	Spin rate = 6.417 Hz
9.2	X4, Y4 signals at uncaging	X res. freq. = 10.11 Hz Y res. freq. = 10.63 Hz
9.3	Z3 signal at uncaging	Z res. freq. = 12.056 Hz
9.4	NUT signal at sphere eject	NUT res freq. = 37.59 Hz
9.5	Z and NUT signals in downleg dynamic range	Precession = .8903 Hz
9.6	Demodulated Z and NUT signals on log scale	Z2 time constant = 3.50 sec Z3 time constant = 3.91 sec Z4, time constant = 5.54 sec NUT time constant = 5.54 sec

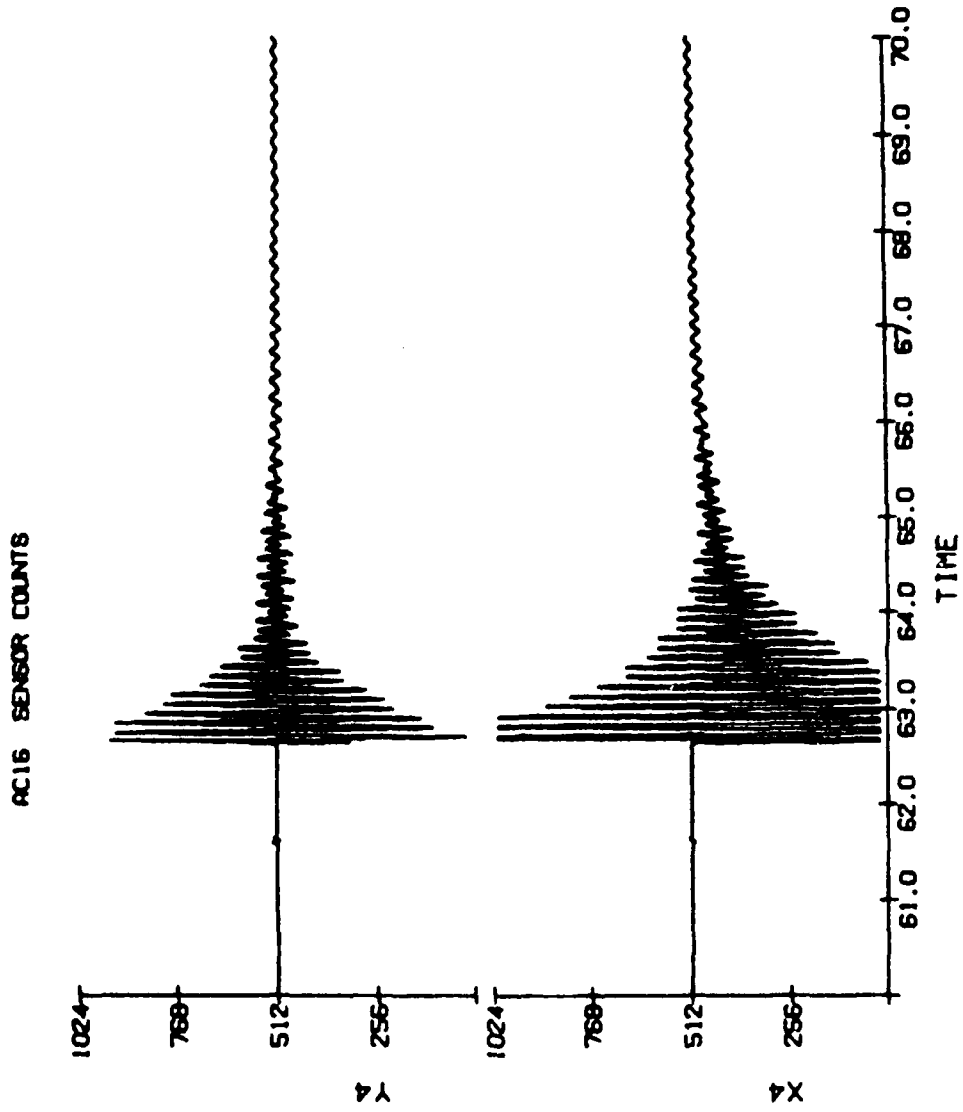


Figure 9.2 X4, Y4 Sensor Signals at Uncaging

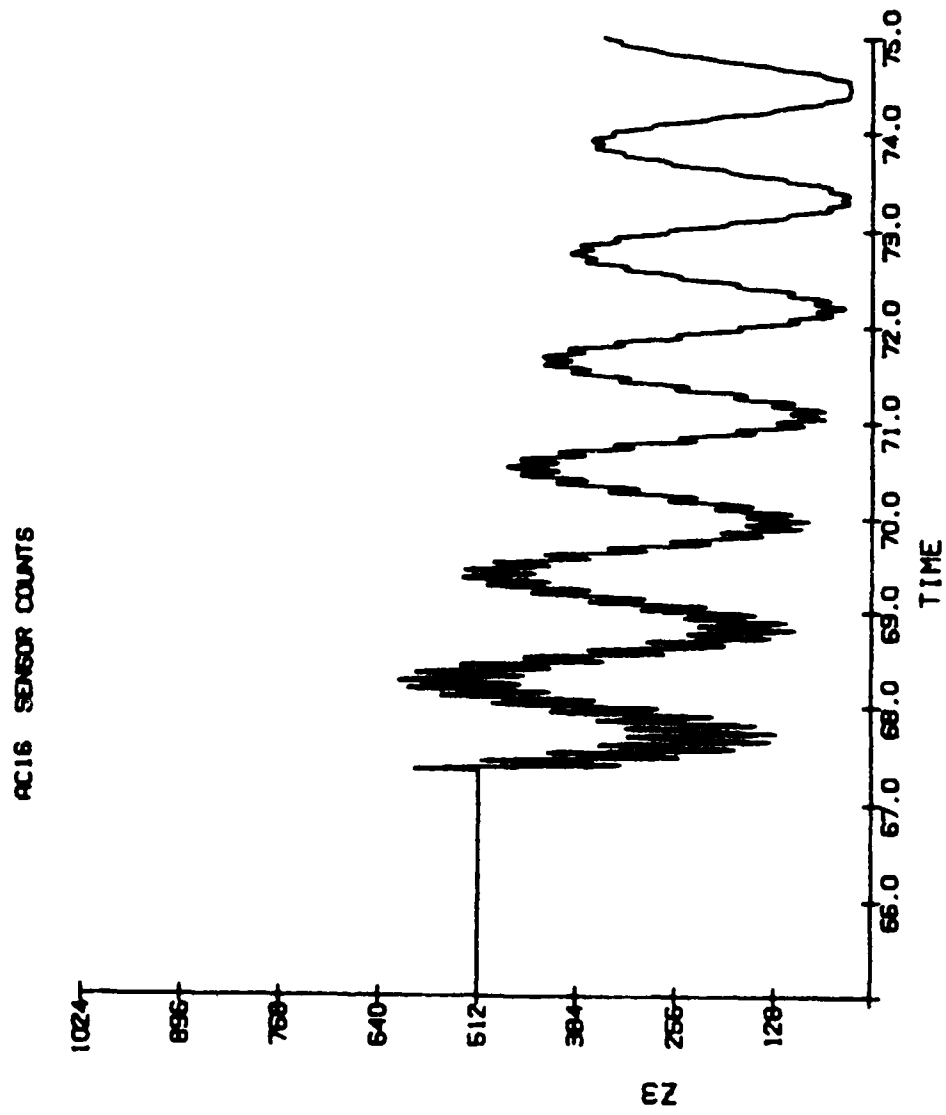


Figure 9.3 Z3 Sensor Signal at Uncaging

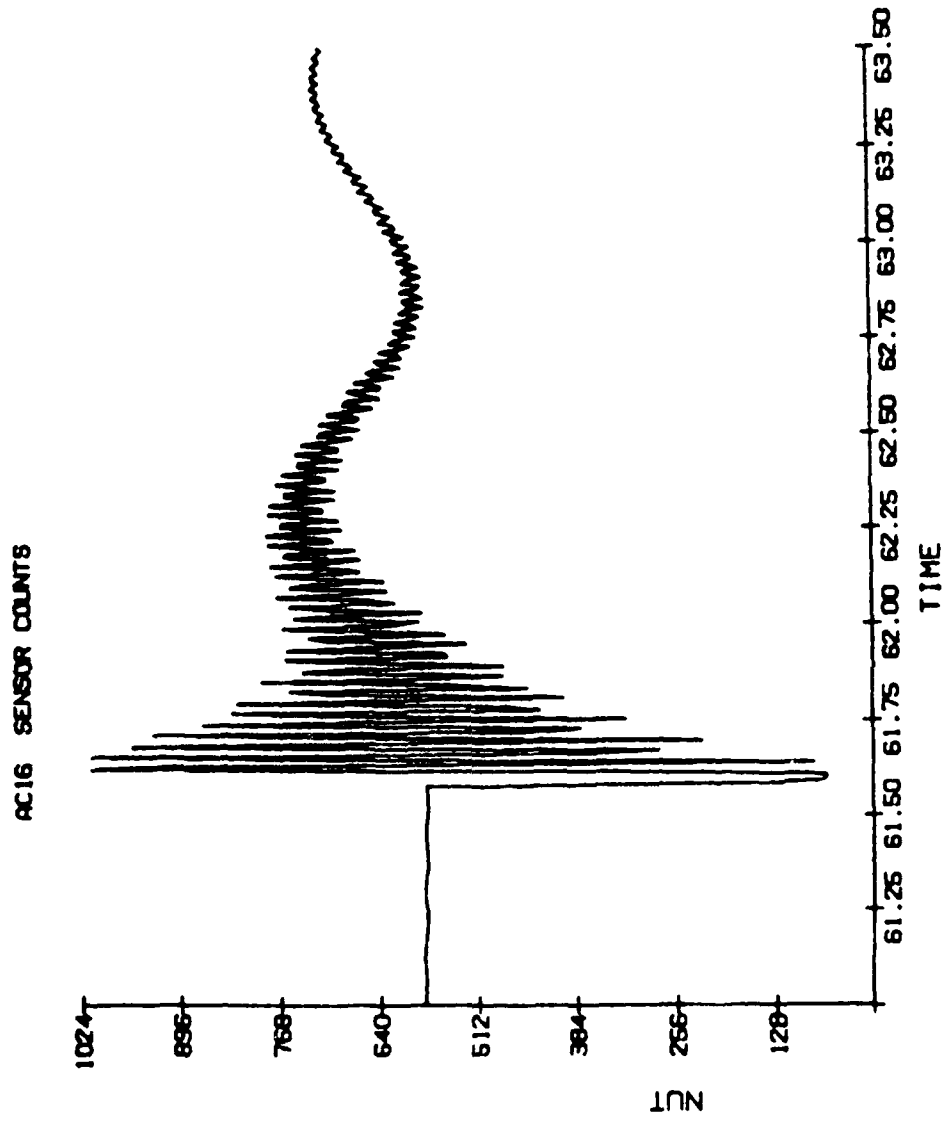


Figure 9.4 Nutation Sensor Signal at Sphere Eject

AC16 SENSOR COUNTS

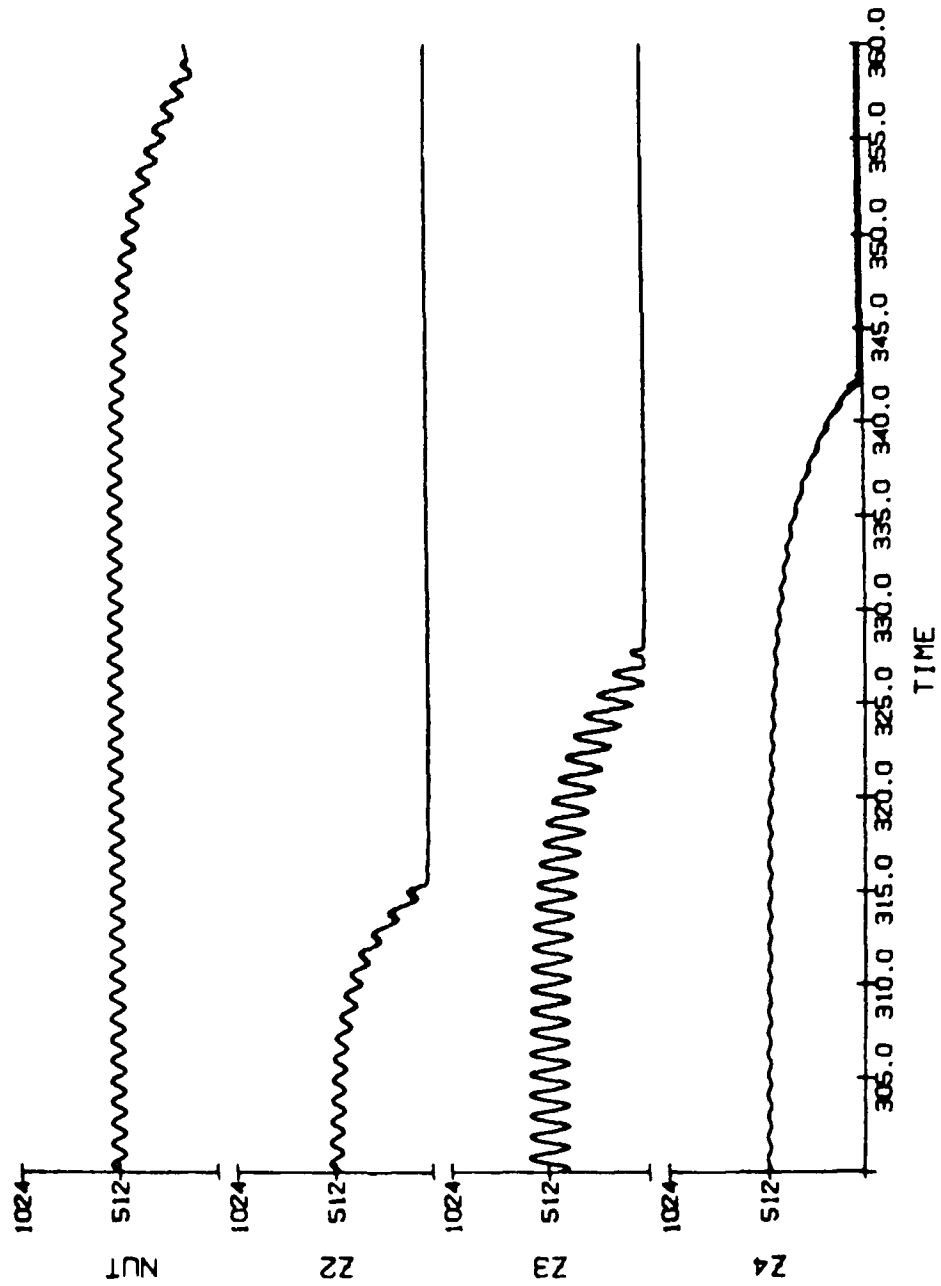


Figure 9.5 Z and Nutation Sensor Signals in Downleg Dynamic Range

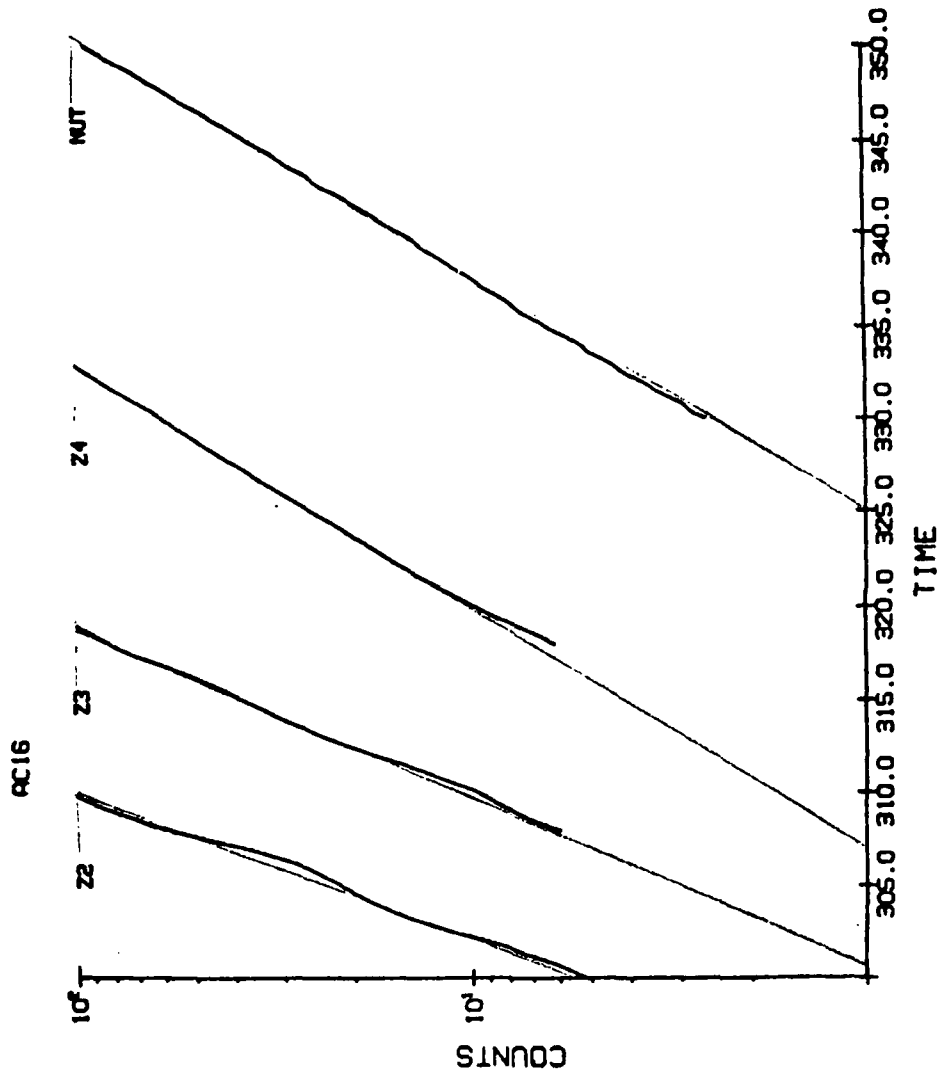


Figure 9.6 Demodulated Z and Nutation Sensor Signals
 (Slopes on Log scale give Time Constants)

9.5 The Resource File

Processing of the rocket sphere data was done progressively using various programs. The packed telemetered data and the intermediate results of processing were saved as computer permanent files that were called by the subsequent programs. However the programs at each stage generally also required other parameters or constants known from the start of the processing, such as sphere mass or trajectory parameters versus time, as well as intermediate derived results such as the sensor transition times or the reference phase. This parameter data base was augmented and/or updated manually with the results from the successive stages; the posting of the accumulated results for all the experiments was made to a common Resource File ACROK in standard card format, and could be automatically accessed by subsequent programs by a simple subroutine call which included the experiment identification. The following pages give listings of all the Resource Files.


```

AC12 11/16/80 17220.00 SEC. ESRANGE
SWASS 540 (KG, M**2)
ALT 24.05108 (LATITUDE, FLIGHT AZIM.)
GRZ 21.5 (NO. OF TRAJ. POINTS)
NDT 66 (TIME AFTER LAUNCH)
TIME 44.5 49.5 54.5 59.5 64.5 69.5 74.5 79.5 84.5 89.5 94.5 99.5 104.5 109.5 114.5 119.5 124.5 129.5 134.5 139.5 144.5 149.5 154.5 159.5 164.5 169.5 174.5 179.5 184.5 189.5 194.5 199.5 204.5 209.5 214.5 219.5 224.5 229.5 234.5 239.5 244.5 249.5 254.5 259.5 264.5 269.5 274.5 279.5 284.5 289.5 294.5 299.5 304.5 309.5 314.5 319.5 324.5 329.5 334.5 339.5 344.5 349.5 354.5 359.5 364.5 369.5 374.5 379.5 384.5 389.5 394.5 399.5 404.5 409.5 414.5 419.5 424.5 429.5 434.5 439.5 444.5 449.5 454.5 459.5 464.5 469.5 474.5 479.5 484.5 489.5 494.5 499.5 504.5 509.5 514.5 519.5 524.5 529.5 534.5 539.5 544.5 549.5 554.5 559.5 564.5 569.5 574.5 579.5 584.5 589.5 594.5 599.5 604.5 609.5 614.5 619.5 624.5 629.5 634.5 639.5 644.5 649.5 654.5 659.5 664.5 669.5 674.5 679.5 684.5 689.5 694.5 699.5 704.5 709.5 714.5 719.5 724.5 729.5 734.5 739.5 744.5 749.5 754.5 759.5 764.5 769.5 774.5 779.5 784.5 789.5 794.5 799.5 804.5 809.5 814.5 819.5 824.5 829.5 834.5 839.5 844.5 849.5 854.5 859.5 864.5 869.5 874.5 879.5 884.5 889.5 894.5 899.5 904.5 909.5 914.5 919.5 924.5 929.5 934.5 939.5 944.5 949.5 954.5 959.5 964.5 969.5 974.5 979.5 984.5 989.5 994.5 999.5 1004.5 1009.5 1014.5 1019.5 1024.5 1029.5 1034.5 1039.5 1044.5 1049.5 1054.5 1059.5 1064.5 1069.5 1074.5 1079.5 1084.5 1089.5 1094.5 1099.5 1104.5 1109.5 1114.5 1119.5 1124.5 1129.5 1134.5 1139.5 1144.5 1149.5 1154.5 1159.5 1164.5 1169.5 1174.5 1179.5 1184.5 1189.5 1194.5 1199.5 1204.5 1209.5 1214.5 1219.5 1224.5 1229.5 1234.5 1239.5 1244.5 1249.5 1254.5 1259.5 1264.5 1269.5 1274.5 1279.5 1284.5 1289.5 1294.5 1299.5 1304.5 1309.5 1314.5 1319.5 1324.5 1329.5 1334.5 1339.5 1344.5 1349.5 1354.5 1359.5 1364.5 1369.5 1374.5 1379.5 1384.5 1389.5 1394.5 1399.5 1404.5 1409.5 1414.5 1419.5 1424.5 1429.5 1434.5 1439.5 1444.5 1449.5 1454.5 1459.5 1464.5 1469.5 1474.5 1479.5 1484.5 1489.5 1494.5 1499.5 1504.5 1509.5 1514.5 1519.5 1524.5 1529.5 1534.5 1539.5 1544.5 1549.5 1554.5 1559.5 1564.5 1569.5 1574.5 1579.5 1584.5 1589.5 1594.5 1599.5 1604.5 1609.5 1614.5 1619.5 1624.5 1629.5 1634.5 1639.5 1644.5 1649.5 1654.5 1659.5 1664.5 1669.5 1674.5 1679.5 1684.5 1689.5 1694.5 1699.5 1704.5 1709.5 1714.5 1719.5 1724.5 1729.5 1734.5 1739.5 1744.5 1749.5 1754.5 1759.5 1764.5 1769.5 1774.5 1779.5 1784.5 1789.5 1794.5 1799.5 1804.5 1809.5 1814.5 1819.5 1824.5 1829.5 1834.5 1839.5 1844.5 1849.5 1854.5 1859.5 1864.5 1869.5 1874.5 1879.5 1884.5 1889.5 1894.5 1899.5 1904.5 1909.5 1914.5 1919.5 1924.5 1929.5 1934.5 1939.5 1944.5 1949.5 1954.5 1959.5 1964.5 1969.5 1974.5 1979.5 1984.5 1989.5 1994.5 1999.5 2004.5 2009.5 2014.5 2019.5 2024.5 2029.5 2034.5 2039.5 2044.5 2049.5 2054.5 2059.5 2064.5 2069.5 2074.5 2079.5 2084.5 2089.5 2094.5 2099.5 2104.5 2109.5 2114.5 2119.5 2124.5 2129.5 2134.5 2139.5 2144.5 2149.5 2154.5 2159.5 2164.5 2169.5 2174.5 2179.5 2184.5 2189.5 2194.5 2199.5 2204.5 2209.5 2214.5 2219.5 2224.5 2229.5 2234.5 2239.5 2244.5 2249.5 2254.5 2259.5 2264.5 2269.5 2274.5 2279.5 2284.5 2289.5 2294.5 2299.5 2304.5 2309.5 2314.5 2319.5 2324.5 2329.5 2334.5 2339.5 2344.5 2349.5 2354.5 2359.5 2364.5 2369.5 2374.5 2379.5 2384.5 2389.5 2394.5 2399.5 2404.5 2409.5 2414.5 2419.5 2424.5 2429.5 2434.5 2439.5 2444.5 2449.5 2454.5 2459.5 2464.5 2469.5 2474.5 2479.5 2484.5 2489.5 2494.5 2499.5 2504.5 2509.5 2514.5 2519.5 2524.5 2529.5 2534.5 2539.5 2544.5 2549.5 2554.5 2559.5 2564.5 2569.5 2574.5 2579.5 2584.5 2589.5 2594.5 2599.5 2604.5 2609.5 2614.5 2619.5 2624.5 2629.5 2634.5 2639.5 2644.5 2649.5 2654.5 2659.5 2664.5 2669.5 2674.5 2679.5 2684.5 2689.5 2694.5 2699.5 2704.5 2709.5 2714.5 2719.5 2724.5 2729.5 2734.5 2739.5 2744.5 2749.5 2754.5 2759.5 2764.5 2769.5 2774.5 2779.5 2784.5 2789.5 2794.5 2799.5 2804.5 2809.5 2814.5 2819.5 2824.5 2829.5 2834.5 2839.5 2844.5 2849.5 2854.5 2859.5 2864.5 2869.5 2874.5 2879.5 2884.5 2889.5 2894.5 2899.5 2904.5 2909.5 2914.5 2919.5 2924.5 2929.5 2934.5 2939.5 2944.5 2949.5 2954.5 2959.5 2964.5 2969.5 2974.5 2979.5 2984.5 2989.5 2994.5 2999.5 3004.5 3009.5 3014.5 3019.5 3024.5 3029.5 3034.5 3039.5 3044.5 3049.5 3054.5 3059.5 3064.5 3069.5 3074.5 3079.5 3084.5 3089.5 3094.5 3099.5 3104.5 3109.5 3114.5 3119.5 3124.5 3129.5 3134.5 3139.5 3144.5 3149.5 3154.5 3159.5 3164.5 3169.5 3174.5 3179.5 3184.5 3189.5 3194.5 3199.5 3204.5 3209.5 3214.5 3219.5 3224.5 3229.5 3234.5 3239.5 3244.5 3249.5 3254.5 3259.5 3264.5 3269.5 3274.5 3279.5 3284.5 3289.5 3294.5 3299.5 3304.5 3309.5 3314.5 3319.5 3324.5 3329.5 3334.5 3339.5 3344.5 3349.5 3354.5 3359.5 3364.5 3369.5 3374.5 3379.5 3384.5 3389.5 3394.5 3399.5 3404.5 3409.5 3414.5 3419.5 3424.5 3429.5 3434.5 3439.5 3444.5 3449.5 3454.5 3459.5 3464.5 3469.5 3474.5 3479.5 3484.5 3489.5 3494.5 3499.5 3504.5 3509.5 3514.5 3519.5 3524.5 3529.5 3534.5 3539.5 3544.5 3549.5 3554.5 3559.5 3564.5 3569.5 3574.5 3579.5 3584.5 3589.5 3594.5 3599.5 3604.5 3609.5 3614.5 3619.5 3624.5 3629.5 3634.5 3639.5 3644.5 3649.5 3654.5 3659.5 3664.5 3669.5 3674.5 3679.5 3684.5 3689.5 3694.5 3699.5 3704.5 3709.5 3714.5 3719.5 3724.5 3729.5 3734.5 3739.5 3744.5 3749.5 3754.5 3759.5 3764.5 3769.5 3774.5 3779.5 3784.5 3789.5 3794.5 3799.5 3804.5 3809.5 3814.5 3819.5 3824.5 3829.5 3834.5 3839.5 3844.5 3849.5 3854.5 3859.5 3864.5 3869.5 3874.5 3879.5 3884.5 3889.5 3894.5 3899.5 3904.5 3909.5 3914.5 3919.5 3924.5 3929.5 3934.5 3939.5 3944.5 3949.5 3954.5 3959.5 3964.5 3969.5 3974.5 3979.5 3984.5 3989.5 3994.5 3999.5 4004.5 4009.5 4014.5 4019.5 4024.5 4029.5 4034.5 4039.5 4044.5 4049.5 4054.5 4059.5 4064.5 4069.5 4074.5 4079.5 4084.5 4089.5 4094.5 4099.5 4104.5 4109.5 4114.5 4119.5 4124.5 4129.5 4134.5 4139.5 4144.5 4149.5 4154.5 4159.5 4164.5 4169.5 4174.5 4179.5 4184.5 4189.5 4194.5 4199.5 4204.5 4209.5 4214.5 4219.5 4224.5 4229.5 4234.5 4239.5 4244.5 4249.5 4254.5 4259.5 4264.5 4269.5 4274.5 4279.5 4284.5 4289.5 4294.5 4299.5 4304.5 4309.5 4314.5 4319.5 4324.5 4329.5 4334.5 4339.5 4344.5 4349.5 4354.5 4359.5 4364.5 4369.5 4374.5 4379.5 4384.5 4389.5 4394.5 4399.5 4404.5 4409.5 4414.5 4419.5 4424.5 4429.5 4434.5 4439.5 4444.5 4449.5 4454.5 4459.5 4464.5 4469.5 4474.5 4479.5 4484.5 4489.5 4494.5 4499.5 4504.5 4509.5 4514.5 4519.5 4524.5 4529.5 4534.5 4539.5 4544.5 4549.5 4554.5 4559.5 4564.5 4569.5 4574.5 4579.5 4584.5 4589.5 4594.5 4599.5 4604.5 4609.5 4614.5 4619.5 4624.5 4629.5 4634.5 4639.5 4644.5 4649.5 4654.5 4659.5 4664.5 4669.5 4674.5 4679.5 4684.5 4689.5 4694.5 4699.5 4704.5 4709.5 4714.5 4719.5 4724.5 4729.5 4734.5 4739.5 4744.5 4749.5 4754.5 4759.5 4764.5 4769.5 4774.5 4779.5 4784.5 4789.5 4794.5 4799.5 4804.5 4809.5 4814.5 4819.5 4824.5 4829.5 4834.5 4839.5 4844.5 4849.5 4854.5 4859.5 4864.5 4869.5 4874.5 4879.5 4884.5 4889.5 4894.5 4899.5 4904.5 4909.5 4914.5 4919.5 4924.5 4929.5 4934.5 4939.5 4944.5 4949.5 4954.5 4959.5 4964.5 4969.5 4974.5 4979.5 4984.5 4989.5 4994.5 4999.5 5004.5 5009.5 5014.5 5019.5 5024.5 5029.5 5034.5 5039.5 5044.5 5049.5 5054.5 5059.5 5064.5 5069.5 5074.5 5079.5 5084.5 5089.5 5094.5 5099.5 5104.5 5109.5 5114.5 5119.5 5124.5 5129.5 5134.5 5139.5 5144.5 5149.5 5154.5 5159.5 5164.5 5169.5 5174.5 5179.5 5184.5 5189.5 5194.5 5199.5 5204.5 5209.5 5214.5 5219.5 5224.5 5229.5 5234.5 5239.5 5244.5 5249.5 5254.5 5259.5 5264.5 5269.5 5274.5 5279.5 5284.5 5289.5 5294.5 5299.5 5304.5 5309.5 5314.5 5319.5 5324.5 5329.5 5334.5 5339.5 5344.5 5349.5 5354.5 5359.5 5364.5 5369.5 5374.5 5379.5 5384.5 5389.5 5394.5 5399.5 5404.5 5409.5 5414.5 5419.5 5424.5 5429.5 5434.5 5439.5 5444.5 5449.5 5454.5 5459.5 5464.5 5469.5 5474.5 5479.5 5484.5 5489.5 5494.5 5499.5 5504.5 5509.5 5514.5 5519.5 5524.5 5529.5 5534.5 5539.5 5544.5 5549.5 5554.5 5559.5 5564.5 5569.5 5574.5 5579.5 5584.5 5589.5 5594.5 5599.5 5604.5 5609.5 5614.5 5619.5 5624.5 5629.5 5634.5 5639.5 5644.5 5649.5 5654.5 5659.5 5664.5 5669.5 5674.5 5679.5 5684.5 5689.5 5694.5 5699.5 5704.5 5709.5 5714.5 5719.5 5724.5 5729.5 5734.5 5739.5 5744.5 5749.5 5754.5 5759.5 5764.5 5769.5 5774.5 5779.5 5784.5 5789.5 5794.5 5799.5 5804.5 5809.5 5814.5 5819.5 5824.5 5829.5 5834.5 5839.5 5844.5 5849.5 5854.5 5859.5 5864.5 5869.5 5874.5 5879.5 5884.5 5889.5 5894.5 5899.5 5904.5 5909.5 5914.5 5919.5 5924.5 5929.5 5934.5 5939.5 5944.5 5949.5 5954.5 5959.5 5964.5 5969.5 5974.5 5979.5 5984.5 5989.5 5994.5 5999.5 6004.5 6009.5 6014.5 6019.5 6024.5 6029.5 6034.5 6039.5 6044.5 6049.5 6054.5 6059.5 6064.5 6069.5 6074.5 6079.5 6084.5 6089.5 6094.5 6099.5 6104.5 6109.5 6114.5 6119.5 6124.5 6129.5 6134.5 6139.5 6144.5 6149.5 6154.5 6159.5 6164.5 6169.5 6174.5 6179.5 6184.5 6189.5 6194.5 6199.5 6204.5 6209.5 6214.5 6219.5 6224.5 6229.5 6234.5 6239.5 6244.5 6249.5 6254.5 6259.5 6264.5 6269.5 6274.5 6279.5 6284.5 6289.5 6294.5 6299.5 6304.5 6309.5 6314.5 6319.5 6324.5 6329.5 6334.5 6339.5 6344.5 6349.5 6354.5 6359.5 6364.5 6369.5 6374.5 6379.5 6384.5 6389.5 6394.5 6399.5 6404.5 6409.5 6414.5 6419.5 6424.5 6429.5 6434.5 6439.5 6444.5 6449.5 6454.5 6459.5 6464.5 6469.5 6474.5 6479.5 6484.5 6489.5 6494.5 6499.5 6504.5 6509.5 6514.5 6519.5 6524.5 6529.5 6534.5 6539.5 6544.5 6549.5 6554.5 6559.5 6564.5 6569.5 6574.5 6579.5 6584.5 6589.5 6594.5 6599.5 6604.5 6609.5 6614.5 6619.5 6624.5 6629.5 6634.5 6639.5 6644.5 6649.5 6654.5 6659.5 6664.5 6669.5 6674.5 6679.5 6684.5 6689.5 6694.5 6699.5 6704.5 6709.5 6714.5 6719.5 6724.5 6729.5 6734.5 6739.5 6744.5 6749.5 6754.5 6759.5 6764.5 6769.5 6774.5 6779.5 6784.5 6789.5 6794.5 6799.5 6804.5 6809.5 6814.5 6819.5 6824.5 6829.5 6834.5 6839.5 6844.5 6849.5 6854.5 6859.5 6864.5 6869.5 6874.5 6879.5 6884.5 6889.5 6894.5 6899.5 6904.5 6909.5 6914.5 6919.5 6924.5 6929.5 6934.5 6939.5 6944.5 6949.5 6954.5 6959.5 6964.5 6969.5 6974.5 6979.5 6984.5 6989.5 6994.5 6999.5 7004.5 7009.5 7014.5 7019.5 7024.5 7029.5 7034.5 7039.5 7044.5 7049.5 7054.5 7059.5 7064.5 7069.5 7074.5 7079.5 7084.5 7089.5 7094.5 7099.5 7104.5 7109.5 7114.5 7119.5 7124.5 7129.5 7134.5 7139.5 7144.5 7149.5 7154.5 7159.5 7164.5 7169.5 7174.5 7179.5 7184.5 7189.5 7194.5 7199.5 7204.5 7209.5 7214.5 7219.5 7224.5 7229.5 7234.5 7239.5 7244.5 7249.5 7254.5 7259.5 7264.5 7269.5 7274.5 7279.5 7284.5 7289.5 7294.5 7299.5 7304.5 7309.5 7314.5 7319.5 7324.5 7329.5 7334.5 7339.5 7344.5 7349.5 7354.5 7359.5 7364.5 7369.5 7374.5 7379.5 7384.5 7389.5 7394.5 7399.5 7404.5 7409.5 7414.5 7419.5 7424.5 7429.5 7434.5 7439.5 7444.5 7449.5 7454.5 7459.5 7464.5 7469.5 7474.5 7479.5 7484.5 7489.5 7494.5 7499.5 7504.5 7509.5 7514.5 7519.5 7524.5 7529.5 7534.5 7539.5 7544.5 7549.5 7554.5 7559.5 7564.5 7569.5 7574.5 7579.5 7584.5 7589.5 7594.5 7599.5 7604.5 7609.5 7614.5 7619.5 7624.5 7629.5 7634.5 7639.5 7644.5 7649.5 7654.5 7659.5 7664.5 7669.5 7674.5 7679.5 7684.5 7689.5 7694.5 7699.5 7704.5 7709.5 7714.5 7719.5 7724.5 7729.5 7734.5 7739.5 7744.5 7749.5 7754.5 7759.5 7764.5 7769.5 7774.5 7779.5 7784.5 7789.5 7794.5 7799.5 7804.5 7809.5 7814.5 7819.5 7824.5 7829.5 7834.5 7839.5 7844.5 7849.5 7854.5 7859.5 7864.5 7869.5 7874.5 7879.5 7884.5 7889.5 7894.5 7899.5 7904.5 7909.5 7914.5 7919.5 7924.5 7929.5 7934.5 7939.5 7944.5 7949.5 7954.5 7959.5 7964.5 7969.5 7974.5 7979.5 7984.5 7989.5 7994.5 7999.5 8004.5 8009.5 8014.5 8019.5 8024.5 8029.5 8034.5 8039.5 8044.5 8049.5 8054.5 8059.5 8064.5 8069.5 8074.5 8079.5 8084.5 8089.5 8094.5 8099.5 8104.5 8109.5 8114.5 8119.5 8124.5 8129.5 8134.5 8139.5 8144.5 8149.5 8154.5 8159.5 8164.5 8169.5 8174.5 8179.5 8184.5 8189.5 8194.5 8199.5 8204.5 8209.5 8214.5 8219.5 8224.5 8229.5 8234.5 8239.5 8244.5 8249.5 8254.5 8259.5 8264.5 8269.5 8274.5 8279.5 8284.5 8289.5 8294.5 8299.5 8304.5 8309.5 8314.5 8319.5 8324.5 8329.5 8334.5 8339.5 8344.5 8349.5 8354.5 8359.5 8364.5 8369.5 8374.5 8379.5 8384.5 8389.5 8394.5 8399.5 8404.5 8409.5 8414.5 8419.5 8424.5 8429.5 8434.5 8439.5 8444.5 8449.5 8454.5 8459.5 8464.5 8469.5 8474.5 8479.5 8484.5 8489.5 8494.5 8499.5 8504.5 8509.5 8514.5 8519.5 8524.5 8529.5 8534.5 8539.5 8544.5 8549.5 8554.5 8559.5 8564.5 8569.5 8574.5 8579.5 8584.5 8589.5 8594.5 8599.5 8604.5 8609.5 8614.5 8619.5 8624.5 8629.5 8634.5 8639.5 8644.5 8649.5 8654.5 8659.5 8664.5 8669.5 8674.5 8679.5 8684.5 8689.5 8694.5 8699.5 8704.5 8709.5 8714.5 8719.5 8724.5 8729.5 8734.5 8739.5 8744.5 8749.5 8754.5 8759.5 8764.5 8769.5 8774.5 8779.5 8784.5 8789.5 8794.5 8799.5 8804.5 8809.5 8814.5 8819.5 8824.5 8829.5 8834.5 8839.5 8844.5 8849.5 8854.5 8859.5 8864.5 8869.5 8874.5 8879.5 8884.5 8889.5 8894.5 8899.5 8904.5 8909.5 8914.5 8919.5 8924.5 8929.5 8934.5 8939.5 89
```


AC16 8/04/82 960.00 SEC. ESRANGE
 SWASS,SAREA (KG, M**2)
 10.998 0.05192
 ALAT,FLAZ (LATITUDE, FLIGHT AZIM.)
 68.335.0
 NDT (NO. OF TRAJ. POINTS)
 61
 TINT (TIME AFTER LAUNCH)
 30.00 63.00 70.00 75.00 80.00
 35.00 68.00 72.00 77.00 82.00
 40.00 73.00 77.00 82.00 87.00
 45.00 78.00 82.00 87.00 92.00
 50.00 83.00 87.00 92.00 97.00
 55.00 88.00 92.00 97.00 102.00
 60.00 93.00 97.00 102.00 107.00
 65.00 98.00 102.00 107.00 112.00
 70.00 103.00 107.00 112.00 117.00
 75.00 108.00 112.00 117.00 122.00
 80.00 113.00 117.00 122.00 127.00
 85.00 118.00 122.00 127.00 132.00
 90.00 123.00 127.00 132.00 137.00
 95.00 128.00 132.00 137.00 142.00
 100.00 133.00 137.00 142.00 147.00
 105.00 138.00 142.00 147.00 152.00
 110.00 143.00 147.00 152.00 157.00
 115.00 148.00 152.00 157.00 162.00
 120.00 153.00 157.00 162.00 167.00
 125.00 158.00 162.00 167.00 172.00
 130.00 163.00 167.00 172.00 177.00
 135.00 168.00 172.00 177.00 182.00
 140.00 173.00 177.00 182.00 187.00
 145.00 178.00 182.00 187.00 192.00
 150.00 183.00 187.00 192.00 197.00
 155.00 188.00 192.00 197.00 202.00
 160.00 193.00 197.00 202.00 207.00
 165.00 198.00 202.00 207.00 212.00
 170.00 203.00 207.00 212.00 217.00
 175.00 208.00 212.00 217.00 222.00
 180.00 213.00 217.00 222.00 227.00
 185.00 218.00 222.00 227.00 232.00
 190.00 223.00 227.00 232.00 237.00
 195.00 228.00 232.00 237.00 242.00
 200.00 233.00 237.00 242.00 247.00
 205.00 238.00 242.00 247.00 252.00
 210.00 243.00 247.00 252.00 257.00
 215.00 248.00 252.00 257.00 262.00
 220.00 253.00 257.00 262.00 267.00
 225.00 258.00 262.00 267.00 272.00
 230.00 263.00 267.00 272.00 277.00
 235.00 268.00 272.00 277.00 282.00
 240.00 273.00 277.00 282.00 287.00
 245.00 278.00 282.00 287.00 292.00
 250.00 283.00 287.00 292.00 297.00
 255.00 288.00 292.00 297.00 302.00
 260.00 293.00 297.00 302.00 307.00
 265.00 298.00 302.00 307.00 312.00
 270.00 303.00 307.00 312.00 317.00
 275.00 308.00 312.00 317.00 322.00
 280.00 313.00 317.00 322.00 327.00
 285.00 318.00 322.00 327.00 332.00
 290.00 323.00 327.00 332.00 337.00
 295.00 328.00 332.00 337.00 342.00
 300.00 333.00 337.00 342.00 347.00
 305.00 338.00 342.00 347.00 352.00
 310.00 343.00 347.00 352.00 357.00
 315.00 348.00 352.00 357.00 362.00
 320.00 353.00 357.00 362.00 367.00
 325.00 358.00 362.00 367.00 372.00
 330.00 363.00 367.00 372.00 377.00
 335.00 368.00 372.00 377.00 382.00
 340.00 373.00 377.00 382.00 387.00
 345.00 378.00 382.00 387.00 392.00
 350.00 383.00 387.00 392.00 397.00
 355.00 388.00 392.00 397.00 402.00
 360.00 393.00 397.00 402.00 407.00
 365.00 398.00 402.00 407.00 412.00
 370.00 403.00 407.00 412.00 417.00
 375.00 408.00 412.00 417.00 422.00
 380.00 413.00 417.00 422.00 427.00
 385.00 418.00 422.00 427.00 432.00
 390.00 423.00 427.00 432.00 437.00
 395.00 428.00 432.00 437.00 442.00
 400.00 433.00 437.00 442.00 447.00
 405.00 438.00 442.00 447.00 452.00
 410.00 443.00 447.00 452.00 457.00
 415.00 448.00 452.00 457.00 462.00
 420.00 453.00 457.00 462.00 467.00
 425.00 458.00 462.00 467.00 472.00
 430.00 463.00 467.00 472.00 477.00
 435.00 468.00 472.00 477.00 482.00
 440.00 473.00 477.00 482.00 487.00
 445.00 478.00 482.00 487.00 492.00
 450.00 483.00 487.00 492.00 497.00
 455.00 488.00 492.00 497.00 502.00
 460.00 493.00 497.00 502.00 507.00
 465.00 498.00 502.00 507.00 512.00
 470.00 503.00 507.00 512.00 517.00
 475.00 508.00 512.00 517.00 522.00
 480.00 513.00 517.00 522.00 527.00
 485.00 518.00 522.00 527.00 532.00
 490.00 523.00 527.00 532.00 537.00
 495.00 528.00 532.00 537.00 542.00
 500.00 533.00 537.00 542.00 547.00
 505.00 538.00 542.00 547.00 552.00
 510.00 543.00 547.00 552.00 557.00
 515.00 548.00 552.00 557.00 562.00
 520.00 553.00 557.00 562.00 567.00
 525.00 558.00 562.00 567.00 572.00
 530.00 563.00 567.00 572.00 577.00
 535.00 568.00 572.00 577.00 582.00
 540.00 573.00 577.00 582.00 587.00
 545.00 578.00 582.00 587.00 592.00
 550.00 583.00 587.00 592.00 597.00
 555.00 588.00 592.00 597.00 602.00
 560.00 593.00 597.00 602.00 607.00
 565.00 598.00 602.00 607.00 612.00
 570.00 603.00 607.00 612.00 617.00
 575.00 608.00 612.00 617.00 622.00
 580.00 613.00 617.00 622.00 627.00
 585.00 618.00 622.00 627.00 632.00
 590.00 623.00 627.00 632.00 637.00
 595.00 628.00 632.00 637.00 642.00
 600.00 633.00 637.00 642.00 647.00
 605.00 638.00 642.00 647.00 652.00
 610.00 643.00 647.00 652.00 657.00
 615.00 648.00 652.00 657.00 662.00
 620.00 653.00 657.00 662.00 667.00
 625.00 658.00 662.00 667.00 672.00
 630.00 663.00 667.00 672.00 677.00
 635.00 668.00 672.00 677.00 682.00
 640.00 673.00 677.00 682.00 687.00
 645.00 678.00 682.00 687.00 692.00
 650.00 683.00 687.00 692.00 697.00
 655.00 688.00 692.00 697.00 702.00
 660.00 693.00 697.00 702.00 707.00
 665.00 698.00 702.00 707.00 712.00
 670.00 703.00 707.00 712.00 717.00
 675.00 708.00 712.00 717.00 722.00
 680.00 713.00 717.00 722.00 727.00
 685.00 718.00 722.00 727.00 732.00
 690.00 723.00 727.00 732.00 737.00
 695.00 728.00 732.00 737.00 742.00
 700.00 733.00 737.00 742.00 747.00
 705.00 738.00 742.00 747.00 752.00
 710.00 743.00 747.00 752.00 757.00
 715.00 748.00 752.00 757.00 762.00
 720.00 753.00 757.00 762.00 767.00
 725.00 758.00 762.00 767.00 772.00
 730.00 763.00 767.00 772.00 777.00
 735.00 768.00 772.00 777.00 782.00
 740.00 773.00 777.00 782.00 787.00
 745.00 778.00 782.00 787.00 792.00
 750.00 783.00 787.00 792.00 797.00
 755.00 788.00 792.00 797.00 802.00
 760.00 793.00 797.00 802.00 807.00
 765.00 798.00 802.00 807.00 812.00
 770.00 803.00 807.00 812.00 817.00
 775.00 808.00 812.00 817.00 822.00
 780.00 813.00 817.00 822.00 827.00
 785.00 818.00 822.00 827.00 832.00
 790.00 823.00 827.00 832.00 837.00
 795.00 828.00 832.00 837.00 842.00
 800.00 833.00 837.00 842.00 847.00
 805.00 838.00 842.00 847.00 852.00
 810.00 843.00 847.00 852.00 857.00
 815.00 848.00 852.00 857.00 862.00
 820.00 853.00 857.00 862.00 867.00
 825.00 858.00 862.00 867.00 872.00
 830.00 863.00 867.00 872.00 877.00
 835.00 868.00 872.00 877.00 882.00
 840.00 873.00 877.00 882.00 887.00
 845.00 878.00 882.00 887.00 892.00
 850.00 883.00 887.00 892.00 897.00
 855.00 888.00 892.00 897.00 902.00
 860.00 893.00 897.00 902.00 907.00
 865.00 898.00 902.00 907.00 912.00
 870.00 903.00 907.00 912.00 917.00
 875.00 908.00 912.00 917.00 922.00
 880.00 913.00 917.00 922.00 927.00
 885.00 918.00 922.00 927.00 932.00
 890.00 923.00 927.00 932.00 937.00
 895.00 928.00 932.00 937.00 942.00
 900.00 933.00 937.00 942.00 947.00
 905.00 938.00 942.00 947.00 952.00
 910.00 943.00 947.00 952.00 957.00
 915.00 948.00 952.00 957.00 962.00
 920.00 953.00 957.00 962.00 967.00
 925.00 958.00 962.00 967.00 972.00
 930.00 963.00 967.00 972.00 977.00
 935.00 968.00 972.00 977.00 982.00
 940.00 973.00 977.00 982.00 987.00
 945.00 978.00 982.00 987.00 992.00
 950.00 983.00 987.00 992.00 997.00
 955.00 988.00 992.00 997.00 1002.00
 960.00 993.00 997.00 1002.00 1007.00
 965.00 998.00 1002.00 1007.00 1012.00
 970.00 1003.00 1007.00 1012.00 1017.00
 975.00 1008.00 1012.00 1017.00 1022.00
 980.00 1013.00 1017.00 1022.00 1027.00
 985.00 1018.00 1022.00 1027.00 1032.00
 990.00 1023.00 1027.00 1032.00 1037.00
 995.00 1028.00 1032.00 1037.00 1042.00
 1000.00 1033.00 1037.00 1042.00 1047.00
 1005.00 1038.00 1042.00 1047.00 1052.00
 1010.00 1043.00 1047.00 1052.00 1057.00
 1015.00 1048.00 1052.00 1057.00 1062.00
 1020.00 1053.00 1057.00 1062.00 1067.00
 1025.00 1058.00 1062.00 1067.00 1072.00
 1030.00 1063.00 1067.00 1072.00 1077.00
 1035.00 1068.00 1072.00 1077.00 1082.00
 1040.00 1073.00 1077.00 1082.00 1087.00
 1045.00 1078.00 1082.00 1087.00 1092.00
 1050.00 1083.00 1087.00 1092.00 1097.00
 1055.00 1088.00 1092.00 1097.00 1102.00
 1060.00 1093.00 1097.00 1102.00 1107.00
 1065.00 1098.00 1102.00 1107.00 1112.00
 1070.00 1103.00 1107.00 1112.00 1117.00
 1075.00 1108.00 1112.00 1117.00 1122.00
 1080.00 1113.00 1117.00 1122.00 1127.00
 1085.00 1118.00 1122.00 1127.00 1132.00
 1090.00 1123.00 1127.00 1132.00 1137.00
 1095.00 1128.00 1132.00 1137.00 1142.00
 1100.00 1133.00 1137.00 1142.00 1147.00
 1105.00 1138.00 1142.00 1147.00 1152.00
 1110.00 1143.00 1147.00 1152.00 1157.00
 1115.00 1148.00 1152.00 1157.00 1162.00
 1120.00 1153.00 1157.00 1162.00 1167.00
 1125.00 1158.00 1162.00 1167.00 1172.00
 1130.00 1163.00 1167.00 1172.00 1177.00
 1135.00 1168.00 1172.00 1177.00 1182.00
 1140.00 1173.00 1177.00 1182.00 1187.00
 1145.00 1178.00 1182.00 1187.00 1192.00
 1150.00 1183.00 1187.00 1192.00 1197.00
 1155.00 1188.00 1192.00 1197.00 1202.00
 1160.00 1193.00 1197.00 1202.00 1207.00
 1165.00 1198.00 1202.00 1207.00 1212.00
 1170.00 1203.00 1207.00 1212.00 1217.00
 1175.00 1208.00 1212.00 1217.00 1222.00
 1180.00 1213.00 1217.00 1222.00 1227.00
 1185.00 1218.00 1222.00 1227.00 1232.00
 1190.00 1223.00 1227.00 1232.00 1237.00
 1195.00 1228.00 1232.00 1237.00 1242.00
 1200.00 1233.00 1237.00 1242.00 1247.00
 1205.00 1238.00 1242.00 1247.00 1252.00
 1210.00 1243.00 1247.00 1252.00 1257.00
 1215.00 1248.00 1252.00 1257.00 1262.00
 1220.00 1253.00 1257.00 1262.00 1267.00
 1225.00 1258.00 1262.00 1267.00 1272.00
 1230.00 1263.00 1267.00 1272.00 1277.00
 1235.00 1268.00 1272.00 1277.00 1282.00
 1240.00 1273.00 1277.00 1282.00 1287.00
 1245.00 1278.00 1282.00 1287.00 1292.00
 1250.00 1283.00 1287.00 1292.00 1297.00
 1255.00 1288.00 1292.00 1297.00 1302.00
 1260.00 1293.00 1297.00 1302.00 1307.00
 1265.00 1298.00 1302.00 1307.00 1312.00
 1270.00 1303.00 1307.00 1312.00 1317.00
 1275.00 1308.00 1312.00 1317.00 1322.00
 1280.00 1313.00 1317.00 1322.00 1327.00
 1285.00 1318.00 1322.00 1327.00 1332.00
 1290.00 1323.00 1327.00 1332.00 1337.00
 1295.00 1328.00 1332.00 1337.00 1342.00
 1300.00 1333.00 1337.00 1342.00 1347.00
 1305.00 1338.00 1342.00 1347.00 1352.00
 1310.00 1343.00 1347.00 1352.00 1357.00
 1315.00 1348.00 1352.00 1357.00 1362.00
 1320.00 1353.00 1357.00 1362.00 1367.00
 1325.00 1358.00 1362.00 1367.00 1372.00
 1330.00 1363.00 1367.00 1372.00 1377.00
 1335.00 1368.00 1372.00 1377.00 1382.00
 1340.00 1373.00 1377.00 1382.00 1387.00
 1345.00 1378.00 1382.00 1387.00 1392.00
 1350.00 1383.00 1387.00 1392.00 1397.00
 1355.00 1388.00 1392.00 1397.00 1402.00
 1360.00 1393.00 1397.00 1402.00 1407.00
 1365.00 1398.00 1402.00 1407.00 1412.00
 1370.00 1403.00 1407.00 1412.00 1417.00
 1375.00 1408.00 1412.00 1417.00 1422.00
 1380.00 1413.00 1417.00 1422.00 1427.00
 1385.00 1418.00 1422.00 1427.00 1432.00
 1390.00 1423.00 1427.00 1432.00 1437.00
 1395.00 1428.00 1432.00 1437.00 1442.00
 1400.00 1433.00 1437.00 1442.00 1447.00
 1405.00 1438.00 1442.00 1447.00 1452.00
 1410.00 1443.00 1447.00 1452.00 1457.00
 1415.00 1448.00 1452.00 1457.00 1462.00
 1420.00 1453.00 1457.00 1462.00 1467.00
 1425.00 1458.00 1462.00 1467.00 1472.00
 1430.00 1463.00 1467.00 1472.00 1477.00
 1435.00 1468.00 1472.00 1477.00 1482.00
 1440.00 1473.00 1477.00 1482.00 1487.00
 1445.00 1478.00 1482.00 1487.00 1492.00
 1450.00 1483.00 1487.00 1492.00 1497.00
 1455.00 1488.00 1492.00 1497.00 1502.00
 1460.00 1493.00 1497.00 1502.00 1507.00
 1465.00 1498.00 1502.00 1507.00 1512.00
 1470.00 1503.00 1507.00 1512.00 1517.00
 1475.00 1508.00 1512.00 1517.00 1522.00
 1480.00 1513.00 1517.00 1522.00 1527.00
 1485.00 1518.00 1522.00 1527.00 1532.00
 1490.00 1523.00 1527.00 1532.00 1537.00
 1495.00 1528.00 1532.00 1537.00 1542.00
 1500.00 1533.00 1537.00 1542.00 1547.00
 1505.00 1538.00 1542.00 1547.00 1552.00
 1510.00 1543.00 1547.00 1552.00 1557.00
 1515.00 1548.00 1552.00 1557.00 1562.00
 1520.00 1553.00 1557.00 1562.00 1567.00
 1525.00 1558.00 1562.00 1567.00 1572.00
 153

9.6 Main Components of the Processing System

A flow chart of the nucleus programs and files comprising the processing system is given in Figure 9.7. After the telemetry data from the available sources were processed, spliced and packed, analyses were performed for calibration constants, and the primary processing and study could begin. Calibration constants and trajectory data were separately entered for each flight and made part of the resource parameters data base ACROK. This file is always required, and is updated as the processing progresses.

The programs used are described briefly below. Auxiliary model density and drag calculating routines are utilized as required at various stages. Utility routines for unpacking, smoothing, interpolation and optimization were required, and were available from the IMSL and other working libraries on the CYBER.

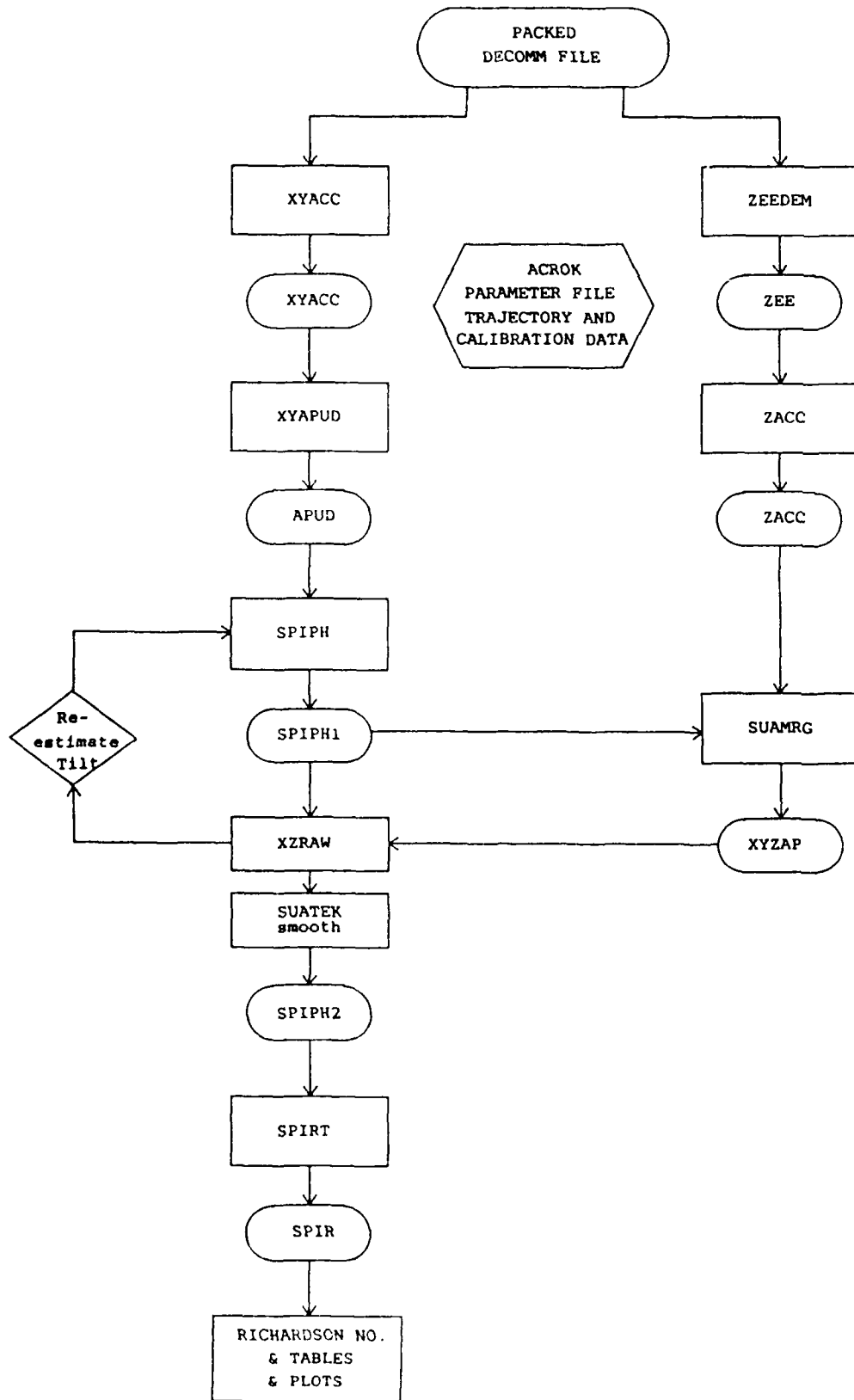


Figure 9.7 Rocket Sphere Processing System
(Main procedures only are shown)

PROGRAM XYACC

Input: The packed Decomm data file

Output: Demodulated X-Y acceleration file XYACC containing

TIM ACC UP PH UP ACC DN PH DN

X then Y sensors ordered 4,3,2,1, 8,7,6,5 of the decomm words are processed. The sensor in the active dynamic range provides the applicable acceleration signal.

If one sensor has not yet successfully demodulated, use the acceleration and phase of the other sensor.

Consecutive samples comprising a full cycle are processed. Sine-wave fitting is used initially to discard fits that give inconsistent Amplitude or Phase.

Least squares fit for DC, Amplitude & Phase is carried out on the accepted spin cycles. A phase adjustment PHC brings X,Y phases near nominal zero, for convenience of subsequent spin rate and phase optimization. The X,Y (1,2,3,4) sensor phases are adjusted for mutual continuity.

PROGRAM XYAPUD

Obtain Upleg & downleg Accel. and Phase for X & Y sensors at uniform altitude increments.

Input: The demodulated file XYACC

Output: Accel. file APUD at uniform altitude increments:

ALT ACUP PHUP ACDN PHDN TUP TDN VXTU VXTD VZTU VZTD

Using trajectory data at uniform altitude increments:

ALT TUP TDN VZU VXU VZD VXD

Determine upleg and downleg range for smoothing
HH is the half height for smoothing.

Plot raw and smoothed sensed acceleration data

PROGRAM SPIPH

Interactively determine sphere spin rate, reference phase and orientation to match upleg-downleg cross-track winds.

Input: APUD file:

ALT, ACUP, PHUP, ACDN, PHDN, TUP, TDN, VXTU, VXTD, VZTU, VZTD
and estimated In-plane axis tilt (ALPHA),

Output: Solution file SPIPH:

ALT VYWU VYWD VXWU VXWD PHUP PHDN

Interactively optimize:

Spin rate increment,
Reference phase,
Out-of-plane inclination (BETA),
and Spin-down model coefficients.

Gain Controls

Gain = 0+ TO 1	Normal Optimization
Gain = 0	Display Wind, Phase, & Revise Ratio
Gain = 2+	Also write SUATEK format TAPE1
Gain = -1	Optimize using last parameters
Gain = -2+	Stop

Select parameter set being optimized using

IIIIIII Controls
I = 0 Parameter fixed
I = 1 Optimize parameter

PROGRAM ZEEDEM

Input: Packed Decomm data file
Output: Demodulated Z-Nut Counts file ZEE

Use two precession cycles for each estimate
Take every other sample (every fourth for AC17)

PROGRAM ZACC

Obtain Zero bias and Gain for cross-over continuity
and create composite ZACC, Counts and Altitude file

Input: Demodulated Z-Nut Counts file ZEE
Output: Calibrated Z-acceleration file ZACC
Merge with APUD file to give XYZAP file

Match optimized Z2-Z3-Z4 Gain ratios to geom. mean of CALS

New $ZCAL2 * ZCAL3 * ZCAL4 = Old ZCAL2 * ZCAL3 * ZCAL4$
New Nut CAL is based on Gain Ratio only.

Full results for sensor transition studies are printed out.

PROGRAM XZRAW

ALPHA, RHOCD, WIND estimate from XYACC, ZACC, and Trajectory

Input: XYZAP file (APUD + ZACC)

Outputs:

Optional SPIPH Wind and Phase results file
Revised SPIPH file including low Alt. In-track Wind

Estimate ALPHA

If Upleg XYACC is unavailable,

Option 1: Assume Zero Wind (DN-Z-Wind mode)
and estimate ALPHA

Option 2: Assume Fixed ALPHA (DN-Z-Alpha mode)
and calculate VXW

PROGRAM ERRAN

Error analysis for RHOCD, VXW, and VYW
as a function of CAL, VXT, VZT, ALPHA, and PHI

Inputs: SPIPH file
XYZAP file (APUD + ZACC)

Output: Tabulated profile of sensitivity of solution
to uncertainties in original input parameters.

PROGRAM SPIRT

Obtain Density and Temperature profiles
from final pass ALPHA, RHOCD, WIND solution.

Inputs:

XYZAP file
SPIPH Wind and Phase results file

Output:

SPIR file includes final density and wind profiles.

Possible processing options:

- 1) ZACC assumed available below XYUP data,
but may end below or above XYDOWN data.

If all upleg and downleg measurements are available,
calculate, but note that results can be unreliable.

Correct Cross-track Wind VYW for new RHOCD; below BOT
use ZACC based VXW solution to revise VXW=0 SPIPH file.

- 2) XYDOWN only, ignoring ZACC and XYUP.

Start iterative solution of Density, Temperature profiles,
processing every record, i.e. at 250 m. intervals.

Temperature iteration loop:

Smooth
Take Antilog before integration
Integrate RHO profile

Calculate the drag coefficient using Whitfield model
and free molecular flow equation.

PROGRAM RICHNO

Richardson Number using SPIR file

Limit the analysis to 1/2 km intervals from 55 to 150 km.

SUBROUTINE ACROK(NNN)

This subroutine reads the "ACROK" resource file data base for the rocket sphere specified alphanumerically as "NNN". The parameters from "ACROK" are stored in labelled COMMON for selective use as required by any processing program.

SUBROUTINE ATMOS

This routine provides the U.S. Std 1976 atmospheric model i.e. Density, Temperature and Molecular Weight vs. Altitude. This routine includes values from 38 to 195 km only. Entry "ATMOQ" simply loads these values into COMMON.

Entry "ATMOS" also reads in the In-track and Cross-track Wind profile solutions determined by the routine SPIPH. The system expects the profile to be covered at 1/4 km intervals over any or all of the range from 50 to 160 km. Unfilled portions are zero-filled.

Entry "ATMOD" replaces the U.S. Std 76 Density and Temperature by the solutions of the rocket sphere processing analysis in order to apply the existing software to simulation studies

SUBROUTINE CDTBL

Provides Drag coefficient values CD as a double-valued function of Mach Number (values from 1.5 to 6.0) and Reynold's Number (values from 3.0 to 1.E6). CD is determined by two-dimensional interpolation.

SUBROUTINE ACC(ALT, RHO, RHOM, TM, TK1)

Calculate the Drag coefficient using Whitfield model and free molecular flow equation.⁽⁷⁾

References

- 1) Philbrick, C.R., McIsaac, J.P., and Bhavnani, K.H., "Atmospheric Structure Associated with Dynamical Processes in the Mesosphere and Lower Thermosphere", IAGA Symposium, Edinburgh, 8/81
- 2) Philbrick, C.R. et al, "Vertical Density and Temperature Structure over Northern Europe", Advances in Space Research, 83, Vol II.
- 3) Philbrick, C.R. et al, "Temperature Measurements during the CAMP Program", Advances in Space Research, 84, Vol IV.
- 4) Sipler, D.P., and Philbrick, C.R., "Neutral Atmospheric Properties Measured during the STATE Experiment", EOS Trans. Amer. Geophys. U., 65:1032, 1984 (Abstract).
- 5) "Analysis of Spacecraft Charging, Particle Beams and Geophysical Data Bases", Radex Final Report, AFGL-TR-83-0140, July 1983. ADA138632
- 6) Faire, A.C. and Champion, K.S.W., Space Research V, 1965.
- 7) Whitfield, D.L., "Mean Free Path of Molecules from a Surface in Rarefied Flow with Application to Correlating Drag Data", AIAA Paper No. 73-198, January 1973.

10.0 Graphics Capability for the SPAN Network

SPAN, the Space Physics Analysis Network, is a computer link between government and industrial laboratories and universities. Through the VAX780 computer, AFGL is a node on SPAN over which data and plots can be transmitted to remote sites. Procedures and programs were developed for producing plot metacode files on the CYBER using the NCAR graphics library, and transmitting these files to the VAX, and thence to the remote sites using SPAN.

Operation from the CYBER has been facilitated by providing a library of routines which are compatible with the TEKSIM library, so that no new programming is required. The resulting metacode may be plotted directly, or it may be hyperchanneled to the VAX. For the latter case, a VAX program CONVMET has been developed to translate the hyperchanneled code into proper VAX/NCAR metacode suitable for plotting or for SPAN.

10.1 Introduction

The presence of large data bases and associated graphics programs on the CYBER at AFGL make it highly desirable that convenient procedures be available to convey CYBER produced plots to other installations. Plotting device independent metacode (low level plotter instructions) can be created and viewed locally. This metacode can also be transmitted to a remote site where the receiver can translate the metacode for whatever device he or she has available. The existing SPAN network makes this process both feasible and attractive. The development described in this report used an existing plot package BDISPLO, resident on the CYBER, as the test vehicle. Figure 10.1 gives a flowchart of the procedures that were employed. Section 10.6 provides a User's Guide.

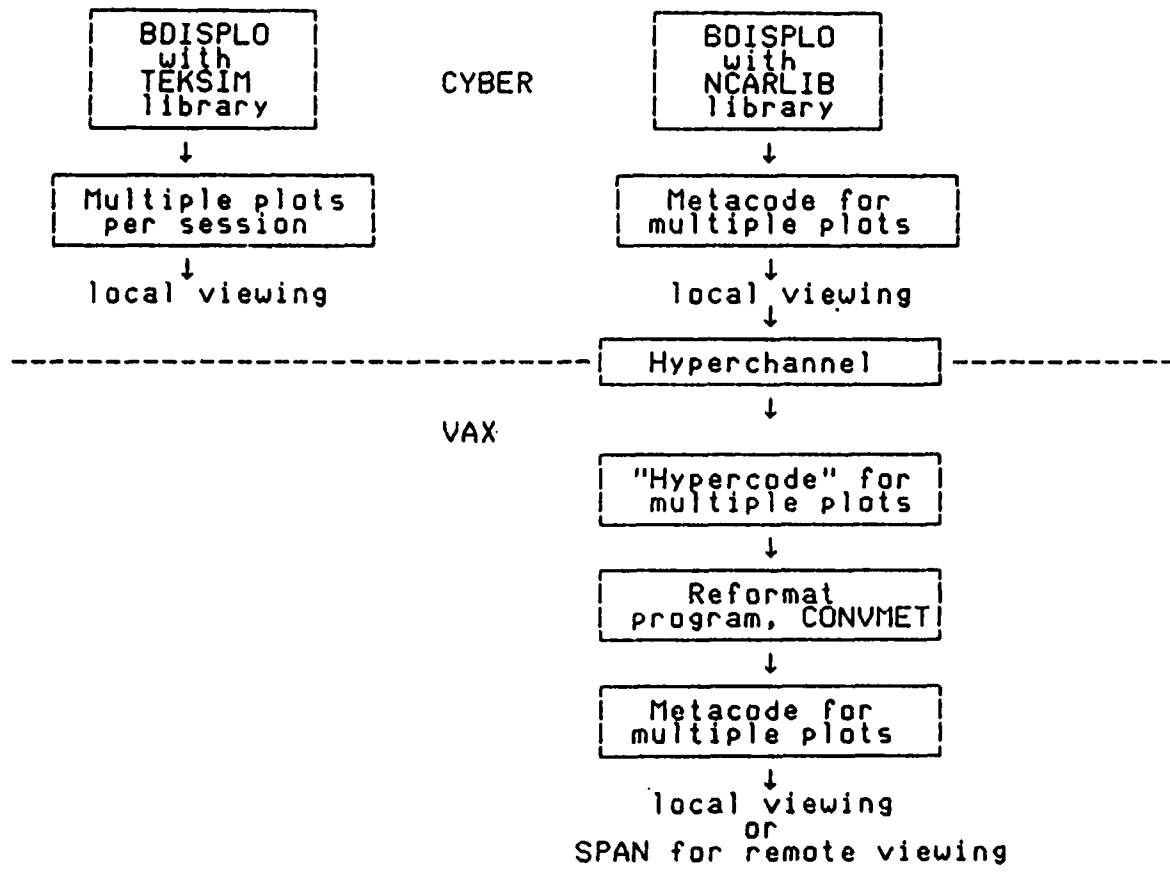


Figure 10.1 Flowchart of Procedure to Transmit BDISPLO Graphics Over SPAN

10.2 Approach

NCAR graphic routines are available on the CYBER or on the VAX and may be used to generate metacode. If the metacode is generated on the VAX, it is directly available for use at a remote site. If the metacode is produced on the CYBER, it must be hyperchanneled over to the VAX. However, metacode files generated on the CYBER are different from those generated on the VAX, and cannot be used directly. To solve this problem a VAX program, CONVNET, was written which converts the CYBER metacode to a format the VAX translator will accept. Details of the structure of the metacode at various stages of the processing are given in Reference 1.

10.3 Generating Metacode on the CYBER

To test the transmission of graphics over SPAN, we used a package BDISPLO. This program plots ground magnetometer data in a variety of ways and is currently located on the CYBER. Figure 10.2 shows a sample plot of the original BDISPLO program which uses TEKSIM plotting routines and provides graphics without producing metacode.

In order to conveniently produce metacode under these circumstances, the TEKSIM routines were equated with NCAR plotting routines, and procedures were written to call these routines in place of the TEKSIM routines. The procedures included NCAR calls for the TEKSIM procedures MICRO, PLOT, SYMBOL, NUMBER, ANMODE, and TEKGO. Also included is subroutine BLOCK, a block data file needed for NCAR. The routines that produce these CYBER metacode files are briefly described in Figure 10.3. Figure 10.4 shows that replacing the TEKSIM calls by the NCAR routines produces the same BDISPLO plot as before, except for some shortening of the X-axis.

AFGL MAGNETOMETER NETWORK FLUXGATE DATA HP .0015 .0033 0.0000 0.0000 1 100
 79 7 5 0700 0.0 79 7 5 0800 0.0

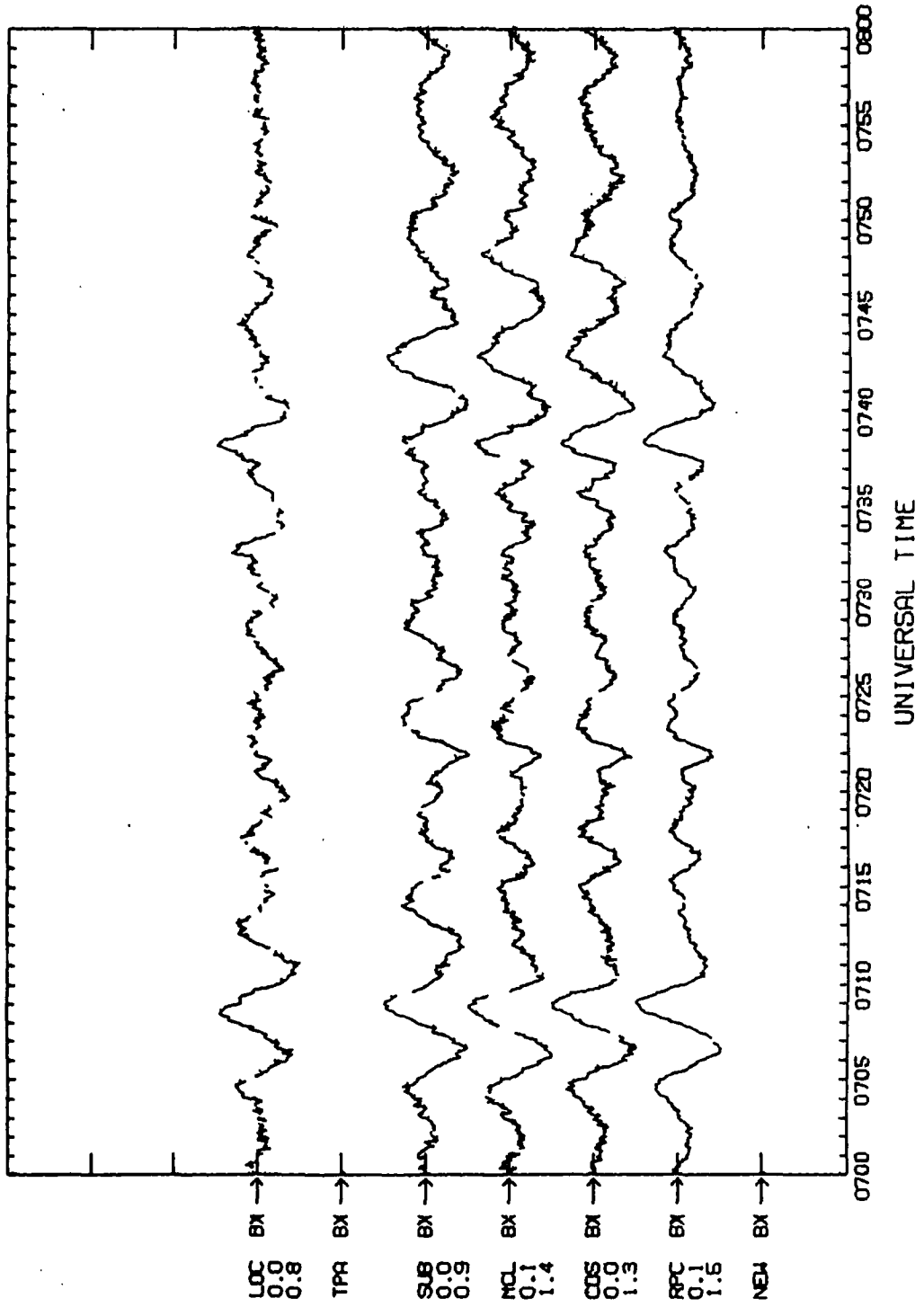


Figure 10.2 : Original BDISPLO Tektronix Plot (CYBER)

Subroutine MICRO

Functions:

Loads BLOCK DATA set into memory
Sets the scale factor for NCAR
Initializes the origin.

Calls NCAR Routines: SET

Subroutine PLOT

Functions:

Defines new coordinates
Defines new origin
Draws a line

Calls NCAR Routines: FRSTPT, VECTOR

Subroutine SYMBOL

Functions:

Defines centering option
Defines new coordinates
Defines number of characters
Defines character size
Writes the characters

Calls NCAR Routines: PWRIT

Subroutine NUMBER

Functions:

Defines centering option
Defines new coordinates
Defines character size
Converts number into characters
Writes the characters

Calls NCAR Routines: PWRIT

Subroutine ANMODE

Functions:

Re-initializes origin for next frame

Calls NCAR Routines: FRAME

Subroutine TEKGO

Functions:

Return

Subroutine BLOCK

Functions:

Loads common block SYSPLT
(variables needed by NCAR)

Figure 10.3 TEKSIM Procedures which call NCAR Routines

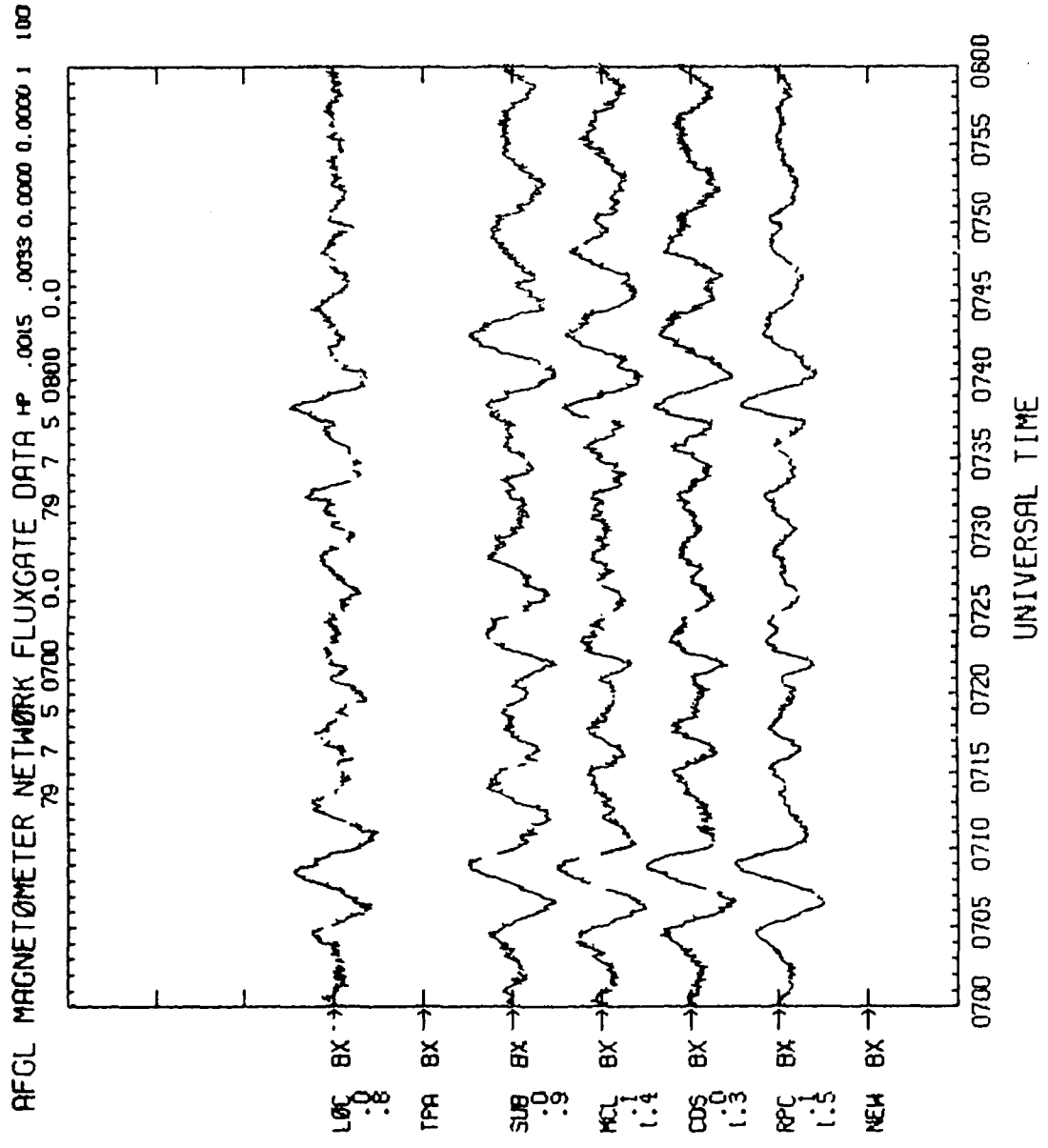


Figure 10.4 : BDISPLO Tektronix Plot Using NCAR Routines (CYBER)

10.4 Transmitting and Converting to VAX Metacode

The metacode file METACDE was then hyperchanneled to the VAX. In order to convert the hyperchanneled metacode into a format the VAX would accept, the record length, control bytes, and order of the bytes had to be changed. Program CONVMET performs these conversions.

CONVMET assumes the input file is METAHYP.DAT in an unformatted format and with variable record length. The output file, METACDE.DAT, has an unformatted format with a fixed record length of 360 longwords (or 1440 bytes since 4 bytes = 1 longword).

Figure 10.5 describes the features of the CONVMET program, and the resulting BDISPLO plot on the VAX duplicates the plot of Figure 10.4. The plots were viewed locally on the CYBER and the VAX and then sent to Marshall Space Flight Center and viewed there.

A procedure is also available for sending the NCAR metacode plot file to the VAX laser printer. The plot of Figure 10.4 is duplicated, but with the excellent quality of the laser. Information for this procedure is included in the User's Guide (Section 10.6).

10.5 Using SPAN

There are two ways to send data or metacode files over the SPAN network. The sender can mail the files to another node using the VAX's mail command. Or, the receiver can copy accessible files directly onto his or her account at the remote site.

Program CONVMET

Converts Hyperchanneled CYBER Metacode into VAX Code
using the following logical operations:

Reads 8 byte control record to establish
of 120 byte records
of last (<120 byte) record

The iterative procedure continues as follows:

Read records, including last record:

Subroutine READIN

Functions:

Reads N byte records

Put bytes into reverse order

Subroutine PUTOUT

Functions:

Move bytes into reverse order

Test for Frame or Range flags

Fill buffer with upto 1440 bytes

Output 1440 byte records

Subroutine WRITREC

Functions:

Creates first 4 control bytes

Possibilities are:

Record which is first and full

Record which is not first but full

Record which is not first and not full

Zero fill rest of record

Record which is first but not full

Zero fill rest of record

Record which is last

Write last empty record at end of file.

Figure 10.5 Description of Program CONVMET.FOR

The capability of flexibly producing and transmitting graphic information over the SPAN network using metacode has been developed and demonstrated. The metacode of choice for the present is the NCAR metacode because of its common acceptance by SPAN/VAX users. The software and procedures provided conveniently originate the plots and the metacode on the CYBER as well as the VAX.

As the requisite specifications become available, extensions to SPAN metacode and color graphics should become possible, employing the techniques described in this report.

10.6 User's Guide

(User's responses are underlined)

10.6.1 To Run BDISPLO and View Locally on the CYBER:

1. GET,BDSPRC,UN=BHAV3 (Figure 10.6 lists the procedure)
2. To run BDISPLO and generate the metacode:
BEGIN,BDSMET,BDSPRC,.....
3. Answer input questions
4. ASSIGN,MS,OUTPUT (Creates the CYBER metacode METACDE)
5. To translate the metacode i.e. see the plot:
BEGIN,TRANMET,BDSPRC
6. At the TEKTRONIX prompt, enter 1 to see next frame of the plot, 2 to save the plot, or 3 to stop.
7. When finished viewing plots, ASSIGN,TT,OUTPUT


```

.PROC, BDSMET, PF, ID.
RETURN, TAPES, TAPE1, LGO, STACK, BDSLIB, NCARLIB, PROCLIB.
RETURN, INPUT.
GET, BDS2/UN=BHAV3.
GET, BDSLIB/UN=.....
DEFINE, TAPES=METACDE.
FILE, TAPES, BT=C, RT=S.
GETP, NCARLIB.
LIBRARY, BDSLIB, NCARLIB.
FTN, I=BDS2, ER, T, EL=F.
ATTACH, TAPE1=PF/UN=ID.
LOAD, LGO.
NOGO.
STACK.
--EOR--
.PROC, TRANMET.
RETURN, TAPES, INPUT.
ATTACH, PEN=TEKSIM/UN=PLIB.
GET, INPUT=BDSBAN/UN=BHAV3.
ATTACH, TAPES=METACDE.
FILE, TAPES, BT=C, RT=S.
GETP, NCRPRO2.
BEGIN, NCARPLT, NCRPRO2.
RETURN, INPUT.
--EOR--
.PROC, HYPERCH.
ATTACH, METACDE.
GETP, HYPER.
LIBRARY, HYPER.
CDCVAX.
--EOR--
END OF FILE

```

Figure 10.8 : Listing of Procedures to Run BDISPLO with NCAR Routines and to Translate the NCAR Metacode on the CYBER

10.6.2 To Hyperchannel the Metacode from CYBER to VAX:

1. On the CYBER, create a batch job with the following:
 - a. ATTACH, METACDE.
 - b. GETP, HYPER.
 - c. BEGIN, CDCVAX, HYPER, SEND, VAX780, METACDE, SMETAHYP.DATS,
VAXUN, VAXPW, XFERID, BIT.
where
 - VAXUN= VAX username
 - VAXPW= VAX password
 - XFERID= 1 to 7 character transfer id

2. Or, interactively: (This can take very long!)
 - a. BEGIN, HYPERCH, BDSPRC
 - b. Answer questions as prompted.

3. Or, if logged onto the VAX:
 - a. \$HYPER
 - b. Press RETURN to transfer a file from the CYBER:<RETURN>
 - c. Enter RECEIVE to transfer a file from the CYBER:SEND
 - d. Enter CYBER username, or press RETURN if same as on the VAX:
 - e. Enter CYBER batch password:
 - f. Enter name of file on CYBER: METACDE
 - g. Enter name to be given to the file after it is transferred to the VAX, or press RETURN to call it filename.ext: METAHYP.DAT
 - h. The file will be placed in DRAN:[username]
 - i. Press RETURN for character file, or type BIT for binary transfer: BIT
 - j. Enter CYBER problem number:
 - k. Enter CYBER project number:
 - l. Log file will be on DRAN:[username]HYPER.LOG
 - m. Job HYPERFX (queue SYSSBATCH, entry n) started on SYSSBATCH
 - n. A message will tell you when it is transferred.

10.6.3 To Convert the Hyperchanneled Metacode from CYBER Format to Vax Format:

1. FOR CONVMET
2. LINK CONVMET
3. RUN CONVMET
4. This creates the file METACDE.DAT.

10.6.4 To Plot the Metacode on the VAX:

1. To assign logicals:
\$NCAR
2. To translate and plot the metacode file:
\$PLOT
\$meta_code option: DEVICE TT 4014
\$meta_code option: READ METACDE.DAT
\$meta_code option: PLOT

After each frame of the plot, it will ask you for another meta_code option. To plot the next frame, enter PLOT. To quit, enter EXIT.

10.6.5 To Send NCAR Metacode Plot File to VAX Laser Printer

1. \$NCAR
2. \$PLOT
3. META OPTION: READ METACDE.DAT (or whatever your metacode file name is called)
4. META OPTION: DEVICE LPC0: 4014
5. META OPTION: PLOT (Nothing will plot on the screen.)
6. META OPTION: EXIT
7. The file has now been sent to the laser printer, but it is set up incorrectly. Therefore you must delete the job from the lpc0 queue:
 - a. get the entry number by:
\$\$HO QUEUE LPC0:
 - b. then delete the job:
DELETE/ENTRY=(ENTRY #) LPC0:
8. Resubmit the job:
\$LASERTEK PLTDAT.PLT

10.7 NCAR Metacode on the CYBER and the VAX

10.7.1 Structure of an NCAR Metacode File

Each record has a fixed length, 1440 bytes on the VAX and 1920 bytes on the CYBER. The first 32 bits of each record is control information, divided into 2 fields. The first field (16 bits) contains the count of the bytes in the record, excluding the control bits. In the next field, the first 4 bits equal 0010_2 to identify the record as containing metacode. The next bit equals 1 if the record is the first one in a new frame and otherwise equals 0. The last 11 bits are unused.

The metacode instructions follow the control bytes. All frames begin on record boundaries, and if the record is not filled, the rest of the record is undefined (000_8).

The frame instruction (342000_8) follows the last metacode instructions in the last record of a frame. The range information (347010_8 plus the next 8 bytes) follows the frame op code. The last metacode instruction will usually be 16 bit no-op instructions (240040_8) which complete the last word.

The final record in the file will have no data and a 0 in the byte count field. This signals the end of the file so that multiple frames can be included in one file. NCAR metacode is always written to TAPE8.

10.7.2 File Structure of Metacode Hyperchanneled to the VAX

The structure of the hyperchanneled CYBER metacode is different from the VAX's metacode. This is caused by the hyperchannel and the difference in word size of the two computers. To simplify conversion, the following file card must be included when the metacode is generated on the CYBER:

FILE,TAPE8,BT=C,RT=S.

This creates 8 byte records, containing only the control bytes. These control records precede the records that contain the actual metacode instructions. The first 2 bytes in these records contain the byte count. Hyperchannel separates the remaining bytes into 120 byte records and any leftover bytes are located in a smaller record before the next 8 byte control record.

Reference

- 1) Hahn, K.J. and Singer, H.J., Private Communication (1986)

END

10-87

DTIC